Suspension of a Point-Mass-Loaded Filament in Non-Uniform Flows: The Ballooning Flight of Spiders

vorgelegt von
M.Eng.
Moonsung Cho
ORCID: 0000-0002-6241-1505

an der Fakultät III-Prozesswissenschaften
der Technischen Universität Berlin
zur Erlangung des akademischen Grades

Doktor der Ingenieurwissenschaften
- Dr.-Ing. -
genehmigte Dissertation

Promotionsausschuss:

Vorsitzender:	Prof. Dr.-Ing. Matthias Kraume, Chair of Chemical & Process Engineering, Technische Universität Berlin
Gutachter:	Prof. Dr. Peter Neubauer, Chair of Bioprocess Engineering, Technische Universität Berlin
Gutachter:	Prof. Dr.-Ing. Ingo Rechenberg, Bionik und Evolutionstechnik
Gutachter:	PD Dr.-Ing. Ulrich Kertzscher, Biofluid Mechanics Laboratory, Charité – Universitätsmedizin Berlin
Gutachter:	Dr.-Ing. Mariano Nicolas Cruz Bournazou, Eidgenössische Technische Hochschule Zürich

Tag der wissenschaftlichen Aussprache: 25. November 2019

Berlin 2020

Abstract

Some spiders can disperse through the air using their fine silk filaments. This is a technique referred to as 'ballooning'. Not only from an ecological point of view, but also from the perspective of physics, spiders' ballooning is an interesting phenomenon, as it relates to the question of how a large particle can disperse long distances through a fluctuating fluid medium (in this case, the Earth's atmosphere). Spiders' buoyancy capabilities can be distinguished from those of other winged insects, as a spider was the only invertebrate to be caught at a height of 15,000 ft by early researchers. It is also known that some spiders aerially disperse over several hundreds of kilometres. However, due to the lack of quantitative data regarding spiders' ballooning, the physical mechanisms of ballooning remain uncertain. Accordingly, this study resolves this uncertainty through the precise observation of spiders' ballooning. Furthermore, the fluid dynamic characteristics of the ballooning spider are described through a simulation of the ballooning structure in various fluid flows. In the present study, the ballooning silks were first identified as aciniform gland silks, which are usually used by other species as wrapping silks. The amount of ballooning silks, which was previously unknown, was also quantified. Large spiders produce tens of nanoscale silks when they engage in ballooning behaviour. A crab spider 20-25 mg in weight spin 50-60 ballooning silks, the thickness and length of which are about 200 nm and 3.22 m respectively. These silks are sizeable enough to lift large spiders into the air even with light upward air currents. It is also suggested that the reason why spiders prefer low wind speeds (under 3 m/s) for their flight is due to their usage of updrafts, which are induced by coherent structures in the atmospheric boundary layer. In a turbulent boundary layer, these updrafts are highly correlated with a low-speed regime. Additionally, the 200 nm scale of the silk thickness is considered as the smallest scale that can efficiently produce a drag force in the air flow. The drag force on a silk decreases drastically as the thickness of the silk becomes smaller than 200 nm. This is because the rarefaction of the air molecules on the silk (the mean path length of the air molecules is 65 nm) builds a slip condition on the silk. From the perspective of physics, the drag anisotropy of a spider silk is highlighted as an important factor that enables its nonlinear suspension in the fluctuating atmosphere.

Moreover, the phenomenon of becoming trapped by an eddy in turbulence is also observed by the simulation. The fibre structure (spider silk) helps a heavy particle (spider body) to remain in an atmospheric vortical structure for a long time. The spider's ballooning silk, which has a filament-like shape (extremely slender and highly flexible), is also compared with the passive flight of a point-like structure such as a dandelion or thistle seed. While a point-like structure in homogeneous turbulence showed a same distribution to the both directions of slow and fast settling, the filament-like structure in homogeneous turbulence showed a biased distribution toward slow settling (or even rising) compared to the settling speed of the structure in the still medium. While the slow decent of a maple seed is allowed by transferring the initial gravitational potential energy to its kinetic energy, the slow sedimentation of a ballooning spider originates from the turbulence by interacting with the filament. Therefore, a point mass attached to a filament-like structure can be considered as an energy-extracting structure from the turbulent flow. As a point mass-attached filament shows a nonlinear character in non-uniform flows, the dynamics of a spiders' ballooning could be interesting for the field of particle sedimentation. In addition, when considering the fact that spiders are often the first migrants to new-born volcanic islands, as well as the adaptability of the flexible filament and robustness of its passive flight dynamics in turbulent conditions, the passive flight mechanism used by spiders could be adapted by humans for the exploration of unknown new environments, such as the investigation of hazardous

weather conditions found in hurricanes or typhoons, or even of extra-terrestrial atmospheres such as those of Saturn or Jupiter.

Zusammenfassung

Einige Spinnen können sich an feinen Spinnenseiden durch die Luft verbreiten. Dieses Phänomenon heißt auf Englisch "Ballooning" bzw. auf Deutsch Fadensegelflug. Der Fadensegelflug der Spinnen ist nicht nur aus ökologischer sondern auch aus physikalischer Sicht ein interessantes Phänomen, das sich mit der Frage auseinandersetzt, wie ein massives Partikel große Entfernungen durch instationäre Luftströmungen zurücklegen kann. Die Schwebefähigkeit der Spinnen unterscheidet sich von denen geflügelter Insekten, da die Spinne der einzige Gliederfüßer ist, der in einer Höhe von 4,5 km entdeckt wurde. Einige Spinnen können sich über mehrere hundert Kilometer durch die Luft verbreiten. Da es kaum quantitative Daten zum Spinnenflug gibt, sind die physikalischen Mechanismen des Fadensegelflugs nicht bekannt. Dementsprechend löst diese Studie diese Frage durch die genaue Beobachtung des Fadensegelflugs der Spinnen und beschreibt dessen fluiddynamische Eigenschaften durch Simulationen mittels eines physikalischen Modells in verschiedenen Strömungen. In der vorliegenden Studie wurden die Flugfäden als Fesselfäden aus aciniformen Drüsen identifiziert. Die bisher unbekannte Zahl der Flugfäden wurde quantifiziert. Große Spinnen produzieren Dutzende von nanoskaligen Seidenfäden wenn sie sich auf ihren Fadensegelflug begeben. Eine Krabbenspinne mit einem Gewicht von 20 bis 25 mg spinnt 50 bis 60 Flugfäden, die etwa 200 nm dick und durchschnittlich 3,22 m lang sind. Diese Fäden sind ausreichend, um auch große Spinnen in leichter Aufwindströmung in die Luft zu heben. Es wird die Hypothese aufgestellt, dass der Grund, warum Spinnen niedrige Windgeschwindigkeiten (unter 3 m/s) für ihren Flug bevorzugen, darin besteht, dass Spinnen Aufwinde nutzen können, die durch kohärente Strukturen in der atmosphärischen Grenzschicht induziert werden. In solch einer turbulenten Grenzschicht korrelieren die Aufwinde häufig mit niedrigen Windgeschwindigkeiten. Zusätzlich wird die 200-nm-Begrenzung der Fadendicke als kleinster Durchmesser erkannt, der Widerstand im Luftstrom effizient erzeugen kann. Der Widerstand auf einen Seidenfaden nimmt drastisch ab, wenn die Dicke des Fadens kleiner als 200 nm ist, da die Verdünnung der Luftmoleküle auf der Seide (die mittlere Weglänge der Luft beträgt 65 nm) eine slip-Bedingung an der Seide erzeugt. Aus physikalischer Sicht wird die Widerstandsanisotropie eines Spinnenfadens als wichtiger Faktor erkannt, der die nichtlineare Schwebefähigkeit in der instationären Atmosphäre ermöglicht.

Darüber hinaus wird bei der Simulation das Phänomen beobachtet, dass eine fadenförmige Struktur von einem Wirbel in der Turbulenz gefangen wird. Die Fadenstruktur (Spinnenfaden) ermöglicht einem schweren Partikel (Spinnenkörper) lange Zeit in einer atmosphärischen Wirbelstruktur zu schweben. Der Fadensegelflug, welcher durch eine fadenförmige Struktur (extrem dünne und hoch flexible Seide) fliegt, wird weiterhin mit dem passiven Flug einer punktförmigen Struktur wie Löwenzahn- oder Distelsamen verglichen. Während eine punktförmige Struktur in homogenen Turbulenzen eine gleichen Verteilung ihrer Fallgeschwindigkeiten in beide Richtungen des langsamen und schnellen Sinkens zeigte, weist die fadenförmige Struktur in homogenen Turbulenzen eine exzentrische Verteilung der Wahrscheinlichkeit zur Richtung des langsamen Absinkens (oder sogar Steigens) im Vergleich zur Fallgeschwindigkeit der Struktur im stillen Medium auf. Während die langsame Absinkgeschwindigkeit eines Ahornsamens durch Übertragung der anfänglichen potentiellen Energie der Schwerkraft auf seine kinetische Energie ermöglicht wird, wird die langsame Sedimentation einer fadenförmigen Struktur durch die Interaktion zwischen den Turbulenzen mit dem Filament. Daher kann eine an einer fadenförmigen Struktur angebrachte Punktmasse als eine energie-extrahierende Struktur in der turbulenten Strömung betrachtet werden. Da eine an einer Punktmasse befestigte Faser in ungleichmäßigen Strömungen einen nichtlinearen Charakter aufweist, könnte die Dynamik

fadenförmiger Schwebekörper für das Gebiet der Partikel-Sedimentation interessant sein. Berücksichtigt man außerdem die Tatsache, dass Spinnen häufig die ersten Migranten auf neuen Vulkaninseln sind, sowie die Anpassungsfähigkeit der flexiblen Faser und die Robustheit des passiven Flugverhaltens unter turbulenten Bedingungen, könnte der passive Flugmechanismus der Spinnen vom Menschen genutzt werden, z. B. für die Erkundung unbekannter Naturphänomene, wie bei der Untersuchung gefährlicher Wetterbedingungen in Hurrikans oder Taifunen oder sogar der Atmosphäre anderer Planeten wie z.B. Saturn oder Jupiter.

List of Contents

Abstract 3
Zusammenfassung 5
List of Contents 7
Declaration of Originality 11
Dedication 13
Acknowledgements 15
List of Abbreviations 17
Symbols *(for mathematical equations)* 17
List of Publications 25
Author Contributions to the Papers 26
1. Introduction 27
2. Scientific Background 29
2.1. About Ballooning 29
2.1.1. What is Ballooning? 29
2.1.2. History 29
2.2. Ecology of a Ballooning Spider 30
2.2.1. Causes of Ballooning 30
2.2.2. Size and Families 30
2.2.3. Ballooning Methods 30
2.2.4. Large Spiders' Ballooning 31
2.2.5. Seasons and Weather Conditions 31
2.2.6. Temporal Activity and Spatial Distribution 32
2.2.7. Types of silk glands and spider silks 33
2.3. Models for Spiders' Ballooning 34
2.3.1. Lollipop Model 34
2.3.2. Flexible and Extendible Filament Model 34
2.3.3. Two-dimensional Numerical Simulation 35
2.3.4. Electric Field Theory 35
2.4. Fluid Dynamics in Ballooning 35
2.4.1. Reynolds Number 35
2.4.2. Low Reynolds Fluid-Dynamics 36
2.4.3. Anisotropic drag of a filament 36
2.4.4. Nonreciprocal Motion 37
2.4.5. Atmospheric Boundary Layer 37

2.4.6. Atmospheric Turbulence ... 38
2.4.7. Coherent Structure in the Turbulence ... 38
3. Research Questions ... 41
4. Observational Study ... 43
4.1. Methods ... 43
4.1.1. Field Observation ... 43
4.1.2. Identification of Ballooning Lines ... 45
4.1.3. Investigation of the Aerodynamic Environment ... 48
4.2. Results ... 48
4.2.1. Field Observation ... 48
4.2.2. Identification of Ballooning Lines ... 57
4.2.3. Investigation of the Aerodynamic Environment ... 61
4.3. Discussion ... 61
4.3.1. Active Sensing Motion ... 62
4.3.2. Ballooning Lines ... 63
4.3.3. Nanoscale Multifibres ... 64
4.3.4. Low Reynolds Number Fluid Dynamics ... 66
4.3.5. Usable Upward Current ... 67
4.3.6. Shear Flow ... 68
5. Dynamics in Spiders' Ballooning ... 71
5.1. Modelling ... 71
5.1.1. Bead-Spring Model ... 71
5.1.2. Shear Flow Model ... 73
5.1.3. Periodic Cellular Flow Model ... 76
5.1.4. Turbulent Model ... 77
5.2. Validation ... 79
5.3. Non-dimensional Parameter ... 81
5.4. Input Parameters ... 81
5.4.1. Shear Flow ... 82
5.4.2. Periodic Cellular Flow ... 83
5.4.3. Homogeneous Turbulence ... 84
5.5. Execution ... 85
5.6. Results ... 86
5.6.1. Shear Flow ... 86
5.6.2. Vortex Field ... 95
5.6.3. Homogeneous Turbulence ... 98

5.7. Discussion ... 105
5.7.1. Role of Anisotropic Drag of a Filament ... 105
5.7.2. Ballooning Structure in a Cellular Flow Field ... 106
5.7.3. Biased Behaviour in a Homogeneous Turbulence ... 107
5.8. Conclusion ... 109
6. Discussion ... 111
6.1. The Amount of Ballooning Silks ... 111
6.2. The Meaning of Hairy Structures ... 111
6.3. Nanoscale Spider Silk and Continuity of a Medium ... 114
6.4. The Ballooning Number ... 117
6.5. Suspension Characteristics ... 118
6.6. Coherent Structures in the Atmosphere ... 118
6.6.1. Take-off Phase ... 119
6.6.2. Suspension and Dispersal Phase ... 122
7. Conclusions ... 125
8. Outlook ... 127
9. References ... 129
10. Theses ... 141
Publications ... 143
Appendix A ... 187
Dynamic Motions in a Periodic Cellular Flow ... 187
Dynamic Motions in Homogeneous Turbulence ... 209
Appendix B ... 221
Calculation of Anisotropic Particle Drag in the High Knudsen Number Flows ... 221
i. Continuum Regime ... 221
a. Elongated Ellipsoid ... 221
b. Long Cylinder ... 222
ii. Free Molecular Regime ... 222
a. Elongated Ellipsoid ... 222
b. Long Cylinder ... 223
iii. Transition Regime ... 223

Declaration of Originality

The presented work was conducted at the chair of Bioprocess Technology, Department of Biotechnology under the scientific supervision and support of Prof. Dr. Peter Neubauer, Prof. Dr.-Ing. Ingo Rechenberg and Prof. Dr.-Ing. Klaus Affeld.

I hereby declare on oath that this submitted dissertation is entirely my own original work and that I did not make use of any other than the cited literature or other means. Working packages, supported by others are clearly indicated.

I am aware of the University's regulations concerning plagiarism, including disciplinary actions that may result from plagiarism. Any use of the published or unpublished works, in any form, of any other author is properly acknowledged and clearly referenced or cited.

This work has not yet been submitted to another examination institution – neither in Germany nor outside Germany and neither in the same nor in a similar way.

A part of the dissertation was previously published in PLoS Biology and Biomimetic and Biohybrid Systems (book).

Berlin, 30th August 2019

Moonsung Cho

Dedication

I would like to dedicate this thesis to Prof. Dr.-Ing. Klaus Affeld, who carefully reviewed this work and expressed his opinion to his replacement on the review committee when he himself was rendered unable to participate. It was a selfless act in the last days of his life for which I am eternally grateful. Thank you so much for your warm and thoughtful mind.

Acknowledgements

I would like to express my sincere gratitude to the many people who contributed in various ways to the success of this work. Firstly, I would like to thank my supervisor, Prof. Dr. Peter Neubauer, for his interest in my project and for giving me the opportunity to finish my work in his group at TU-Berlin. His supervision, support and academic guidance have genuinely shaped my scientific attitudes. My sincere thanks also go to my PhD advisor, Prof. Dr.-Ing. Ingo Rechenberg, who introduced me to the field of biomimetics (Bionik in German). His encouragement and valuable discussions on the topic made my studies more meaningful. Moreover, I would like to thank Prof. Dr.-Ing. Klaus Affeld, who engaged in many discussions with me and suggested ideas about the simulation of the model. His interest and suggestions encouraged me greatly.

Secondly, I would like to express my greatest appreciation to Dipl.-Math. Iván P. Santibáñez Koref for his incredible support, valuable and constructive suggestions and discussions throughout the entire project. I would like to thank all colleagues who helped me with the experimental setup and the establishment of the simulation model, as none of the experiments and simulations in this work would have been possible without their help: Dr. Ing. M Nicolas Cruz Bournazou, Dipl. Phys. Christoph Fahrenson, and Ulrich Berg. Furthermore, I would like to express my deepest gratitude to all members of Akaflieg Berlin. Without your assistance, encouragement, valuable discussion, and help with setting up the experiment, these results would not have been possible. I am also very thankful to Dr.-Ing. Alexander Bormann (Enerkite GmbH) and Dr. Rudolf Bannasch (Evologics GmbH); your support, both material and in terms of discussion, greatly assisted this study. I am also grateful to the Elsa-Neumann Foundation and the German Academic Exchange Service (DAAD) for their financial support, which formed the foundation stone for this study.

I would like to express my sincere gratitude to Prof. Dr. Robert B. Suter and Dr. Jason Dunlop. Although I have not yet met them, the short email communications we had during the study were very helpful to my research. In particular, Prof. Suter's previous research gave me highly valuable insights and ideas for my experiments.

I also appreciate my friends for their encouragement throughout this study, particularly Jang In-jong, Kim Hee-tae, Jo Do-yeon, Maria Fey, Klaus Fey, Ernst Schmutterer, Giesela Schmutterer, Philip Döring, Lea Eichhorn, Pia Eichhorn, Sebastian Schwabl, Alex Hadyhiski, Daniel Schramm, Vivi Waldheim, Alexandra Müller, Hendrik Kramer, Julian Schick, Julian Marzik, Tobias Beelitz, Maurice Dalton, Larissa Reuter, Zemra Skenderi, Dr.-Ing. Wladyslaw Chrusciel, Hanna Sammler-Cumana, Hwang-bo Dong-hwan, Kim Hyun-sik, Dr. Kim Jin-won, Kim Mi-jin, You Byung-jun, Seo Bong-kyun, Bong Jin-young, Dr.-Ing. Yoon Zizung, Kim Byoung-ju, Marie-yon Strücker und Luisa Keinprecht. Without their support, I would not have been able to conduct my PhD studies in Germany. My sincere and deepest thanks to my parents, Choi Chu-ja and Cho Song-jae, my brother, Cho Ji-hoon, my sister in law, Kim Eun-kyoung and my sisters, Cho Ji-young and Cho Ji-eun, my brother in law, Yang Chul-mo. Your patience, encouragement and support were vital to the success of this study. I am also very thankful to my nephews Yang Jung-yoon and Cho Hyun-woo for their joy and excitement regarding this topic.

List of Abbreviations

Symbols *(for mathematical equations)*

A	Bending stiffness
a	Radius of a sphere
a_i	Radius of the i-th bead
a_j	Radius of the j-th bead
$\boldsymbol{a}_n$	Amplitude vector of the n-th mode
$\boldsymbol{b}_n$	Amplitude vector of the n-th mode
Bn	Ballooning number
c	Characteristic length
d	Thickness of a filament (diameter, in the case of a cylindrical rod)
D_b	Horizontal component of drag on the spider's body
D_H	Drag of multiple fibres by Humphrey's equation in μN
d_i	Diameter of i-th silk fibre in m
d_L	Characteristic Diameter of a non-spherical particle
D_S	Drag of multiple fibres by Suter's equation in μN
$E(k)$	Dimensionless form of energy spectrum function
E^B	Total bending free energy
E^S	Total stretching free energy
F	Fluid dynamic force
$F_{D,con}$	Stokes' Drag of a non-spherical particle in the continuum regime
$F_{D,free}$	Drag of a non-spherical particle in the free molecular regime
$F_{D,tran}$	Drag of a non-spherical particle in the transition regime

$\boldsymbol{F}_i$	Fluid dynamic force on the i-th bead
f_i	Factor for the consideration of free end condition of the beads
$f_{i,j}$	A normalised frequency of the transition from the i-th to j-th behaviour
F_N	Resistance force (drag force) of a cylindrical slender body in the direction normal to the axis of the cylindrical slender body
F_T	Resistance force (drag force) of a cylindrical slender body in the direction tangential to the axis of the cylindrical slender body
f_{tur}	Factor of the total integration time for the simulation in a homogeneous turbulence
f_{vor}	Factor of the total integration time for the simulation in a periodic cellular flow
F_z	Resistance force of an object during sedimentation in a low Reynolds number flow
$\boldsymbol{F}_i^B$	A bending force on the i-th bead in a bead-spring model
$\boldsymbol{F}_i^F$	A fluid-dynamic force on the i-th bead in a bead-spring model
$\boldsymbol{F}_i^H$	Fluid-dynamic force on the i-th bead, which is induced by the horizontal component of the relative flow velocity (shear-induced fluid dynamic force on the i-th bead)
$\boldsymbol{F}_i^G$	A gravity force on the i-th bead in a bead-spring model
$\boldsymbol{F}_i^S$	A stretching force on the i-th bead in a bead-spring model
$\boldsymbol{F}_i^{total}$	A net force on the i-th bead in a bead-spring model
$\boldsymbol{F}_i^V$	Fluid-dynamic force on the i-th bead, which is induced by the vertical component of the relative flow velocity (geometric fluid dynamic force on the i-th bead)
F_z^H	Vertical component of net shear-induced fluid-dynamic force
$F_{z,i}^H$	Vertical component of shear-induced fluid-dynamic force on the i-th bead
F_z^V	Vertical component of net geometric fluid-dynamic force
$F_{z,i}^V$	Vertical component of geometric fluid-dynamic force on the i-th bead
g	Acceleration of gravity
g_1	Numerical constant

g_2	Numerical constant
H	Threshold parameter (size of a hole)
K	Dynamic shape factor in the continuum regime
k	Wavenumber
K'	Dynamic shape factor in the free molecular regime
k_n	Length of the n-th wavenumber vector
$\boldsymbol{k}_n$	Wavenumber vector of the n-th mode
K_N	Translational resistance coefficient of a cylindrical slender body in the direction normal to the axis of the cylindrical slender body
K_T	Translational resistance coefficient of a cylindrical slender body in the direction tangential to the axis of the cylindrical slender body
K_z	Translational resistance coefficient of an object during sedimentation in a low Reynolds number flow
k_0	Elastic constant of a spring
$K_\perp$	Dynamic shape factor of a non-spherical particle in the direction normal to the axis of the non-spherical particle for the continuum regime
$K_\parallel$	Dynamic shape factor of a non-spherical particle in the direction tangential to the axis of the non-spherical particle for the continuum regime
$K'_\perp$	Shape factor of a non-spherical particle in the direction normal to the axis of the non-spherical particle for the free molecular regime
$K'_\parallel$	Shape factor of a non-spherical particle in the direction tangential to the axis of the non-spherical particle for the free molecular regime
Kn	Knudsen number
L	Initial length of a filament (a silk or a slender body, in equilibrium state)
l	Length of a filament or a cylindrical rod
L_c	Cell size of a periodic cellular flow
l_i	Length of i-th silk fibre in m (Chapter 4)

l_i	Length of a spring between the i-th bead and the (i+1)-th bead (Chapter 5)
$l_{large\ eddy}$	Size of the largest eddy in the turbulence
L_s	Initial length of a silk
l_s	Instantaneous length of a silk
$l_{s,mid}$	Instantaneous length of a silk from the first bead to the middle between (N/2)-th and (N/2+1)-th beads
l_0	Length of the unstretched spring between the beads (chapter 5)
L_{11}	Integral length scale
m	Number of categorised behaviours
m_{spider}	Mass of a spider
N	Number of beads; number of modes
n	Number of silks
$n_{i,j}$	The number of the transition from the i-th behaviour to the j-th behaviour
N_{tur}	The total number of integration time-steps for the simulation in a homogeneous turbulence
N_{vor}	The total number of integration time-steps for the simulation in a periodic cellular flow
$p_{i,j}$	Probability of the transition from the i-th to j-th behaviour
$\boldsymbol{r}$	Position vector
R_e	End-to-end distance
$R_{e,z}$	Vertical length of an end-to-end vector
R_g	Radius of gyration
$R_{g_{lower}}$	Radius of gyration for the lower part of a silk
$R_{g_{upper}}$	Radius of gyration for the upper part of a silk

$\boldsymbol{r}_i$	Position vector of the i-th bead
$\boldsymbol{r}_j$	Position vector of the j-th bead
$\boldsymbol{r}_{ij}$	Position vector of the j-th bead from the local coordinate of the i-th bead
$\hat{\boldsymbol{r}}_{ij}$	Unit vector of the vector $\boldsymbol{r}_{ij}$
$\boldsymbol{r}_{mid}$	Position vector of a middle point in a silk
R_N	Non-dimensional resistance coefficient of a cylindrical slender body in the direction normal to the axis of the cylindrical slender body
R_T	Non-dimensional resistance coefficient of a cylindrical slender body in the direction tangential to the axis of the cylindrical slender body
R_z^H	Shear-induced non-dimensional vertical resistance coefficient
R_z^V	Geometric non-dimensional vertical resistance coefficient
Re	Reynolds number
s	Distance along a filament
t	Time
$\boldsymbol{t}_i$	Link vector between the i-th bead and the (i+1)-th bead
$\hat{\boldsymbol{t}}_i$	Unit vector of the vector $\boldsymbol{t}_i$
U	Flow velocity
$\boldsymbol{U}$	Flow velocity vector
u	Horizontal component of the flow velocity
$\boldsymbol{u}$	Flow velocity vector
u'	Streamwise fluctuating velocity
$\boldsymbol{u}'$	Fluctuating velocity vector
$\boldsymbol{u}^\infty$	Background flow velocity field
U_c	Characteristic flow velocity

U_H	Required vertical wind speed for ballooning using Humphrey's equation in m s^{-1}. (The spider's body drag is estimated from Suter's empirical relationship)
$\boldsymbol{U}_j$	Background (absolute) flow velocity on the j-th bead
$\boldsymbol{U'}_j$	Relative flow velocity on the j-th bead
u'_{rms}	Root mean squared fluctuation velocity of u'
U_S	Required vertical wind speed for ballooning using Suter's equation in m s^{-1}.
U_0	Maximum flow velocity in a periodic cellular flow
$\boldsymbol{U'}_j^H$	Horizontal component of the relative flow velocity at the j-th bead
$\boldsymbol{U}_j'^V$	Vertical component of the relative flow velocity at the j-th bead
v	Spanwise component of the flow velocity
v'	Transverse fluctuating velocity
v_{body}	Volume of a spider's body
V_D	Drift speed of a ballooning structure
v_i	Volume of the i-th bead
$\boldsymbol{V}_j$	Translational velocity of the j-th bead
V_{wG}	Wind speed profile relative to ground
V_{wR}	Wind speed profile relative to a ballooning structure
V_z	Sediment velocity (z-direction)
$V_{z,still}$	Sediment velocity (z-direction) in the still air
W	Weight of the spider body in μN
w	Vertical component of the flow velocity
w'	Vertical fluctuating velocity
W_b	Weight of the spider body

$W_{eq,i}$	Equivalent weight of the spider body corresponding to the diameter of a ballooning fibre in μN
w'_{rms}	Root mean squared fluctuation velocity of w'
W_T	Terminal velocity or sediment velocity
w_*	Convective velocity
x	Streamwise coordinate (in three dimensions)
x	Horizontal coordinate (in two dimensions)
x_0	Horizontal coordinate of the release position of the body
y	Transverse coordinate (in three dimensions)
z	Vertical coordinate
α	Particle momentum accommodation coefficient
β	Slenderness (aspect ratio) of a non-spherical particle
γ	Shear rate of a shear flow
Δt	Integration time-step
$\boldsymbol{\zeta}_{ij}$	Resistance tensor
η	Dynamic viscosity of the fluid
λ	The mean free path of a particle or a molecule
$\boldsymbol{\mu}_{ij}$	Bead mobility tensor
$\xi_\perp$	Resistance coefficient of a cylindrical slender body in the direction normal to the axis of the cylindrical slender body
$\xi_\parallel$	Resistance coefficient of a cylindrical slender body in the direction tangential to the axis of the cylindrical slender body
ρ	Density of the fluid
ρ_{air}	Density of the air
ρ_{body}	Density of a spider body or a weight

ρ_{fluid}	Density of fluid
ρ_f	Density of fluid
ρ_i	Density of the i-th bead
σ	Root-mean-square fluctuation velocity
ψ	Stream function
ω_n	Frequency of the n-th mode
$<>$	Average
$\otimes$	Tensor product

List of Publications

Peer-Reviewed Journal Publications and Chapters

I. **Cho MS**, Neubauer P, Fahrenson C, Rechenberg I. (2018) An observational study of ballooning in large spiders: Nanoscale multifibres enable large spiders' soaring flight. *PLoS Biology* 16(6): e2004405. https://doi.org/10.1371/journal.pbio.2004405 Selected **as Research Highlights in Nature** (Nature 558, 347 (2018))

II. **Cho MS**, Affeld K, Neubauer P, Rechenberg I. (2018) Spiders' ballooning flight as a model for the exploration of hazardous atmospheric weather conditions. *In book: Biomimetic and Biohybrid Systems* January 2018, 110-114. https://doi:10.1007/978-3-319-95972-6_12

Articles in Magazines and Media

I. **Cho MS.** (2019) How spiders catch the air for their flight. *TheScienceBreaker* - ISSN 2571-9262 https://doi.org/10.25250/thescbr.brk188

II. Schumacher M, **Cho MS**, Morley EL, Hormiga G, Suter RB. (2019) 'Soaring spiders.' *National Geographic*, May 2019, pp. 28-29.

Author Contributions to the Papers

Paper	Co-author	Contribution
I	Moonsung Cho	Writing the paper, all experimental work, analysis, simulations
	Peter Neubauer	Supervision, project conceptualization, major input in the storyline/framework of the paper
	Christoph Fahrenson	SEM operation and observation
	Ingo Rechenberg	Supervision, project conceptualization
II	Moonsung Cho	Writing the paper, all experimental work, simulations, analysis
	Klaus Affeld	Supervision, helped in simulation concept, framework of the paper
	Peter Neubauer	Supervision
	Ingo Rechenberg	Supervision

* All co-authors read the papers and did minor corrections to the write-up.

1. Introduction

The aerial dispersal of spiders, which is known as 'ballooning,' enables their wide range of migration. It has been well understood that spiders can disperse over hundreds of kilometres since the phenomenon was famously documented by Charles Darwin (1845). Later, some spiders were caught a few kilometres above sea level (Glick 1939). However, due to the difficulties associated with observing the ballooning silks and the limited awareness of spiders' ballooning flight, little is known about the ballooning mechanism of spiders.

Spiders' ballooning is an important factor in agricultural economy and ecology, as spiders are highly ranked predators of arthropods and impact on prey populations (Reynolds et al. 2006). Spiders' ballooning is interesting not only from the standpoint of biology, but also from that of physics, as a spider is regarded as the heaviest particle (object) that passively disperses through the air. What enables these large particles to disperse all over the globe?

A number of models have tried to explain spiders' high buoyant[(1)] capability (aerial dispersal capability). There are two representative aspects to the study of ballooning. One is from the viewpoint of fluid dynamics, which is a primary factor in the passive aerial dispersal of animals and plant seeds (Humphrey 1987, Suter 1991, 1992, 1999, Reynolds 2006, Zhao et al. 2017). The other is from the viewpoint that tries to find clues from the Earth's electric field (Gorham 2013, Morley and Robert 2018). In the fluid dynamic approach, the atmospheric turbulent flow has been examined as an influential factor for high aerial dispersal capability (Suter 1999, Reynolds 2007, Zhao et al. 2017), because flexible spider silks are deformed by turbulent flows and fall slowly (Reynolds 2006). However, the question of how the physical mechanism behind this works has not yet been answered. In the Earth's electric field approach, moreover, it has recently been reported that the electric field induces spiders' pre-ballooning (tiptoe) behaviour (Morley and Robert 2018). Despite this, we still do not understand how spiders utilise electricity, how spiders charge their silks, whether the charges on the silks are enough to lift off a spider's body, etc.

From the viewpoint of fluid dynamics, the ballooning spider has a unique feature that consists of a single or many silks and a body. One end of a filament is constrained by the weight of a spider's body, while the opposite end is suspended and moves freely in the air. As, until now, particle dynamics in turbulent flow (Yudine 1959, Csanady 1963, Boyadzhiev 1973, Manton 1974, Snyder and Lumley 1971, Reeks 1977, Wells and Stock 1983, Maxey and Corrsin 1986, Maxey 1987a, 1987b, Squires and Eaton 1990, 1991, Wang and Maxey 1993, Stout et al. 1995, Fung 1997, Toschi and Bodenschatz 2009, Bergougnoux et al. 2014) and fibre dynamics in non-uniform flows (Yamamoto and Matsuoka 1993, Ning and Melrose 1999, Schroeder et al. 2005, Delgado-Buscalioni 2006, Gerashchenko and Steinberg 2006, Winkler 2006, Lindström and Uesaka 2007, Das and Sabhapandit 2008, Jo et al. 2009, Brouzet and Le Gal 2014, Delmotte et al. 2015, Verhille and Bartoli 2016, Rosti et al. 2018) have been studied separately, it is not known how the asymmetrically constrained fibre behaves in fluid flows.

The purpose of this study is to elucidate the physical mechanism of spiders' ballooning from the viewpoint of fluid dynamics. To acquire behavioural clues and quantitative data on ballooning flight, an observational study in fields and a wind tunnel experiment in the laboratory were implemented. Furthermore, to investigate the fluid-dynamical characteristics of the ballooning flight, a numerical simulation was employed and the dominant physical factors in spiders' ballooning were surveyed.

This thesis consists of eight chapters. The first chapter provides a brief introduction to the present research. The second chapter reviews and outlines the physics related to spiders' ballooning. The third

chapter introduces the research questions. The fourth chapter is concerned with observational study. The fifth chapter describes the numerical simulation of a ballooning spider under various fluid flow conditions. In the sixth chapter, all results will be discussed and compared with previous research. The seventh chapter concludes the present work and suggests possible applications of spiders ballooning. Finally, the eighth chapter outlines some suggested avenues of future research.

(1) The terms ‘buoyant’ and ‘buoyancy’ in this study do not refer the buoyant force which is exerted by a surrounding fluid, but refer ‘suspension’ or ‘floating’ in the air.

2. Scientific Background

2.1. About Ballooning

2.1.1. What is Ballooning?

In the German language, there is a specific word, 'Altweibersommer', used to indicate a period of abnormal warm and clear days from late summer to autumn. (In North America, this is referred to as 'Indian summer'.) Literally translated, the German word means 'old women's summer', because of the silvery threads often seen floating and drifting in the air during this period, which were thought to resemble an old woman's hair. The threads, however, are not in fact hair, but rather spiders' silks, also referred to as 'gossamer' in English-speaking countries. Where do these thin threads come from? At the beginning of autumn, some spiders (those that are young or small) disperse through the air using their fine silks. These spiderlings and small spiders crawl to the top of a blade of grass and spin either a single silk or multiple silks out into the wind. When the threads are pulled up by the updraft, the spiders float up into the air. In English, this phenomenon is called either the 'aerial dispersal of a spider' or 'spiders' ballooning'; in the German language, I would like to name this 'Fadensegelflug (silk-soaring flight)'.

2.1.2. History

The aerial dispersal of a spider was first reported in 1678 by Martin Lister in his book 'Historiae Animalium Angliae' (Crosby and Bishop 1936). The earliest detailed observation of a ballooning spider was documented in 1715 by a thirteen-year-old boy, Jonathan Edwards (Crosby and Bishop 1936, McCook 2006), who sketched the take-off phase of a ballooner in the rafting position (Bell et al. 2005; see Figure 2.1B). In 1827, Blackwall provided the first scientific description of tip-toe behaviour as the initial stage of spider ballooning (Blackwall 1827). The most famous observation of this phenomenon may have been that carried out and documented by Charles Darwin (1845). During his travels with the HMS Beagle near the Rio Plata Gulf in Argentina, 60 miles off the seacoast, he encountered a vast number of gossamer spiders. At first, they were captured by the rigging on the ship; later, they flew off again. From his observations, we learned that spiders can travel over hundreds of kilometres. Nowadays, many sailors report encountering spiders while sailing in the middle of the sea (Hormiga 2002). Another interesting observation is the invertebrate collection carried out by the Entomology and Plant Laboratory at the United States Department of Agriculture (Glick 1939). From 1926 to 1931, the laboratory installed insect-collecting traps on a biplane and collected flying invertebrates at various altitudes from 6 m to 4.5 km above the ground. They found a spider at an altitude of 4.5 km, the only invertebrate to be captured at such a high altitude. From these early observations, we know that the buoyant capability of a ballooning spider is somewhat different from that of other winged insects.

2.2. Ecology of a Ballooning Spider

2.2.1. Causes of Ballooning

Some spiders from different families choose aerial dispersal as their locomotion strategy. The purposes of aerial dispersal are various. Usually, spiderlings (young spiders, just a few days after eclosion from their eggs) balloon to avoid cannibalism at their birth sites, which are densely populated by hundreds of young spiders, and to reduce competition for resources (Weyman 1993, Sheldon et al. 2017). Moreover, some adult female spiders balloon to find a place for a new colony (Dean and Sterling 1985, Wickler and Seibt 1986, Schneider et al. 2001), while others balloon to search for food and mates (Dean and Sterling 1985, Simonneau et al. 2016).

2.2.2. Size and Families

Most ballooning spiders tend to be spiderlings and spiders under 3 mm in length and 0.2 to 2 mg in mass (Richter 1970, Salmon and Horner 1977, Tolbert 1977, Coyle et al. 1985, Dean and Sterling 1985, Greenstone et al. 1987, Greenstone 1990). Nevertheless, there are also a few reports on the ballooning of large spiders (3-10 mm in length, 5-150 mg in mass) (Dean and Sterling 1985, Wickler and Seibt 1986, Greenstone et al. 1987, Schneider et al. 2001). The ballooning phenomenon has been observed in families including the Linyphiidae (sheet-weaver spiders), Araneidae (orb-weaving spiders), Lycosidae (wolf spiders) and Thomisidae (crab spiders) (Richter 1970, Salmon and Horner 1977, Tolbert 1977, Dean and Sterling 1985, Greenstone et al. 1987, Morse 1992). The ballooning of adult spiders tends to be observed in wandering spiders rather than web-building spiders.

2.2.3. Ballooning Methods

There are two representative take-off methods in ballooning flight; ‘tiptoe’ and ‘rafting’ (Blackwall 1827, Cbosby et al. 1936, McCook 2006, Bell et al. 2005). If spiders perceive appropriate weather conditions for ballooning, they climb up to the highest position on a blade of grass or a tree branch and raise their abdomen, as though standing on their tiptoes, in order to position their abdomen at the highest possible level before spinning the ballooning lines. They then release a single silk, or a number of silks, into the wind current and wait until a sufficient updraft draws their body up in the air; this is known as a ‘tiptoe’ take-off (Blackwall 1827, Bell et al. 2005) (see Figure 2.1A). Another take-off method, known as ‘rafting’, involves spiders releasing their ballooning lines from a hanging position, relying on their drag line (Cbosby et al. 1936, McCook 2006, Bell et al. 2005) (see Figure 2.1B).

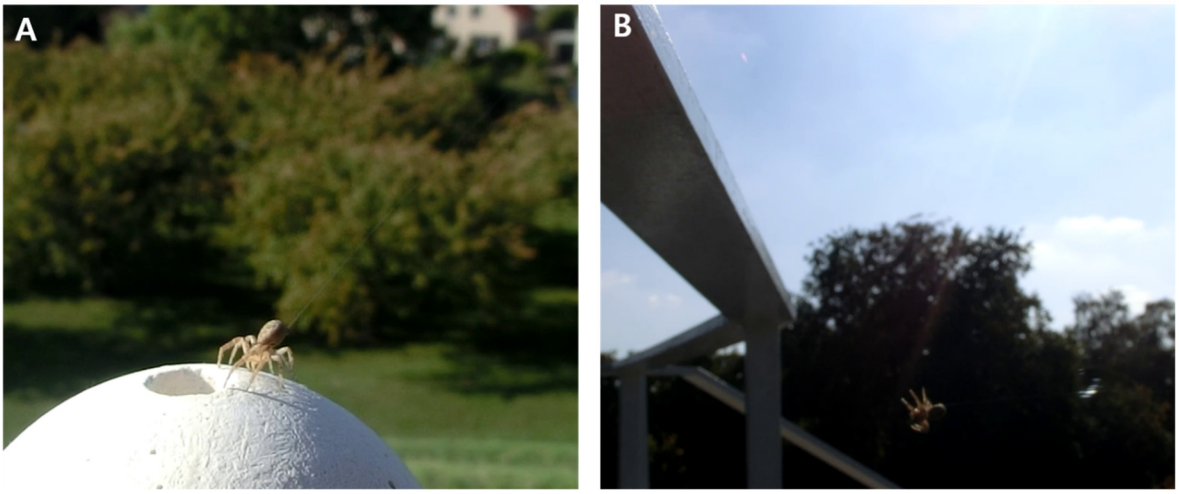

Figure 2.1 Representative ballooning behaviours of *Xysticus* spp. (A) Tiptoe take-off. (B) Rafting take-off.

2.2.4. Large Spiders' Ballooning

There has been one observation of the ballooning of large spiders, *Stegodyphus mimosarum* (85–150 mg body weight) (Wickler and Seibt 1986). This was considered very questionable at first, since the observed ballooning silks (3–4 silk threads with a length of 60–80 cm) were not enough to allow such a large spider to become airborne. From Henschel's calculations, the required vertical wind speed was 9.2–21.6 m s^{-1} (Suter 1991, Henschel 1995). However, at a later date, Schneider et al. observed that adult females of the *Stegodyphus* genus, 80–150 mg in weight, balloon using at least tens and up to hundreds of threads (Schneider et al. 2001).

2.2.5. Seasons and Weather Conditions

Spiders balloon most frequently during late spring and autumn (Salmon and Horner 1977, Dean and Sterling 1985, Greenstone 1990). The influences of microclimates on ballooning, such as temperature, humidity and wind conditions, have been extensively studied: (i) Many studies agree on a positive correlation of temperature (Richter 1970, Tolbert 1977, Vugt and van Wingerden 1976), or a rapid increase in temperature (Duffey 1956, Vugt and van Wingerden 1976, Bishop 1990, Bristowe 2004), with ballooning; (ii) low humidity is favourable for spiders to balloon (Richter 1970, Bishop 1990, Bristowe 2004); (iii) for small spiders (0.2–2 mm in length), the favourable mean wind speed is limited to 3 m s^{-1} at a level of 2 m (van Wingerden and Vugt 1974, Vugt and van Wingerden 1976, Greenstone 1990). The local favourable wind speeds were 0.35–1.7 m s^{-1} in experiments and 0.55–0.75 m s^{-1} in nature (Richter 1970, Salmon and Horner 1977, Tolbert 1977). However, these values differ for spiders of different sizes (between 0.78–1.21 mm) (Richter 1970, Richter 1971). Recently, Lee and Kuntner showed that not only the mean wind speed at a level of 2 m, but also the local wind speed needs, where spiders are located, to be below 3 m s^{-1} for spiderlings to balloon (Lee and Kuntner 2015). Atmospheric instability was also identified as an influential factor (van Wingerden and Vugt 1974, Vugt and van Wingerden 1976, Greenstone 1990, Thomas et al. 2003). Suter (1999) and Reynolds et al. (2006) additionally suggested a possible relation between spiders' ballooning behaviour and turbulent atmospheric flow.

2.2.6. Temporal Activity and Spatial Distribution

Very valuable work on the aerial distribution of arthropods has been carried out by the Entomology and Plant Laboratory at the United States Department of Agriculture (Glick 1939). From 1926 to 1931, the laboratory installed insect-collecting traps on a biplane and collected flying arthropods at various altitudes ranging from 6 m to 4.5 km. In this collection, not only winged insects but also wingless arthropods were caught; for example, spiders, mites, springtails, etc. According to the results, the flight of spiders and bees mostly happens during the day, while many other insects were active at night (see Figure 2.2). Another interesting result was that a spider's spatial density is much higher than that of other wingless arthropods (see Figure 2.3). When compared with other winged insects, the highest population density for spiders occurred at an altitude of 200 ft (about 60 m), while the population density of the other winged insects was highest near the Earth's surface (about 6 m) (see Figure 2.4). A similar tendency was found among the other wingless insects that disperse passively with the wind (see Figure 2.3).

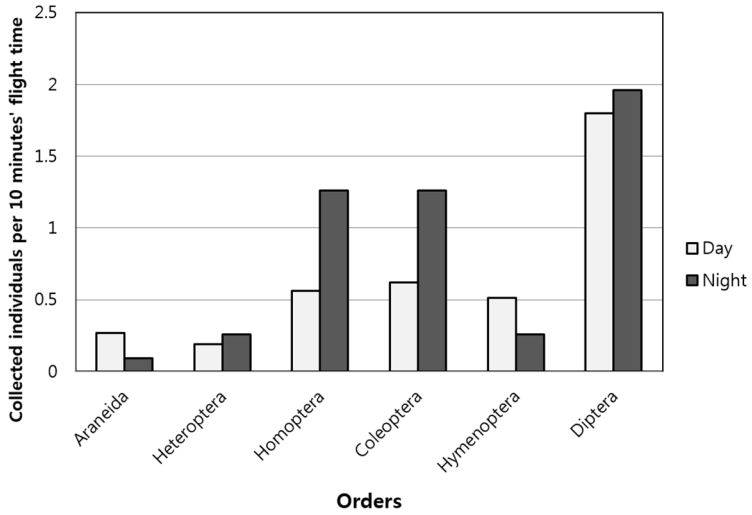

Figure 2.2 Comparison of invertebrate population between day time and night time. (Drawn from the data in Glick 1939)

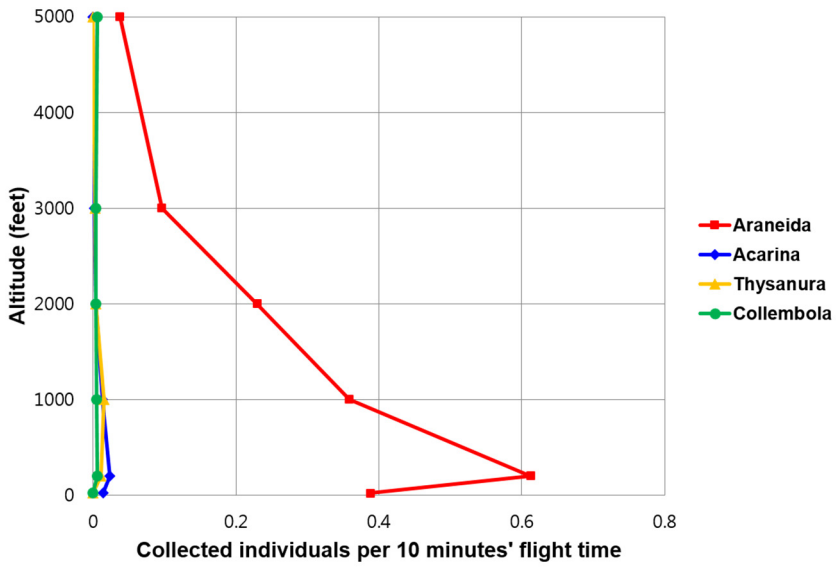

Figure 2.3 Density of wingless invertebrates versus altitude. (Drawn from the data in Glick 1939)

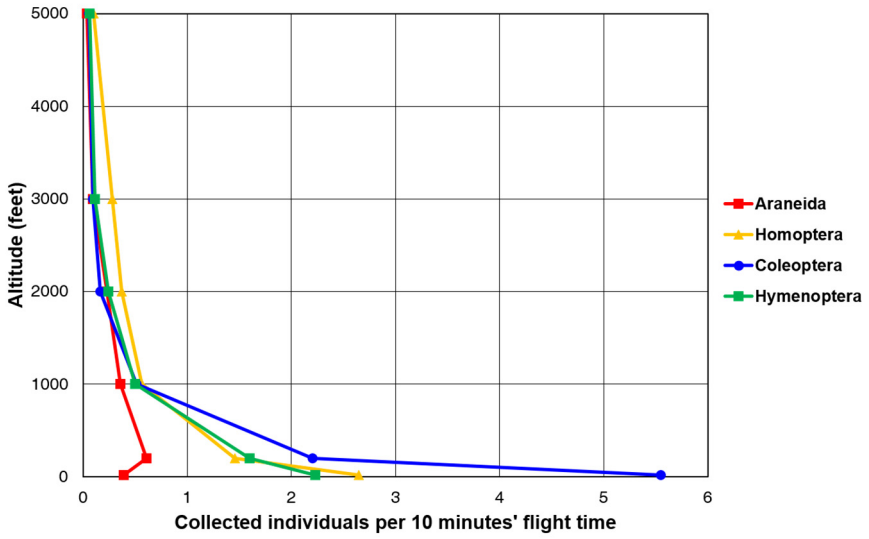

Figure 2.4 Population density plots of winged insects and one spider versus altitude.
(Drawn from the data in Glick 1939)

2.2.7. Types of silk glands and spider silks

Many spiders have six silk-spinning organs (spinnerets) in pairs (left and right): two anterior spinnerets, two median spinnerets and two posterior spinnerets. Total seven silk-glands are positioned on these spinnerets. Two to four major-ampullate silk glands, from which a dragline is produced, are on the anterior spinnerets. The silk from these major glands is used as a safety line and for the web's outer rim. Another two to four minor-ampullate silk glands are positioned in the median spinnerets. The silk from these minor-silk glands is used for temporary scaffolding during her web construction. The anterior spinneret has many piriform silk glands in addition to a few major ampullate silk glands. The silks from the piriform silk glands are used for bonding between separate spider silks, for example, during her web building. Aciniform silk glands are spread a few on the median spinneret and tens of on a posterior spinneret. The aciniform silks are used as wrapping silks for her captured prey and a sperm web in male spiders. Tubiliform (cylindriform) silk glands are on a posterior spinneret. The tubiliform silks are used as an egg cocoon silk. Flagelliform silk glands and aggregate glands are located on the posterior spinnerets. Flagelliform silk glands produce the capturing lines of the web. Aggregate glands produce a silk glue of sticky globules. (Vollrath 2000, Foelix 2011, Babu 2013; see Figure 2.5) However, this is a general description of spiders' spinnerets. The configuration of spinnerets and composition of silk glands and spigots differ depending on the genus and species. Among those various spider silks, the drag line has been known that it is used for ballooning of spiders, previously (Bell et al. 2005, Foelix 2011,).

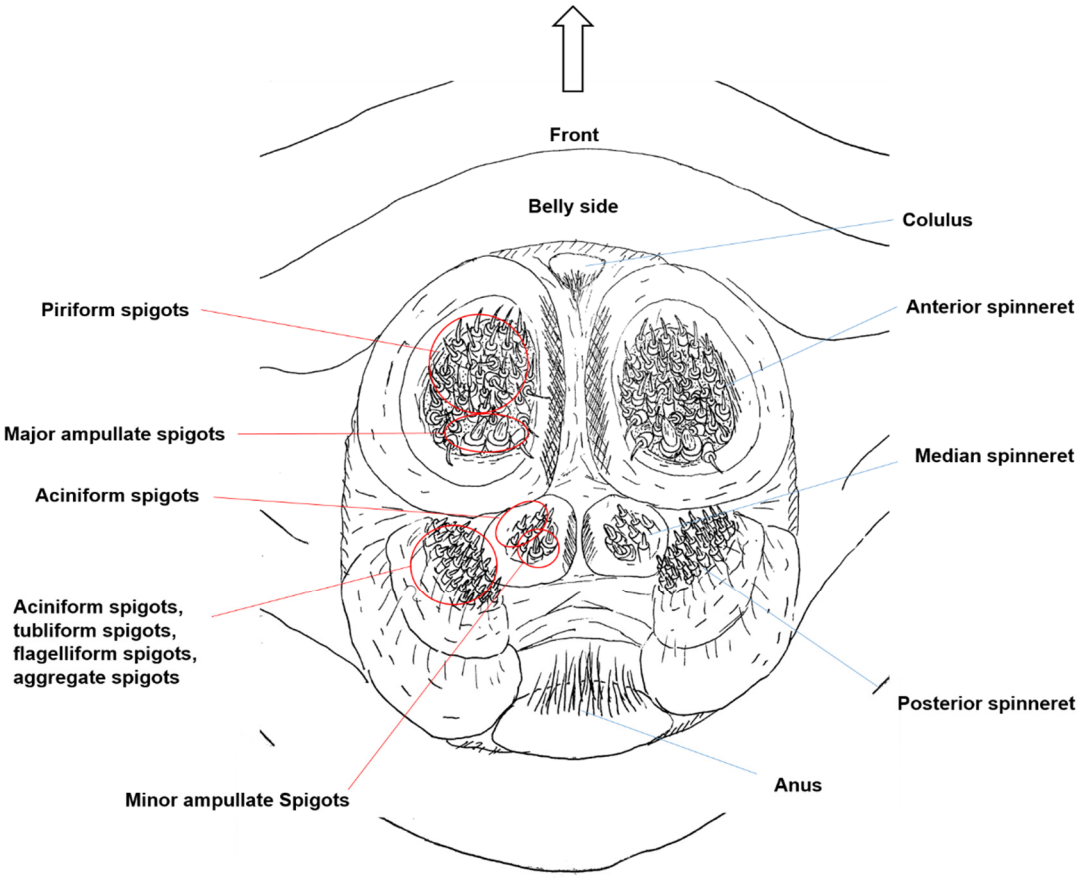

Figure 2.5 The spinnerets of a spider. Most spinnerets consist of six spinnerets (seven spinnerets including a colulus, a vestigial spinneret). Seven silk glands are distributed on the six spinnerets. Depending on the species, the number of silk spigots varies and some silk glands are omitted.

2.3. Models for Spiders' Ballooning

2.3.1. Lollipop Model

A number of models have attempted to explain spiders' high buoyancy capability (aerial dispersal capability). The first systematic study, conducted by Humphrey (1987), assumed that a spider silk was a thin, rigid and straight wire. Using the lollipop model, he identified the possible features of a ballooning spider and its silk: namely, a silk length of 0.5-4 m and a body weight of 0.5-9 mg. However, Humphrey's model could not explain the ballooning flight of spiders weighing over 9 mg, despite the fact that the ballooning of large spiders had been reported (Dean and Sterling 1985, Wickler and Seibt 1986, Greenstone et al. 1987, Schneider et al. 2001).

2.3.2. Flexible and Extendible Filament Model

A flexible and extendible filament model was suggested by Reynolds (2006). In turbulence, the flexible and extendible filament is stretched, becomes highly contorted, and exhibits a slower settling speed than that of a single-link model (this model was similar to that of Humphrey).

2.3.3. Two-dimensional Numerical Simulation

Recently, Zhao et al. (2017) implemented a two-dimensional numerical simulation using an immersed boundary method, which enabled a more detailed simulation of ballooning dynamics. The results showed that atmospheric instability facilitates longer suspension of a ballooner in the air, which agrees with the result of Reynolds' simulation. However, we still do not understand what physical properties of this structure reduce the settling speed of a ballooning structure, or how the underlying physical mechanisms work.

2.3.4. Electric Field Theory

It has also been proposed that spiders may use electrostatic charges while ballooning, a concept first put forward by Murray (Blackwall 1827). Darwin further explained that the observation of divergence among fibres may be caused by those fibres having a similar electrical condition (Darwin 1845). Gorham suggested that electrostatically charged spider silks may be pulled by the charge of the mesosphere (Gorham 2013); later, Morley and Robert (2018) demonstrated that a relatively strong electric field 6.25 kV/m induces pre-ballooning behaviour in *Erigone* spp. This is a very interesting result; however, the case in which a spider may misunderstand the motion of its sensory hairs (trichobothria) by an electric field as being caused by turbulent flow should be considered, because the study compared the response characteristic of a trichobothria by DC electric field only with the case in the uniform flow, not with the case of a turbulent flow, to which the ballooning spiders in the nature are frequently exposed and reacts (Barth et al. 1991, Suter 1999, Reynolds et al. 2006).

2.4. Fluid Dynamics in Ballooning

2.4.1. Reynolds Number

If a fluid flows over an object, the geometry, the size of the object and the properties of the fluid characterise the flow. The most basic and popular non-dimensional parameter employed to represent a flow is the Reynolds number, first introduced by George Stokes (Stokes 1851) and later popularised by Osborn Reynolds (Reynolds 1883, Rott 1990). This dimensionless quantity refers to the ratio of the inertia of fluid flow to the viscosity. The inertia force can be described by means of the dynamic pressure of the fluid flow $\rho {U_c}^2$ multiplied by the area c^2, while the viscous force can be represented by the dynamic viscosity η times the velocity shear rate U_c/c times the area c^2. Accordingly, we obtain the Reynolds number as follows:

$$Re \equiv \frac{(\rho {U_c}^2)c^2}{\eta(U_c/c)c^2} = \frac{\rho U_c c}{\eta} \tag{2.1}$$

The Reynolds number varies linearly in proportion to the density of the medium, flow velocity and the size of the object or characterised size of the fluid, but is reciprocal to the dynamic viscosity of the medium. If the Reynolds number is below 1, we conclude that the viscous force is dominant on the

fluid flow; if the Reynolds number is above 1, the inertia of the fluid flow becomes dominant. As the Reynolds number becomes larger, the fluid flow transits from a laminar flow to a turbulent flow.

2.4.2. Low Reynolds Fluid-Dynamics

As explained above, when the Reynolds number is below 1, the viscous force is dominant on the object. We term this type of flow a 'low Reynolds number flow' (Purcell 1977; this used to be referred to as a 'Stokes flow' or 'creeping flow' in other literature). A low Reynolds number flow is usually characteristic for a microscopic flow or very viscous medium. When a tiny fruit fly is wetted by a drop of water, the fruit fly struggles to escapes from the water drop; this is due to the fly's very small size compared with the kinetic viscosity of water. Additionally, the flows around microorganisms such as paramecia, E. coli, sperm, etc. also belong to the category of low Reynolds number flows (Purcell 1977). In a very viscous medium, we can also regard the flow as having a low Reynolds number. The flow of lava, a moving object in a swamp, and a spoon falling in a honey jar are further examples of low Reynolds number flows.

2.4.3. Anisotropic drag of a filament

In the fluid dynamics of spiders' ballooning, the fluid dynamic of a fibre (or filament) is very important, as spiders generally utilise their fine silk fibres for their flight. The thickness of a normal drag line ranges from 1 μm to 10 μm. Therefore, a low Reynolds number flow is also important flow characteristic on a fibre. Accordingly, we should review the dynamics of a fine fibre in a low Reynolds number flow. A very small portion of a fibre can be described as a thin and straight circular cylinder. When this thin circular cylinder moves in a thick fluid, the magnitude of the force depends on the angle of inflow. We refer to this angle-related drag as an anisotropic drag. In the case of a circular cylinder in a viscous fluid, the drag force in the direction normal to the axis of the cylinder is about twice as large as that in the direction parallel to the axis (see Purcell 1977, Childress 1981, Happel and Brenner 1986, Gauger and Stark 2006). Exact solution for an infinite cylinder has not yet been obtained. This is known as Stokes' paradox. The solution of a finite cylinder is obtained h by Burgers approximating the contour of an ellipsoid, which has the exact solution, to the more similar contour with a cylinder (Burgers 1938). Eqns. of (2.2) and (2.3) shows resistance forces of a cylindrical slender body in the direction normal and tangential to the axis of the cylindrical slender body, respectively. There are a few alternatives to express these forces in general forms. Eqns. of (2.4) and (2.5) are the resistance coefficients of a cylindrical slender body in the direction normal and tangential to the axis of the cylindrical slender body. The coefficients are independent expression of forces from the flow velocities. The forces can also be normalized by dynamic viscosity and flow velocity (see eqns. of (2.6) and (2.7)). These coefficients describe translational characteristics of an object, which is generalized from the viewpoint of flow conditions, in the low Reynolds number flow (Happel and Brenner 1986).

$$F_N = \frac{4\pi\eta U l}{ln\left(2\frac{l}{d}\right) + 0.5} \tag{2.2}$$

$$F_T = \frac{2\pi\eta U l}{ln\left(2\frac{l}{d}\right) - 0.72} \tag{2.3}$$

$$\xi_\perp = \frac{F_N}{U} = \frac{4\pi\eta l}{ln\left(2\frac{l}{d}\right) + 0.5} \tag{2.4}$$

$$\xi_\parallel = \frac{F_T}{U} = \frac{2\pi\eta l}{ln\left(2\frac{l}{d}\right) - 0.72} \tag{2.5}$$

$$K_N = \frac{F_N}{\eta U} = \frac{4\pi l}{ln\left(2\frac{l}{d}\right) + 0.5} \tag{2.6}$$

$$K_T = \frac{F_T}{\eta U} = \frac{2\pi l}{ln\left(2\frac{l}{d}\right) - 0.72} \tag{2.7}$$

2.4.4. Nonreciprocal Motion

The dynamics of a filament-shaped structure in a low Reynolds number flow was frequently studied in connection with the motion of cilia and flagella of microorganisms or cells. A sperm uses a flagellum to move forward. When a sperm in a viscous medium (Newtonian fluid) wants to move, it requires a nonreciprocal motion (see Purcell 1977). A nonreciprocal motion is one in which the motion is not identical to the previous motion in reverse (Purcell 1977, Becker et al. 2003, Najafi and Golestanian 2004, Dreyfus 2005, Gauger and Stark 2006). This non-reciprocal motion transfers the active motions of a filament in fluid medium to a force, which causes an animal to move forward. By analogy, it can be surmised that the passive motions of a spider silk in non-uniform air flow might also conduct a force that increases or reduces the settling speed of a ballooner.

2.4.5. Atmospheric Boundary Layer

In fluid dynamics, a boundary layer is defined as follows: when fluid flows around an object, the relative speed of a fluid on the surface of the object is zero, because of the viscosity of the fluid, and as the distance between the surface of the object and the measuring point increases, the relative speed of the fluid approximates the speed of a fluid flow at infinity. This velocity-changing layer is defined as the boundary layer; normally, the upper boundary is defined as 99% of the speed of a fluid flow.

This layer is influenced not only by the viscosity of the fluid, but also by additional factors; these include the temperature, the roughness of the surface, the injected flow rate at the surface, etc. In the Earth's atmosphere, we can also define the atmospheric boundary layer. This layer is affected by the strength of the wind, the heat provided by the sun rays and the moisture of the air.

The thickness (depth) and structure of the Earth's atmospheric boundary layer always changes depending on the time of day. In the daytime, the air usually becomes unstable due to the energy provided by the sun, resulting in a thicker atmospheric boundary layer. At night, the influence of the sun is reduced and the boundary layer becomes thinner and more stable (Stull 1988).

2.4.6. Atmospheric Turbulence

In fluid dynamics, turbulent flow is defined as when the flow velocity at a fixed point varies erratically in magnitude and direction (Merriam 2019). This flow is generally observed in cases where the velocity gradient of a fluid flow exists. If the velocity gradient is not strong, only a laminar flow exists; by contrast, if the gradient is strong enough to make the flow unstable, then the flow becomes a turbulent flow and exhibits chaotic motion of the fluid flow. The flow of air over the wing of a fast-flying aircraft, the wake flow behind the chimney in wind and the quickly upward developing cumulus cloud are good examples of turbulent flow.

In the atmospheric boundary layer, where wind blows over various surface terrains (such as grasses, forests and houses), the turbulent flow exists and is easily excited. This turbulence is referred to as mechanical turbulence, which is caused by surface geometry and friction on the Earth. In addition, when the sun shines, the density of the air becomes nonhomogeneous (depending on the specific heat conditions of the ground surfaces), and the buoyant instabilities cause convective turbulence. While the thickness of a boundary layer in the laboratory ranges from a few millimetres to centimetres, that of the atmospheric boundary layer extends from a few hundreds of meters to kilometres.

One of the important aspects of these atmospheric turbulent flows is the exchange of the heat, moisture and momentum of the air between the upper and lower atmospheric boundary layers (Robinson 1991, Adrian 2007, Rossi et al. 2010). Therefore, the influence of atmospheric turbulence should be studied in relation to the aerial dispersal of spiders.

2.4.7. Coherent Structure in the Turbulence

Recently, it has been revealed that the coherent structure in the turbulent boundary layer plays an important role in this vertical momentum transfer (Lu and Fitzjarrald 1994, Raupach et al. 1996, Brunet and Irvine 2000, Finnigan 2000, Ganapathissubramani et al. 2002, Thomas and Foken 2007, Finnigan et. al 2009, Steiner et al. 2011, Damian 2016, Harun and Reda Lofty 2018). The coherent structure in the turbulent boundary layer is defined as a flow structure that maintains its form for long periods so as to catch our eye in a flow visualisation and/or contribute significantly to time-averaged statistics of the flow (Adrian 2007). The simplest model of this, as introduced by Theodorsen (1952), is a horseshoe vortex (see Figure 2.6). The horseshoe vortex is a curved vortex filament that has a head and their two legs touch the wall. The two legs of the vortex filament inclined to the direction of a down flow (Theodorsen 1952, Adrian 2007, Dennis 2015). An upward current exists inside of this horseshoe

vortex. It has been noted that this upward current transfers mass, momentum and heat to the outer layer of the boundary layer (Robinson 1991, Adrian 2007, Rossi et al. 2010). Coherent structures can be found in the form of horseshoe vortex, hairpin vortex and hairpin packet structures (Ganapathissubramani et al. 2002, Hommema and Adrian 2003, Adrian 2007). Moreover, these structures do not only exist within laboratory experiments; recently, they have been found in the atmospheric boundary layer over plant canopies, forests, etc. (Raupach et al. 1996, Brunet and Irvine 2000, Finnigan 2000, Ganapathissubramani et al. 2002, Thomas and Foken 2007, Finnigan et. al 2009, Steiner et al. 2011, Damian 2016, Harun and Reda Lofty 2018).

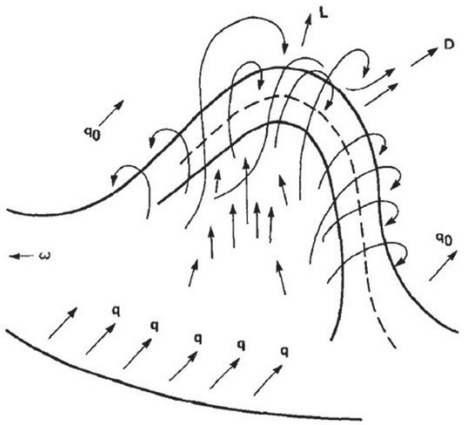

Figure 2.6 Theodorsen’s depiction of a horseshoe vortex (from Theodorsen 1952)

3. Research Questions

In this study, I would like to introduce four research questions. Two of these are concerned with biological phenomena related to spiders' ballooning, while the other two aim to address the physical mechanisms of spiders' ballooning.

1. *How do large spiders balloon?*

One of the main problems emerging from research of spiders' ballooning involves the difficulty of obtaining quantitative data. This occurs because spiders in nature fly in turbulent wind conditions, in which the ballooning silks are almost invisible. This lack of quantitative information has given rise to the question of whether large spiders (9-150 mg in weight), can balloon with light upward currents.

2. *Why do spiders prefer low wind speeds, under 3 m/s, when engaging in their ballooning behaviour?*

The most interesting question related to spiders' ballooning concerns the fact that spiders usually fly in wind speeds under 3 m/s (Richter 1970, van Wingerden and Vugt 1974, Vugt and van Wingerden 1976, Salmon and Horner 1977, Tolbert 1977, Greenstone 1990, Lee and Kuntner 2015). We do not understand why spiders select low wind speed conditions for their flight; could it be that low wind speed is advantageous for their take-off, or do spiders simply prefer no-violent and mild conditions?

3. *What is the role of the anisotropic drag of spider silks in ballooning?*

In the locomotion of the micro-swimmer, the anisotropic drag of a cilium and a flagellum is a very important characteristic during their undulatory and/or non-reciprocal motions. A spider silk is also a filament structure in a low Reynolds number flow. Therefore, the anisotropic character of a spider silk may play a role in spiders' aerial dispersal capability.

4. *If a flexible silk is exposed to wind velocity fields with different magnitudes and vectors, are there any advantages compared with a point-like drag producer (for example, dandelion seeds and thistle seeds)?*

Compared to other passive flyers (such as dandelion and thistle seeds), the unique aspect of spiders' ballooning is that a spider silk is generally a few metres in length, far larger than the size of an aerial seed. Therefore, each segment of a spider silk is exposed to various wind velocity fields, while the aerial seed is exposed to an almost uniform velocity field because of its tiny scale. The integrated force along the silk in non-uniform flows may be related to spiders' high buoyancy capability.

4. Observational Study

Despite the existence of a large body of previous research investigating spiders' aerial dispersal, the dynamics underpinning spiders' ballooning are still not well understood owing to the small number of observations of ballooning behaviour and related studies. Many of the ballooning spiders are very small, with weights of 0.2–2 mg, and are thus difficult to study (Richter 1970, 1971, Tolbert 1977, Lee and Kuntner 2015). Moreover, many experiments have assumed that spiders use a drag line of a certain length (Suter 1991, 1992, Bell et al. 2005). Therefore, as a first step towards clarifying this phenomenon, I studied the ballooning behaviour of relatively large spiders (heavier than 5 mg) in nature. Additional wind tunnel tests to identify ballooning silks were implemented in the laboratory. From our observations, it appears obvious that spiders actively evaluate the wind conditions with their front leg (leg I) and wait for the wind conditions to be preferable for their ballooning take-off. Furthermore, in the wind tunnel tests, previously unknown physical properties of ballooning fibres (length, thickness, and number of fibres) were identified.

4.1. Methods

4.1.1. Field Observation

Crab spiders *(Xysticus cristatus*, *X. audax*, etc., see Figure 4.1) were collected at Lilienthal Park and along the Teltow Canal in the Berlin area, Germany, and observed each autumn, especially during October, from 2014 to 2016. Lilienthal Park was selected for the observation of pre-ballooning behaviour as the ballooning phenomenon is frequently observed among adult and subadult crab spiders in this region.

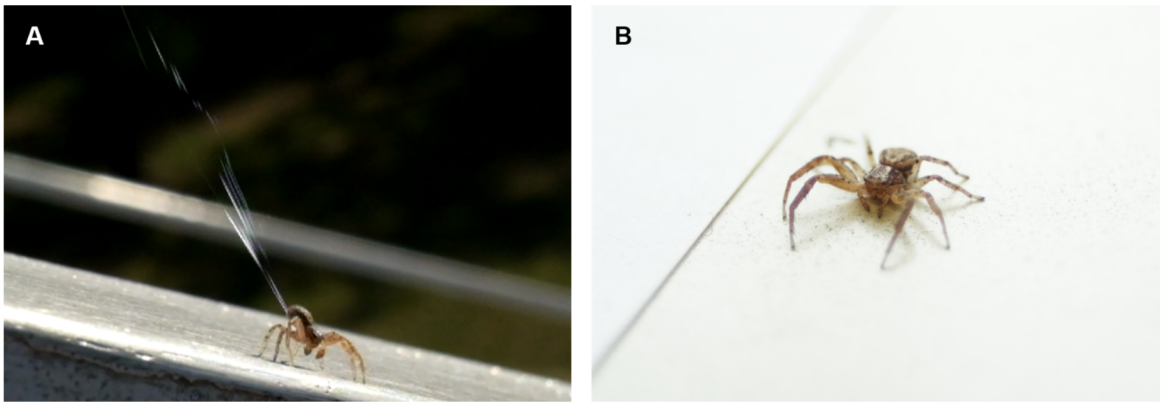

Figure 4.1 The photos of a crab spider (*Xysticus genus*) (A) Tiptoe take-off in the field (the moment just before takeoff). (B) The photo of a *Xysticus cristatus.*

4.1.1.1. Take-off

On sunny and partly cloudy days in autumn, 14 crab spiders (eight females, two males, and four not identified; adults or subadults) were collected at Lilienthal Park. These spiders were released in the same place on a self-built artificial mushroom-like platform (a 5.5 cm diameter half-sphere, 1.2 m above a ground surface, gypsum material). This platform was intended to stimulate tiptoe pre-

ballooning behaviour. Because of its convex (half-sphere) surface, spiders could easily recognise the top of the convex surface as the highest position, which was believed to encourage tiptoe behaviour. Moreover, the white colour of this platform enhanced the visual clarity when observing the spiders' behaviour. During those observations, the ballooning behaviours were recorded by digital camera. Additionally, titanium tetrachloride was used for the visualisation of the wind flow. While the local wind speed and temperature were not measured directly, the values from the Dahlem weather station (4.5 km distance from the observation site; anemometer installed 36 m above the ground in the 20 m-high forest canopy) can provide approximate conditions.

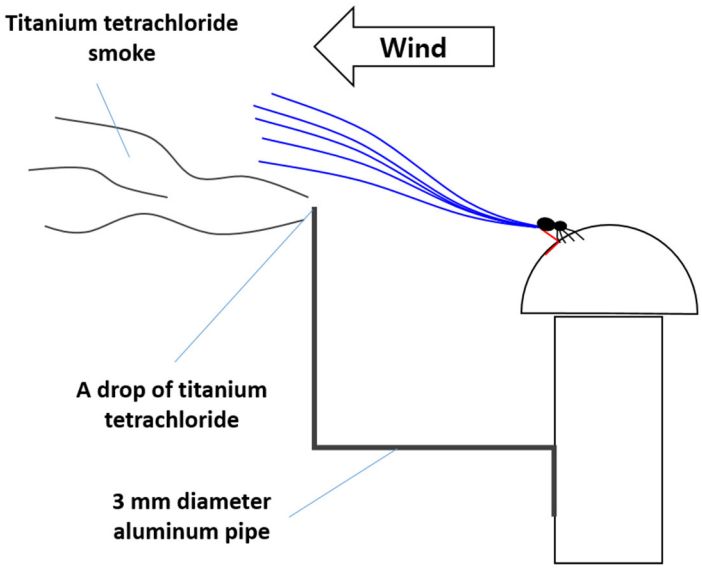

Figure 4.2 The take-off platform setup for ballooning. The device producing titanium tetrachloride smoke was installed behind the mushroom-like platform. This minimised the likelihood of the smoke affecting the spiders' behaviour.

4.1.1.2. Statistical Analysis of Pre-ballooning Behaviours

The 14 crab spiders were set onto the mushroom-shaped platform a total of 27 times in natural weather. The detailed pre-ballooning behaviours in the 'take-off' observation were analysed statistically according to the following categories: (i) active sensing motion; (ii) tiptoe motion; (iii) tiptoe take-off; (iv) drop down; and (v) rafting take-off (see 'Take-off' in the results section). If they did not tend to balloon or hid for about five minutes, they were recollected. If a spider raised one or both front legs (leg I) and then put them back down again on the platform, this was considered to be an active sensing motion and was counted as one behaviour. A tiptoe motion, i.e. raising the abdomen and putting it down again, was also counted as one motion. The transitions between behaviours were also counted. These numbers were first expressed as a percentage frequency by normalising with the total number of transitions (see Eqn (4.1)). The probability of moving from one behaviour to the next behaviour is expressed by normalising with the total number of previous behaviours (see Eqn (4.2)).

$$f_{i,j} = \frac{n_{i,j}}{\sum_{i=1}^{m}\sum_{j=1}^{m} n_{i,j}}, \sum_{i=1}^{m}\sum_{j=1}^{m} f_{i,j} = 1 \tag{4.1}$$

$$p_{i,j} = \frac{n_{i,j}}{\sum_{j=1}^{m} n_{i,j}}, \sum_{j=1}^{m} p_{i,j} = 1 \tag{4.2}$$

4.1.1.3. Gliding

The gliding of crab spiders was observed in the autumn along the Teltow Canal, due to the ecological and topographical benefits offered by this location for the observation of ballooners: (i) crab spiders frequently glide along the canal during autumn; (ii) the angle of the sun's rays in the morning was appropriate for the detection of the ballooning silks during their flight; (iii) the dense trees on the opposite side of the canal provide a dark background, which facilitated the observation of floating silks. The shape of the threads during flight could not be photographed nor recorded on video, as only limited parts of the ballooning threads were reflected by the sun's rays; however, the movement and shape of the threads could be recognised with the naked eye, and these shapes could be quickly sketched by hand.

4.1.1.4. Landing

The landing of crab spiders was also observed along the Teltow canal due to the abovementioned benefits offered by this location. Again, the shapes of ballooning silks were sketched and documented. Two landing events on the water surface were observed. These spiders were collected and identified in the laboratory.

4.1.2. Identification of Ballooning Lines

4.1.2.1. Sampling of Ballooning Lines

Twelve crab spiders (nine females and three males; adults or subadults) were used for the wind tunnel experiment. Pre-ballooning behaviour of these spiders was induced in front of an open jet wind tunnel where the diameter of the nozzle exit is 0.6 m (see Figure 4.3A). The spinning behaviours that led to the ballooning silks could be observed precisely under these conditions. There were no obstacles next to the wind tunnel, leaving about 9 m of free space from the nozzle to allow ballooning fibres to float horizontally without any adhesion to other objects. The wind speed and temperature were measured using a PL-135HAN hot-wire anemometer. Moreover, to enable sampling of the ballooning fibres, the wind speed was adjusted to 0.9 m s^{-1}, as spiders would drift downstream if the wind speed was above

1 m s^{-1}. The room temperature was 22–25 °C. Ballooning behaviour was stimulated with a 1,000-watt hair dryer (low-wind-speed mode) that produces warm air (28–33 °C) and wind fluctuations. The hair dryer was positioned beneath the nozzle of the wind tunnel and turned upward to avoid the spiders being directly exposed to hot wind from the hair dryer (see Figure 4.4). As soon as spiders showed tiptoe behaviour, the hair dryer was turned off. The turbulent intensity of the wind tunnel was 1.1% (without the hair dryer) and 11.3% (when the hair dryer was turned on).

There was a difference in temperature between the laboratory and the field. This difference can be explained as follows: first, ballooning behaviour is coupled not only with weather conditions but also with biological conditions, e.g., seasonal dispersal, mating, insufficient resources, etc. (Salmon and Horner 1977, Dean and Sterling 1985, Greenstone 1990, Schneider et al. 2001). If the biological pressure for spiders to disperse is high, spiders may try to disperse even though the temperature is low. Second, the sudden increase of temperature acts on ballooning behaviour as an influential factor (Duffey 1956, Vugt and van Wingerden 1976, Bishop 1990, Bristowe 2004). If there is a sudden increase in temperature—e.g., because of sunshine in the morning—the ballooning behaviour can be triggered even in low-temperature conditions. There are also some reports of spiders ballooning at relatively low temperatures (10–20 °C (Duffey 1956, Bishop 1990); 13–19 °C (the author's field observation)).

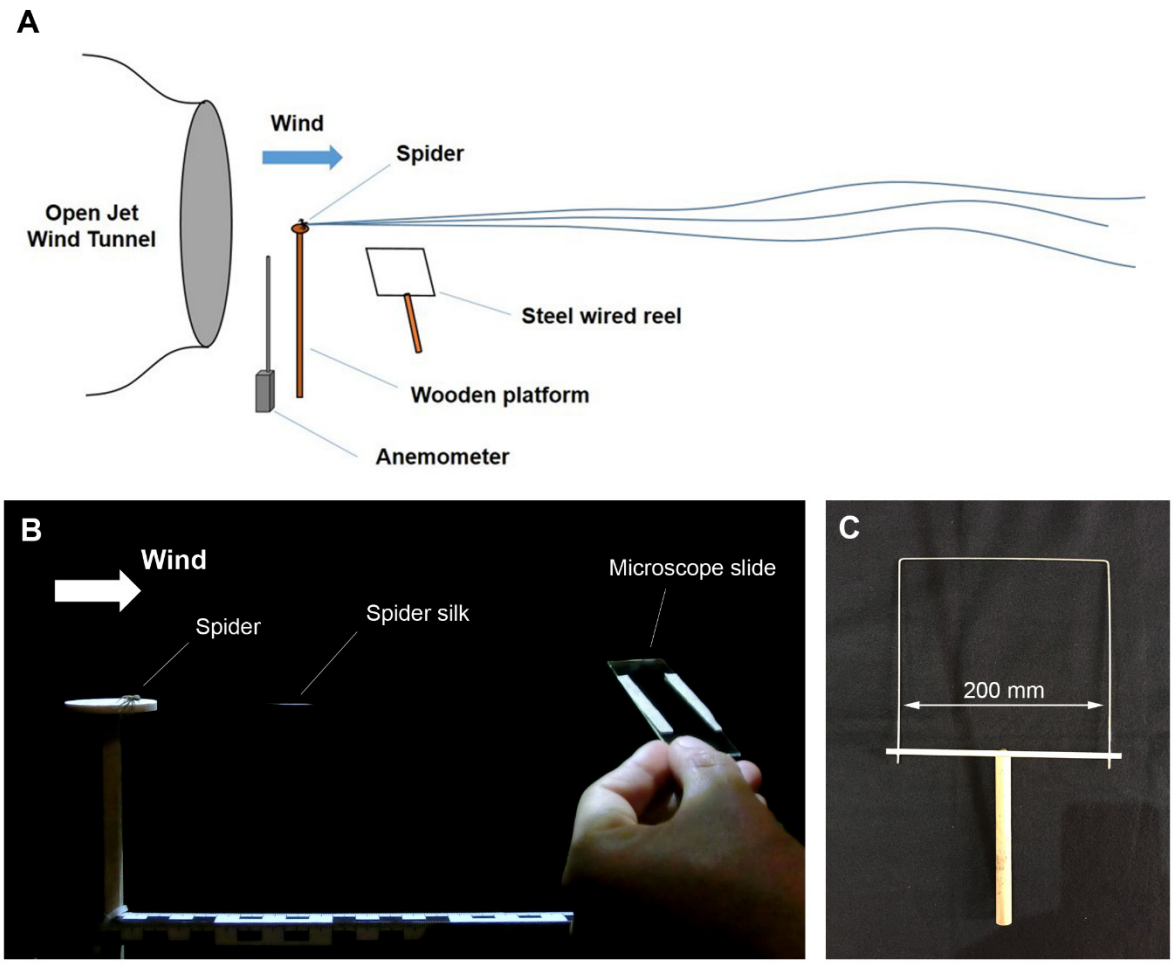

Figure 4.3 Experimental materials and methods for the identification of ballooning lines. (A) A schematic view of wind tunnel tests; (B) Sampling of ballooning fibres in front of an open jet wind tunnel; (C) Reel with a steel wire to measure the length of ballooning silks.

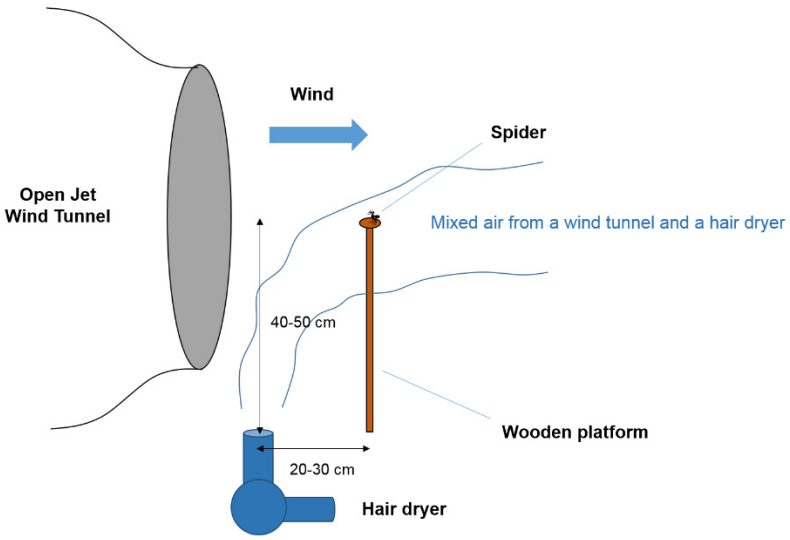

Figure 4.4 A sketch describing the position of the hair dryer. The mixed air zone generates 30°–35°C warm air and a fluctuating updraft (horizontal mean wind speed: 0.58 m s^{-1}, vertical mean wind speed: 0.40 m s^{-1}).

Ballooning fibres were collected on a microscope slide to which two narrow strips of a double-sided bonding tape were attached. The ballooning fibres were sampled near the spinnerets (see Figure 4.3B). A total of 11 samples were prepared from 28 spinning events of ballooning silks. In the experiment, a total of four spiders responded and showed ballooning behaviour—two of these were very active. Two samples were selected, either because the other samples failed to capture all ballooning fibres on a single microscope slide or because the fibres on the slides were deranged (disordered) during the capturing process. Simultaneously, silk fibres were captured on a square wire frame and carefully wound around it in order to measure the length of ballooning threads (see Figure 4.3C). The length of the silks was calculated by multiplying the total number of half-revolutions by the width of the square wire frame (20 cm). The successfully sampled ballooning fibres were later studied using a field emission scanning electron microscope (FESEM).

4.1.2.2. FESEM

The sampled ballooning fibres were coated with gold using a sputter coater (SCD 030, Balzers Union) and observed using a FESEM (DSM 982 Gemini, ZEISS, with 5–10 kV accelerating voltage). The number of ballooning fibres was carefully counted and the thickness of fibres measured. The spinnerets of a female *X. cristatus* were also observed using the FESEM. For sample preparation, the female spider was fixed in 2.5% glutaraldehyde and dehydrated in ascending concentrations of ethyl alcohol from 30% to 100% (10 min at each concentration). After dehydration, the sample was dried with a critical point dryer (CPD 030, BAL-TEC). The prepared sample was coated with gold using a sputter coater (SCD 030, Balzers Union) and observed using the FESEM (SU8030, Hitachi, with 20 kV accelerating voltage).

4.1.3. Investigation of the Aerodynamic Environment

To investigate the turbulent atmospheric boundary layer, ultrasonic three-dimensional wind speed measurement took place on a grass field (53° 11′ 42″ N, 12° 09′ 40″ E; see Figure 4.5 (A) and (B)). This place is a habitat of the *Erigone* and *Xysticus* genus, both of which engage in ballooning behaviour. To avoid mechanically induced updrafts caused by hills, trees, and rocks, a flat grass field was selected. The three-dimensional wind speed data at two different mean wind speeds (1.99 m s^{-1} and 3.07 m s^{-1}) were measured on a sunny day in autumn for five minutes with a sampling frequency of 20 Hz. In order to eliminate small-scale fluctuations in the turbulent boundary layer, a quadrant analysis was introduced (Willmarth and Lu 1972, Lu and Willmarth 1973, Adrian 2007, Steiner et al. 2011) (see Eqn. (4.3)).

$$u'w' \geq H(u'_{rms}w'_{rms}) \tag{4.3}$$

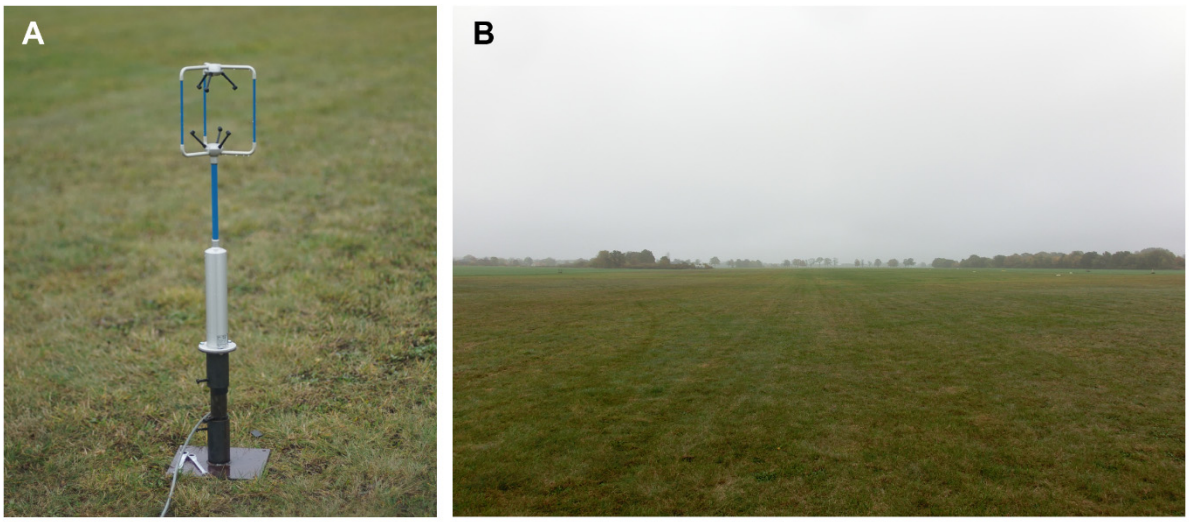

Figure 4.5 Experimental material and positioning of three-dimensional wind velocity measurement. (A) A three-dimensional ultrasonic anemometer (Windmaster 1590-PK-020, Gill Instruments) is installed 0.95 m above the ground; (B) The simplest conditions (i.e., a flat surface) were selected. The flat area is covered with short-cut grass 6 cm in length. There are no obstacles within a radius of 300 m.

4.2. Results

4.2.1. Field Observation

Crab spiders *(Xysticus cristatus*, *X. audax*, etc.) were collected at Lilienthal Park and along the Teltow Canal in the Berlin area, Germany, and observed each autumn, especially during October, from 2014 to 2016. Lilienthal Park was selected for the observation of pre-ballooning behaviour because the ballooning phenomenon among adult and subadult crab spiders is frequently observed in this region.

4.2.1.1. Take-off

In the Thomisidae family, not only female but also male adult spiders exhibited ballooning behaviours (see S1 Fig.). During the observation period, the temperature was 16–19 °C, and the mean wind speed was 6–7 m s^{-1} (gust 14–17 m s^{-1}), as reported by the nearest weather station in Dahlem. As the weather station wind sensor was installed 36 m above the ground, the local wind speed at 1.2 m above the ground can be concluded to be much lower than these values. Later, we checked the wind speed on a similar day, on which the mean wind speed from the weather station showed 6–7 m s^{-1}. The mean wind speed over 10 min was 2.11 m s^{-1}.

On the experiment day, the spiders mostly exhibited tiptoe behaviour. At the first stage of tiptoe behaviour, the tiptoeing crab spiders evaluated the wind conditions not only passively, through the sensory hairs on their legs, but also actively, by raising one front leg (leg I), or sometimes both, and waiting in this position for 5–8 s (see Figure 4.6A, B, C). This sensing behaviour was often repeated a few times before the tiptoe pose was adopted. After each sensing step, the crab spider rotated its body in the direction of the wind (see Figure 4.6C, D).

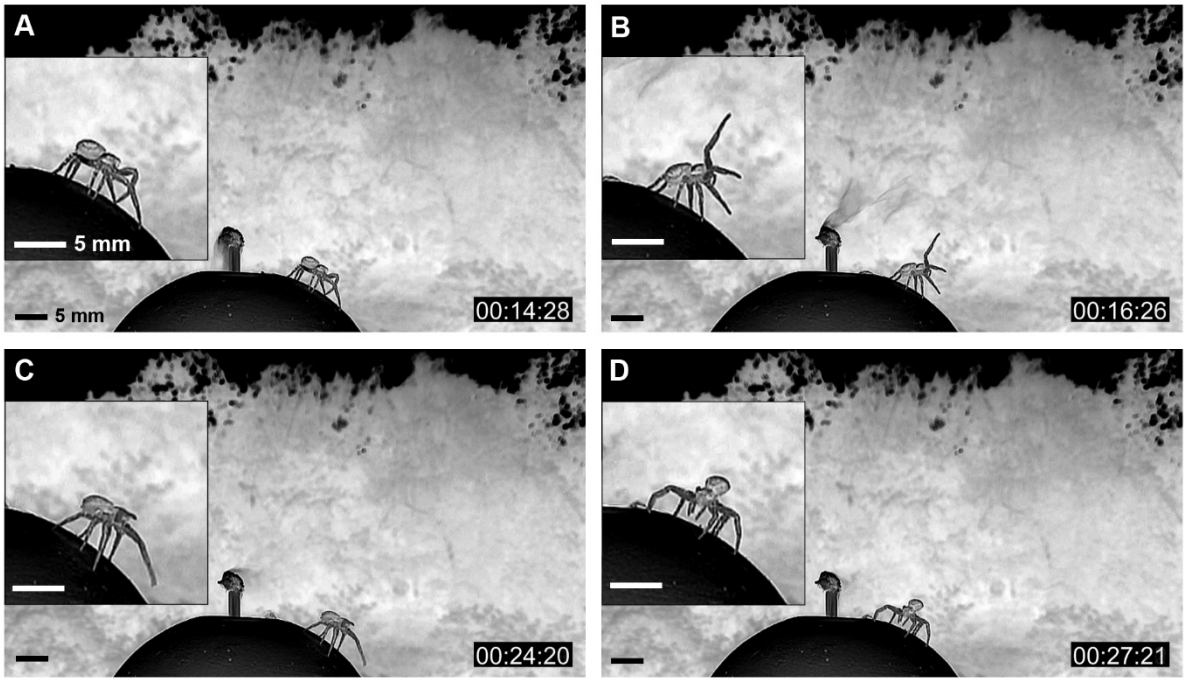

Figure 4.6 Sequence of active sensing motion with front leg (leg I) (negative images). (A) The spider first sensed the condition of the wind current through only the sensory hairs on its legs; (B) Then, if conditions seemed appropriate, the spider sensed more actively by raising leg I and maintaining this pose for eight seconds; (C) If the spider decided to balloon, it altered its posture; (D) The spider rotated its body in the direction of the wind and assumed the tiptoe posture.

If the spider decided that the wind conditions were suitable for ballooning, it raised its abdomen (already understood as a tiptoe behaviour; see Figure 4.6D) and spun its ballooning silks without any help from its legs. Before spinning ballooning silks, there was a motion of a rear leg (leg IV) (see Figure 4.7), with which the spider held its safety line that connected its spinnerets to the substrate and then placed it on the substrate (see Figure 4.7A, B).

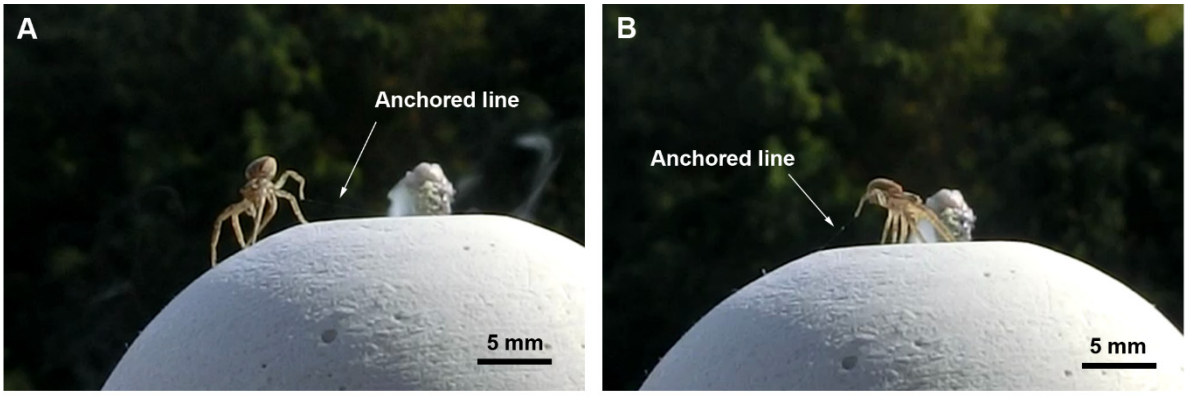

Figure 4.7 Tidying-up motion of safety line (anchored line) with leg IV. Two independent events: a front view (A); and a side view (B). Both spiders hold their safety line and then place it on the substrate before the spinning of ballooning lines.

The crab spider first spun a single fibre or a few fibres, and later many more fibres (see Figure 4.8A–G). The spun ballooning fibres were approximately 2–4 m long and formed a triangular sheet, which fluttered in the turbulent flows of the wind. The vertex angle of this triangular sheet was about 5–35° (see Figure 4.8C–G). If the wind conditions were not appropriate, the spider cut the silk fibres and spun them again. Alternatively, if the ballooning silks generated enough drag, the spider released the substrate and became airborne (see Figure 4.8H). From careful video investigation, it was observed that the spiders stretched all their legs outward as soon as they achieved take-off. Many ballooned crab spiders soared diagonally upwards along the wind flows. These paths had a 5–20° inclination above the horizon. Some spiders travelled quasi-horizontally, while others soared along a steep path (about 45°). During this steep take-off, the spiders took off with a relatively slow speed. The anchored drag line (safety line) between the platform and the spider's spinneret could be observed. This anchored line endured without breaking until it reached a length of 3–5 m; after a while it broke mechanically. From the wind tunnel experiment, it was discovered that the anchored line consisted of two fibres.

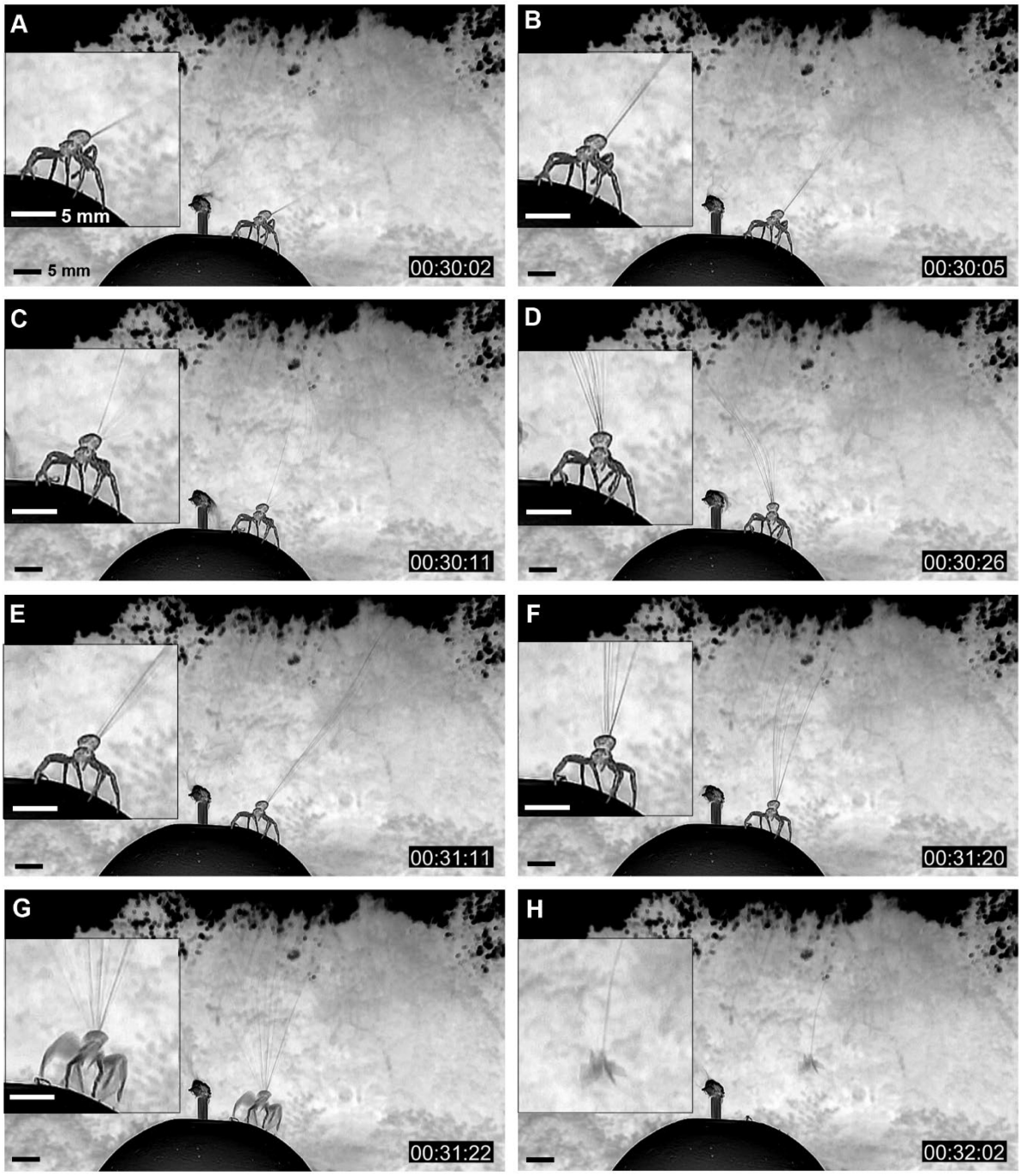

Figure 4.8 A crab spider's ballooning process (images were converted to negative images to visualise ballooning lines). (A, B) Initial phase of spinning ballooning lines; (C, D, E, F) Fluttering of a bundle of ballooning lines. Because of turbulent wind flows, the ballooning threads fluttered unsteadily; (G) Take-off moment; (H) Airborne state of a ballooning spider. [Scan the right QR code or click the text to connect to the video]

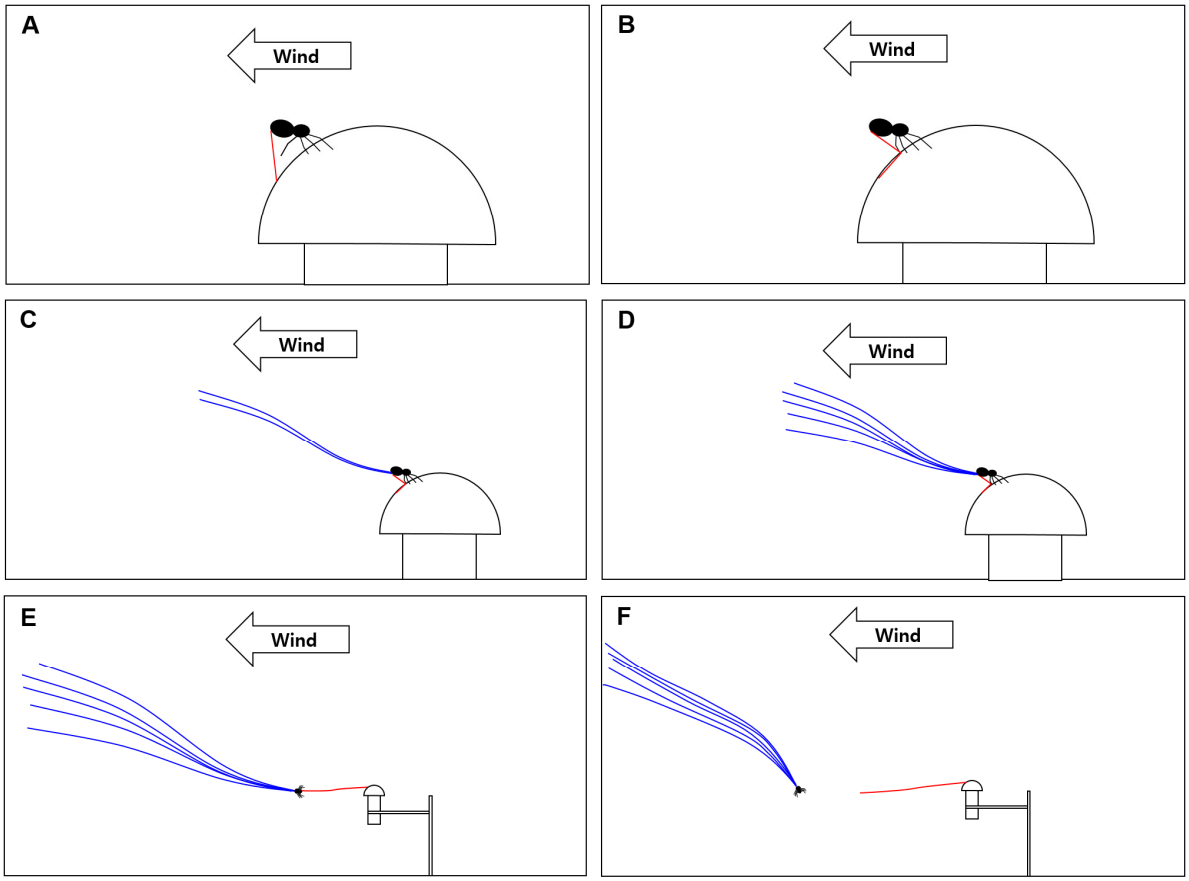

Figure 4.9 Sequential sketches of 'tiptoe' take-off in the field experiment. Red lines: An anchored line (a drag line); Blue lines: Ballooning lines. (A) A spider, *Xysticus* species, tries to hold the anchored line with one of its legs IV. (B) The spider holds the anchored line and then places it on the substrate; (C) The spider first spins a single fibre or a few number of fibres; (D) The spider then spins many split fibres; (E) If the wind conditions are appropriate, the spider releases holding of the substrate; (F) In a very short time, the anchored line is cut and the crab spider becomes airborne.

Three new facts about ballooning were revealed. First, the crab spider does not evaluate the wind condition passively, but rather actively, by raising one of its legs I. Second, this adult ballooner anchors its drag lines on the platform not only during its rafting take-off but also during tiptoe take-off. Third, the crab spider postures all its legs outwards and stretches, when airborne, not only at the take-off moment but also during the gliding phase (see Figure 4.10A–D).

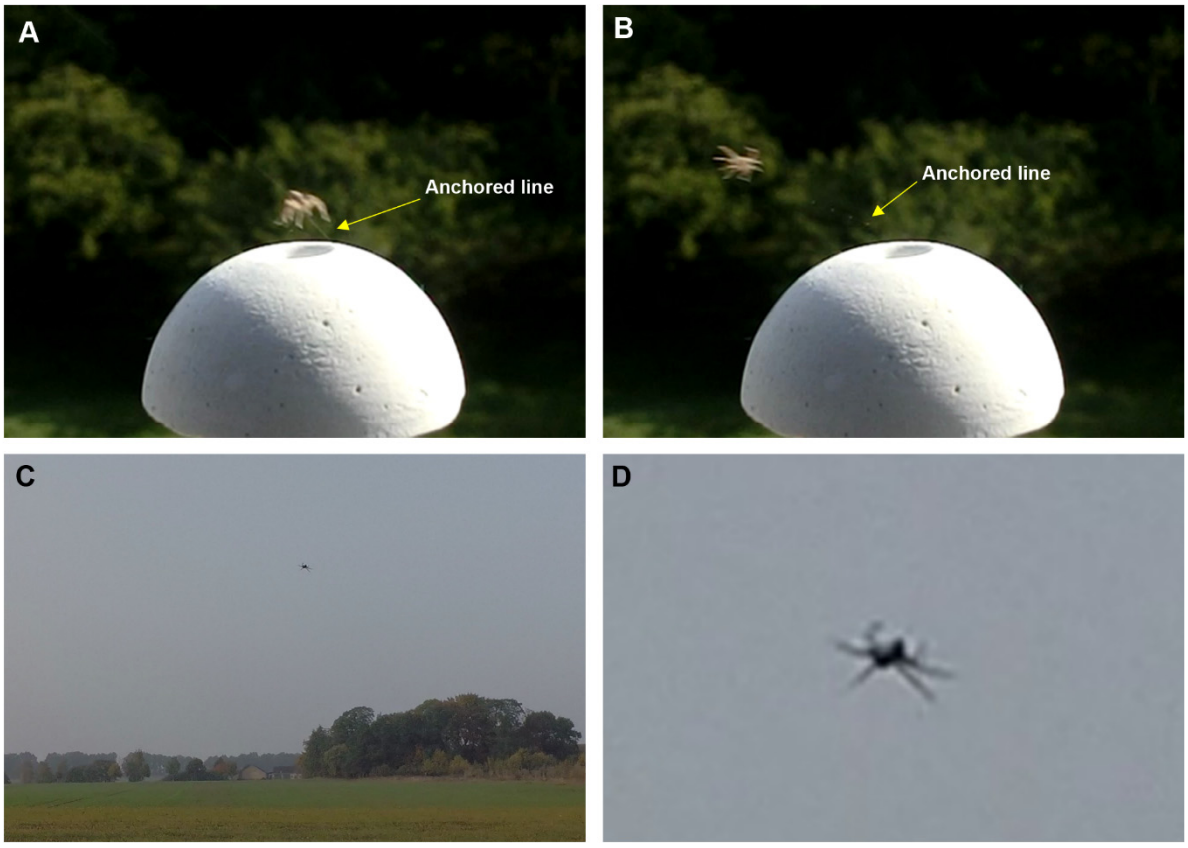

Figure 4.10 Spiders' posture in take-off and flight. (A, B) An anchored line was found during a tiptoe take-off. As soon as spiders were airborne, they stretched their legs outwards; (C) To ensure the behaviour of outstretched legs during flight, the pose of a spider was observed during its gliding phase; (D) The spider kept its legs outstretched.

Rafting pre-ballooning behaviour was also observed. The local weather conditions were slightly colder and windier than the case on the previous tiptoe take-off observation day. The crab spiders were not active on this day. As soon as they were set on the platform, they exhibited one of two behaviours: either they hid on the opposite side of the platform to avoid the wind, or they quickly retreated downward about 0.4–1.1 m, relying on their drag lines (see Figure 4.11A, B), and spun their ballooning fibres downstream of the wind. At this time, the spiders first spun a single fibre or a few fibres and then many fibres, as it was the case during the tiptoe take-off (see Figure 4.11C, D). During this process, the spiders also postured all their front legs and second legs outward and backward so that they hung and directed their bellies in the upward direction of the wind (see Figure 2.1B). The backward (downstream)-spun threads then slowly curved upward, and the spiders' bodies also moved slowly upward (see Figure 4.11D). At a certain point, when the threads had generated enough drag and lift, the drag lines near the spinnerets were cut and the spider finally ballooned (see Figure 4.11E, F).

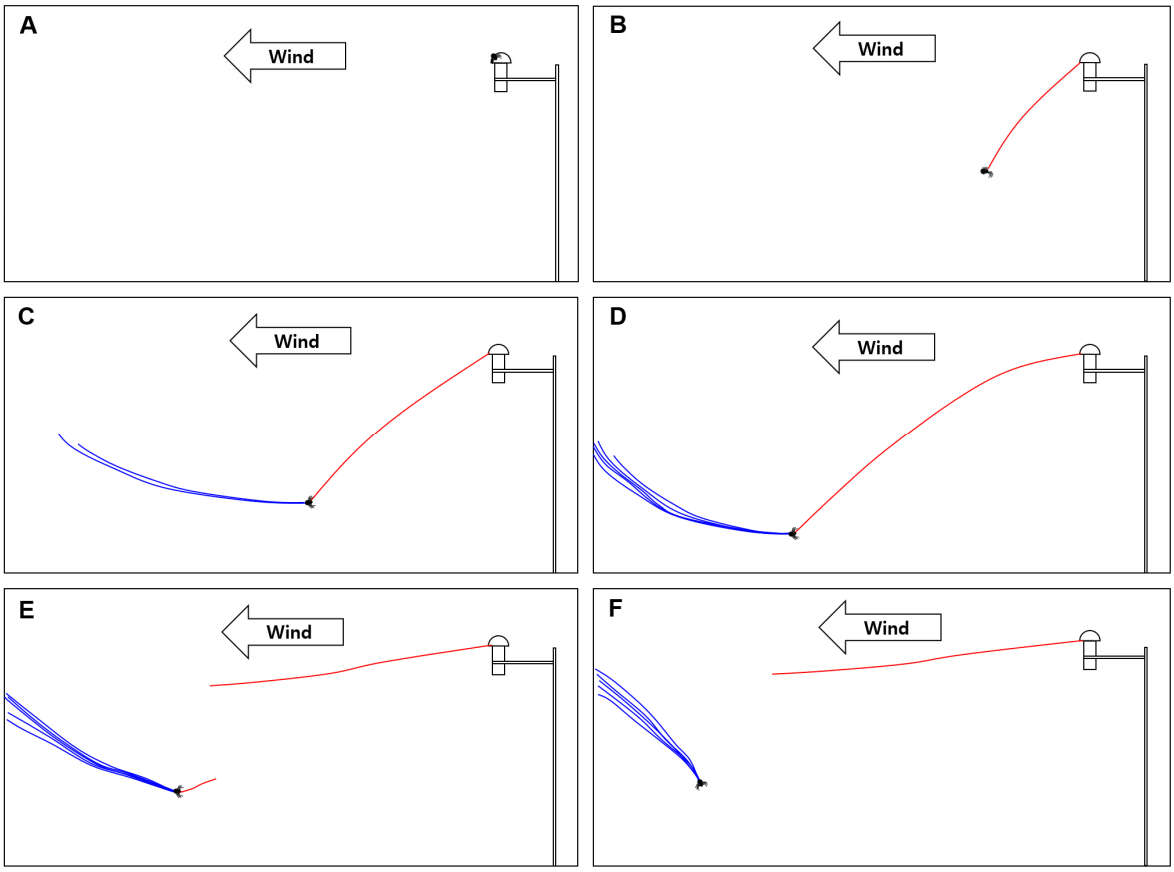

Figure 4.11 Sequential sketches of rafting take-off in the field experiment. Red lines: An anchored line (a drag line); Blue lines: Ballooning lines. (A)(B) A spider, *Xysticus* species, drops down about 0.4 to 1.1 m, relying on its anchored line (a drag line); (C) The spider first spins a single fibre or a few number of fibres downstream of the wind; (D) The spider then spins many fibres continuously; (E)(F) The spun ballooning lines slowly curve upwards. At a certain point, the anchored line near the spinnerets is cut mechanically (seems to be cut by the sufficient drag on the ballooning fibres) and the spider balloons.

4.2.1.2. Statistical Analysis of Pre-ballooning Behaviours

In total, the spiders made 68 active sensing motions with leg I, while 42 tiptoe pre-ballooning motions could be observed. Six spiders ballooned successfully following their tiptoe pose. The spiders also dropped down eight times, relying on their drag line. Moreover, three of them performed a rafting take-off (see Table 4.1).

Table 4.1 Ballooning behaviours on the artificial platform.

2015 Date (time)	Temp. (°C)	Wind (mean /gust) (m s⁻¹)	Number of specimens	Number of tests	Sensing motion	Tiptoeing		Rafting		Total ballooned spiders	Escape (fall down)
						Tried	Ballooned	Drop & climb	Ballooned		
9.24 (13:00–14:30)	19	6/17	7	14	48	30	4	1	0	4	3
9.26 (13:00–15:30)	16 ± 1	7/14	5	11	20	12	2	5	1	3	2
9.28 (12:00–12:30)	16	6/16	2	2	0	0	0	2	2	2	0
Total			14	27	68	42	6	8	3	9	5

The initial behaviours mostly began with a sensing motion. Frequent transitions occurred between sensing motions and tiptoe motions (see Figure 4.12A). Spiders flew from either only the tiptoe pose or the dropping and hanging pose (see Figure 4.12B). The probability of a ballooning take-off occurring following tiptoe behaviour was 9.8%, while the probability of a ballooning take-off following the rafting pose was 37.5%.

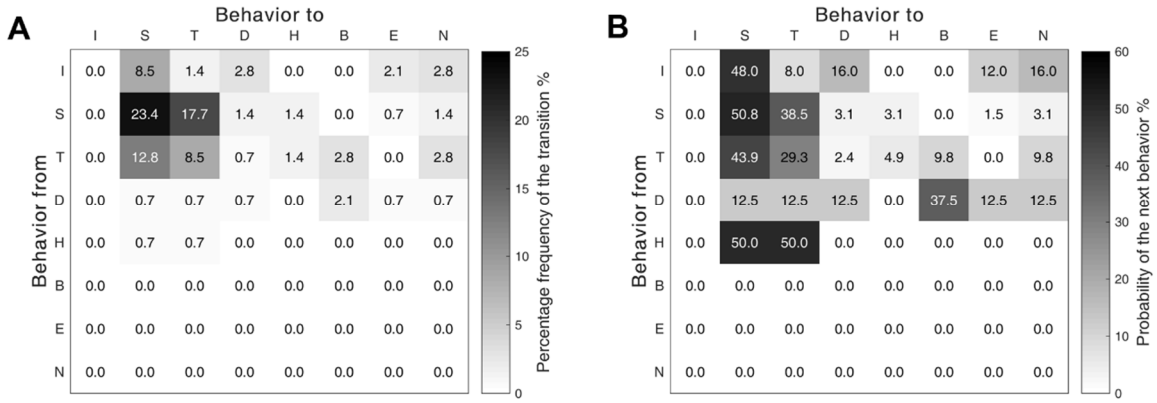

Figure 4.12 Sequential relations between ballooning behaviours. (A) The percentage frequency of the behaviour transition (the total number of transitions: N = 141); (B) The matrix of transitions between behaviours (total numbers of categorised behaviours: N_I=25, N_S=65, N_T=41, N_D=8, N_H=2). Here, B = take-off; D = dropping and hanging behaviour; E = escape; H = hiding motion; I = initial state; N = not flown; S = sensing motion; T = tiptoe behaviour.

The duration of each tiptoe behaviour was measured, and their frequencies analysed. Short-period tiptoe poses, which lasted for less than 5 s, were the most frequent. The longest tiptoe event lasted 65 s. The observed successful ballooning take-offs were not biased in relation to tiptoe duration (see Figure 4.13).

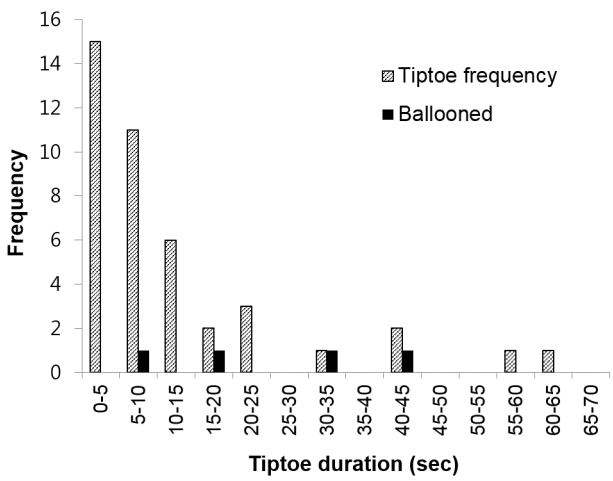

Figure 4.13 Frequency diagram of tiptoe behaviours according to tiptoe duration (N = 42). Black columns represent tiptoe behaviours that were connected to subsequent successful ballooning take-offs (N = 4).

4.2.1.3. Gliding

A total of 32 floating threads were observed at the Teltow Canal. Most of these were horizontally transported along the channel at about 1–8 m above the water surface. The threads drifted passively, due to light wind, but rarely fell down. Some of their silks were inclined downstream, while the others were inclined upstream. Two of the 32 observed floating threads were just threads alone without a spider. The number of observed fibres was 1–5. However, as not all threads were visible to the naked eye, some of these may have been multiple threads that were stuck together, although they appeared to be single threads. Moreover, some threads may not have been visible because of their inappropriate angles and positions in relation to the sun. Most spiders were positioned at the lower end of their threads. Although there were different numbers and shapes of threads, they were usually laid out diagonally (see Figure 4.14).

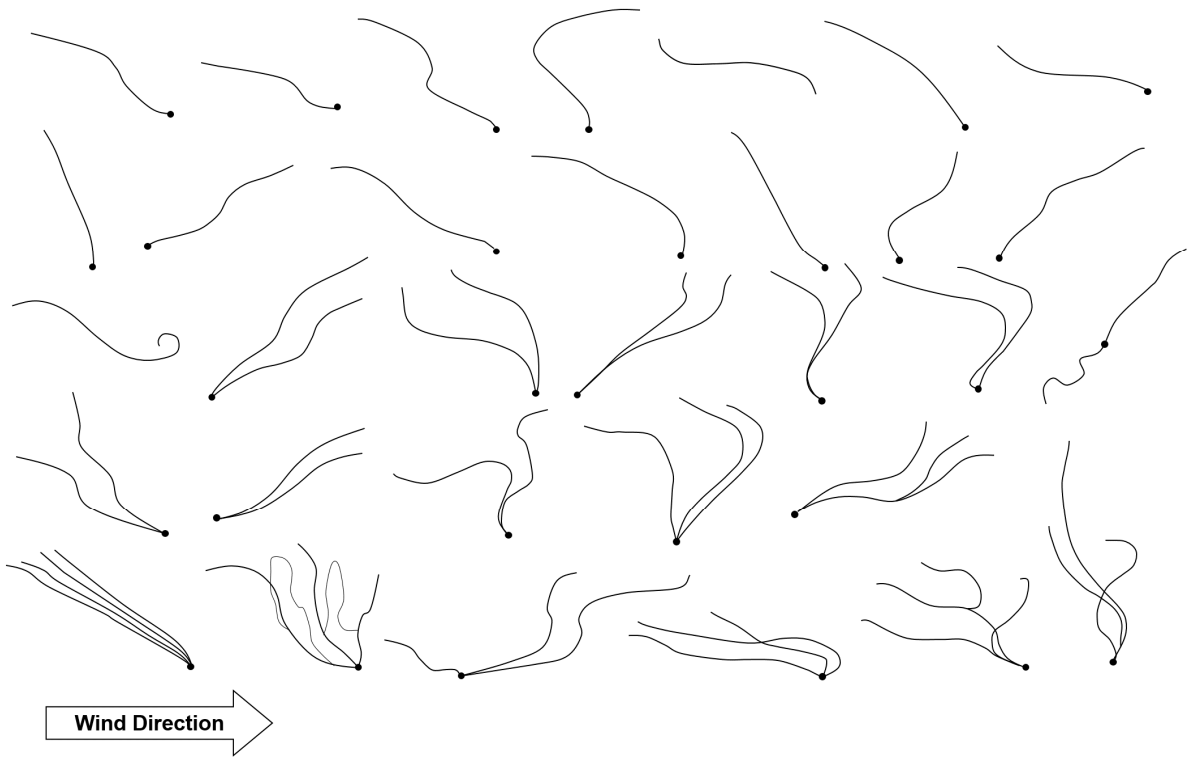

Figure 4.14 Sketches of ballooning structures (body + ballooning threads). These structures were observed above the water surface at heights of 1–8 m. Wind was blowing from left to right; therefore, these structures were transported in the same direction as the wind. Black, thick points represent the spider's body; black lines represent ballooning threads.

4.2.1.4. Landing

The landing of a crab spider on the water surface was observed at the Teltow canal in the afternoon of November 2, 2015, at a temperature of about 12-13°C. Although the temperature was relatively cold, the sun was shining and the wind was a very light breeze (0.3-1.5 ms^{-1} by the Beaufort wind speed scale). The ballooning lines of this spider were 4 to 5 m long and consisted of five to six threads. These threads were tangled at a couple of points and were inclined at about 35 degrees from the horizontal surface (see Figure 4.15A). The landed spider did not sink, as it was able to float on the water surface,

supported by the water surface tension and the threads that hung on the bank of the canal. The spider did not move in over 30 min and also did not adopt any sailing pose, as was recently observed by Hayashi in the laboratory (Hayashi et al. 2015). The spider was rescued and identified as a female with a weight of 12.9 mg. Another landing was observed on the same day. At this time, the air movement was very calm, moving at about 0-0.3 ms^{-1} (according to the Beaufort wind speed scale). About 10 m of long silk floated horizontally 2-3 m above the water surface. One end of the silk was connected to the crab spider, which was on the surface of the water. Other threads 6-8 m in length were floating in the opposite direction to the 10 m thread. Light wind pulled those threads and the spider in the direction of the bank and hung the threads on the bank (see Figure 4.15B). There were two crab spiders, big and small, with weights of 23.8 mg and 6.6 mg respectively. For about five minutes, the bigger spider did not exhibit any sailing posture, or even any movement; it then started to wind up its thread in order to climb up from the water surface. Both spiders were females.

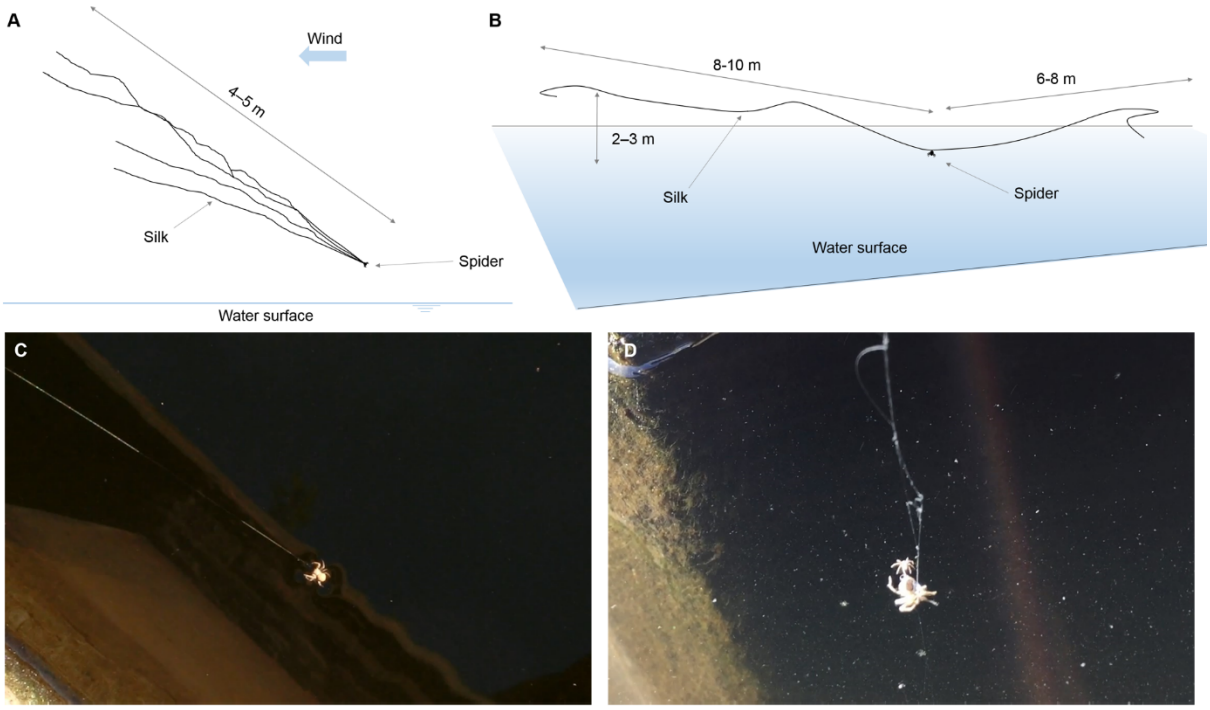

Figure 4.15 (A) Sketches of the landing of a 12.9 mg female crab spider, *Xysticus* spec; (B) Sketches of the landing of 23.8 mg and 6.6 mg crab spiders, *Xysticus* spec; (C) The 12.9 mg female crab spider on the water surface; (D) The 23.8 mg and 6.6 mg crab spiders on the water surface.

4.2.2. Identification of Ballooning Lines

The separation of glands for a drag line and ballooning lines was observed in ballooning behaviours in the laboratory. The anchored drag line was connected to the anterior spinnerets and the ballooning fibres were spun from either one or both posterior and/or median spinnerets (see Figure 4.16A, B). The lengths of the ballooning fibres were measured, 3.22 ± 1.31 m (N = 22), from 22 spinning events of two crab spiders (16.4 and 18 mg) (see Figure 4.17). The maximum length of the spun ballooning lines was 6.2 m.

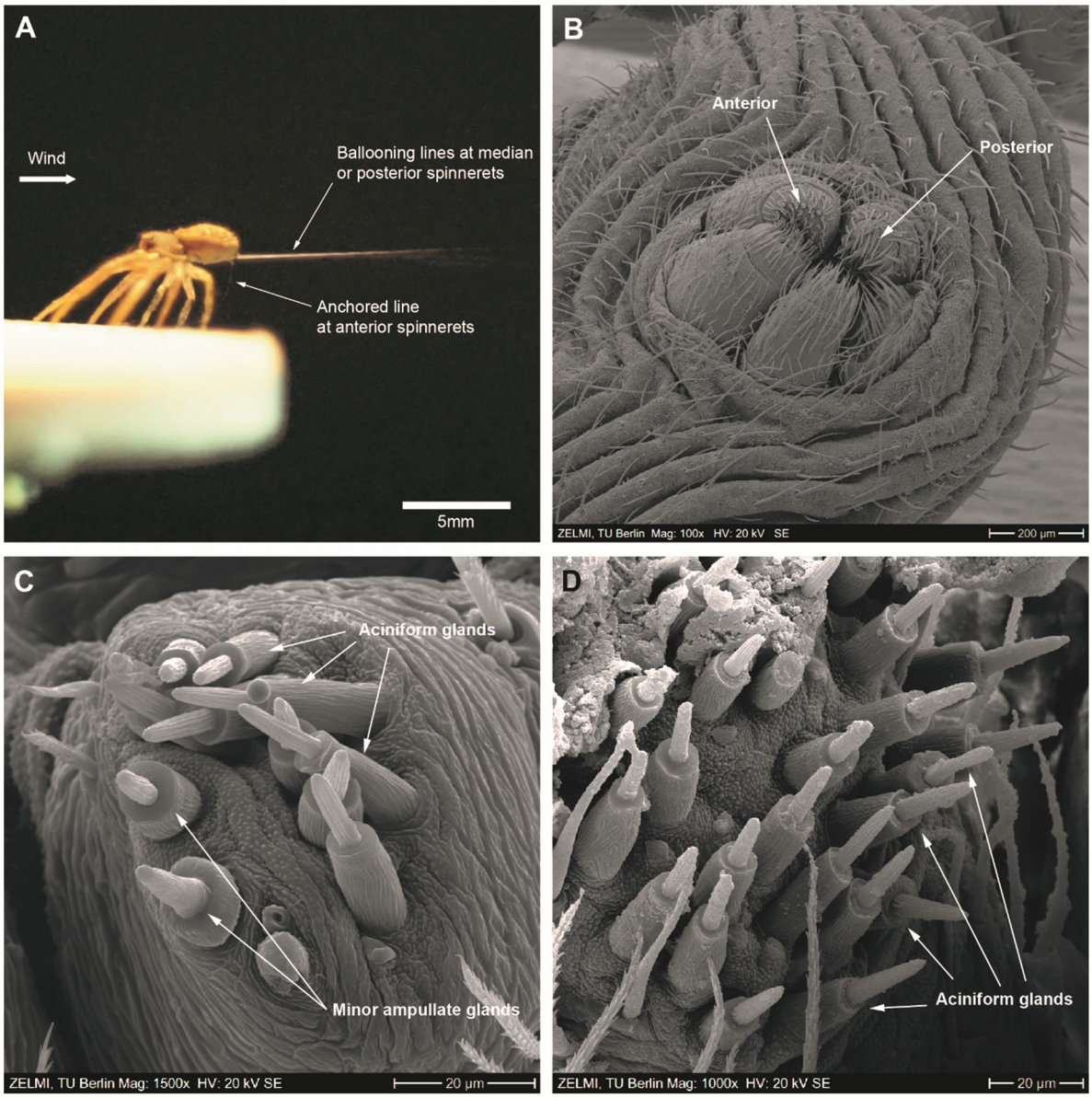

Figure 4.16 Spinning behaviour for ballooning and scanning electron microscopic images of spinnerets. (A) Spinning motion of ballooning silks in front of the open jet wind tunnel. Ballooning lines were spun from either or both of the median or/and posterior spinnerets; (B) Spinnerets of *Xysticus cristatus* seen under FESEM; (C) Median spinneret of Xysticus species. Two minor ampullate glands and 10 aciniform glands are distributed on the median spinneret; (D) A number of aciniform glands on the posterior spinneret.

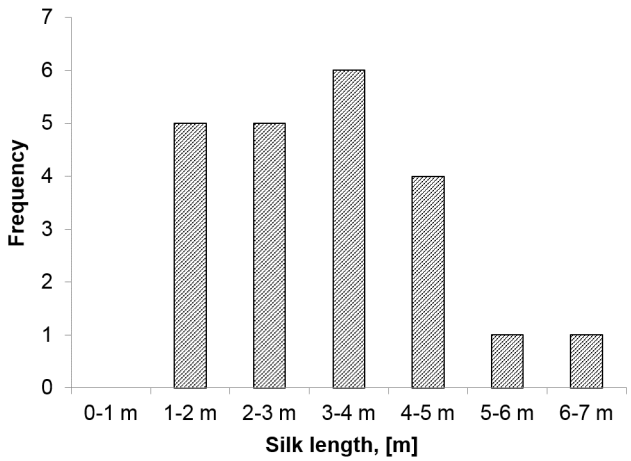

Figure 4.17 Distribution of the length of ballooning lines (N = 22).

The successfully collected ballooning fibres of both *X. cristatus* and *Xysticus* spp. were observed using the FESEM. Ballooning fibres consisted of two thick nanoscale fibres that were attached together (see Figure 4.18B, C) and many thin nanoscale fibres (see Figure 4.18A–D). The two adult spiders, of *Xysticus* species, spun 48–58 thin nanofibres and two thick nanofibres. The thickness of the thin nanofibres ranged from 121 to 323 nm, with an average of 211.7 ± 45.2 nm (*N* = 40). The thickness of the thick nanofibres was 698–768 nm, with an average of 722.2 ± 32.5 nm (*N* = 4) (see Table 4.2). The spun fibres were split independently (see Figure 4.18A–D).

On the other hand, drag lines consisted of one pair of fibres (see Figure 4.18E) (sometimes two pairs, from left and right; see Figure 4.18F), which were spun from the major ampullate glands on the anterior spinnerets. The thickness of these major ampullate silks was about 500 to 800 nm (see Figure 4.18E, F).

Table 4.2 Identification of the number and thickness of ballooning fibres through FESEM.

	Species	Weight	Thin nanoscale fibres		Thick nanoscale fibres	
			Number of fibres	Thickness of fibres	Number of fibres	Thickness of fibres
Spider 1	*Xysticus* spp *(f.)*	20.8 mg	58	192.3 ± 36.3 nm (*N* = 20)	2	734.0 ± 48.1 nm (*N* = 2)
Spider 2	*X. cristatus (f.)*	18 mg	48	231.1 ± 45.6 nm (*N* = 20)	2	710.5 ± 17.7 nm (*N* = 2)
Average	-	-	53 ± 7.1 (*N* = 2)	211.7 ± 45.2 nm (*N* = 40)	2 (*N* = 2)	722.2 ± 32.5 nm (*N* = 4)

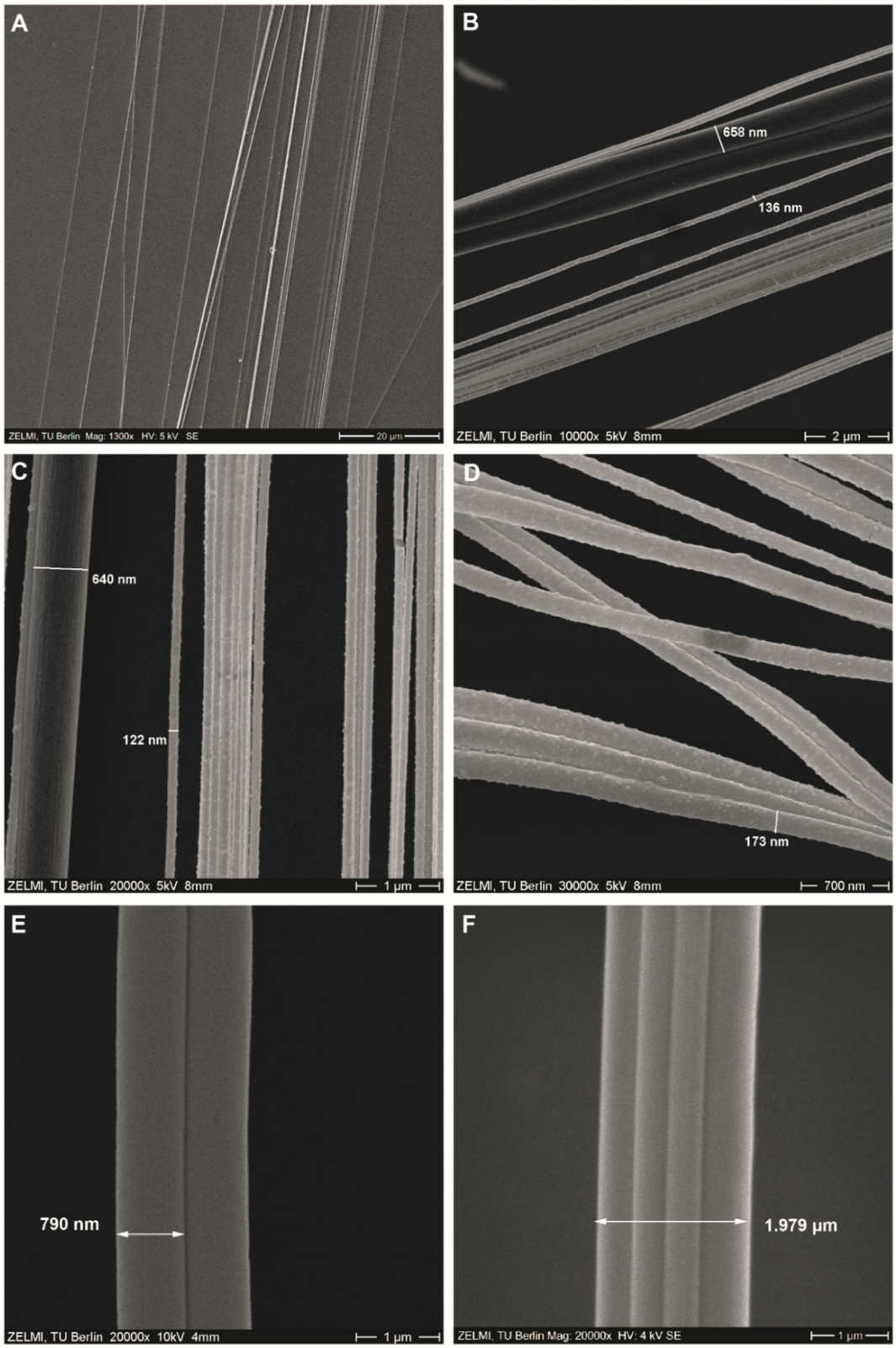

Figure 4.18 Scanning electron microscopic images of ballooning lines and drag lines. (A) Ballooning fibres of *X. cristatus* (1,300×); (B) Ballooning fibres of *X. audax* (10,000×). (C) Middle part of ballooning fibres of *X. audax* (20,000×); (D) Ballooning fibres of *X. cristatus* (30,000×); (E) One pair of drag fibres of *X. cristatus* (a weight of 18 mg) (20,000×); (F) Two pairs of drag fibres of *Xysticus* spp. (a weight of 15.6 mg), attached together (20,000×).

4.2.3. Investigation of the Aerodynamic Environment

Two data sets were collected at different mean wind speeds (1.99 m s^{-1} and 3.07 m s^{-1}) for five minutes. Usable updrafts in the turbulent atmospheric boundary layer were investigated. Each of the cases showed vertical deviations of ±0.225 m s^{-1} and ±0.267 m s^{-1}, respectively, ranging from −0.5 to 0.5 m s^{-1} and from −0.6 to 0.7 m s^{-1} (see Figure 4.19A, B). The turbulent intensities were 21% and 23.7% in the mean wind speeds of 1.99 m s^{-1} and 3.07 m s^{-1}, respectively. The vertical wind speed of both cases was negatively correlated to the horizontal wind speed. The slopes of regression fits are −0.235 (r = -0.575) and −0.077 (r = -0.259), respectively. The horizontal wind speeds of both Q2s are positioned below the wind speed of 3 m s^{-1}.

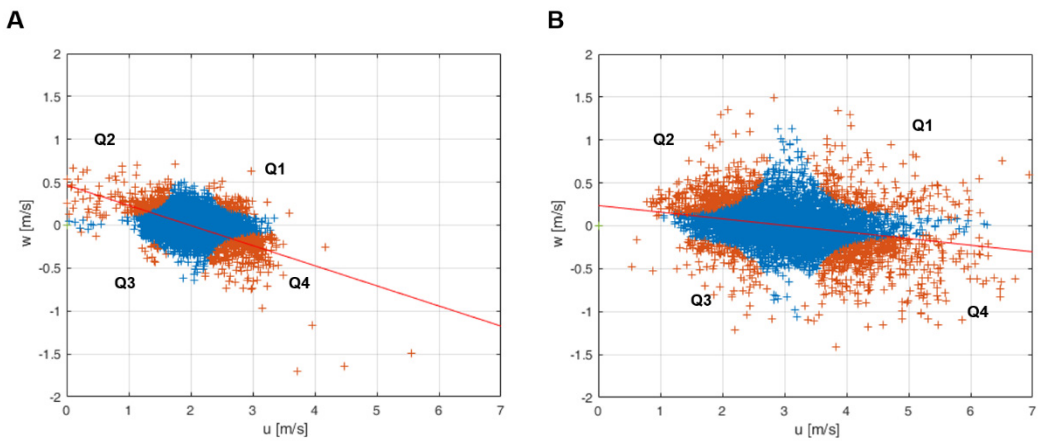

Figure 4.19 Horizontal and vertical components of the wind speeds for 5 min on u – w domain. (20-Hz sensing rate). (A) The case of 1.99 m s^{-1} mean wind speed (30 October 2016 12:39–12:45 LT). (B) The case of 3.07 m s^{-1} mean wind speed (29 October 2016 10:54–11:00 LT). Orange cross points: the quadrant data (Q1–Q4) of the measured wind speeds according to u' and w'; Blue cross points: the ignored data regarded as small-scale fluctuations (H < 1). Red lines are linear regression fit lines. The corresponding underlying data can be found in S3 Data.

4.3. Discussion

From our observations, the physical properties of ballooning silks were identified, together with previously undescribed behaviours undertaken during ballooning: (i) an active sensing motion of the wind; (ii) an anchoring behaviour during tiptoe take-off; (iii) a tidying-up motion of an anchor line (drag line, safety line); and (iv) an outward stretching pose during flight. Accordingly, these findings provide some clues and answers that were previously unsolved regarding the ballooning flight of spiders. The measured wind data also provides hints as to a possible underlying mechanism from the environmental perspective. We interpret these observations as follows.

4.3.1. Active Sensing Motion

Crab spiders engaged in a motion that seemed to be an active evaluation of the meteorological conditions before their take-off. Normally, ballooning behaviour is first triggered either by a warm ambient temperature or by a rapid increase in ambient temperature (Richter 1971, Vugts and Van Wingerden 1976). Additionally, if they are exposed to a wind that is slower than 3 m s^{-1} (favourable winds speed is 0.35–1.7 m s^{-1} for spiderlings), they show tiptoe behaviour (Richter 1970, 1971, Vugts and Van Wingerden 1976, Tolbert 1977, Lee and Kintner 2015). Until now, it had been thought that spiders sense the wind speed passively through the sensory hair (trichobothria) on their legs (Palmgren 1936, Vugts and Van Wingerden 1976, Humphrey 1987). However, the present observations demonstrate that spiders may sense the aerodynamic wind conditions not just passively, but rather actively, by raising leg I high and shaking it. The strong interactive behaviour transition between a sensing motion and tiptoe motion (see Figure 4.20, Figure 4.12A) supports that active sensing motions are related to the spiders' ballooning flight, because the tiptoe behaviour is prerequisite behaviour for ballooning take-off (see Figure 4.20). The leg-raising behaviour can be interpreted as follows: the spider enhances the sensibility of its sensory hairs by raising its legs upward in the outer region of the boundary layer, where airflows are faster than near the substrate and undisturbed by the spiders' bodies themselves. The first instars of the coccid *Pulvinariella mesembryanthemi* exhibit a similar behaviour by standing on their hind legs to capitalise on higher air speed in the thin boundary layer for their aerial dispersal (Washburn and Washburn 1984).

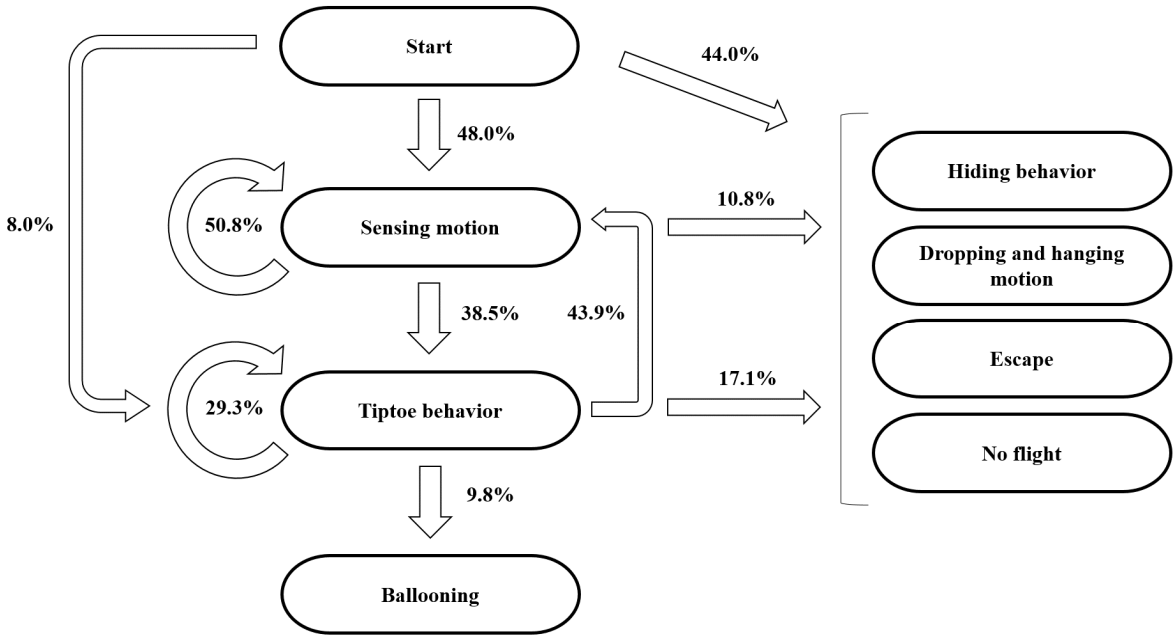

Figure 4.20 Take-off process for tiptoe ballooning. The probabilities are calculated based on the total number of behaviours at each stage (see Fig. 5B).

The spider's active sensing motion of the wind tells us two important things. First, aerodynamic force may be a dominant factor in spiders' ballooning. One hypothesis claims that an electrostatic charge on

ballooning silks could generate lifting forces in the earth's vertical atmospheric electrostatic field (Gorham 2017). However, the leg-raising behaviour indicates that, from the spider's viewpoint, airflow is an important factor for its ballooning. Second, the spiders' ballooning may not be random flight that simply relies on random wind conditions; but they may sense and evaluate the wind conditions and wait for the appropriate moment to initiate ballooning. Thirty-eight percent of tiptoe behaviours lasted 10–65 s, which are relatively long periods. This can be interpreted to suggest that there may be favourable wind conditions for spiders to balloon. If spiders evaluate wind conditions and wait before embarking on their aerial dispersal, this could be a distinct feature of spiders' ballooning that contrasts with other passive aerial dispersal like that of seeds or aeroplanktons. Additionally, this evaluating behaviour can also preserve their silk dope during their take-off trials by reducing failure cases (for example, by avoiding unfavourable wind conditions after spinning the ballooning silks).

In the near-surface atmospheric boundary layer, the updraft is initiated not by thermal buoyancy forces, but rather by the shear winds, which generate shear-driven turbulent flows (Hunt and Morrison 2000, McNaughton 2004). The generated turbulent eddies build intermittent updraft and downdraft regions, which drift in the downwind direction. If spiders either directly sense this moving updraft zone or indirectly sense the appropriate wind conditions that could build this moving updraft structure, the spiders' sensing motion and timing of the decision may be helpful in increasing the chances of successful take-off.

However, there are still other questions that remain unanswered. If spiders sense these wind conditions, what type of information do spiders need before making their decision to balloon? From previous studies and the author's observations, we can deduce that several factors may be involved. (i) Wind speed: A spider does not exhibit tiptoe behaviour under conditions of high wind speed, i.e. over 3 m s^{-1} (Richter 1970, 1971, Vugts and Van Wingerden 1976, Tolbert 1977, Lee and Kintner 2015). (ii) Vertical wind speed: Favourable conditions for ballooning, usually the vertical acceleration of wind, persist only for a few seconds. Under such conditions, the spider spins its silk fibres rapidly into the wind and releases its substrate (Suter 1999, Richter 1971). (iii) Wind direction: From our observations, spiders rotate their body in the direction of the wind as soon as they have evaluated the wind conditions; therefore, it seems likely that spiders can at least perceive wind direction. (iv) Wind fluctuation: For drop and swing dispersal, spiders were noticeably more active during turbulent flows (Barth et al. 1991). This shows that spiders can perceive the fluctuation of a turbulent flow. Suter (1999) demonstrated that the ballooning site is usually located within chaotic air flows. Reynolds et al. (2006) further showed that the chaotic motion of the turbulent flow reduces the terminal speed of ballooners, and that this feature enables long permanence in the air. Therefore, it can be deduced that spiders may sense the fluctuation of wind.

4.3.2. Ballooning Lines

For crab spiders, ballooning lines and drag lines were not identical. The source of ballooning lines is not well understood (Tolbert 1977, Suter 1992). One report suggested that some primitive spiders—*Sphodros* spiderlings and *Ummidia* spiderlings, which do not use the complex pre-ballooning behaviours such as tiptoe and rafting—use a drag line as a ballooning line, a method known as 'suspended ballooning' (Bell et al. 2005). Here, spiders drop down from the end of a branch, relying on

their drag line. If there is a breeze, the drag line near its point of attachment to the platform will be sheared and drift through the air (Coyle 1983, 1985). From this context, many previous studies have proposed that spiders use their drag line for ballooning dispersal (Humphrey 1987, Reynolds 2006, Gorham 2013, Sheldon et al. 2017, Zhao et al. 2017). Some experiments substituted a drag line for a ballooning line (Suter 1991, 1992, Bell et al. 2005). However, Suter guessed from Tolbert's observation that ballooning lines might be different from the drag line (Tolbert 1977, Suter 1992, Suter 1999). Our observations assure that, in crab spiders, these ballooning lines are not identical with a drag line, as the former were spun from either or both of the median and/or posterior spinnerets (see Figure 4.16A, B). Normally, the drag line is spun from the major ampullate glands in the anterior spinneret (Vollrath 2000). The crab spiders spun 48 to 58 thin nanofibres and 2 thick nanofibres. These thin nanoscale fibres seemed to be aciniform fibres (wrapping silk) from the median/posterior spinnerets. The thick nanoscale fibres seemed to be minor ampullate silks from the median spinnerets. Moon and An (2005) observed that one of the median spinnerets (left and right) of *Misumenops tricuspidatus* (crab spider) contains two pairs of ampullate glands and 20 (±3) pairs of aciniform glands, and that one of its posterior spinnerets includes 50 (±5) pairs of aciniform glands. Our observation in *Xysticus* spp. revealed features similar to Moon and An's observations (see Figure 4.16C, D).

It is possible that the anchored drag lines are normal drag lines (major ampullate silks), which a spider spins constantly while it is crawling and attaching its silk fibres to the ground surface for safety purposes. The anchored line was observed to be connected to the anterior spinnerets (see Figure 4.16A) and to consist of two fibres. According to Osaki's (1999) observation, drag lines are also composed of two fibres. The anchored line can be observed in each ballooning behaviour, i.e. not only in rafting take-off (Bell et al. 2005) but also in tiptoe take-off.

Before the spinning motion of ballooning lines, there was a motion of a rear leg (leg IV) (see Figure 4.7A, B), resembling 'wrap spinning,' during which spiders use leg IV to initiate ballooning lines by wiping their spinnerets (Eberhard 1987). However, in our case, it was obvious that the spiders used their leg IV not to initiate ballooning lines, but rather to tidy up the unfamiliarly positioned anchored line (safety line), which might have otherwise obstructed the spinning of ballooning silks (see Figure 4.7A, B). During the tiptoe take-off, this anchored line is normally cut mechanically over a short time, when a spider drifts rapidly either horizontally or at a small inclination. However, when a spider becomes slowly airborne with a very steep inclination because of a local updraft, this line remains intact until it is lengthened to 3–5 m. In our opinion, this line is not stretched; instead, the spider lengthens the safety silk by spinning an additional safety line. The reason for this is that the maximum elongation of spider silks is limited by about 30% (Ko et al. 2001, Bonino 2003). This means that spiders control their anchored line during the steep or slow take-off.

4.3.3. Nanoscale Multifibres

While the ballooning of small spiders, i.e. those that are lighter than 2.0 mg, has been investigated by calculation (Humphrey 1987), experiments (Suter 1991, Bell et al. 2005), and observation (Richter 1970, Tolbert 1977), the plausibility of a large spider engaging in ballooning remained unexplored (Humphrey 1987, Henschel 1995). The mysterious flying behaviour of large spiders can be explained by their nanoscale multifibres. From our wind tunnel test, we found that the *Xysticus* genus uses tens

of nanofibres (with diameters of 121 to 323 nm) for their aerial dispersal (see Figure 4.18A–D). The number of ballooning fibres and their lengths were identified. Based on these measured values, the updraft speed required to facilitate the ballooning take-off was calculated using modified Humphrey's and Suter's equations (Eqns. (4.4)–(4.8)) (Humphrey 1987, Suter 1991). The fluid-dynamic interaction between each fibre is not considered. The split case of fibres is calculated. The drag force on multiple fibres (Eqn. (4.4)), which is suggested by Humphrey is based on Burgers' approximated solution (see Eqn. (2.3)). By equating a gravity force on a spider's body to the sum of drag forces on multiple fibres and a spider's body drag (empirical estimation by Suter 1991), the settling speed is acquired (see Eqn. (4.6)). Suter suggested an estimation method of drag forces on a spider silk in accordance with a weight of a spider (Suter 1991; see Eqn. (4.5)). As the Suter's estimation is based on a spider's drag line, the empirical drag forces on the ballooning fibres are obtained by calculating an equivalent weight of the spider body corresponding to the diameter of a ballooning fibre (see Eqn. (4.8)). The empirical settling speed of a ballooning spider is obtained by equating the modified empirical drag forces of a ballooning spider to the weight of a spider (see Eqn. (4.7)) For a crab spider weighing 10–25 mg, the required vertical wind velocities are, according to Humphrey's theoretical formula, 0.08–0.20 m s^{-1}; according to Suter's empirical formula, these velocities are 0.04–0.09 m s^{-1}. These values are much smaller than the values of 9.2–21.6 m s^{-1}, which were calculated for *Stegodyphus* spp. (Wickler and Seibt 1986, Henschel 1995). Accordingly, we calculated the required length of ballooning fibres for *Stegodyphus* spp. according to the updraft air speeds (see Figure 4.21). Our result shows that *Stegodyphus* spp. can also balloon with a relatively light updraft, 0.2–0.35 m s^{-1}, with a total of 80 ballooning fibres measuring around 3 m in length. These results support Schneider's observation that adult females of the *Stegodyphus* genus, weighing 80–150 mg, balloon using at least tens to hundreds of threads (Schneider et al. 2001). In this calculation, the number of ballooning fibres utilised by the *Stegodyphus* genus is conservatively assumed that only one side (left or right) of the median and posterior spinnerets is used for spinning ballooning fibres. This number of fibres is estimated by counting the fibre glands of *S. mimosarum*'s spinnerets (the number of minor ampullate fibres is 2; the number of aciniform fibres is 78) (Griswold 2005). This number is reasonable because *Xysticus* spp. was found to spin a similar order of the number of fibres (two thick fibres and 58 thin fibres) in our experiments. The thicknesses of a minor ampullate fibre and an aciniform fibre are assumed to be 80% and 25% of that of the major ampullate fibre, respectively. The thickness of a major ampullate fibre estimated from Suter's body weight and silk thickness relationship (Eqn. (4.8); Suter 1991) as follows:

$$D_H = \sum_{i=1}^{n} \frac{2\pi \cdot \eta \cdot U \cdot l_i}{ln(2l_i/d_i) - 0.72} \times 10^6 \tag{4.4}$$

$$D_S = \sum_{i=1}^{n} 11.5 \cdot l_i \cdot V \cdot W_{eq,i}^{0.094} \tag{4.5}$$

$$U_H = \frac{W}{\sum_{i=1}^{n} \frac{2\pi \cdot \eta \cdot l_i}{ln(2l_i/d_i) - 0.72} \times 10^6 + 1.94 \cdot W^{0.366}} \tag{4.6}$$

$$U_S = \frac{W}{\sum_{i=1}^{n} 11.5 \cdot l_i \cdot W_{eq,i}^{0.094} + 1.94 \cdot W^{0.366}} \tag{4.7}$$

$$W_{eq,i} = \frac{\pi(d_i \times 10^6)^2 + 0.184}{0.0277} \tag{4.8}$$

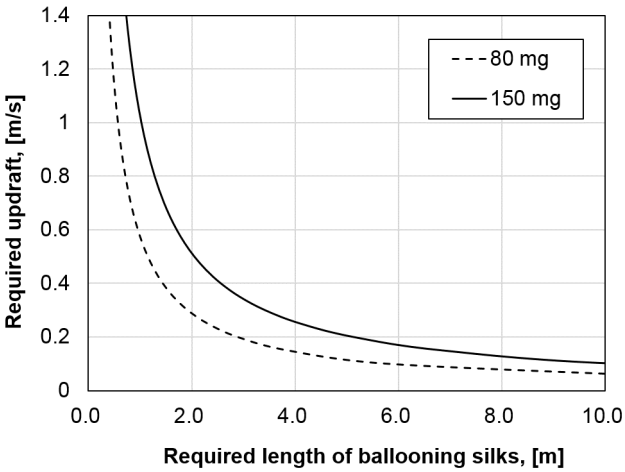

Figure 4.21 Required updraft wind speed and length of ballooning silks for the ballooning of 80–150 mg *Stegodyphus* spp. It is assumed that *Stegodyphus* spp. use two minor ampullate silks (2.1–2.9 µm thickness) and 78 aciniform silks (650–900 nm thickness) for their ballooning. The corresponding underlying data can be found in S4 Data.

4.3.4. Low Reynolds Number Fluid Dynamics

The ballooning silks, when exposed to the air, experience a low Reynolds number flow (or Stokes flow; their Reynolds number is lower than 1). The upper limit of the Reynolds number is about 0.04 ($Re = \rho V d/\mu$; the air density: 1.225 kg m^{-3}, the maximum possible velocity: 3 m s^{-1}, the thickness of spider silk: 211 nm, the dynamic viscosity of air: 1.837 × 10^{-5} kg m^{-1} s^{-1}). The maximum possible speed experienced by the thread is assumed to be 3 m s^{-1}, as a spider seldom flies above this wind speed. Once a spider is airborne, the relative air speed with respect to the silk is reduced. Therefore, the Reynolds number of spiders' silks during their flight is much smaller than 0.04, and the spider's flight is thus dominated by low Reynolds number fluid dynamics. However, a large spider's body shows much larger scales than those of a spider silk, not only in size but also in weight. In the case of a free-falling spider body without any silks, the Reynolds number is about 2,300 ($Re = \rho V_t D / \mu$, $V_t = \sqrt{2\,\mathrm{mg} / (\rho A C_D)}$, where a spider's body is assumed as a 5 mm diameter sphere with 25 mg weight; the projected area of the sphere: $19.6\ \mathrm{mm}^2$, the drag coefficient of the sphere: 0.43, the terminal speed: 6.2 m s^{-1}) (Roos and Willmarth 1971). In this Reynolds number flow regime, the drag of a body is proportional to almost the square of relative wind speed. This is because the Reynolds number region of $5 < Re < 3{,}000$ is categorised as within the range of moderate Reynolds numbers, in

which the inertial force of flow is still dominant (as compared to a viscous flow; Pelegrini and Vieira 2003). On the other hand, the drag of spider silk is proportional to relative wind speed because a viscous force is dominant in this low Reynolds number regime ($Re \ll 5$) (Pelegrini and Vieira 2003). Therefore, the macroscale spider's body, which would fall with acceleration in the absence of ballooning silks, is suspended by high-tensile-strength nanoscale fibres (silks) that experience microscale fluid dynamics (low Reynolds number flow). This enables a spider to float in the air like a particle that experiences a relatively low Reynolds number flow. The Reynolds number of a spider's body with ballooning fibres attached is about 30 ($Re = \rho VD / \mu$; minimum possible velocity: 0.09 m s^{-1} by the lowest terminal speed from modified Suter's formula). The utilisation of low Reynolds number fluid dynamics in ballooning flight differs from the flight mechanics of other membranous-winged insects, which mostly use moderate or high Reynolds number aerodynamics, i.e. $10^3 < Re < 10^5$ (Dudley and Robert 2002, Sane 2003, Bomphrey 2017). Low Reynolds number flight, which uses a so-called hairy structure, can also be found in thrips and very small chalcid wasps (Weis-Fogh 1973, Kuethe 1975, Santhanakrishnan et al. 2014). However, while these species produce drag during passive flight mode (parachuting) by using 200–300-μm-long stiff setae, spiders use about 3 m long flexible multifibres for ballooning flight. This scale difference (10^4) enables large spiders to balloon (the weight of *Xysticus* spp. is 25 mg; the weight of *Encarsia formosa* [Chalcid wasp] is 2.55 µg) (Weis-Fogh 1973).

4.3.5. Usable Upward Current

The measured vertical wind speeds of updrafts ranged 0–0.5 m s^{-1} at the mean wind speed of 1.99 m s^{-1} and 0–0.7 m s^{-1} at the mean wind speed of 3.07 m s^{-1}. These values are adequate to facilitate spiders' ballooning; the required vertical wind speeds were 0.04–0.2 m s^{-1} for 10–25 mg *Xysticus* spp. and 0.2–0.35 m s^{-1} for 80–150 mg *Stegodyphus* spp. The observed negative correlation between vertical wind speed and horizontal wind speed in the turbulent boundary layer, which has also been studied in the fields of fluid dynamics and meteorology (Adrian 2007, Zhu and Katz 2007, Steiner et al. 2011), suggests to us that the reason spiders engage in their pre-ballooning behaviour at a low-wind-speed regime (smaller than 3 m s^{-1}) is because they may make use of the 'ejection' regimes in turbulent flows, which contain updraft components and are induced by a 'coherent structure' near the surface boundary layer. A shear wind on a planted field, a meadow, or relatively short plants forms an organised structure called the 'coherent structure' (possibly 'hairpin vortex' or 'horseshoe vortex', see Figure 4.22A, B; 'hairpin vortex packets' over relatively short plants and 'dual hairpin vortex structures' over planted fields [see Figure 4.22C, D]) (Theodorsen 1952, Adrian et al. 2000, Hommema and Adrian 2003, Adrian 2007, Finnigan et al. 2009, Dennis 2015). These structures intermittently produce up- and downdrafts (Adrian et al. 2000, Adrian 2007, Finnigan et al. 2009). The point of interest here is that these updrafts are highly correlated with a decrease in wind speed, which is categorised as Q2 ($u' < 0$ and $v' > 0$), an 'ejection' region in a quadrant analysis (Adrian 2007, Zhu and Katz 2007, Steiner et al. 2011) (see Figure 4.19). Therefore, the phenomenon of spiders usually ballooning in a low-wind-speed regime (lower than 3 m s^{-1}) could be explained with reference to this organised structure in the atmospheric turbulent flows above the ground. However, the frequency and duration of these updrafts are not well understood.

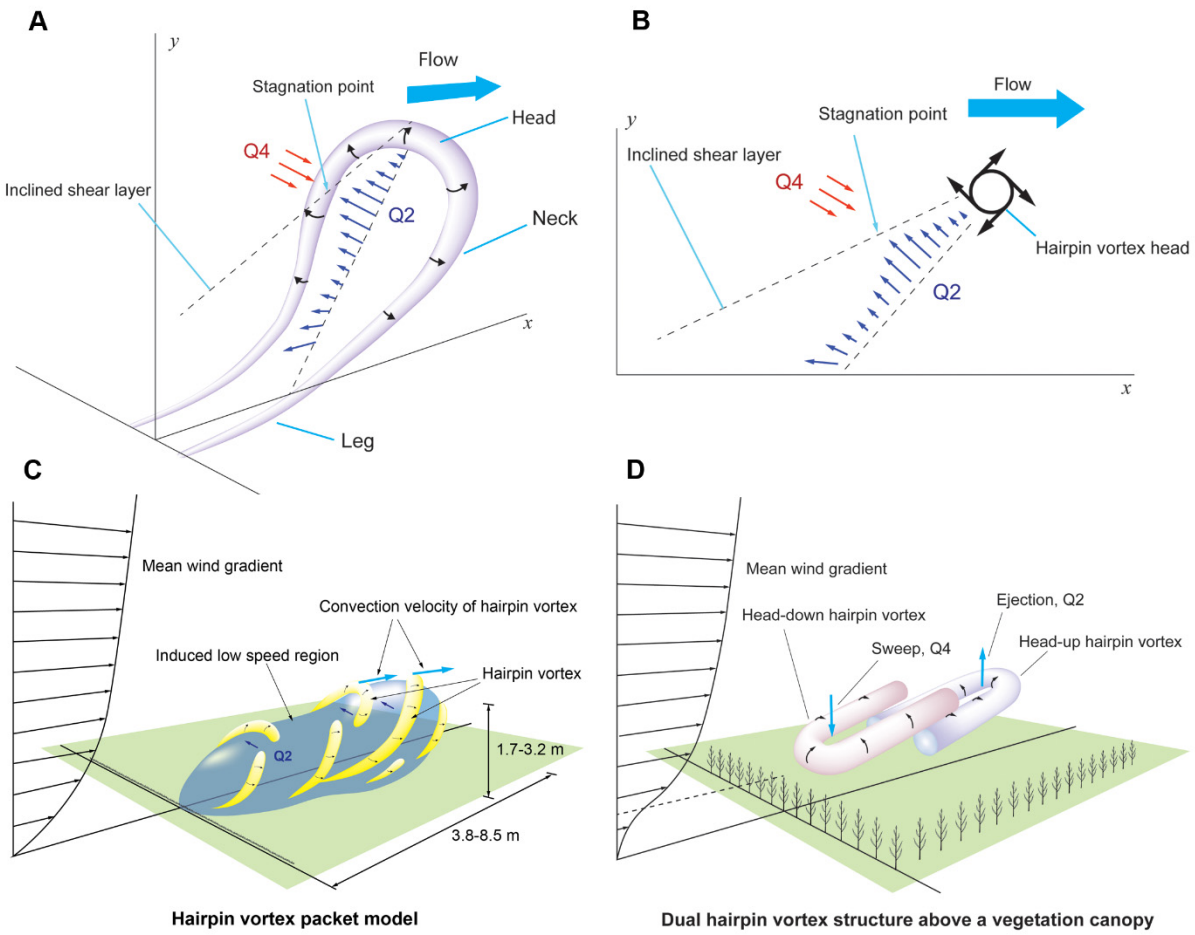

Figure 4.22 Schematic diagram of updraft generation by a vortex and vortices in near-surface atmospheric boundary layer. (A) Schematic diagram of a single hairpin vortex in the wall boundary layer. Q2 is an 'ejection' region whose velocity vectors are u' < 0 and v' > 0. Q4 is a 'sweep' region whose velocity vectors are u' > 0 and v' < 0; (B) Cross-section of the x-y plane of the hairpin vortex; (C) Schematic diagram of the hairpin vortex packet. Yellow colours indicate hairpins or cane-type vortices, while blue regions are low momentum regions, which contain upward air currents; (D) Coherent structure, 'dual hairpin vortex,' on the plant field. A head-down hairpin vortex produces a 'sweep' event, while a head-up hairpin vortex produces an 'ejection' event. (A, B) Redrawn from Adrian et al. (2000); (C) Redrawn from Adrian et al. (2000), Hommema and Adrian (2003); (D) Redrawn from Finnigan et al. (2009).

4.3.6. Shear Flow

While Reynolds postulated the tangled shape of ballooning fibres in his simulation, the diagonally lying shape of the spider's ballooning fibres was observed in our field observations in the Teltow Canal (see Figure 4.14) (Reynolds et al. 2006). The difference between our observation and Reynolds' simulation stems from the fact that, while Reynolds introduced homogeneous turbulence in his simulation, the real turbulence near the surface boundary layer includes instantaneous horizontal wind shears that are largely induced by vertical differences in wind speed (Grass 1971, Dennis 2015). This diagonally stretched shape of ballooning fibres may be caused by the shear wind in the atmospheric boundary layer. We think this may be helpful for long-endurance ballooning flight because horizontally stretched silks produce more drag (up to a factor of 2) than vertically distributed shapes of silk due to the anisotropic drag of silks in a low Reynolds number flow (Childress 1981) (see Figure 4.23A–C).

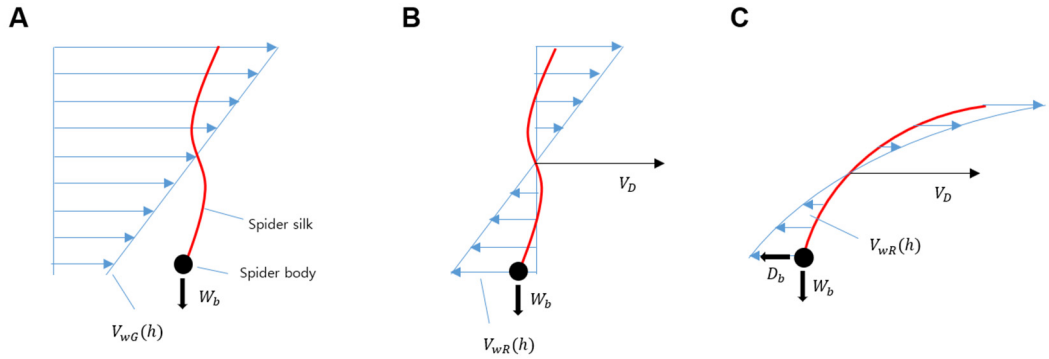

Figure 4.23 Schematic diagrams of the ballooning structure in a shear flow. (A) Ballooning structure in a shear flow; (B) Drift of a ballooning structure along with wind. The upper and lower parts of the silk are exposed to the flow fields, which exert in the other directions; (C) The ballooning structure exposed in a shear flow is stretched horizontally. If the drag of a body increases, the structure is stretched more horizontally. (V_{wG}: Wind speed profile relative to ground, V_D: Drift speed of a ballooning structure, V_{wR}: Wind speed profile relative to a ballooning structure, D_b: Horizontal component of drag on the spider's body, W_b: Weight of the spider's body, h : Vertical coordinate).

The observed fact that spiders outstretch all their legs during their flight is puzzling because of the small drag ratio of spiders' legs compared to the drag of their ballooning silks. Suter (1992) concluded that when a spider uses a relatively short length of silk, the influence of posture on its terminal speed is greater than when the silk is very long. However, our observations reveal that spiders spin abundant ballooning fibres. From Suter's empirical formula, the drags per unit velocity of a spider's body weighing 10 to 25 mg, which are 10.4–14.5 $\mu\mathrm{N} \times \mathrm{m}^{-1} \times \mathrm{s}$, make up only 0.4–0.56% of the whole drag (silks + body) per unit velocity, 2576.5–2580.5 $\mu\mathrm{N} \times \mathrm{m}^{-1} \times \mathrm{s}$. Even if a spider stretches its legs outward, the percentage of body drag is still 2.0–2.8% (a five-fold change is applied as per Suter's research; Suter 1991, 1992). Despite such a small drag effect of spiders' posture, spiders still stretch their legs outward during flight (see Figure 4.10C, D). The following question therefore arises: what role do these outstretched legs play in ballooning flight? This phenomenon should be studied in future work.

5. Dynamics in Spiders' Ballooning

According to the data acquired in Chapter 4, the spider silks are locally exposed to a low Reynolds number flow. However, the silks as a whole are passively governed by the chaotic motions of turbulence (Suter 1999, Reynolds et al. 2006), as their length on average is 3.22 m, which represents a much larger scale than the Kolmogorov scale of the air flow. Additionally, most of the weight of the airborne object is concentrated at one end of the silk. This asymmetric (eccentric) feature may in fact be the point of interest when investigating its behaviour in turbulent conditions. This idea will now be investigated with the help of numerical computation. For the concentration on the asymmetric distribution of the mass on a fibre, several things are assumed: (i) a single silk ballooner; (ii) ignorance of the effect of the body size (the diameter of a spider body equals to the thickness of a silk); (iii) no consideration of the inertia of the spider body.

5.1. Modelling

The realistic numerical simulation of ballooning flight is somewhat difficult because of the extremely high aspect ratio of ballooning lines (length to thickness ratio). Based on the data presented in Chapter 4, the aspect ratio of a ballooning fibre is 1.61×10^7 (length: 3.22 m, thickness: 200 nm). Due to the extreme thinness and long length of each fibre, high computational performance and extensive time are required to solve the dynamics of this flexible thin filament. Therefore, we employ a relatively simple method, the bead-spring model, to describe a flexible filament and simulate the motion of a ballooning structure in various non-uniform fluid-flows. Owing to its fast calculation capacity, this model offers a significant advantage for the investigation of wide ranges of various simulation parameters.

5.1.1. Bead-Spring Model

When a spider floats in the air, the whole structure can be described as a very light and thin single filament (relatively heavy spiders spin multiple silks) with the weight of a body at the end. We refer to this as the 'ballooning structure'. Spider silk is highly flexible and experiences low Reynolds number flow, which can be regarded as a Stokes flow, because the upper limit of the Reynolds number is about 0.04 ($Re = \rho V d/\mu$; air density: 1.225 kg m^{-3}; maximum possible velocity: 3 m s^{-1}; thickness of spider silk: 211 nm; dynamic viscosity of air: 1.837 x 10^{-5} kg m^{-1} s^{-1}). To model a ballooning silk that is suspended in the air flow, we introduce the bead-spring model (Zimm model), which is frequently used to approach the polymer physics and dynamics of a micro-swimmer (Doi and Edwards 1986, Yamamoto and Matsuoka 1993, Gauger and Stark 2006, Lindström and Uesaka 2007). Each bead is connected to the other with a tensile and a bending spring. By adjusting each stiffness value, we can simulate various extensibility and flexibility values of a filament. Moreover, each bead experiences hydrodynamic viscous drag in a low Reynolds number flow, which is governed by Stokes' law (see Eqn. (5.1); Happel and Brenner 1986). The Zimm model considers hydrodynamic interactions between beads. This consideration can describe the anisotropic drag of a thin filament in a low Reynolds number flow, which show the drag different between a transverse drag and a longitudinal drag (Purcell 1977, Childress 1981, Happel and Brenner 1986, Gauger and Stark 2006).

$$F = 6\pi\eta a U \tag{5.1}$$

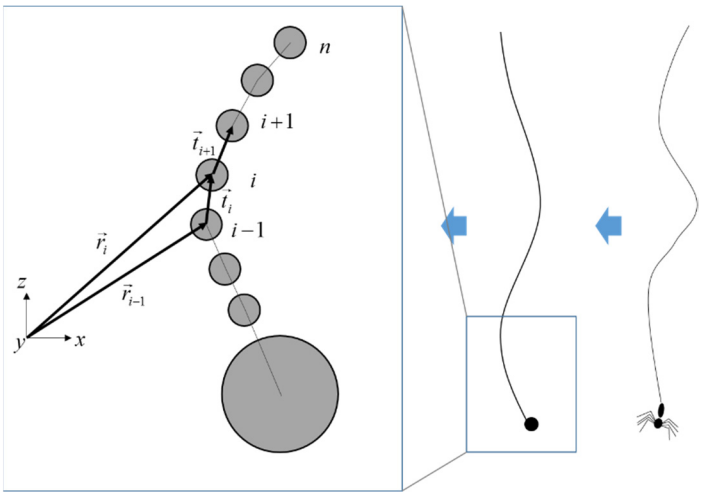

Figure 5.1 Bead-spring model for a ballooning spider.

In a low Reynolds number flow, the influence of inertia is almost negligible. This means that at every moment, the net force on the structure is zero (see Eqn. (5.2); Doyle and Underhill 2005). The net force $\boldsymbol{F}_i^{total}$ on each bead includes a fluid-dynamic force $\boldsymbol{F}_i^F$, a gravity force $\boldsymbol{F}_i^G$, a stretching force $\boldsymbol{F}_i^S$ and a bending force $\boldsymbol{F}_i^B$:

$$\boldsymbol{F}_i^{total} = \boldsymbol{F}_i^F + \boldsymbol{F}_i^G + \boldsymbol{F}_i^S + \boldsymbol{F}_i^B \approx 0 \tag{5.2}$$

The fluid-dynamic force is proportional to the fluid velocity. Therefore, resistances are defined as an inverse tensor of a bead mobility tensor $\boldsymbol{\mu}_{ij}$:

$$\boldsymbol{F}_j^F = \boldsymbol{\mu}_{ij}{}^{-\mathbf{1}}\left(\boldsymbol{u}^{\infty}(\boldsymbol{r}_i) - \frac{d\boldsymbol{r}_i}{dt}\right) \tag{5.3}$$

The bead mobility is derived through the consideration of the hydrodynamic interactions between beads. Here, we introduce the Rotne-Prager approximation, which can be applied to different sizes of beads (see Eqn. (5.6); Jeffrey and Onishi 1984, Gauger and Stark 2006):

$$\frac{d\boldsymbol{r}_i}{dt} = \boldsymbol{u}^{\infty}(\boldsymbol{r}_i) + \sum_j \boldsymbol{\mu}_{ij}\left(\boldsymbol{F}_j^G + \boldsymbol{F}_j^S + \boldsymbol{F}_j^B\right) \tag{5.4}$$

$$\boldsymbol{\mu}_{ii} = \mu_0 \mathbf{1} \text{ with } \mu_0 = \frac{1}{6\pi\eta a_i} \tag{5.5}$$

$$\boldsymbol{\mu}_{ij} = \frac{1}{6\pi\eta \boldsymbol{r}_{ij}}\left[\frac{3}{4}\left(\mathbf{1} + \hat{\boldsymbol{r}}_{ij} \otimes \hat{\boldsymbol{r}}_{ij}\right) + \frac{1}{4}\frac{a_i^2 + a_j^2}{\boldsymbol{r}_{ij}^2}\left(\mathbf{1} - 3\hat{\boldsymbol{r}}_{ij} \otimes \hat{\boldsymbol{r}}_{ij}\right)\right] \tag{5.6}$$

The gravity forces can be defined as follows:

$$\boldsymbol{F}_i^G = [0 \quad 0 \quad -v_i(\rho_i - \rho_{air})g]^{\mathrm{T}} \tag{5.7}$$

Here, we consider a linearly varying spring. Therefore, the total stretching energy can be described as in Eqn. (5.8), while the stretching force on a bead can be obtained by differentiating Eqn. (5.8):

$$E^S = \frac{1}{2}k_0 \sum_{i=2}^{N}(l_i - l_0)^2 \tag{5.8}$$

$$\boldsymbol{F}_i^S = -\boldsymbol{\nabla}_{\boldsymbol{r}_i} E^S = -k_0(l_i - l_0)\hat{\boldsymbol{t}}_i + k_0(l_{i+1} - l_0)\hat{\boldsymbol{t}}_{i+1} \tag{5.9}$$

The bending force can also be obtained by differentiating the bending energy on a bead (see Eqn. (5.11)):

$$E^B = \frac{A}{l_0}\sum_{i=1}^{N} f_i(1 - \hat{\boldsymbol{t}}_{i+1} \cdot \hat{\boldsymbol{t}}_i) \text{ where } f_i = \begin{cases} 1 & for\ 2 \le i \le N-1 \\ 0 & for\ i = 1, N \end{cases} \tag{5.10}$$

$$\begin{aligned} \boldsymbol{F}_i^B = -\boldsymbol{\nabla}_{\boldsymbol{r}_i} E^B = \frac{A}{l_0}\Bigg\{ & \frac{f_{i-1}}{l_i}\hat{\boldsymbol{t}}_{i-1} - \left[\frac{f_{i-1}}{l_i}\hat{\boldsymbol{t}}_{i-1} \cdot \hat{\boldsymbol{t}}_i + \frac{f_i}{l_{i+1}} + \frac{f_i}{l_i}\hat{\boldsymbol{t}}_i \cdot \hat{\boldsymbol{t}}_{i+1}\right]\hat{\boldsymbol{t}}_i \\ & + \left[\frac{f_i}{l_{i+1}}\hat{\boldsymbol{t}}_i \cdot \hat{\boldsymbol{t}}_{i+1} + \frac{f_i}{l_i} + \frac{f_{i+1}}{l_{i+1}}\hat{\boldsymbol{t}}_{i+1} \cdot \hat{\boldsymbol{t}}_{i+2}\right]\hat{\boldsymbol{t}}_{i+1} - \frac{f_{i+1}}{l_{i+1}}\hat{\boldsymbol{t}}_{i+2}\Bigg\} \end{aligned} \tag{5.11}$$

For details, please refer to Gauger and Stark 2006.

5.1.2. Shear Flow Model

The simplest non-uniform flow is a shear flow. Only horizontal components exist in a shear flow. Therefore, it is a very good model to investigate the sediment characteristic (vertical motion) of a ballooning structure in a non-uniform flow. Shear flow can be described as in Eqn. (5.12) (γ refers to shear rate, which has units of s^{-1}, while z is the vertical coordinate; see Figure 5.2):

$$\boldsymbol{U}(z) = [\gamma z \quad 0 \quad 0] \tag{5.12}$$

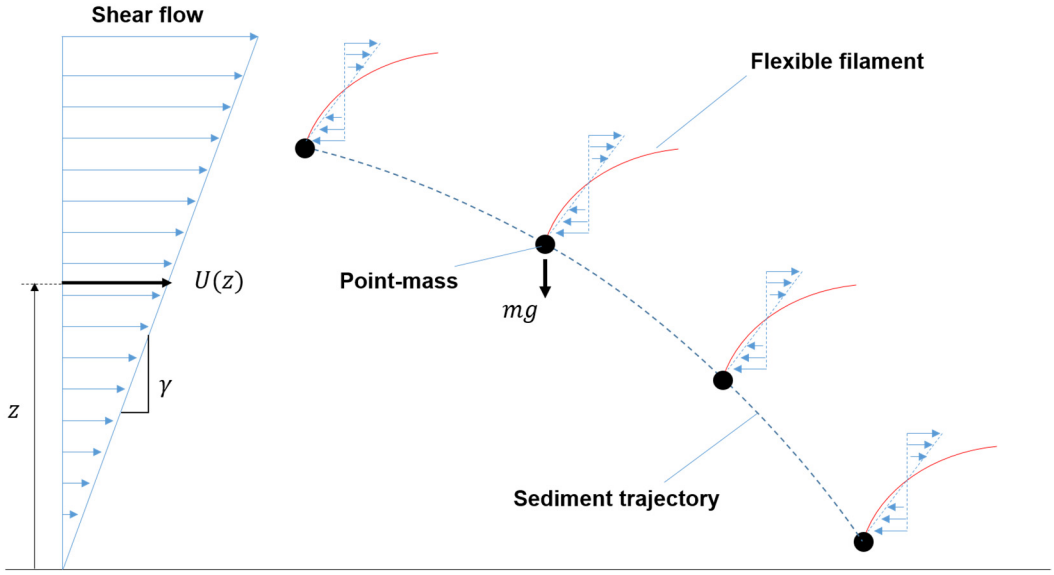

Figure 5.2 Schematic of the simulation in a shear flow.

5.1.2.1. Decomposition of Velocity Fields

To figure out the physical cause of settling speed reduction of a ballooning structure in a shear flow, we decompose the relative flow velocities $\boldsymbol{U'}_j$ on beads into the vertical and horizontal components of the relative flow velocities (see Eqns. (5.14), (5.15) and Figure 5.3). This decomposition is valid because bead spring models are governed by linear relations. From the vertical components of the relative velocities on beads $\boldsymbol{U'}_j^V$, we can calculate the vertical resistance force due to the pure geometric shape of a filament by multiplying a resistance tensor $\boldsymbol{\zeta}_{ij} = \boldsymbol{\mu}_{ij}{}^{-1}$ with the vertical components of the relative flow velocities $\boldsymbol{U'}_j^V$ (see Eqn. (5.16)). From the horizontal components of the relative flow velocities $\boldsymbol{U'}_j^H$, moreover, we can calculate the vertical resistance force that is caused by the pure horizontal shear flow multiplying a resistance tensor $\boldsymbol{\zeta}_{ij}$ with the horizontal components of the relative flow velocities $\boldsymbol{U'}_j^H$ (see Eqn. (5.17)). The horizontal flows on a thin filament can induce a vertical force because of the anisotropic character of the filament drag and the asymmetrically curved shape of the filament (see Figure 5.4BC). In the low Reynolds number flow, the drag (resistance) force of a thin filament depends on the angle of inflow. If the shape of the filament is asymmetric between the upper and lower halves of a filament, the total integrated fluid dynamics forces along the filament are not zero, but should produce a force in either the upward or downward direction. This is analogous with the swimming mechanism of a sperm. A sperm uses the drag anisotropy of a flagellum, when it moves forward. The drag anisotropy provides a force perpendicular to the direction of the local undulatory motion (Lowe 2003, Lauga and Powers 2009). The direction of the force depends on the direction of wave propagation of the undulatory motion (Fung 1990, Dreyfus et al. 2005). In this way, a sperm can move forward. The same mechanism may occur passively in a ballooning structure by the asymmetric constraint.

$$\boldsymbol{F}_i = \boldsymbol{\zeta}_{ij}\boldsymbol{U'}_j \text{ with } \boldsymbol{U'}_j = \boldsymbol{U}_j - \boldsymbol{V}_j \tag{5.13}$$

$$\boldsymbol{U}'_j = \boldsymbol{U}'^V_j + \boldsymbol{U}'^H_j \tag{5.14}$$

$$\boldsymbol{F}_i = \boldsymbol{\zeta}_{ij}\left(\boldsymbol{U}'^V_j + \boldsymbol{U}'^H_j\right) = \boldsymbol{F}^V_i + \boldsymbol{F}^H_i \tag{5.15}$$

$$\boldsymbol{F}^V_i = \boldsymbol{\zeta}_{ij}\boldsymbol{U}'^V_j \tag{5.16}$$

$$\boldsymbol{F}^H_i = \boldsymbol{\zeta}_{ij}\boldsymbol{U}'^H_j \tag{5.17}$$

Once the forces have been calculated, the non-dimensional vertical resistance coefficient of a ballooning structure can then be calculated by dividing the vertical components of forces (see Eqns. (5.18) and (5.19)) by the viscosity, settling speed and silk length (see Eqns. (5.20), (5.21) and Figure 5.3):

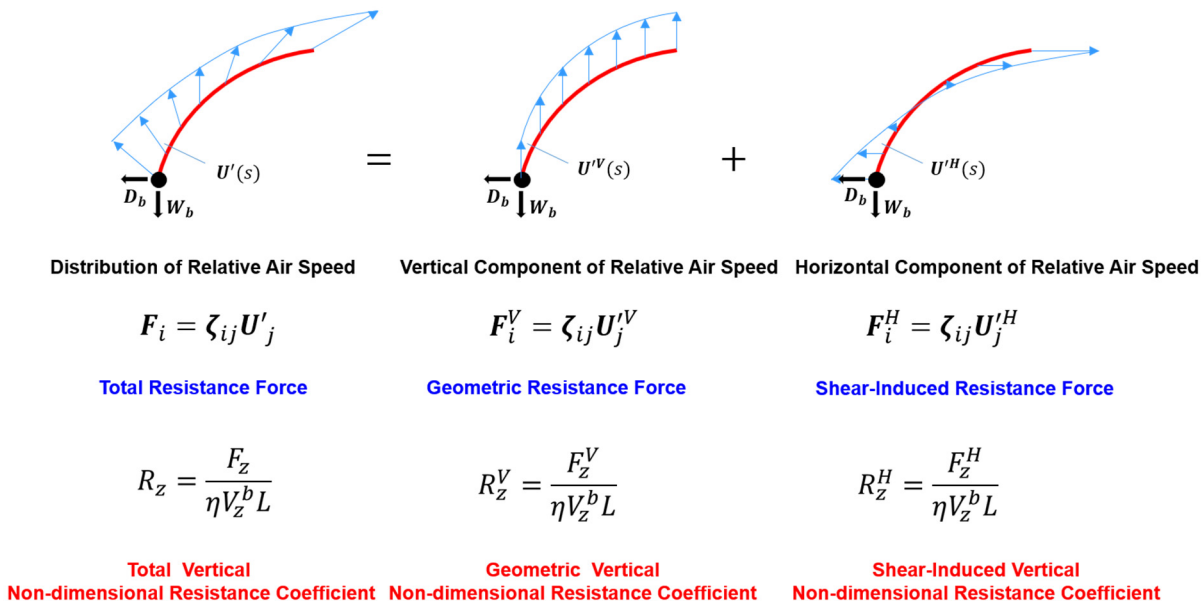

Figure 5.3 Schematic diagrams showing the decomposition process of the fluid-dynamic forces on the ballooning structure in a shear flow. (While the structure is positioned in a shear flow to build an equilibrium state in the x-direction, the point, where its relative flow velocity (in the x-direction) is zero, is always positioned on the filament structure.)

$$F^V_z = \sum_i F^V_{z,i} \tag{5.18}$$

$$F^H_z = \sum_i F^H_{z,i} \tag{5.19}$$

$$R^V_z = \frac{F^V_z}{\eta V_z^b L} \tag{5.20}$$

$$R_z^H = \frac{F_z^H}{\eta V_z^b L} \tag{5.21}$$

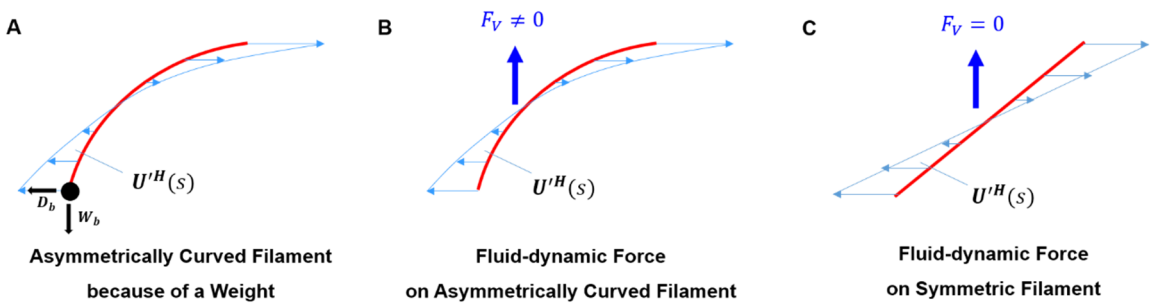

Figure 5.4 Schematic diagrams of the ballooning structure in a shear flow. (A) Ballooning structure in a shear flow; (B) In the case of an asymmetrically curved filament in a shear flow, the integrated net fluid-dynamic force along the filament is not zero; (C) In the case of a symmetrically curved or symmetric filament in a shear flow, the integrated net fluid-dynamic force along the filament is zero.

5.1.3. Periodic Cellular Flow Model

The periodic cellular flow model is used to study the settling behaviour of a particle (Maxey and Corrsin 1986, Maxey 1987a, Fung 1997, Bergougnoux et al. 2014). The cellular flow field was first used by Stommel to investigate plankton suspension in Langmuir circulation, and has since been frequently used for the study of particle sediment in turbulent flow (Stommel 1949, Maxey and Corrsin 1986, Maxey 1987a, Fung 1997, Bergougnoux et al. 2014). The flow field can be described by means of two-dimensional convection cells (see Figure 5.5). This flow field is similar with Taylor-Green vortices, but does not decay with time (Taylor and Green 1937). The flow is two dimensional, incompressible and steady and specified by a streamfunction ψ (see Eqn. (5.22)). U_0 and L_c are maximum velocity in the flow field and size of a convection cell, respectively. The velocity field of the cellular flow can be expressed by spatially differentiating the given streamfunction ψ (see Eqns. (5.23) and (5.24)).

$$\psi(x,z) = \frac{U_0 L_c}{\pi} sin\left(\frac{\pi x}{L_c}\right) sin\left(\frac{\pi z}{L_c}\right) \tag{5.22}$$

$$u = \frac{\partial \psi}{\partial z} = U_0 sin\left(\frac{\pi x}{L_c}\right) cos\left(\frac{\pi z}{L_c}\right) \tag{5.23}$$

$$w = -\frac{\partial \psi}{\partial x} = -U_0 cos\left(\frac{\pi x}{L_c}\right) sin\left(\frac{\pi z}{L_c}\right) \tag{5.24}$$

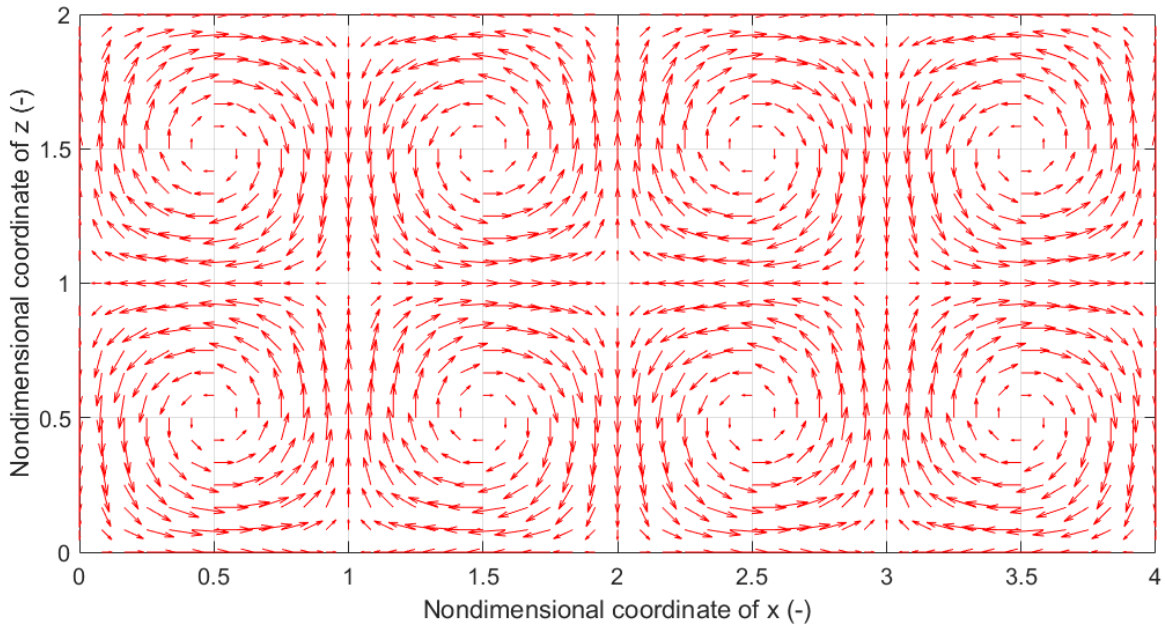

Figure 5.5 Velocity field of a periodic cellular flow model at $\boldsymbol{U_0} = \mathbf{1}$ and $\boldsymbol{L_c} = \mathbf{1}$

5.1.4. Turbulent Model

The chaotic motion of flows is modelled by Fung's kinematic simulation, which describes the turbulent flow with multiple Gaussian random velocity fields (see Figure 5.6). This model was originally developed by Kraichnan (1970), modified by Drummond et al. (1984), Turfus (1985) and Fung et al. (1992), and later used to model turbulent flows for various purposes: for example, the study of turbulent structures (Fung 1996, Vassilicos and Fung 1995, Fung and Perkins 2008, Suzuki and Sakai 2012, Lafitte et al. 2014), investigation of particle dynamics (Fung 1993, Sakai et al. 1993, Fung 1998, Fung and Vassilicos 1998, Fung 2003, Gustavsson et al. 2012), etc. The turbulence model is intended to be homogeneous and to show von Karman energy spectrum, which can describe grid-generated turbulence and the spectrum in natural wind (Harris 1971, Bearman 1972, Hunt 1973).

$$\boldsymbol{u}(\boldsymbol{r},t) = \sum_{n=1}^{N}\left[\frac{\boldsymbol{a}_n \times \boldsymbol{k}_n}{|\boldsymbol{k}_n|} cos(\boldsymbol{k}_n \cdot \boldsymbol{r} + \omega_n t) + \frac{\boldsymbol{b}_n \times \boldsymbol{k}_n}{|\boldsymbol{k}_n|} sin(\boldsymbol{k}_n \cdot \boldsymbol{r} + \omega_n t)\right] \tag{5.25}$$

The subscript n refers to the quantity of the n-th Fourier mode. The wavenumber vectors $\boldsymbol{k}_n$ are randomly chosen on each spherical shell of radius k_n. The coefficients $\boldsymbol{a}_n$ and $\boldsymbol{b}_n$ are determined by picking independently random vectors from a three-dimensional isotropic Gaussian distribution, with zero mean vector and variance $3\,\gamma \int_{k_n-\delta k/2}^{k_n+\delta k/2} E(k)dk$, where $\gamma = \int_0^\infty E(k)dk / \int_0^{k_\eta} E(k)dk$ and $\delta k = (k_\eta - k_c)/(N_k - 1)$ (Fung et al. 1992). Wavenumbers range from $k_c = 1$ to $k_\eta = 10$. For 10 Fourier modes, $k_n = k_c + (k_\eta - k_c)\,(n-1)/(N_k - 1)$, where $N_k = 10$ (Fung et al. 1992). Therefore, the sizes of eddies range from 0.628 to 6.28.

The 'von Karman' energy spectrum is expressed as follows (Hinze 1975, Fung et al. 1992):

$$E(k) = \frac{g_2 k^4}{(g_1 + k^2)^{17/6}} \tag{5.26}$$

$E(k)$ is normalised to give $\langle u_1^2 \rangle = \langle u_2^2 \rangle = \langle u_3^2 \rangle = 1$, meaning that the turbulent kinetic energy is $3/2$ (Fung 1990, Fung et al. 1992):

$$\frac{1}{2}\langle \boldsymbol{u}^2 \rangle = \int_0^\infty E(k)dk = \frac{3}{2} \tag{5.27}$$

The integral length scale is also normalised as Eqn. (5.27) (Monin and Yaglom 1977):

$$L_{11} = \frac{3\pi}{4}\int_0^\infty k^{-1}E(k)dk \Big/ \int_0^\infty E(k)dk = 1 \tag{5.28}$$

We thus obtain the numerical constants $g_1 = 0.558$ and $g_2 = 1.196$ (Hunt 1973).

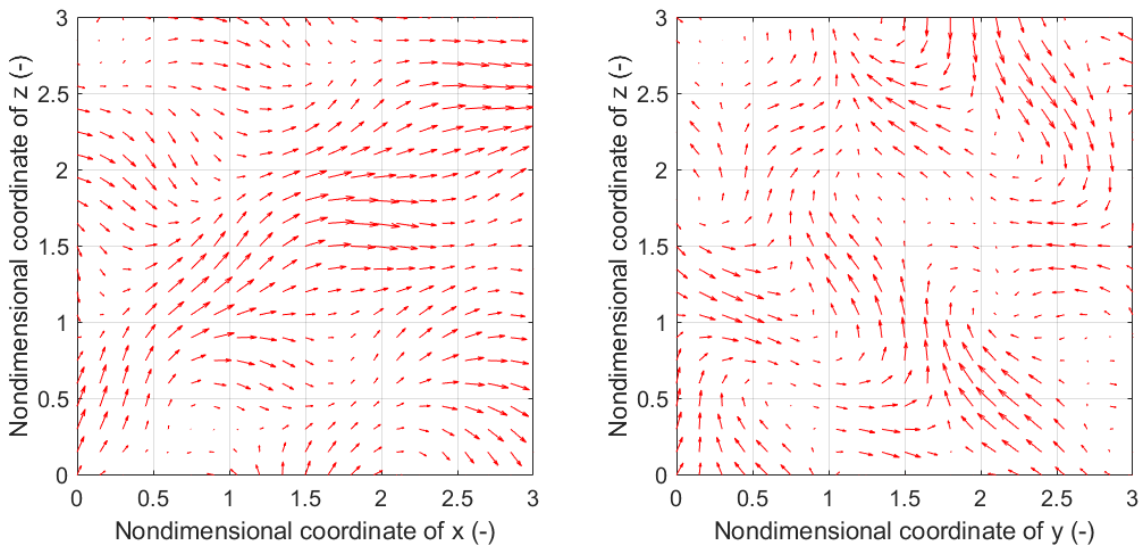

Figure 5.6 Cross-sectional velocity fields of the 3-dimensional homogeneous turbulence.

5.2. Validation

To validate the anisotropic character of the bead model, we compared the results of hydrodynamic simulation with the results of the approximate method proposed by Burgers (1938, Happel and Brenner 1991) and experimental data. The experiment is implemented using straight and cylindrical steel wires with thicknesses ranging from 0.3-0.8 mm. The drag forces of these steel wires are measured in both directions (transverse, in the direction perpendicular to the axis, and longitudinally, in the direction of the axis) by dropping the wires into corn syrup with viscosities ranging from 2-3 kg/ms. The simulation values coincide very well with those of the experiments and the theoretical values. The experiment shows the 1.3-2.2 factors of the ratio between a transverse drag and a longitudinal drag. The values from the approximated method indicate the factors of 1.5-1.6. The simulation shows the factors of 1.3-1.5. This ratio of the drag on a wire moving perpendicular to the axis to the drag on a wire moving parallel to its length is supposed to be a factor of 2, however Purcell proposed that it may be around 1.5 from his experiment (Purcell 1977). Although there are large differences in the slenderness of filaments between real ballooning phenomena and our model, a simulation with slenderness of 45 to 120 can describe the anisotropic character of a filament in a low Reynolds flow and can also be used for the study of fibre motion in various fluid flows (Lauga and Powers 2009).

The non-dimensional resistance coefficients, which are based on Burgers' approximated methods (Eqns. (2.2) and (2.3)), are calculated by means of Eqns. (5.29) and (5.30). The non-dimensional resistance coefficients differ from the translation tensor, which has length scale (Happel and Brenner 1991).

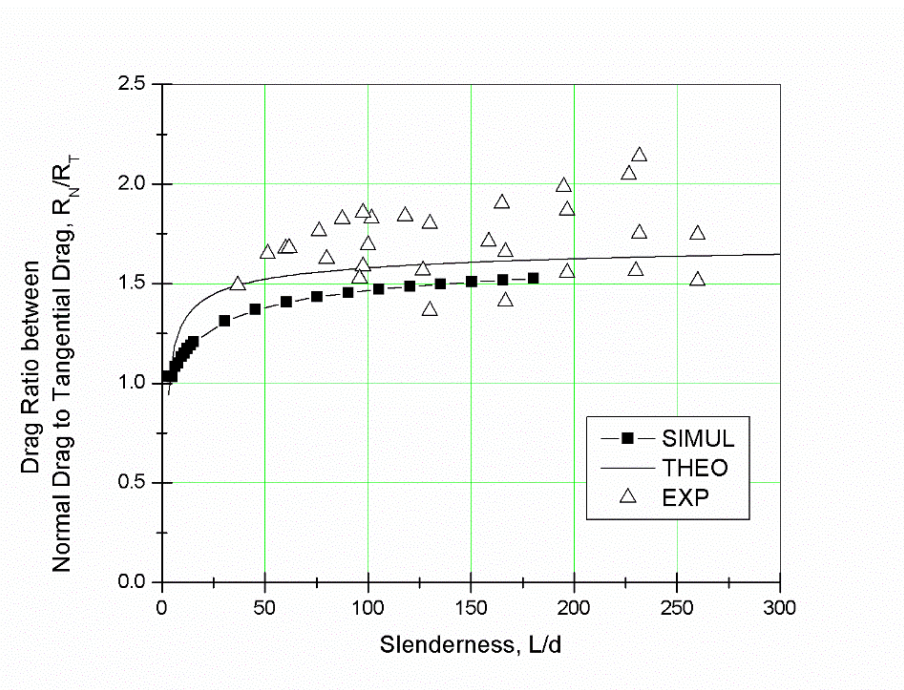

Figure 5.7 Ratio of the transverse drag force to the longitudinal drag force of a thin cylindrical rod.

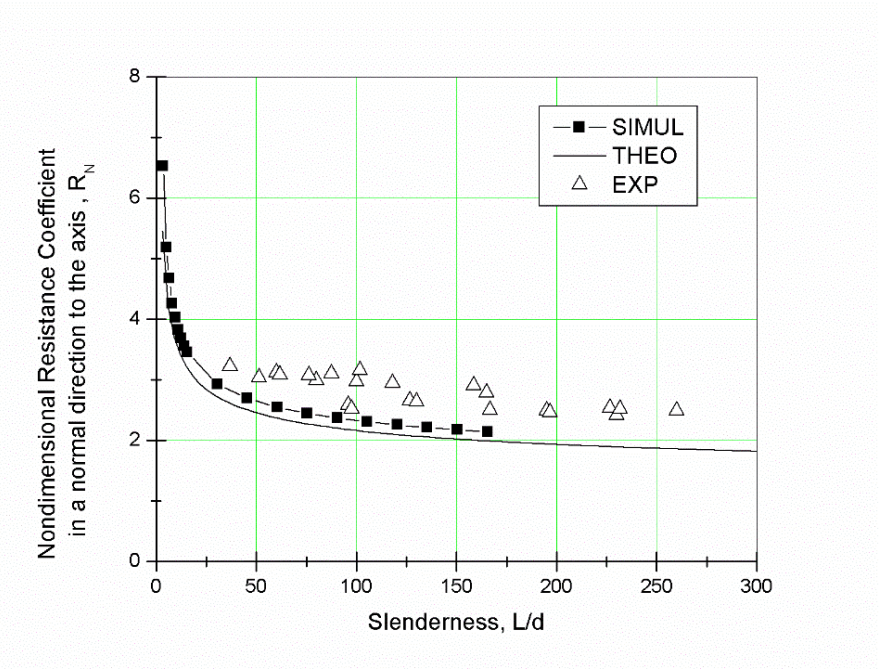

Figure 5.8 Dimensionless transverse (normal) resistance coefficients of a thin cylinder as a function of the slenderness of the cylinder.

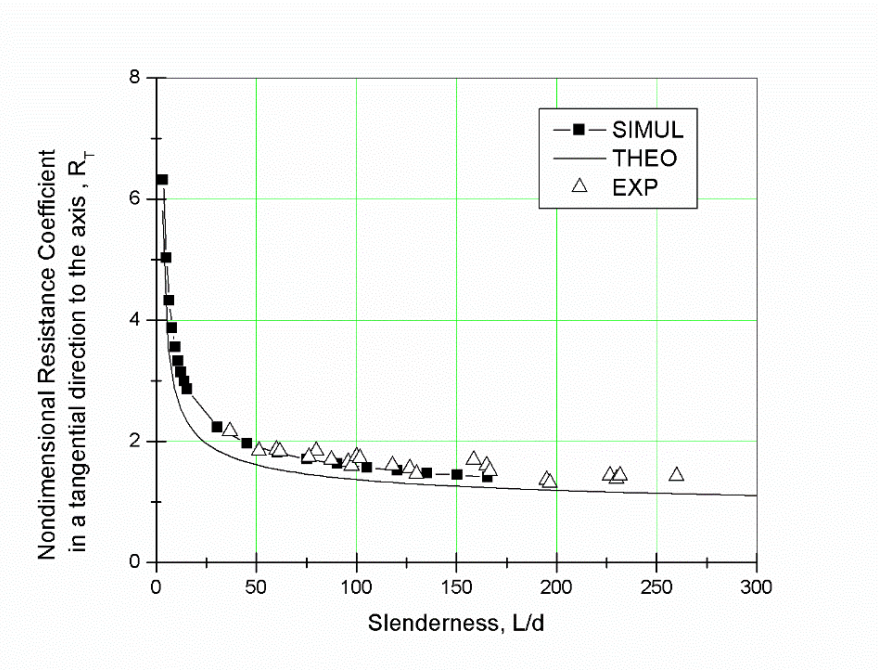

Figure 5.9 Dimensionless longitudinal (tangential) resistance coefficients of a thin cylinder as a function of the slenderness of the cylinder.

$$R_N = \frac{K_N}{L} = \frac{F_N}{\eta U L} \tag{5.29}$$

$$R_T = \frac{K_T}{L} = \frac{F_T}{\eta U L} \tag{5.30}$$

5.3. Non-dimensional Parameter

In order to consider a wide range of physical scales, we define a non-dimensional parameter, referred to as the 'ballooning number', by comparing the Stokes force on a filament to a gravity force on the weight, i.e. a spider's body at the end of a slender and flexible filament (see Eqn. (5.32)). The Stokes force on a filament is described by multiplying the viscosity, characteristic velocity and length of a filament. In the formula, we do not consider the thickness of the filament, as the influence of filament thickness on the fluid- dynamic force in a low Reynolds number flow is relatively smaller than that of filament length. The gravity force on a weight is defined as the mass of the weight multiplied by a gravity acceleration, 9.8 m/s^2. The characteristic velocity can be defined in various ways according to the flow conditions. For a shear flow, it is defined as the value of the shear rate multiplied by the length of the filament, $U = \gamma L$ (see Eqn. (5.33)). In the case of a cellular flow, moreover, the characteristic velocity is the maximum velocity in the flow, U_0 (see Eqn. (5.34)). For a homogeneous turbulence, the characteristic velocity is the root-mean-square fluctuation velocity, σ (see Eqn. (5.35)):

$$Ballooning\ Number = \frac{Stokes\ force\ on\ a\ filament\ by\ nonuniform\ flow}{Gravity\ force\ on\ a\ body} \tag{5.31}$$

$$Bn = \frac{\eta U L}{(\rho_{body} - \rho_{fluid}) v_{body} g} \tag{5.32}$$

$$Bn_{shear} = \frac{\eta \gamma L^2}{(\rho_{body} - \rho_{fluid}) v_{body} g} \tag{5.33}$$

$$Bn_{vor} = \frac{\eta U_0 L}{(\rho_{body} - \rho_{fluid}) v_{body} g} \tag{5.34}$$

$$Bn_{tur} = \frac{\eta \sigma L}{(\rho_{body} - \rho_{fluid}) v_{body} g} \tag{5.35}$$

5.4. Input Parameters

As mentioned in 5.1, a ballooning fibre has an extreme high aspect ratio of 1.61×10^7. This unique characteristic enables to include two different flow regimes, low Reynolds number flow and turbulent flow (a representative flow phenomenon in high Reynolds number flow), in its dynamics. However, modelling such a high aspect ratio structure requires extreme high computational costs. In this simulation, the difficulty is overcome by defining the nondimensional parameter of the ballooning number and introducing an artificial fluid, the motion which resembles that of homogeneous turbulence of the air, but that has high viscosity. These treatments enable the incorporation of the two different flow regimes in a single model, which has relatively small slenderness of 45-120, and the universal analysis under the condition of different scales of the structure and various properties of fluids is possible.

5.4.1. Shear Flow

Table 5.1 shows input parameter sets for a shear flow. Different sets and combinations of input parameters are used, in order to cover the wide range of the ballooning number. The sets of 1-3 in Table 5.1 are used for the model with the hydrodynamic interaction between beads. The set 4 is used for the model without with the hydrodynamic interaction between beads. The variation of the spring constants is applied in order not to exceed elongation of 1.2 of the chain, because the drag anisotropy diminishes as the distance between beads increases.

Table 5.1 Input parameters for a shear flow.

	Set 1	**Set 2**	**Set 3**	**Set 4 (No Hydro.)**
Bn_{shear}	0.011 - 57	0.042 - 1133	1.9 - 4539	0.047 - 155
n	20, 30, 40	40, 60	40, 80	30, 40, 50
γ [/s]	0.1, 0.2, 0.5, 1, 2, 5	0.1, 0.2, 0.5, 1, 2, 5	1, 2, 5, 10	0.1, 0.2, 0.5, 1, 2, 5
η $[kg/(m \cdot s)]$	0.1, 0.2, 0.5, 1, 2, 5	0.1, 0.2, 0.5, 1, 2, 5	0.5, 1, 2, 5, 10	0.1, 0.2, 0.5, 1, 2, 5
a $[m]$	0.1	0.1	0.1	0.1
a_1	a	a	a	a
$a_2, \cdots, a_n$	a	a	a	a
g_0	a	a	a	a
l_0	$3a$	$3a$	$3a$	$3a$
w_1 $[kg]$	0.1, 0.2, 0.5, 1	0.1, 0.2, 0.5, 1	0.1, 0.2, 0.5, 1	0.1, 0.2, 0.5, 1
$\rho_2, \cdots, \rho_n$ $[kg/m^3]$	1.225	1.225	1.225	1.225
ρ_f $[kg/m^3]$	1.225	1.225	1.225	1.225
k $[N/m]$	200	300	1000	200
A $[Nm]$	1.0×10^{-4}	1.0×10^{-4}	1.0×10^{-4}	1.0×10^{-4}
Δt $[sec]$	0.001	0.001	0.0005	0.001

5.4.2. Periodic Cellular Flow

The wide range of the ballooning number is achieved by varying the characteristic velocity of the periodic cellular flow and the weight of the ballooning structure. The input parameters are summarised in Table 5.2. The ratio of the filament length to the diameter of a vortex cell is additionally considered by simulating in various sizes of cellular vortex fields. The three different x-axis positions are employed to observe the dependency of the initial condition at the release.

Table 5.2 Input parameters for a periodic cellular flow.

	Values
Bn_{vor}	0.064 - 3.42
n	30
U_0 [m/s]	0.25, 0.5, 1, 1.5
L_c	0.25, 0.5, 0.75, 1, 1.25, 1.5, 2 $\times L$
x_0	0.25, 0.5, 0.75 $\times L$
η $[kg/(m \cdot s)]$	0.5
a $[m]$	0.1
a_1	a
$a_2, \cdots, a_n$	a
g_0	a
l_0	$3a$
w_1 $[kg]$	0.1, 0.2, 0.5, 1
$\rho_2, \cdots, \rho_n$ $[kg/m^3]$	1.225
ρ_f $[kg/m^3]$	1.225
k $[N/m]$	200
A $[Nm]$	1.0×10^{-4}
Δt $[sec]$	0.002

5.4.3. Homogeneous Turbulence

The ballooning number is varied by composing different parameters, e.g. the length of the structure, the viscosity of the medium, the turbulent kinetic energy and its weight. Table 5.3 shows the input parameters which are used in the simulation. The elastic constant of the tensile spring is increased, because the elongation of a spider silk is limited to the 30% of the initial length (Ko et al. 2001, Bonino 2003). The divergence problem of the bead-spring model in the turbulent flow field is corrected by adjusting the bending stiffness of the bending spring to 0.1 Nm.

Table 5.3 Input parameters for a homogeneous turbulence.

	Values
Bn_{tur}	0.022 - 445
n	20, 30, 40
$TKE\ [m^2/s^2]$	0.23 - 2.45
σ	0.68 - 2.22
$\eta\ [kg/(m \cdot s)]$	0.1, 0.2, 0.5, 1, 2, 5
$a\ [m]$	0.1
a_1	a
$a_2, \cdots, a_n$	a
g_0	a
l_0	$3a$
$w_1\ [kg]$	0.01, 0.02, 0.05, 0.1, 0.2 0. 5, 1
$\rho_2, \cdots, \rho_n$ $[kg/m^3]$	1.225
$\rho_f\ [kg/m^3]$	1.225
$k\ [N/m]$	300
A $[Nm]$	0.1
$\Delta t\ [sec]$	0.001

5.5. Execution

The motion of the bead-spring model is numerically integrated by using the Euler method (see Figure 5.10). The external flow field influences the motion of the bead-spring model. However, the structure does not affect the flow field. The integration of the simulation in a shear flow is performed until the simulation reaches to the steady state. The execution time for the simulation in a periodic cellular flow and in homogeneous turbulence are defined by comparing the settling speed of the model in the still fluid-medium and the strength of a cellular flow U_0 / the root-mean-square fluctuation velocity of the homogeneous turbulence σ, respectively. The total number of integration time-steps are calculated by equations (5.36), (5.37), (5.38), and (5.39). If the sedimentation is more dominant than the background velocity fields, the length of a fiber L is divided by the possible smallest sediment velocities of $|V_{z,still} + U_0|$ and $|V_{z,still} + \sigma|$. This time is defined as one time-revolution. In order to collect enough data for the average, 20 times longer period of this one time-revolution is used for the total simulation time ($f_{vor} = 20$, $f_{tur} = 20$). The total number of integration time-steps are acquired by dividing it by the time-step Δt. (see Eqns. (5.36) and (5.38)) If the strength of the background velocity field is more dominant than the sedimentation, the perimeters of a vortex in a periodic cellular flow and the largest eddy in the turbulence, πL_c and $\pi l_{large\ eddy}$, are divided by the possible smallest drift velocities of $|V_{z,still} + U_0|$ and $|V_{z,still} + \sigma|$, respectively. As the same with above, this time is defined as one time-revolution. For the collection of enough data, 20 times longer period of this one time-revolution is used for the total simulation time ($f_{vor} = 20$, $f_{tur} = 20$). The total number of integration time-steps are acquired by dividing it by the time-step Δt. (see Eqns. (5.37) and (5.39))

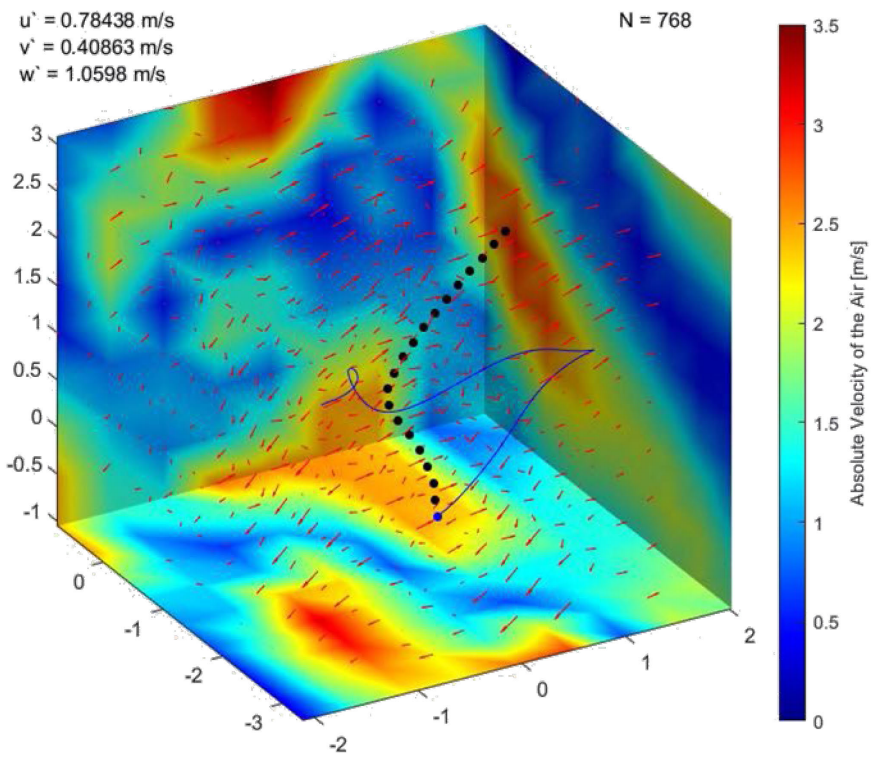

Figure 5.10 Simulation of the filament-like structure in the homogeneous turbulence. The bold points describe the bead-spring model. The blue point is the bead on which the point mass is applied. The blue solid line is the trajectory of the point mass. The colour bar represents absolute velocities of the flow. [Scan the right above QR code or click the text to connect to the video]

$$N_{vor} = f_{vor} \frac{L}{|V_{z,still} + U_0|\Delta t} \qquad \text{if } |V_{z,still}| > U_0 \tag{5.36}$$

$$N_{vor} = f_{vor} \frac{\pi L_c}{|V_{z,still} + U_0|\Delta t} \qquad \text{if } |V_{z,still}| < U_0 \tag{5.37}$$

$$N_{tur} = f_{tur} \frac{L}{|V_{z,still} + \sigma|\Delta t} \qquad \text{if } |V_{z,still}| > \sigma \tag{5.38}$$

$$N_{tur} = f_{tur} \frac{\pi l_{large\ eddy}}{|V_{z,still} + \sigma|\Delta t} \qquad \text{if } |V_{z,still}| < \sigma \tag{5.39}$$

5.6. Results

Spiders fly passively in chaotic air currents. Accordingly, the influence of various non-uniform flows on the spider fibre is explored using the bead-spring model.

5.6.1. Shear Flow

5.6.1.1. Sediment Event in a Shear Flow

The shear flow has a constant horizontal velocity gradient, which is referred as Couette flow. The velocity on the ground surface is zero. As the ballooning structure sediments in the flow, the entire structure drifts with the flow. The upper and lower parts of the filament are exposed to different flow velocity fields because of the velocity gradient (see Figure 5.2). The different velocity fields deform the filament structure. As the shear rate increases, the deformation becomes larger and the deformed geometry in the shear flow effects on the sediment velocity of the structure (see Figure 5.11). The influence of strength of the shear flow on the sedimentation is universally investigated by introducing the non-dimensional parameter of the “ballooning number” (see Eqn. (5.33)) and applying various compositions of the parameters e.g. viscosity of the medium, shear rate of the flow, length of the filament and weight of the point mass.

5.6.1.2. Influence of Anisotropic Drag

The influence of the anisotropic drag is studied by comparing two results: namely, those with and without hydrodynamic interaction. The settling speed of a ballooning structure is non-dimensionalised by the settling speed of the same structure in still conditions (i.e. zero shear rate). Therefore, the

dimensionless settling speeds (which are above 1) indicate fast falling (faster than the settling speed in still medium), while the dimensionless settling speeds (which are below 1) indicate slow settling events caused by shear flow. As the dimensionless shear rate (ballooning number for shear flow, Bn_{shear}) increases, the ballooning structure stretches horizontally (see Figure 5.11) and the settling speed is reduced. These results are not seen in cases in which the hydrodynamic interaction is ignored (considering the isotropic drag of a fibre) (see Figure 5.12). The settling speed is reduced by 40% at the high ballooning number (Bn_{shear}=1000).

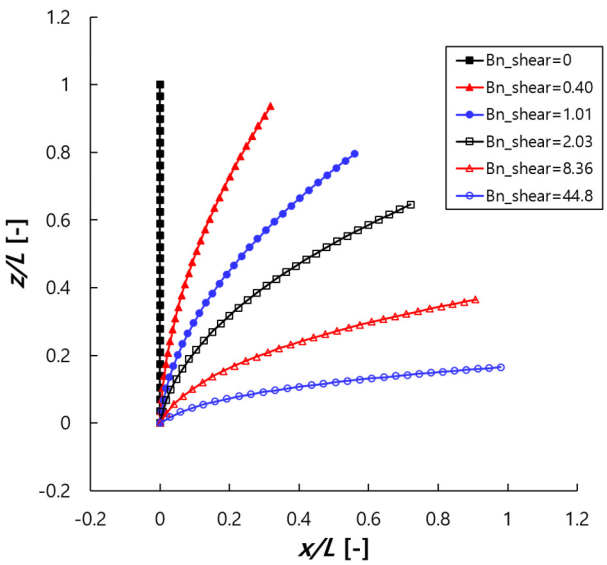

Figure 5.11 Shapes of a filament in various strengths of a shear flow (various ballooning numbers).

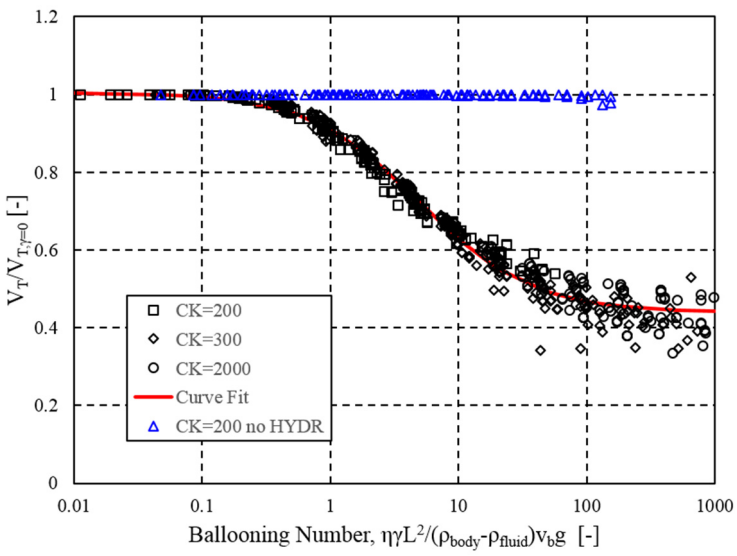

Figure 5.12 Variation of dimensionless settling velocity of the ballooning structure in a shear flow with variation of the ballooning number. Black marks indicate the cases with hydrodynamic interaction (considering the anisotropic drag of the filament), while blue marks are the cases without hydrodynamic interaction (considering the isotropic drag of the filament). CK refers to the spring constants between beads.

5.6.1.3. *Cause of Reduction of the Settling Speed*

The parameter most associated with settling speed is the translational resistance coefficient of the object. The translational resistance coefficient of a filament-like object is expressed by a vertical drag force divided by the dynamic viscosity and the settling speed. For general analysis, the translational resistance coefficient in vertical direction is nondimensionalized.

$$R_z = \frac{K_z}{L} = \frac{F_z}{\eta V_z L} \tag{5.40}$$

To elucidate the causes of the reduction of the settling speed, the nondimensional resistance coefficient is decomposed into geometric (see Eqn. (5.20)) and shear-induced (see Eqn. (5.21)) nondimensional resistance coefficients (see Figure 5.3).

The variation of the dimensionless resistance coefficient is presented in Figure 5.13. As the ballooning number increases, so too does the total nondimensional resistance coefficient. This coincides with the fact that the nondimensional settling speed decreases as the ballooning number increases (see Figure 5.12). The increase of the nondimensional resistance coefficient at the beginning, $0.1 < Bn_{shear} < 3$, is mostly caused by the geomeric shape of a filament, which is stretched horizontally and falls in a transverse attitude (see red triangular marks in Figure 5.13). At ballooning numbers over 3, the increase of the nondimensional resistance coefficient is caused by a shear flow (see blue circular marks in Figure 5.13).

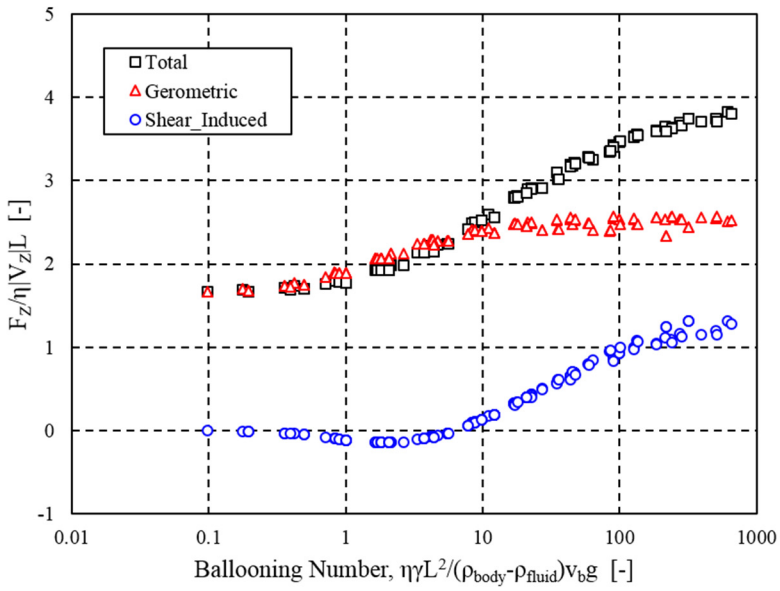

Figure 5.13 Variation of dimensionless resistance coefficients with the ballooning number for a shear flow. The dimensionless resistance coefficient is decomposed into geometric coefficient and shear-induced coefficient.

The vertical component of the total drag of the object is always equal to its weight in the case of a free-falling object in a fluid medium. Therefore, the nondimensionalised vertical drag force is 1 and is independent of the ballooning number (see black square marks in Figure 5.14). However, the causes

of the drag force vary as the ballooning number varies. First, when the shear flow is very small, the vertical drag force mostly depends on the geometry (attitude) of a filament (see red triangular marks in Figure 5.14). After the ballooning number of 0.15, a shear-induced drag force contributes to the ballooning structure falling faster; however, this is compensated by its geometrical drag force. Above the ballooning number of 3, the shear-induced drag force contributes to the ballooning structure falling slower than would be the case in a still medium (see blue circular marks in Figure 5.14).

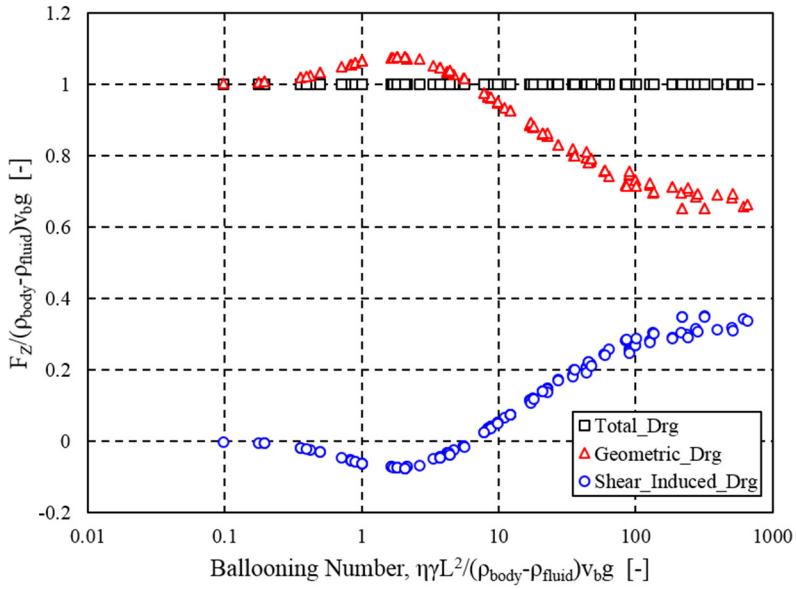

Figure 5.14 Variation of decomposed resistance forces over the ballooning number for a shear flow. The forces are nondimensionalised by the net force of gravity and buoyancy.

5.6.1.4. Sectional Feature of the Spider Silk

The distributions of relative velocities of the fluid flow and fluid dynamic forces are expressed on the ballooning structure (see Figure 5.15). In the case of the small ballooning number Bn_{shear}=0.104, the ballooning spider falls vertically and the flow velocity vectors direct upward (see Figure 5.15AB). In the case of the ballooning number Bn_{shear}=1.4, however, the lower and upper sections of a spider silk have opposite (left/right) velocity vector components; because of these opposite-velocity components, the silk is stretched horizontally while it settles (see Figure 5.15CD). In the case of the high ballooning number Bn_{shear}=20.7, the silk is stretched almost horizontally, and the flow velocity vectors also show almost horizontal (left/right) components (see Figure 5.15EF).

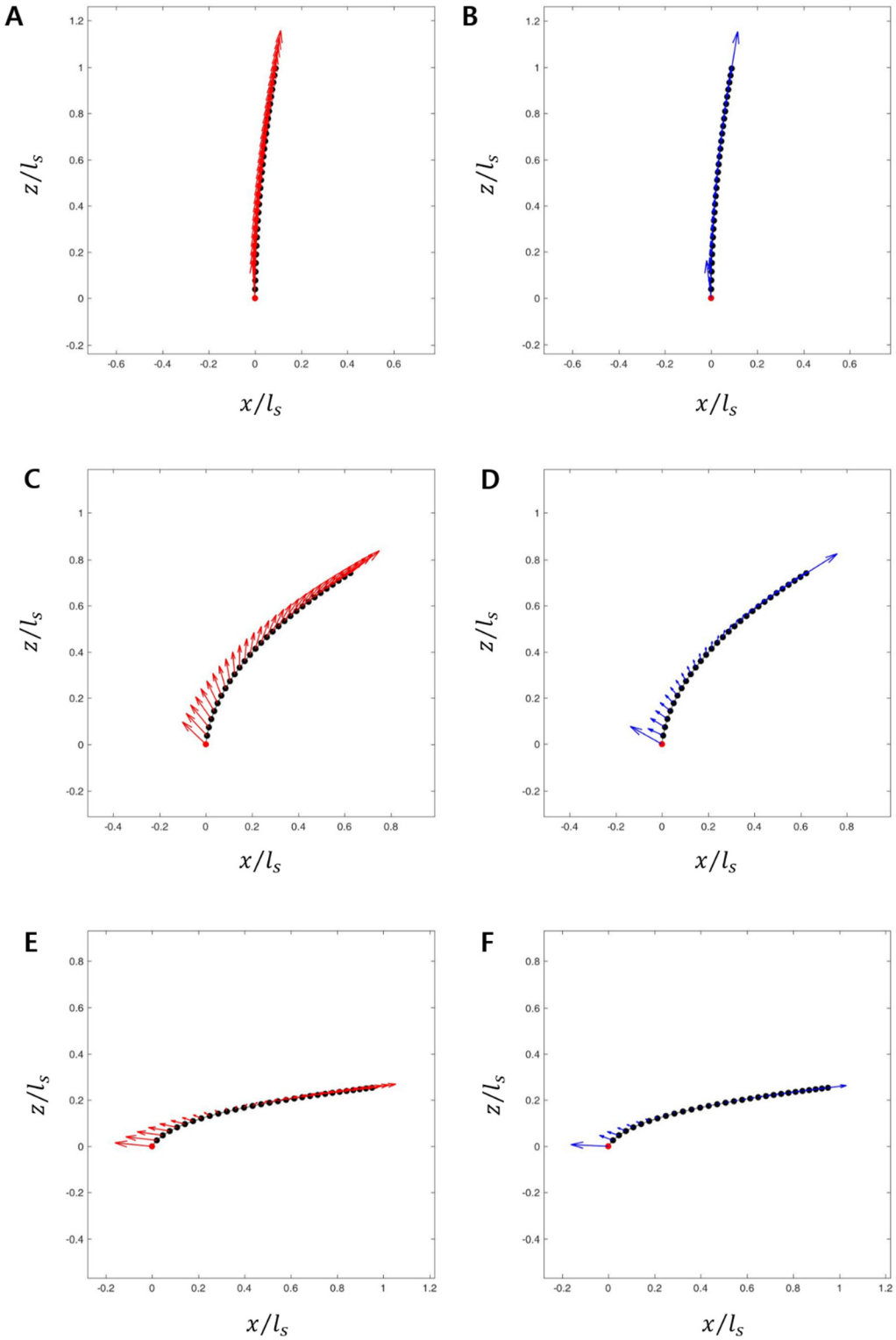

Figure 5.15 Relative flow velocity and resistance force vector distributions on the ballooning structure in a shear flow. (A) Velocity vector distribution when Bn_{shear}= 0.104; (B) Force vector distribution when Bn_{shear}= 0.104; (C) Velocity vector distribution when Bn_{shear}= 1.4; (D) Force vector distribution when Bn_{shear}= 1.4. (E) Velocity vector distribution when Bn_{shear}= 20.7; (F) Force vector distribution when Bn_{shear} =20.7. (Red dots indicate weight, while black dots describe a flexible filament structure.)

From the decomposed velocity vectors, we can understand the role of shear flow in the spider's ballooning. If the ballooning numbers are relatively small, the shear-induced fluid dynamic force vectors are downward, while the geometric fluid dynamic force vectors are upward (see Figure 5.16BD, Figure 5.17BD). However, if the ballooning number is high, shear-induced fluid dynamic forces become positive. Moreover, most forces are produced near the spider's body (see Figure 5.18BD and Figure 5.19BDF).

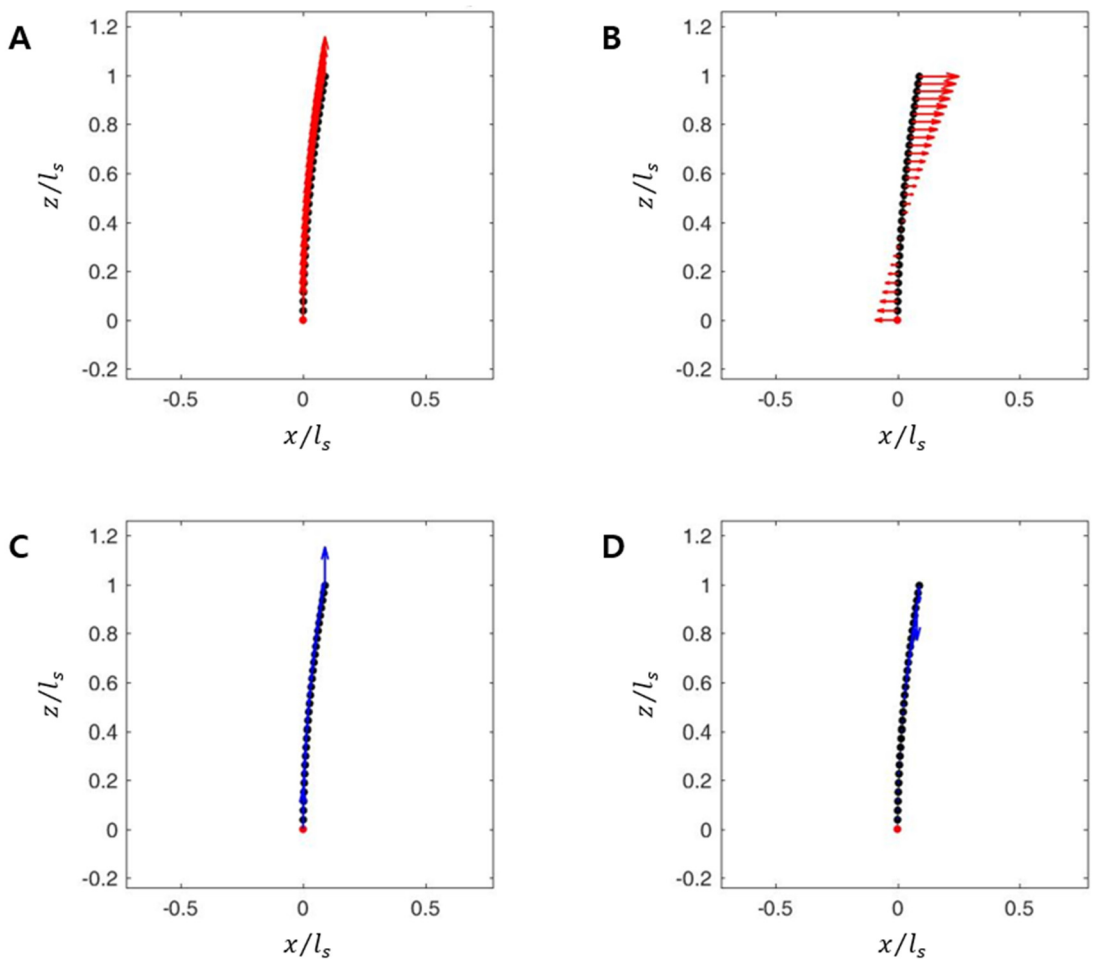

Figure 5.16 Decomposition of relative flow velocity vectors and resistance force vectors on the ballooning structure in the case of the ballooning number Bn_{shear}= 0.104. (A) Vertical components of relative flow velocity vectors; (B) Horizontal components of relative flow velocity vectors; (C) Geometric vertical resistance forces (vertical components of resistance force vectors due to vertical relative flow velocities); (D) Shear-induced vertical resistance forces (vertical components of resistance force vectors due to horizontal relative flow velocities).

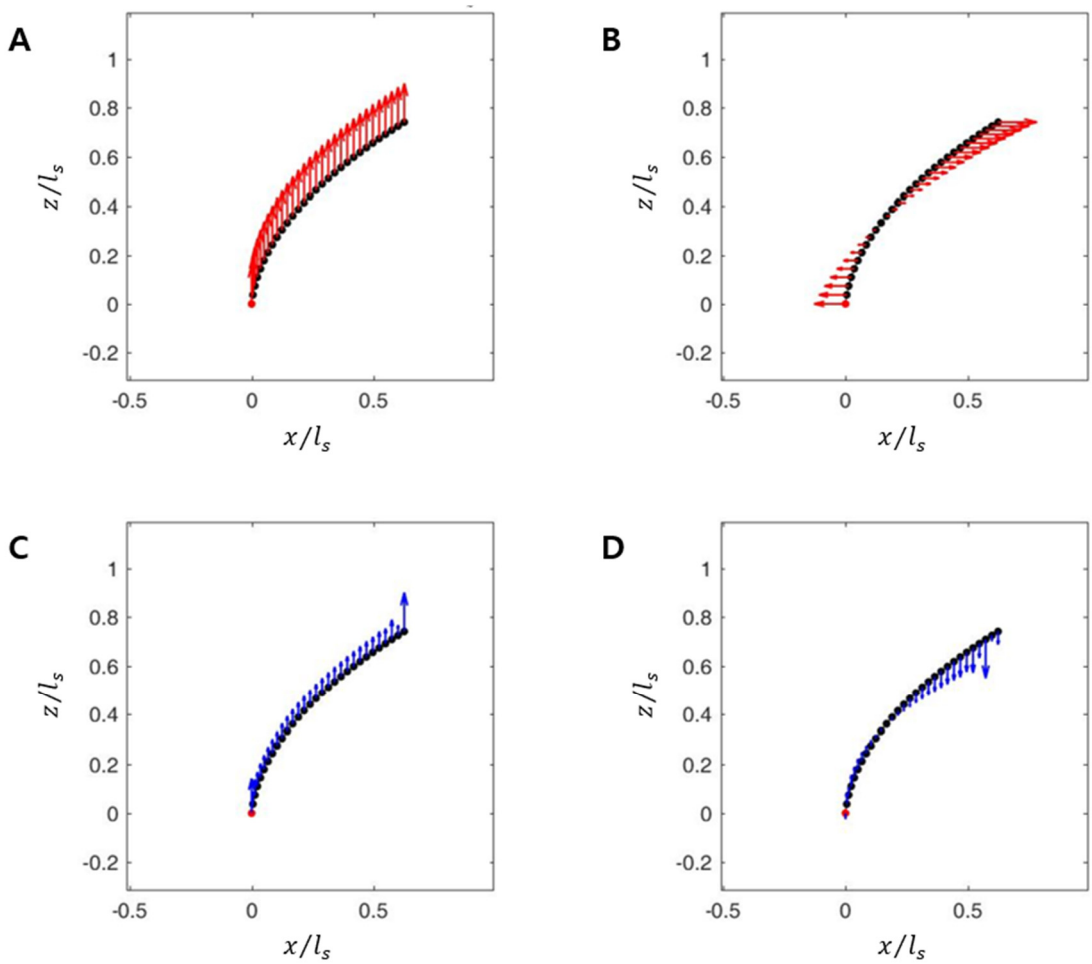

Figure 5.17 Decomposition of relative flow velocity vectors and resistance force vectors on the ballooning structure in the case of the ballooning number Bn_{shear}= 1.4. (A) Vertical components of relative flow velocity vectors; (B) Horizontal components of relative flow velocity vectors; (C) Geometric vertical resistance forces (vertical components of resistance force vectors due to vertical relative flow velocities); (D) Shear-induced vertical resistance forces (vertical components of resistance force vectors due to horizontal relative flow velocities).

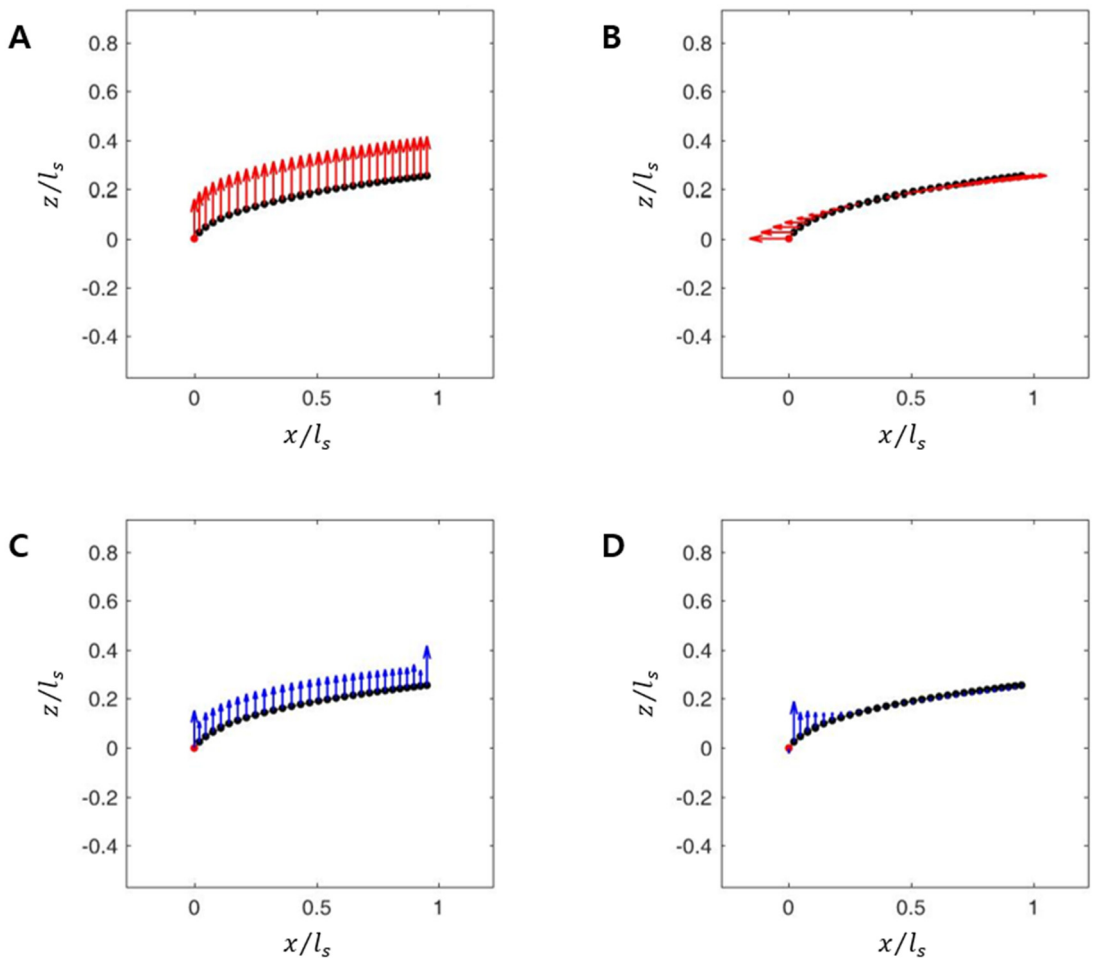

Figure 5.18 Decomposition of relative flow velocity vectors and resistance force vectors on the ballooning structure in the case of the ballooning number Bn_{shear}= 20.7. (A) Vertical components of relative flow velocity vectors; (B) Horizontal components of relative flow velocity vectors; (C) Geometric vertical resistance forces (vertical components of resistance force vectors due to vertical relative flow velocities); (D) Shear-induced vertical resistance forces (vertical components of resistance force vectors due to horizontal relative flow velocities).

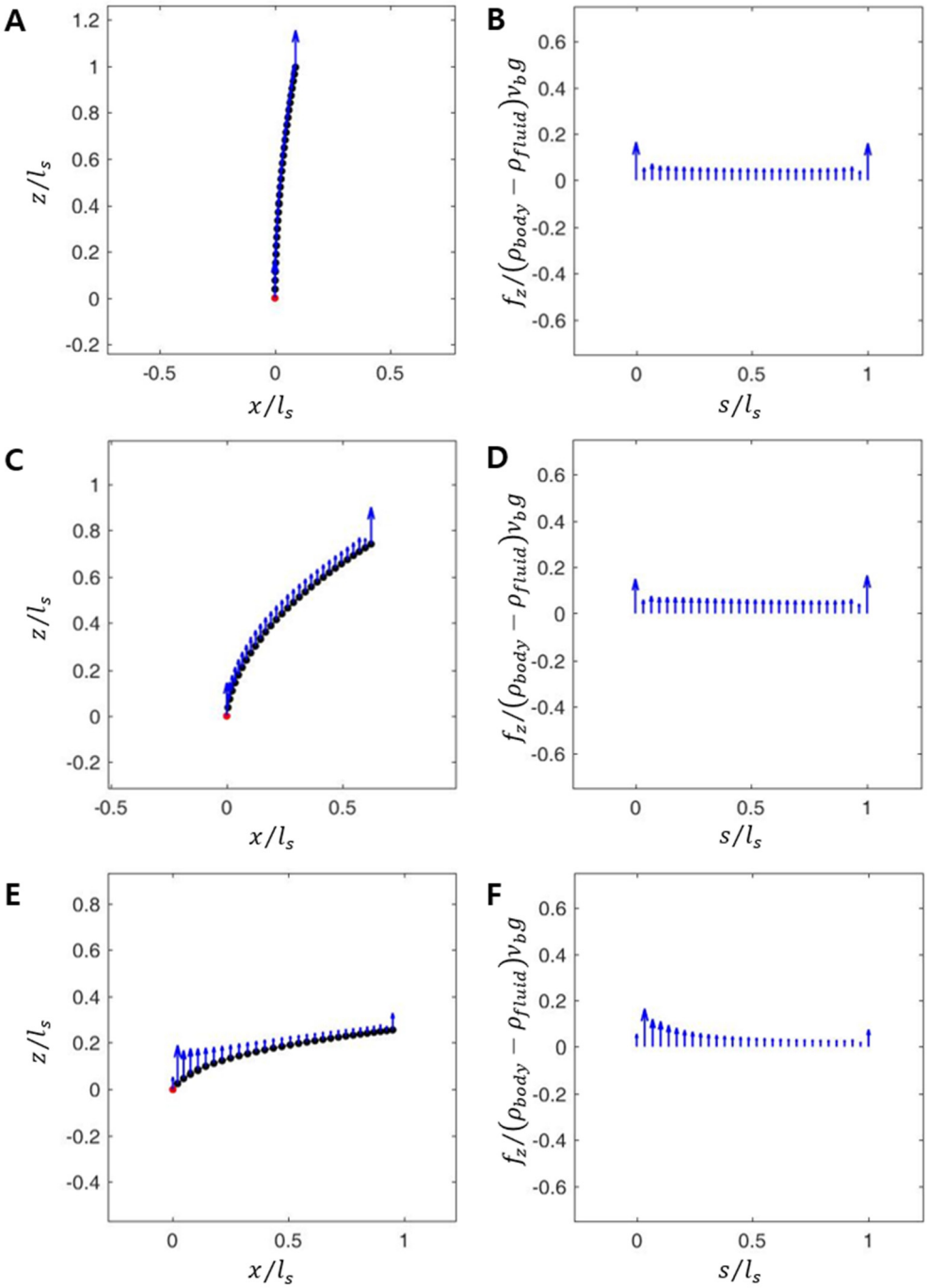

Figure 5.19 (A) Vertical components of net resistance forces in the shear flow of Bn_{shear}= 0.104; (B) Vertical resistance coefficient distribution along the silk in the shear flow of Bn_{shear}= 0.104; (C) Vertical components of net resistance forces in the shear flow of Bn_{shear}= 1.4; (D) Vertical resistance coefficient distribution along the silk in the shear flow of Bn_{shear}= 1.4; (E) Vertical components of net resistance forces in the shear flow of Bn_{shear}= 20.7; (F) Vertical resistance coefficient distribution along the silk in the shear flow of Bn_{shear}= 20.7.

5.6.2. Vortex Field

The ballooning structure exhibits various behaviours in a cellular flow field (Taylor-Green vortex field). According to the size and strength of the vortices, the ballooning structure exhibits the following motions: (i) 'vortex crossing'; (ii) 'fast settling'; (iii) 'slow settling'; and (iv) 'vortex trapping'. At low ballooning numbers ($Bn_{vor} < 2$), the ballooning structure falls crossing the vortices. The influence of flow eddies on their settling speed are small; therefore, their dimensionless settling speeds are around 1 ($0.9 \leq \langle V_{z,last} \rangle / V_{z,still} < 1.1$, see Figure 5.20, Appendix A Figure A 1-Figure A 6). As the ballooning number increases, the motions split into three different behaviours. The split depends on the size of the vortices and the initial positions. If the sizes of the eddies are under 1.2 times the silk length, the ballooning structure falls faster than it would in still air (see Appendix A Figure A 7Figure A 10, Figure A 13Figure A 16); if the eddies are larger than 1.2 times the silk length, however, the ballooning structure falls slower than it would in still air. At higher ballooning numbers, the ballooning structure is trapped by an eddy and the mean settling speed approaches zero (see Figure 5.20 and Figure 5.21; see Appendix A Figure A 11Figure A 12, Figure A 17 and Figure A 22).

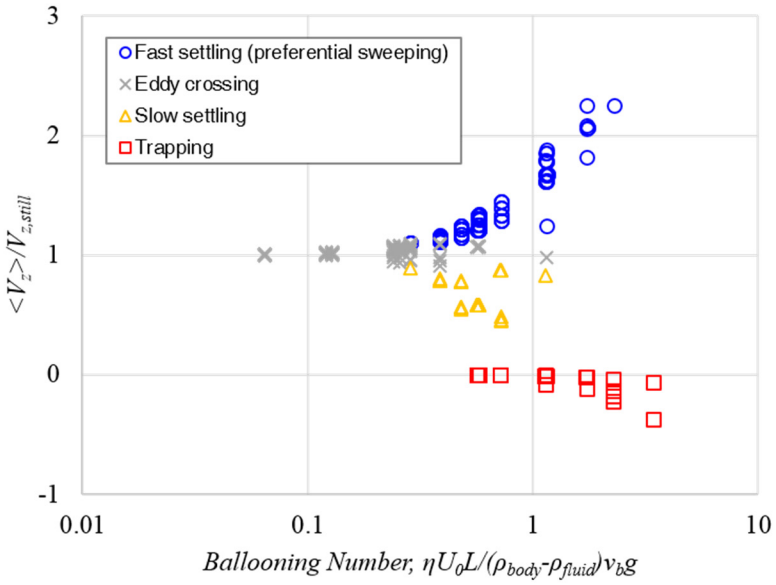

Figure 5.20 Dimensionless settling speed of a ballooning structure in a cellular vortex (eddy) field versus ballooning number. If the settling behaviour converges to a periodic motion, the dimensionless settling velocity of the last two periodic motions is averaged as a representative value.

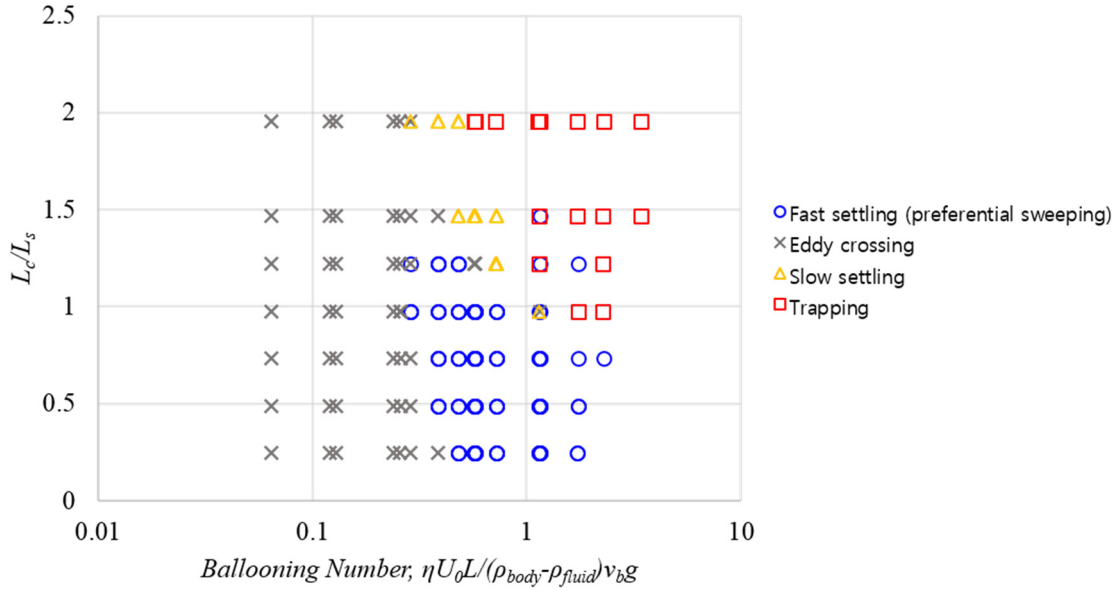

Figure 5.21 Different behavioural modes according to eddy size and ballooning number. The behavioural modes are categorized by the motion and settling speed of the structure. 'Eddy crossing' is the mode in which their dimensionless settling speeds are between 0.9 and 1.1; 'slow settling' is where speeds are slower than 0.9; 'fast settling' is the mode that falls faster than 1.1. The 'trapping motion' is recognised by detecting the averaged settling speed of 0 (or near 0).

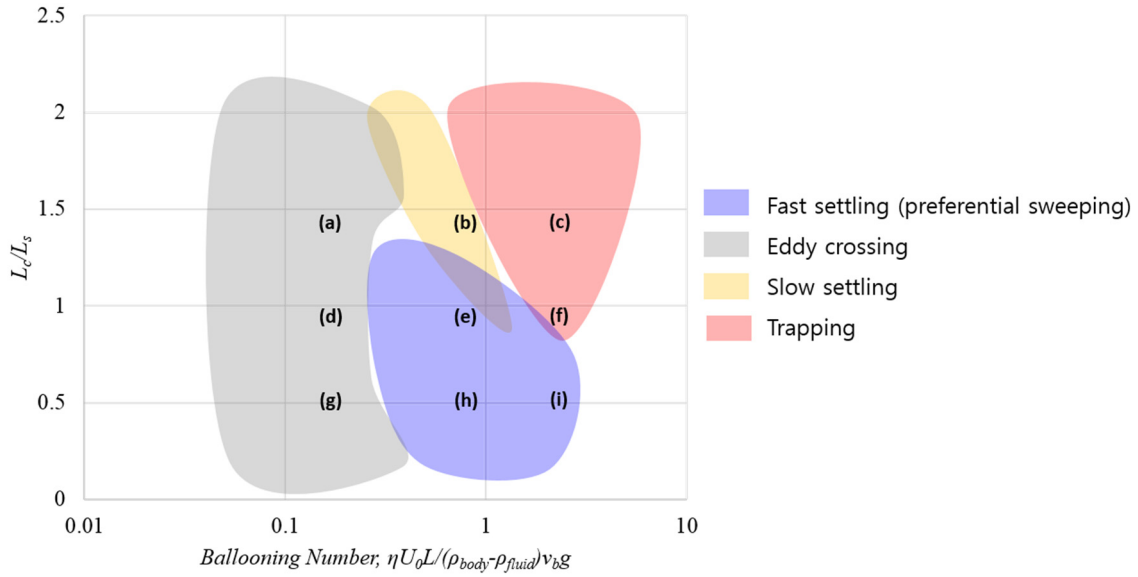

Figure 5.22 Area diagram for different sediment modes in a cellular vortex field.

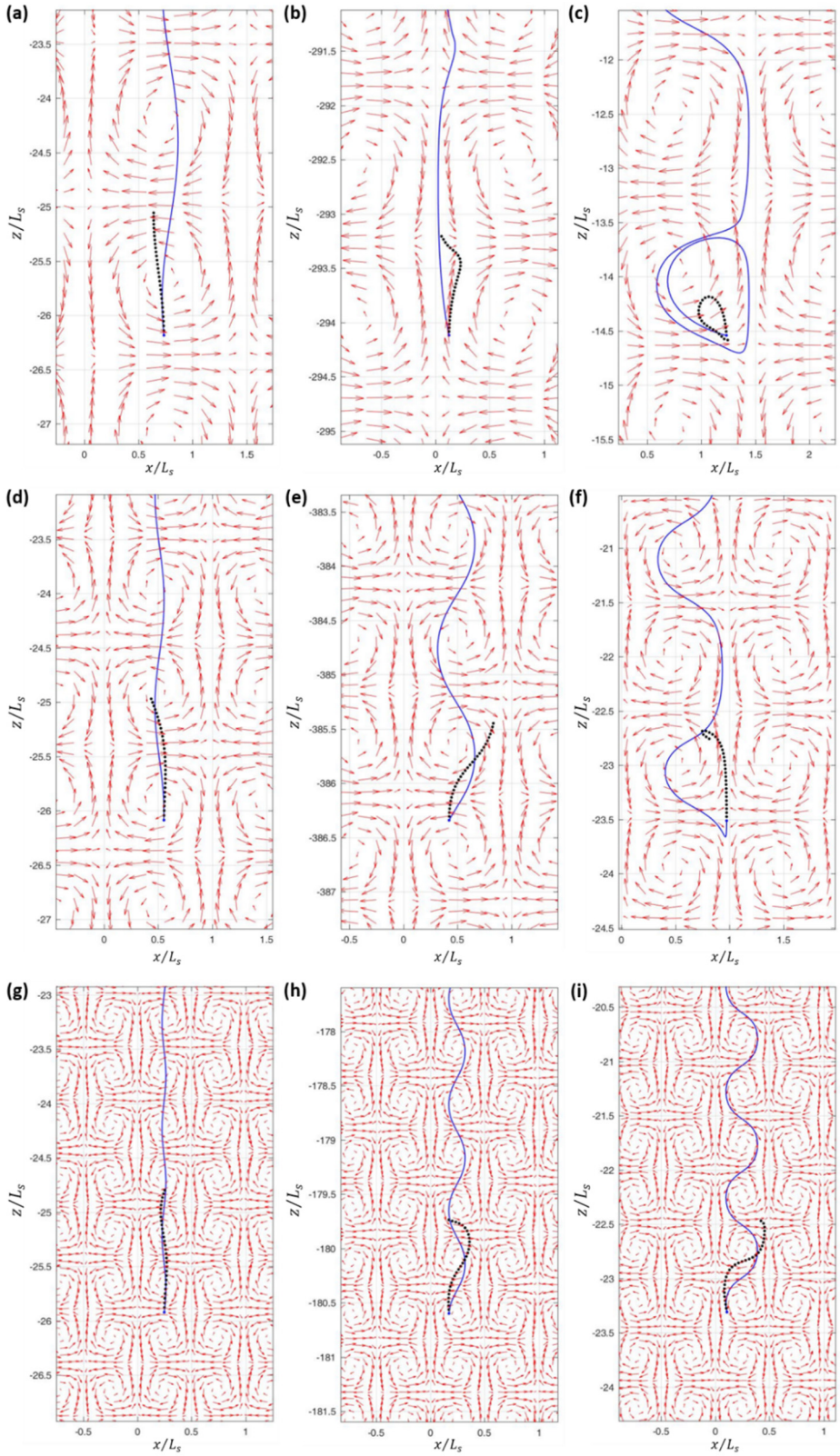

Figure 5.23 Trajectory of the ballooning structure in a cellular vortex field. (a)(d)(g) Eddy crossing: the ballooning structure falls crossing the eddies; (b) Slow settling: the ballooning structure stays between two vortex columns and falls slower than the structure in still air; (c)(f) Trapping: the ballooning structure is trapped by a vortex after a few or many periodic sediment motions; (h)(i) Fast settling (preferential sweeping): the ballooning structure deforms and passes through a curved high strain path, and the structure falls faster than it would in still air.

Some interesting features emerging from these results include the fact that the ballooning structure is preferentially trapped by a vortex in certain flow conditions (high ballooning number and in large vortex cells). There are two trapping modes. First, the structure falls slowly between the columns of vorticities; then, after a few oscillations in sediment progress, the structure becomes trapped in a vortex. Second, the structure travels fast through the high-strain region between vortices; then, after some downward travel, the structure becomes trapped in a vortex. The distances travelled by sediment before the trapping events depend on its initial positions. However, at the end, all structures were trapped in a vortex. This suggests that a biased character exists in the suspension of the ballooning structure in vortex fields: namely, the ballooning structure is preferentially trapped by a vortex at high ballooning numbers. Moreover, two trapping motions can be observed in the events: cycling trapping, which shows a closed loop trajectory of the body (see Figure 5.24A), and stationary trapping, which converges to the equilibrium states in the position and shape of the filament (see Figure 5.24B).

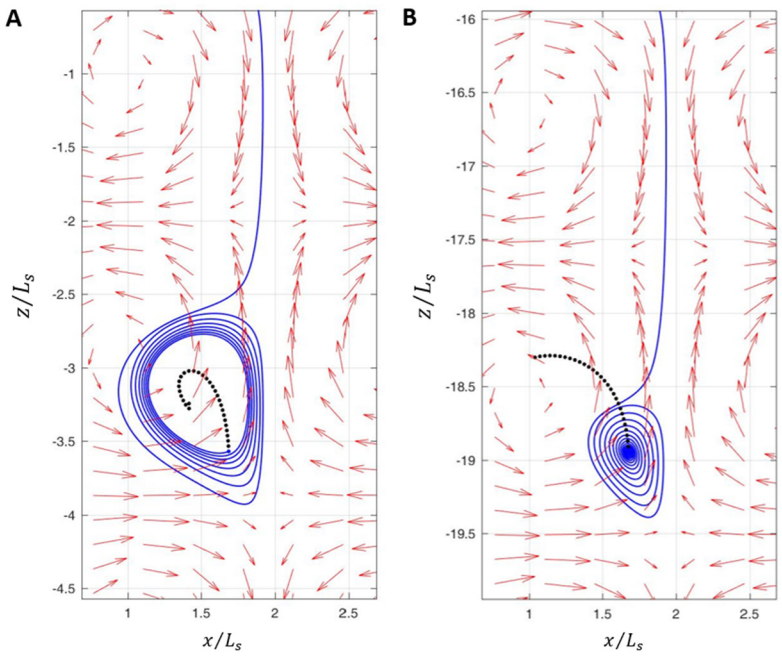

Figure 5.24 Two different trapping modes in a cellular vortex field. (A) Cycling trapping building a closed loop; (B) Stationary trapping remaining in an equilibrium state.

5.6.3. Homogeneous Turbulence

The dimensionless mean settling velocities for different ballooning numbers are presented in Figure 5.25. As the strength of flow fluctuation becomes more dominant, the ballooning structure exhibits a slow settling character (see Figure 5.25). There are two reasons for the scatter at high ballooning numbers. First, as the ballooning number increases, the settling speed of the ballooning structure in the still air becomes smaller because of its light weight, which is used for the nondimensionalisation of the settling speed. Therefore, the scatter of the data is amplified at the high ballooning numbers. Second, the finite number (n=10) of Fourier modes in the turbulent model is limited to describe an isotropic homogeneous turbulence. Each experimental simulation has a different turbulent structure.

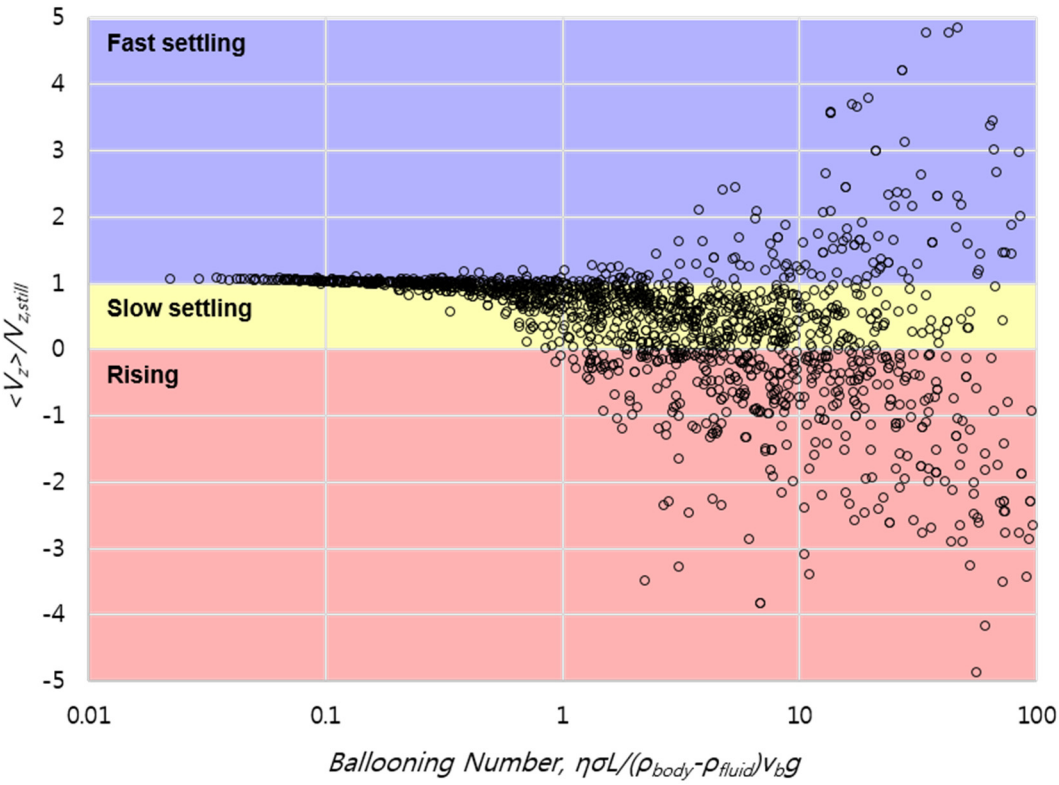

Figure 5.25 Dimensionless settling speed distribution of the ballooning structure in the homogeneous turbulence model according to the ballooning number. Fast settling: the structure falls faster than it would in still air. Slow settling: the structure falls slower than it would in still air. Rising: the structure does not fall, but rises upward.

An end-to-end vector represents the statistical shape of the ballooning structures during their suspension in turbulence (see Figure 5.26). The averaged z component of the end-to-end vector approximates 1 as the ballooning number decreases (see Figure 5.27 and Appendix A Figure A 24 (f)Figure A 27 (f)Figure A 30 (f)). The averaged square of the end-to-end vector converges to 0.3 as the ballooning number increases (see Figure 5.28).

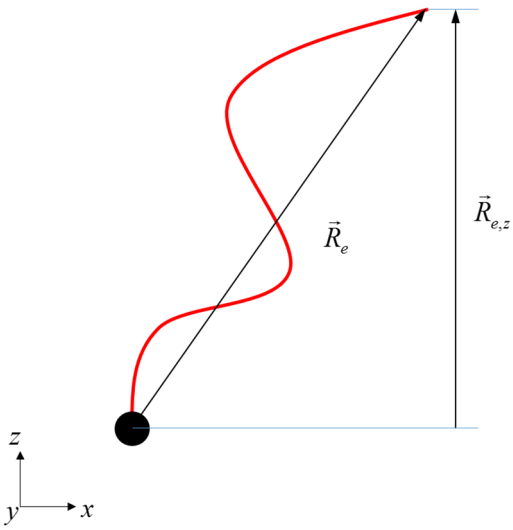

Figure 5.26 Definition of an end-to-end vector and its z component.

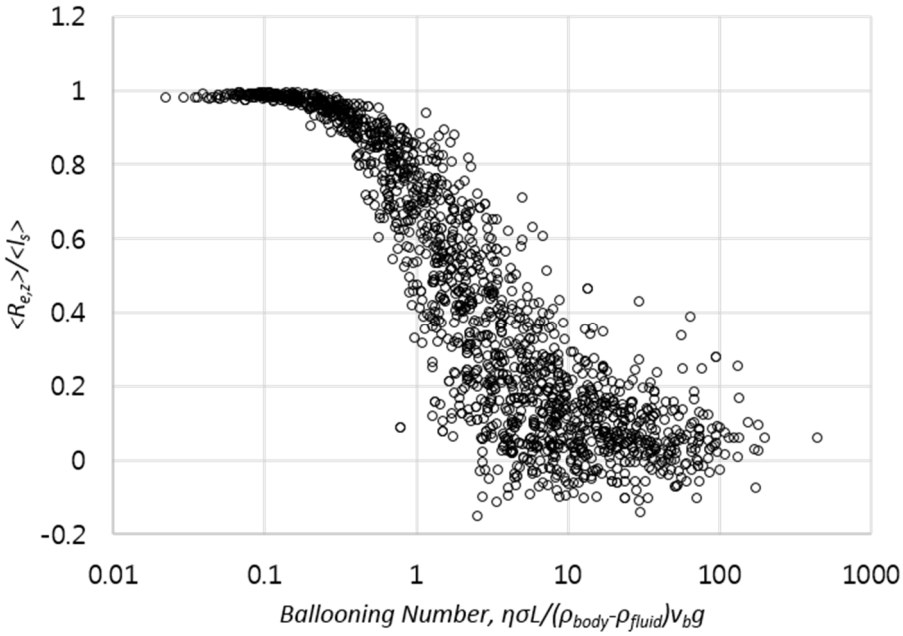

Figure 5.27 Distribution of the mean vertical (z-direction) components of end-to-end vectors according to the ballooning number for homogeneous turbulence.

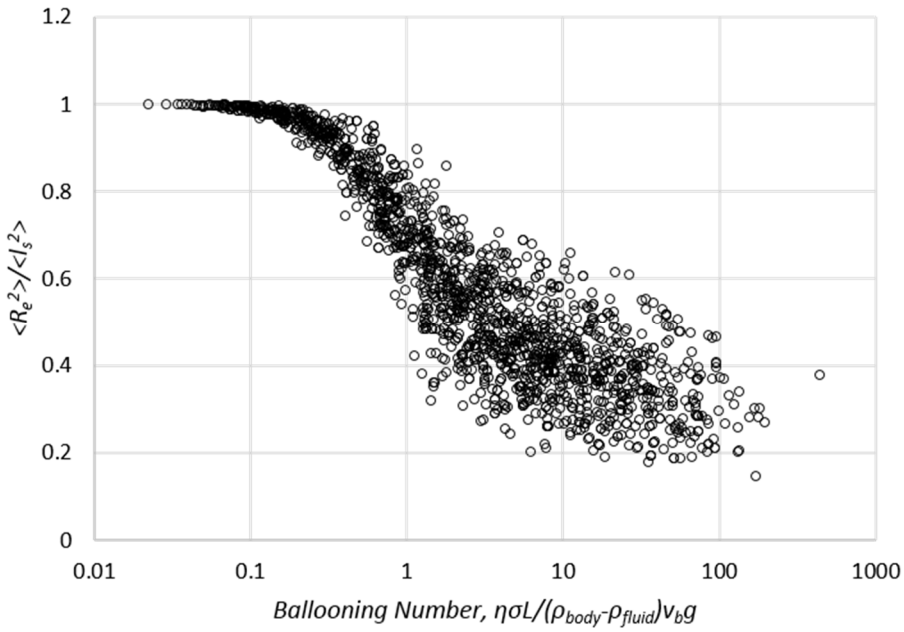

Figure 5.28 Distribution of the dimensionless mean square value of the end-to-end vector according to the ballooning number for homogeneous turbulence.

Next, the sediment behaviour of a ballooning spider is compared with a point-like parachuter, which represents dandelion and thistle seeds. The size of the point-like parachuter is adjusted to give it the same settling speed as the ballooning spider; therefore, both structures have the same weights and settling speeds in still air. Both are released from identical locations in the identical turbulence model.

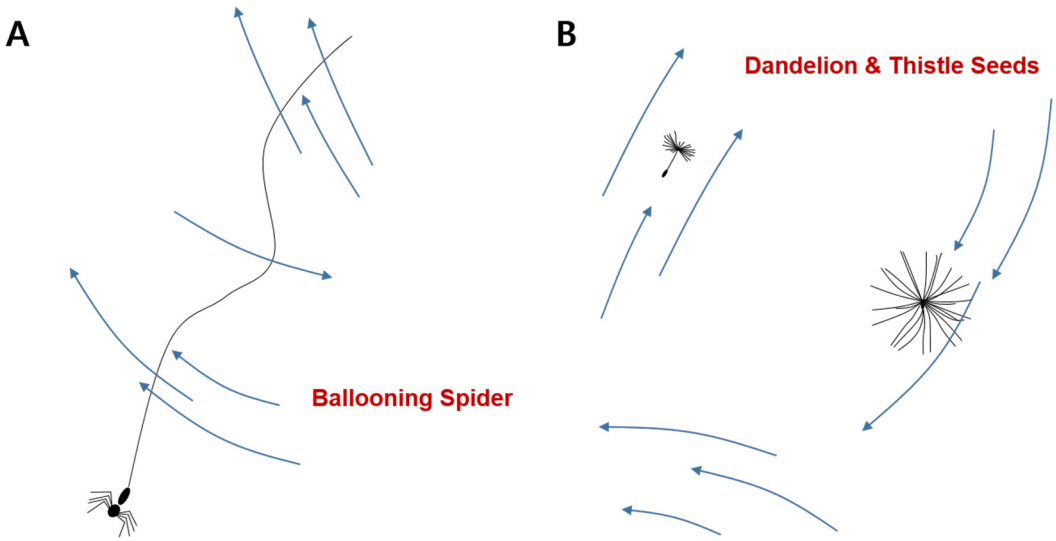

Figure 5.29 Comparison between the flight of a ballooning spider and the flight of a dandelion (or thistle) seed. (A) Sketch of a spider's ballooning; (B) Sketch of the flight of dandelion and thistle seeds.

While the point like-parachuter showed a mirror-symmetric distribution about $\langle V_z \rangle / V_{z,still} = 1$ (see Figure 5.30C), the filament-like parachuter showed a biased distribution about $\langle V_z \rangle / V_{z,still} = 1$ (see Figure 5.30A). To reduce the scattered distribution at high ballooning numbers, both sediment speeds are nondimensionalised by the root-mean-square fluctuation velocity $\sigma = \sqrt{\overline{\boldsymbol{u}'(t)^2}} = \sqrt{(1/3)\overline{\left(u'^2 + v'^2 + w'^2\right)}}$. The dimensionless settling speeds for the ballooning structure exhibit a wider distribution compared with those for the point-like parachuter. For ease of comparison, both sets of data are plotted in one chart (see Figure 5.30EF). The red points are the biased plots of the filament-like parachuter (the data of a point-like parachuter are plotted on the data of a filament-like parachuter). The dimensionless settling speeds for the filament-like parachuter are biased to the region where the structure falls slower than it would in still air, or sometimes even the rising region. Figure 5.31 clearly shows the biased motion of the filament-like parachuter in comparison with the point-like parachuter.

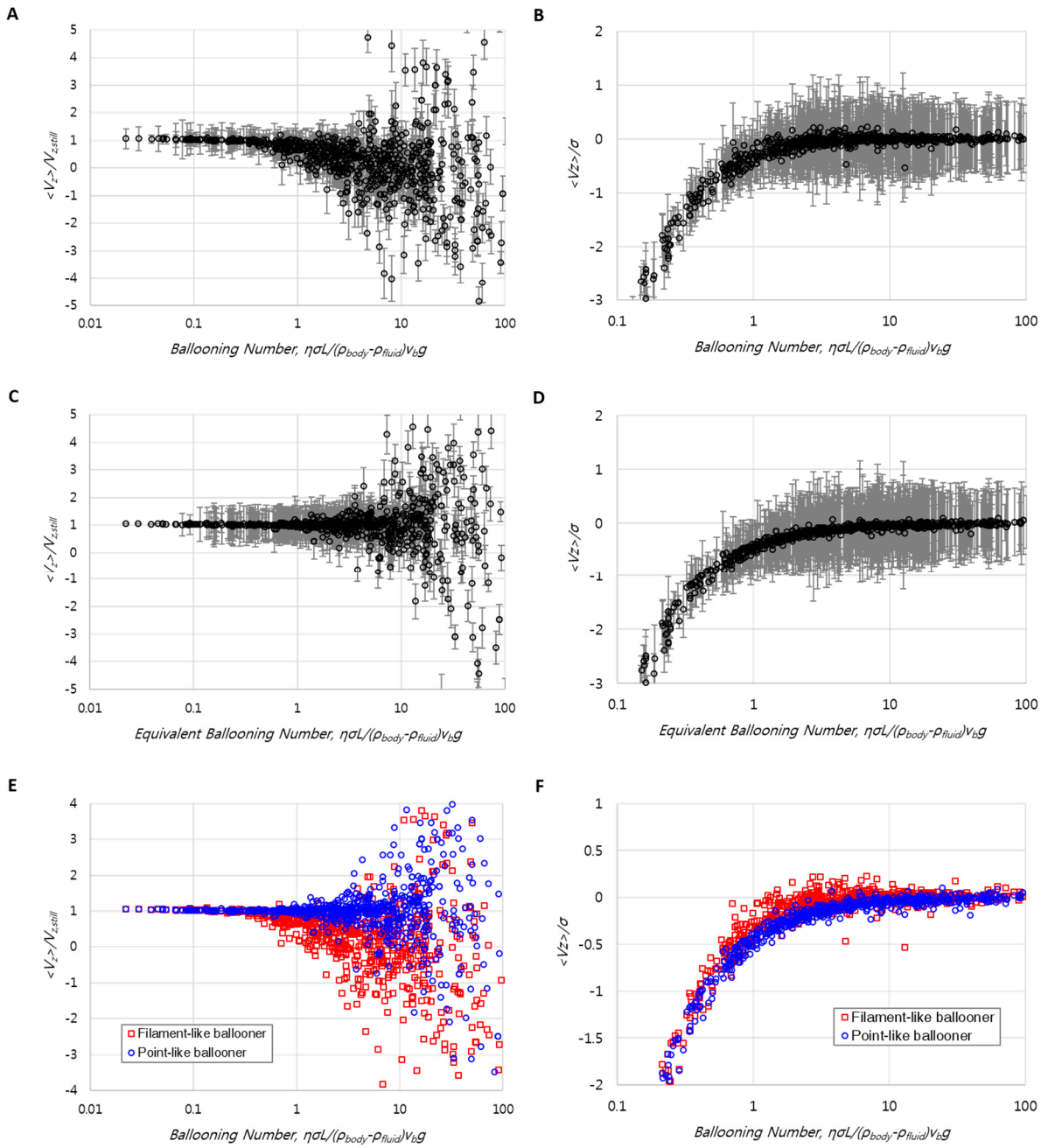

Figure 5.30 Comparison between a filament-like parachuter and a point-like parachuter under dimensionless settling speed. (A) Dimensionless settling speed (divided by the settling speed in the still medium) of a filament-like parachuter in homogeneous turbulence; (B) Dimensionless settling speed (divided by the root-mean-square fluctuation velocity) of a filament-like parachuter in homogeneous turbulence; (C) Dimensionless settling speed (divided by the settling speed in the still medium) of a point-like parachuter in homogeneous turbulence; (D) Dimensionless settling speed (divided by the root-mean-square fluctuation velocity) of a point-like parachuter in homogeneous turbulence; (E) Comparison of dimensionless settling speeds (divided by the settling speed in the still medium) between filament-like and point-like parachuters in homogeneous turbulence; (F) Comparison of dimensionless settling speeds (divided by the root-mean-square fluctuation velocity) between filament-like and point-like parachuters in homogeneous turbulence.

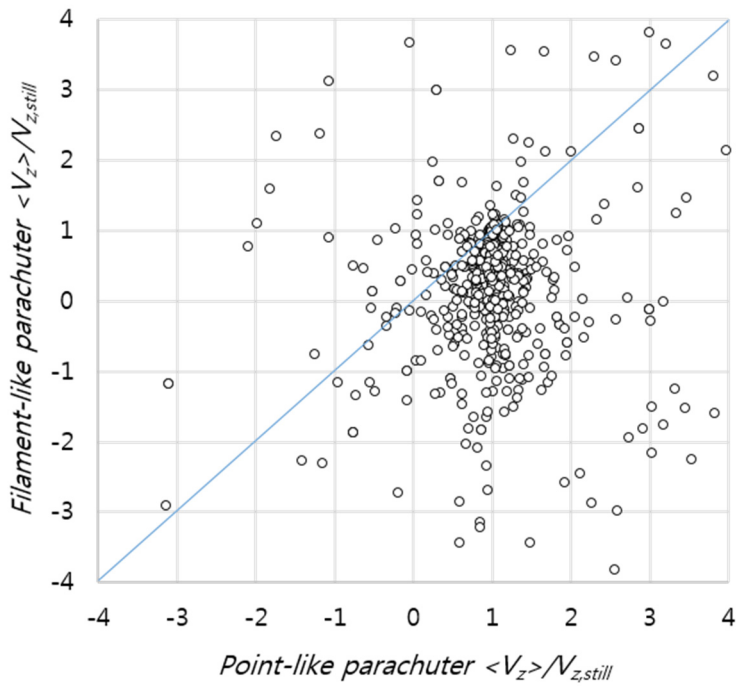

Figure 5.31 Simultaneous plot of the dimensionless settling speeds for a filament-like parachuter and a point-like parachuter. Both cases are simultaneously simulated in an identical turbulence model.

The characteristics of the shape of the ballooning structure can be described by averaging the radius of gyration of the filament during the event. Eqns. (5.41) and (5.42) are used for the lower and upper half parts respectively.

$$R_{g\,lower}^2 = \frac{\int_0^{l_{s,mid}} (\boldsymbol{r} - \boldsymbol{r}_{mid})^2 ds}{\int_0^{l_{s,mid}} ds} \tag{5.41}$$

$$R_{g\,upper}^2 = \frac{\int_{l_{s,mid}}^{l_s} (\boldsymbol{r} - \boldsymbol{r}_{mid})^2 ds}{\int_{l_{s,mid}}^{l_s} ds} \tag{5.42}$$

At the very small ballooning number $Bn_{tur} = 0.02$, both dimensionless squared radiuses of gyration are around 0.33, $\langle R_{g\,lower}^2 \rangle \approx \langle R_{g\,upper}^2 \rangle \approx 0.33$, meaning that the shapes of both filaments are similar (resembling a straight line; see Appendix A Figure A 24 (f)Figure A 27 (f)Figure A 30 (f)). As the ballooning number increases ($0.1 \leq Bn_{tur} < 10$), the dimensionless squared radius of gyration of the lower half part of the filament is larger than that of the upper half part. This means that the upper part of the filament is more curved than the lower part (see Figure 5.32 and Appendix A Figure A 24(c)(d)(e), Figure A 27(c)(d)(e), Figure A 30(c)(d)). At high ballooning numbers ($10 \leq Bn_{tur} < 100$), the differences are small and both squared radiuses of gyration are reduced (see Appendix A Figure A 24(a)(b), Figure A 27(a)(b), Figure A 30(a)(b)). This tendency can be seen more clearly in Figure 5.33.

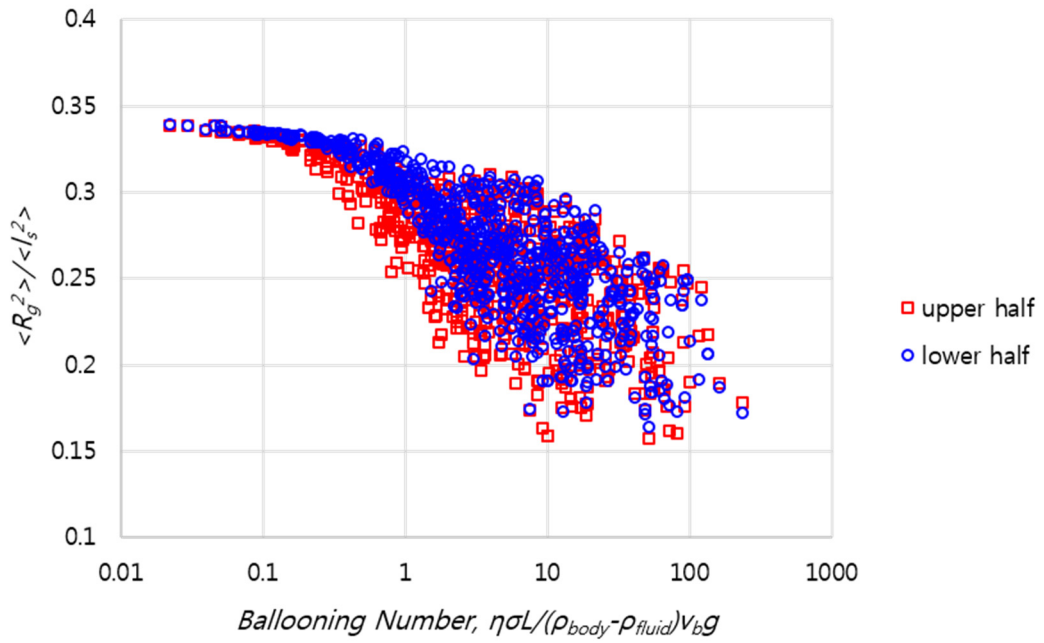

Figure 5.32 Distribution of the dimensionless mean square value of the upper half and lower half radiuses of gyration according to the ballooning number for homogeneous turbulence.

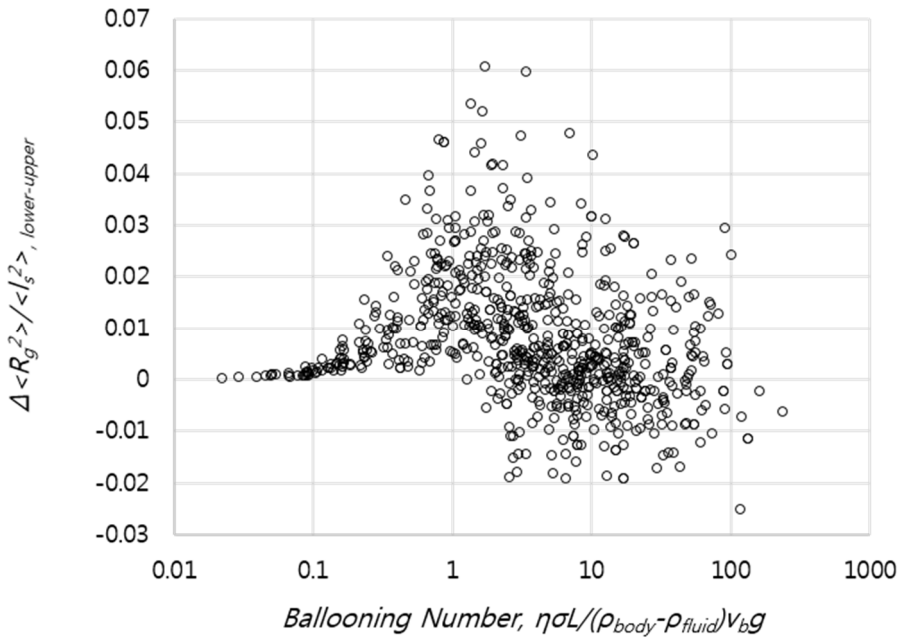

Figure 5.33 Distribution of the difference of the dimensionless mean square values between the upper half and lower half radiuses of gyration according to the ballooning number for homogeneous turbulence.

5.7. Discussion

Spiders fly passively in unordered air currents, which results in chaotic motions because of turbulence (Suter 1999). The influence of various non-uniform flows on the spider silk fibre has been explored using the bead-spring model.

5.7.1. Role of Anisotropic Drag of a Filament

The anisotropic drag of a thin filament structure (see Chapter 2) is a crucial aspect of the dynamics of a microswimmer. The cilia and flagella of a microswimmer enable organisms and cells to move forward in a viscous medium (Purcell 1977, Brennen and Winet 1977, Fung 1990, Happel and Brenner 1991, Lauga and Powers 2009). Because of this drag anisotropy, a flagellum can slip in a certain direction in a viscous fluid and can also regulate the fluid-dynamic force on it by deforming its shape for the locomotion of a microswimmer. This character of the anisotropic drag is valid not only in the active dynamics of a swimming microorganism, but also in the passive dynamics of an artificial microswimmer, such as a flexible magnetic filament in an oscillating external magnetic field (Dreyfus et al. 2005, Gauger and Stark 2006). From this, we may infer that the anisotropic drag is also an important factor in the passive dynamics of a flexible filament moved by an external fluid flow.

In the simulation, the influence of the anisotropic drag is checked by releasing the ballooning structure in various shear flow strengths. In the bead-spring model, the drag anisotropy is described by the Rotne-Prager hydrodynamic interaction between beads (Rotne and Prager 1969, Dhont 2003, Gauger and Stark 2006). The drag anisotropy modelled by the hydrodynamic interaction was shown in Figure 5.9 and compared with the experimental data. The velocity reduction of the ballooning structure in a shear flow shows that the reduction is due to the drag anisotropy; this is because the model without hydrodynamic interaction did not exhibit any velocity reduction effect during sedimentation in a shear flow (see Figure 5.12).

To determine how the drag anisotropy reduces the settling speed of a ballooning structure, the cause of the sediment speed reduction is decomposed into a geometric component and a shear-induced component, as shown in Section 5.6.1.3. The geometric component depends solely on the geometry of the filament; therefore, the geometric resistance coefficient is the same as the resistance coefficient of the same geometry structure in the still medium. The settling attitude of a thin rod in a viscous medium results in different settling speeds for the object. Maximum resistance force occurs in the case of a settling event with horizontal attitude. Many studies regard the drag difference between normal and tangential attitudes to the flow direction as being a factor of two, $\xi_{\perp}/\xi_{\parallel} \approx 2$ (Fung 1990, Happel and Brenner 1991, Lauga and Powers 2009), while Purcell (1997) guessed that this factor was around 1.5 ($\xi_{\perp}/\xi_{\parallel} \approx 1.5$) from his measurements. We can thus calculate that the maximum settling speed reduction due to the geometry of a filament is 0.5 ($V_{z,\perp}/V_{z,\parallel} \approx 0.5$) in the case of $\xi_{\perp}/\xi_{\parallel} \approx 2$. Moreover, the shear-induced resistance coefficient may be caused by the point-asymmetry of the filament in a shear flow (see Figure 5.4). This shear-induced resistance coefficient contributes to the settling speed reduction in the relatively strong shear rate $Bn_{tur} > 3$ (see Figure 5.13). In addition, Figure 5.18EF demonstrates that the majority of the upward forces are produced on the section of the filament near the spider's body at higher ballooning numbers, while the vertical forces are almost uniformly

distributed in the other cases (small or moderate ballooning numbers, $Bn_{tur} < 3$; see Figure 5.16, Figure 5.17, Figure 5.19A-D) .

Particle sedimentation has been widely studied in physics: for example in a fluctuating fluid (Boyadzhiev 1973), in a cellular flow field (Maxey and Corrsin 1986, Maxey 1987a, Fung 1997, Bergougnoux et al. 2014), and in an isotropic turbulence (Snyder and Lumley 1971, Riley 1974, Reeks 1977, Well and Stock 1983, Maxey 1987b, Squires and Eaton 1990, 1991, Wang and Maxey 1993). Some studies have observed retardation of the settling velocity (Snyder and Lumley 1971, Well and Stock 1983, Squires and Eaton 1991, Stout et al. 1995, Fung 1998), while others have observed fast falling (Maxey 1987b, Fung 1997, 1998). In the Stokes regime (no inertia), in which all dynamics are under a linear relation, there are no differences in their mean sediment velocities, one in a still medium and the other is in a fluctuating fluid (Riley 1974, Reeks 1977). However, it was later found that the retardation is caused by the nonlinear drag of the heavy particles in the range of Reynolds number $1 < Re < 5000$ (Stout et al. 1995, Fung 1998). The fast falling is caused by the inertia of a particle, which induces the particles toward regions of high strain rate and/or low vorticity (Maxey 1987b, Fung 1997, 1998). This increases the settling speed of a particle in comparison with the same particle settling in a still medium. In line with these previous studies on particle sedimentation, the present work finds that the observed nonlinearity, which retards the settling speed of a spider, is due to the anisotropic drag of their flexible filament in nonuniform flows.

5.7.2. Ballooning Structure in a Cellular Flow Field

The simulation in a cellular vortical flow field reveals various motions according to the flow conditions (see Figure 5.20). In the simulation, two flow condition parameters are applied: the size L of a vortex, and the strength (vortex velocity U_0) of the vortex. In a previous study of particle sedimentation, Stout et al. (1995) categorised three regimes of heavy particle motion in turbulent flow (see Figure 5.34): (i) suspension for $\sigma/W_T \gg 1$ (Stommel 1949, Manton 1974); (ii) preferential sweeping for $\sigma/W_T \approx 1$ (Maxey and Corrsin 1986, Maxey 1987b, Wang and Maxey 1993, Fung 1997, 1998, Toschi and Bodenschatz 2009, Balachandar and Eaton 2010); (iii) eddy crossing for $\sigma/W_T \approx 1$ (Stout et al. 1995; see Figure 5.34). The ballooning structure in a cellular flow field exhibited similar behaviours to particle motions in the turbulent flow (Maxey and Corrsin 1986, Maxey 1987a, Stout et al. 1995, Fung 1997, Bergougnoux et al. 2014). The eddy crossing motion of the ballooning structure in Figure 5.20 and Figure 5.23(a)(d)(g) is similar to the eddy crossing motion of the heavy particle (see Figure 5.34(a)). If the point mass of the ballooning structure is heavy enough compared with the resistance force applied to a filament by the eddies, the structure crosses eddies (vortices) in a cellular flow field, and there is no retardation of the settling speed. However, if the mass is comparable to the resistance force on a filament, then the fast settling motion of the ballooning structure in Figure 5.20 and Figure 5.23(e)(h)(i) is very similar to the preferential sweeping motion in Stout's theory of heavy particle motion (see Figure 5.34(b)). The ballooning structure is preferentially swept into the regions of the downdraft path (Maxey 1987, Stout et al. 1995). This preferential sweeping of the heavy particle is caused by its inertia; however, the present simulation does not consider the inertia of the point mass. The preferential sweeping of the ballooning structure may thus be caused by the anisotropic drag of a filament structure. In the case of slow settling motion, the ballooning structure is not swept into the downdraft path, but periodically crosses downwards the updraft and downdraft regions (see Figure 5.23(b)). In this case, the large cell size is an important factor, because a large vortex cell produces small angular velocity in the same vortex velocity. Therefore, the small angular velocity cannot sweep the ballooning

structure into the path of the neighboured downdraft (periodic outside of a column of vortex series). If the vortex velocity is dominant and the vortex is large, the ballooning structure is trapped by the vortex. This is very interesting, because the heavy particle does not settle down with the help of a filament (see Figure 5.23(c)(f)).

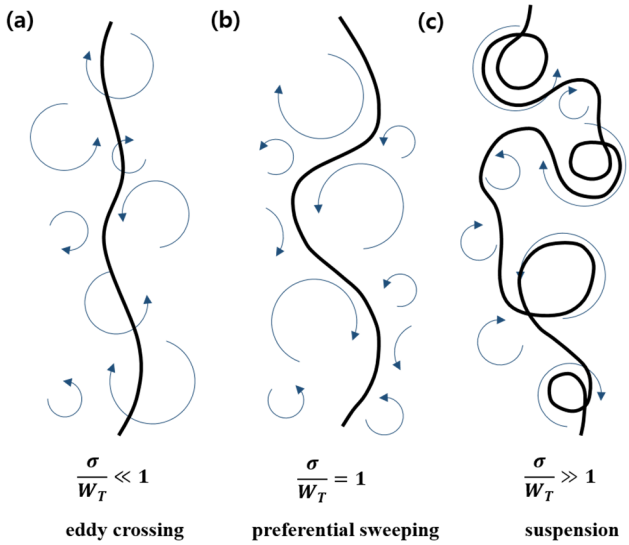

Figure 5.34 Three different regimes of heavy particle motion (redrawn from Stout el al. 1995)

The upward and downward currents coexist around the vortex which is induced by wind gradient on the Earth. Although the ballooning structure produces negative buoyancy (toward a ground), the ballooning structure either stays in the upward current region of a vortex (see Figure 5.24B) or gains energy by cycling with a passive motion (see Figure 5.24A). Abundant turbulent eddies exist in the atmospheric boundary layer. These are mostly produced (i) by mechanical terrains on the Earth's surface, (ii) by rising thermal air parcels, and (iii) by the shear-winds on the surface. These eddies, which have certain sizes and strengths, may be helpful to the ballooning spiders by trapping them and allowing them to stay in the air for longer periods. This trapping motion was also observed by Zhao et al. (2017), who simulated the structure in a cavity flow.

5.7.3. Biased Behaviour in a Homogeneous Turbulence

As previously discussed (see Sections 5.7.1 and 5.7.2), a thin filament structure (spider silk) shows a nonlinear drag character on a point mass (spider) in a non-uniform flow. In a simple shear flow, the ballooning structure settles slower than it would in a still medium. In a cellular flow field, the same structure settles faster in small-size and relatively strong vortex cells, while either moving slower or becoming trapped in large-size and relatively strong vortex cells. This nonlinear character in homogeneous turbulence also results in a biased settling behaviour (biased toward slow settling) of the structure (see Figure 5.25). Reynolds et al. (2006) first proposed that turbulent wind may reduce the rate of fall of the spider by deforming and stretching the flexible fibres. Their study points out that the extensibility and flexibility of a filament may be the causes of the settling retardation. However, as previously discussed in Sections 5.7.1 and 5.7.2, the cause of the settling retardation seems to be the anisotropic drag character of a thin filament and flexible deformation in vortex eddies in turbulence. As the model (extendible and flexible filament) proposed by Reynolds et al. did not consider the

hydrodynamic interaction between beads (Rouse model; Rouse 1953, Dhont 2003, Reynolds 2006, Doi and Edwards 2007), the cause of the retardation in Reynolds' simulation seems to be flexibility (not extensibility), which helps the filament to become deformed and quasi-trapped in a vortical flow in the turbulence model. From the simple calculation, the extensibility of a spider silk during a flight is almost negligible, because the 0.5 mg spider weight extends only 47 mm in length (1.5% elongation) in the case of a spider silk that is 3 m long and 200 nm thick (elastic modulus: 10 Gpa; Gosline et al. 1999).

From a filament-stretching perspective, the vertical fractional extension $\langle R_{e,z}\rangle/\langle l_s\rangle$ of the ballooning structure under homogeneous turbulence may be qualitatively compared with the fractional extension x/L by a uniform flow of a deformed DNA filament (see Figure 5.35; Perkins et al. 1995). This is because, as the spider's weight increases, the deformed silk by the turbulence is increasingly stretched (see Figure 5.27, Figure 5.28 and Appendix A Figure A 24, Figure A 27, Figure A 30). In the case of a DNA filament, the filament's deformation is caused by its entropic elasticity, which depends on the temperature (Bustamante et al. 1994, Perkins et al. 1994, 1995). As the flow velocity around the DNA increases, the fractional extension also increases.

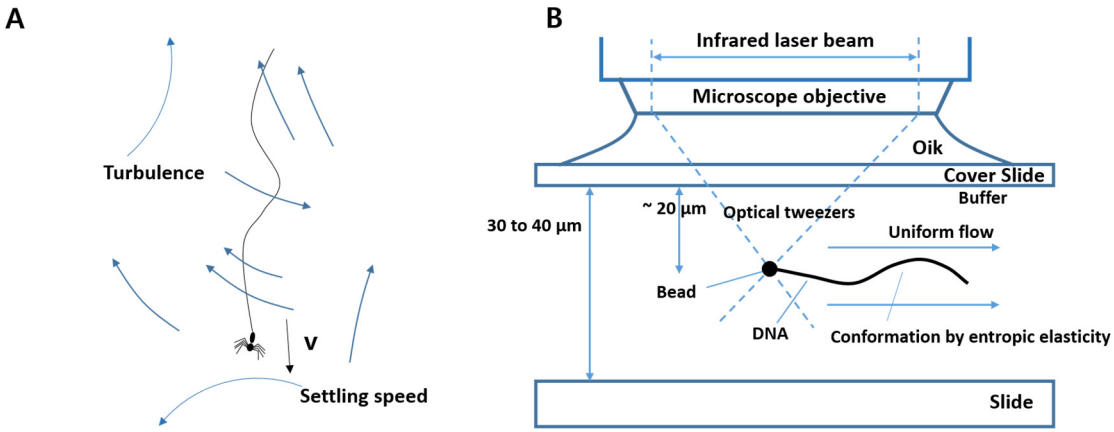

Figure 5.35 (A) A ballooning spider in turbulent flow; (B) Schematics of the DNA extension in a uniform flow between the slides (redrawn from Perkins 1995).

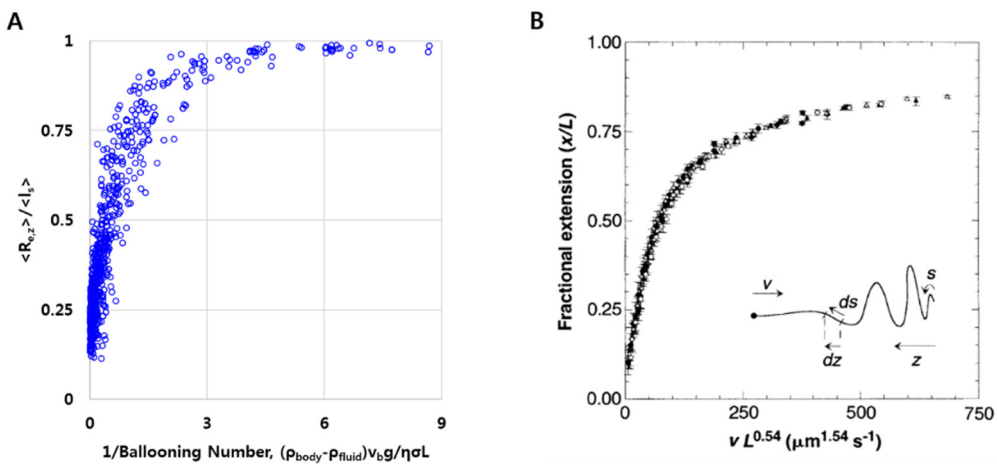

Figure 5.36 (A) The fractional extension $\langle R_{e,z}\rangle/\langle l_s\rangle$ of a ballooning spider in turbulent flow. (B) Plots of the fractional extension (x/L) versus $vL^{0.54}$ for DNA molecules with a viscosity of q = 0.95 Cp (from Perkins 1995).

The square of the end-to-end vector also reveals the geometrical character of the ballooning structure. If the ballooning number decreases, the dimensionless square of the end-to-end vector becomes its

maximum (1), as in this case the filament is stretched out straight and there is no wind fluctuation. As the ballooning number increases, however, this number decreases to 0.2, as the filament is entangled by the wind fluctuation (see Figure 5.28).

The strong uniform velocity in DNA stretching means less conformation (stretched DNA), while the conformation of a spider silk is reduced by increasing its weight (increasing its settling speed). The x-axis of Figure 5.36A is defined as a reciprocal of the ballooning number, Bn_{tur}. Thus, we can qualitatively compare the vertical fractional extension $\langle R_{e,z}\rangle/\langle l_s\rangle$ of the ballooning silk with the fractional extension x/L of a DNA filament.

Ballooning silks have a longer length-scale (i.e. a few metres) compared to an aerial seed (a few centimetres) (see Table 4.1; Suto et al. 2008). Therefore, each segment of the ballooning silk is exposed to different wind flow fields in direction and magnitude. By contrast, an aerial seed is exposed to quasi-uniform airflow, although it still drifts in the fluctuating winds (see Figure 5.29). Accordingly, the question is whether the exertion of these non-uniform flows on the ballooning silk generates extra buoyancy capability during a ballooning flight. To clarify this, the behaviour of a filament-like parachuter under homogeneous turbulence was compared with that of an equivalent point-like parachuter (adjusted so that both have the same settling speed in a still medium) in the identical turbulent flow. As shown in Figure 5.30, the filament-like parachuter evidently shows biased behaviour towards either slow settling (in comparison with that of the point-like parachuter) or rising. Figure 5.31 clearly shows the difference in sediment characters between these two. This biased behaviour may be induced by the different (eccentric) characters of filament segments. The free-moving end easily drifts with the wind flows, while the point-mass-attached end is constrained by gravity. The point-mass-attached end filament segment mostly stays vertical under the constraint. This statistical difference is elucidated in Figure 5.32 by comparing the radiuses of gyration of the upper and lower parts. The result is reasonable: at low ballooning numbers $Bn_{tur} < 0.1$, the settling behaviour is dominant, such that the shape of the filament is vertically straight and there is no difference in the radius of gyration. However, at moderate ballooning numbers $0.1 < Bn_{tur} < 10$, the radius of gyration of the lower half segment is larger than that of the upper half segment, because the upper half segment can be more easily deformed by the turbulent flow. At high ballooning numbers $Bn_{tur} > 10$, the turbulent flow is dominant; therefore the shape of the filament is randomly distorted, and there is statistically no difference in the radius of gyration between the upper and lower half segments (see Figure 5.33 and Appendix A Figure A 24, Figure A 27, Figure A 30). As discussed in Sections 5.7.1 and 5.7.2, this biased behaviour seemed to be induced by both the anisotropic drag of a filament and the vortical flows in homogeneous turbulence. It is possible that the ballooning structure passively performs the unordered nonreciprocal motion in randomly moving fluid, while micro-swimmers actively swim and generate periodic nonreciprocal motion (Purcell 1977, Becker et al. 2003, Najafi and Golestanian 2004, Dreyfus 2005, Gauger and Stark 2006). This unordered nonreciprocal motion may be the physical explanation for the slow-settling of the ballooning structure in turbulence. This phenomenon should be explored further in future work.

5.8. Conclusion

While the dynamics of a particle or a filament in a fluid flow have been independently and widely studied, the combined asymmetric structure of the two has been investigated far less extensively. This ‘combined asymmetric structure’ refers to a filament, at the end of which a point-mass is attached.

This structure is also a physical model of a ballooning spider in the air. Here, the suspension dynamics of the structure were studied using numerical simulation. For the generalisation of the parameters, the ballooning number is newly defined as the ratio of the Stokes force on a filament to the gravity force on the weight. The simulation results revealed interesting characteristics of the ballooning structure in the non-uniform flows. First, the structure in a shear flow settles slower than would be the case in a still medium. This slow settling is caused by the anisotropic drag of a filament in a low Reynolds number flow. The slow settling occurs primarily due to the geometric attitude of a filament; secondarily, it occurs due to the force induced by and from a shear flow. Moreover, in a cellular flow field, the structure showed various settling and suspension modes. These motions mostly depend on the size and the strength of a cellular flow, and are thereby categorised according to these parameters. At the low ballooning number $Bn_{vor} < 1$, the structure behaved like a heavy particle; there is neither a retardation effect nor an acceleration effect $\langle V_z \rangle / V_{z,still} \approx 1$. At the high ballooning number $Bn_{vor} > 1$ and small vortex cell size $L_c/L_s < 1.2$, the structure is swept up by the vortical flows and settled faster than would be the case in a still medium. Furthermore, if the size of a vortex cell is larger than $1.2\ L_s$ and Bn_{vor} is larger than 1, the ballooning structure settles slowly or is trapped by a vortex and suspends with $\langle V_z \rangle / V_{z,still} \approx 0$. Different initial conditions of x_0 were also applied. They converged at the end trapping motion by vortex cells. While the point mass (spider's body) alone cannot be trapped by a vortex, this heavy particle is trapped with the help of the filament (spider silk). The ballooning structure also shows biased behaviour toward slow settling under homogeneous turbulence, while that of a point-like aerial seed was not similarly biased under identical turbulence conditions. As the nonlinearity of anisotropic drag of a flexible filament, which is deformed by non-uniform flows, was recognised as the cause of retardation of the ballooning structure in a shear flow and a cellular flow field, the bias under homogeneous turbulence appears to be caused by the drag anisotropy of a spider silk and the vortex trapping phenomenon. Due to the abundance of turbulent eddies in the atmosphere, this trapping motion may be a key physical feature in spiders' ballooning flight that enables their long journey.

6. Discussion

6.1. The Amount of Ballooning Silks

The most cumbersome problem to solve when considering spiders' ballooning is that not much has historically been known about ballooning silks (e.g. types of silk, the number of silks, lengths, thicknesses etc.). Because of this lack of quantitative information, there have been many discussions on the flight of spiders (e.g. Tolbert 1977, Humphrey 1987, Wickler and Seibt 1986, Henschel 1995, Suter 1991, 1992, 1999, Schneider et al. 2001, Reynolds 2006, Gorham 2013, Zhao et al. 2017). Quantitative information about ballooning silks was required so as to form a stepping-stone to more precise discussion. From the observational study conducted in the field and the laboratory as part of the present research, the ballooning behaviour was observed in detail and the physical properties of the ballooning silks were determined. The *Xysticus* species, 16-20 mg in weight, spun 50-60 thin nanoscale silks of about 200 nm in thickness. The length of the ballooning silks was 3.22 m on average (N = 22), while the maximum length was up to 6.2 m. According to the theoretical and empirical calculations (Humphrey 1987, Suter 1991), the amount of these ballooning silks is sufficient to allow large spiders (10-25 mg) to become airborne with the help of very light updrafts, 0.1-0.2 m s^{-1} in the vertical direction. The measured wind data shows that these light updrafts last for a few seconds in a light breeze of 1.5-3.3 m s^{-1} (horizontal wind speed). Although the question had arisen as to whether the ballooning fibres were enough to take them aloft (Henschel 1995), from our laboratory observations, it can be concluded that spiders spin enough ballooning silks to facilitate their aerial dispersal. In the case of large spiders (10-150 mg in weight), this is enabled by spinning multiple tens of nanoscale fibres.

6.2. The Meaning of Hairy Structures

While other comparable insects usually use their membranous structures (wings) to achieve flight (Dudley and Robert 2002, Sane 2003, Bomphrey 2017), spiders use filament-like structures for aerial dispersal (see Figure 4.18). These so-called 'hairy structures' (filament structure) are usually found in micro-organisms (*E coli.*, paramecia, etc.) or cells (e.g. sperm) that actively locomote in a liquid medium. Because of the extreme thinness of their cilia and flagella, the flow condition around them is a Stokes regime ($Re < 1$) in which the viscosity of the fluid medium is far more dominant than its inertia. However, some plants and animals also use filament-like structures for their aerial journey. Plumed seeds like those of the dandelion and thistle use pappus as a parachute for their passive dispersal (Green and Johnson 1990, Minami et al. 2003, Casseau et al. 2015, Cummins et al. 2017, 2018). The structure and morphological shape of the pappus are efficient at producing drag in the case of low ratios of mass to projected area, and can enable the stable flight of the seeds by allowing for the production of a vortical flow above it (Casseau et al. 2015, Cummins et al. 2017, 2018). Thrips and very small chalcid wasps (fairyfly) also use their unique wing structure, which consists of many 200–300-μm-long bristles (stiff setae), to accomplish this (Weis-Fogh 1973, Kuethe 1975, Wu et al. 1975, Santhanakrishnan et al. 2014). If we calculate the Reynolds numbers of all these structures, they all fall below 1 (see Table 6.1).

Table 6.1 Reynolds numbers and Knudsen numbers of various filament structures in nature. The thickness (diameter) of a filament structure is used as the characteristic length in the calculation number of the Reynolds number. The radius of a filament structure is used for the calculation of the Knudsen number.

	Spp.	Thickness	Length	Aspect Ratio	Numbers	Weight	Speed	Medium	Density	Viscosity	Mean free path	Reynolds number	Knudsen number	Ref.
Spider silk	Xysticus.	200 nm	3.22 m	16.1×10^{7}	50-60	18-21 mg	0.1-0.2 m/s (Settling speed in still air)	Air	1.2047 kg/㎥ (20℃)	1.8205×10^{-5} kg/(ms)	65.44 nm	0.002	0.654	Chapter 4
Pappus	Dandelion Seed	15 µm	7 mm	467	170-200	0.6 mg	0.26 m/s (Settling speed in still air)	Air	1.2047 kg/㎥ (20℃)	1.8205×10^{-5} kg/(ms)	65.44 nm	0.258	8.7×10^{-3}	Sudo et al. 2008
Stiff setae	*Encarsia formosa*	1.5 µm (1-2 µm)	330 µm	220		2.55 µg	1.08 m/s (Wing length: 0.7 mm; Stroke frequency: 370 Hz; Stroke angle 2.09: rad)	Air	1.2047 kg/㎥ (20℃)	1.8205×10^{-5} kg/(ms)	65.44 nm	0.107	8.7×10^{-2}	Weis-Fogh 1973
Flagella	Sperm	1 µm	56 µm	56	1		455 µm/s (Amplitude: 15.6 µm; Stroke frequency: 14.6 Hz)	Water (≈Hydrated mucus)	993 kg/㎥	0.000692 kg/(ms) (37℃)	~0.3 nm	0.00065	6×10^{-4}	Woolley 2003 Smith et al. 2009 Burkman 2009
Cilia	Parameciu m	250 nm	12 µm	48			1.8 mm/s (Stroke frequency: 30 Hz; Stroke angle: 2.51 rad)	Water	998.2 kg/㎥ (20℃)	0.001003 kg/(ms) (20℃)	~0.3 nm	0.00045	2.4×10^{-3}	Blake and Sleigh 1975 Wu et al. 1975
DNA Molecule		2.4 nm (2.2-2.6 nm)	84 µm (The largest human chromosome: 85 mm)	3.5×10^{4} (max. 3.54×10^{7})			80 µm s^{-1}	Concentrated polymer solution	~98.2 kg/㎥ (20℃)	0.0029 kg/(ms)	~0.3 nm	6.6×10^{-8}	0.25	Mandelkern et al. 1981 Perkins et al. 1995

Mean free path (Jennings 1988, Marable et al. 2017)

Why do all these micro-organisms, seeds and cells utilise hairy structures for their locomotion or aerial dispersal? The answer can be found in the characteristic of the low Reynolds number flow. In a flow of this kind, where the viscosity of the fluid medium is dominant, the fluid-dynamic force is proportional to the size (length scale) of the object. Table 6.2 shows that the fluid dynamic forces (resistance force) on various geometries in the low Reynolds number flow ($Re < 1$) are proportional to its either a diameter ($\propto a$: radius) for a sphere and a circular disk or a length L, which is the dominant length scale in the case of a fibre. On the other hand, the fluid dynamic force is proportional to the area ($\propto a^2$) in cases of moderate and high Reynolds number flows ($Re > 1000$). This is because the fluid dynamic force in a high Reynolds number flow is proportional to the dynamic pressure of the fluid flow, which acts on the surface of an object. However, the weight of each geometry, which is proportional to its volume, increases in proportion to a^3 for a sphere, a^2 for a disk, and L for a thin cylindrical rod, respectively. The ratio of a drag force to a weight represents a cost efficiency that means how much fluid dynamic force is gained by investing certain amount of a protein from the viewpoint of an organism (6.1). The independent efficiencies from their sizes are obtained by the uses of a thin rod in the low Reynolds number flow and a disk in the moderate/high Reynolds number flow (see Table 6.2). A disk means a two-dimensional membranous structure. This is why macro-insects over a few milligrams in weight tend to utilise membranous structures for their flight. This is the same in the case of birds and airplanes, the Reynolds numbers of which are in the range of 10^3 to 10^7 (Lissaman 1983). On the other hand, microorganisms mostly utilise filament-like structures, for example, flagella and cilia, as they are exposed to flow conditions of the low Reynolds number. Such filament-like structures are also found in passive flyers as the morphological structures of pappus, stiff setae, and spider silks. In conclusion, the filament-like structure is regarded as a materially-efficient structure for production of fluid dynamic forces (mostly a viscous force) in the low Reynolds number flow. The interesting point to note here is that a spider is the heaviest organism that use fibre structures for their flight even the weights of some species exceed a few milligrams. This is possible, because spiders can spin extremely thin, strong fibres, meaning that they can harvest the micro-scale resistance forces exerted on each tiny segment of silk due to the extreme thinness and length of the silks overall.

Table 6.2 Comparison of fluid dynamic and geometric characteristics of various shapes of an object according to flow conditions (see Eqns. of (2.2), (2.3) and (5.1)).

Flow	Geometry	Drag Formula	Drag	Weight	Cost Efficiency (Drag/Weight)
$Re < 1$	Sphere	$F = 6\pi\eta a U$	$\propto a$	$\propto a^3$	$\propto \frac{1}{a^2}$
$Re < 1$	Disk	$F = 16\eta a U$	$\propto a$	$\propto a^2$	$\propto \frac{1}{a}$
$Re < 1$	Rod	$F_T = \frac{2\pi\eta U L}{ln\left(2\frac{L}{d}\right) - 0.72}$	$\propto L$	$\propto L$	$\propto 1$
$Re > 1000$	Sphere	$F = C_D \frac{1}{2}\rho V^2(\pi a^2)$	$\propto a^2$	$\propto a^3$	$\propto \frac{1}{a}$
$Re > 1000$	Disk	$F = C_D \frac{1}{2}\rho V^2(\pi a^2)$	$\propto a^2$	$\propto a^2$	$\propto 1$

$$Cost\ efficiency = \frac{Acquired\ fluid\ dynamic\ force}{Invested\ weight\ of\ a\ material} \tag{6.1}$$

Figure 6.1 presents the flight Reynolds number spectrum, as developed by Lissaman (1983). The organisms that utilise hairy structures have been added to the plot. Not only spiders, but also dandelion seeds, thrips and small chalcid wasps are categorised as belonging to the group of the 'hairy structure flyers'. The spider is the heaviest organism among them that disperses aerially using filament-like structures. This is only possible because the spider can produce extremely thin and strong spider silks.

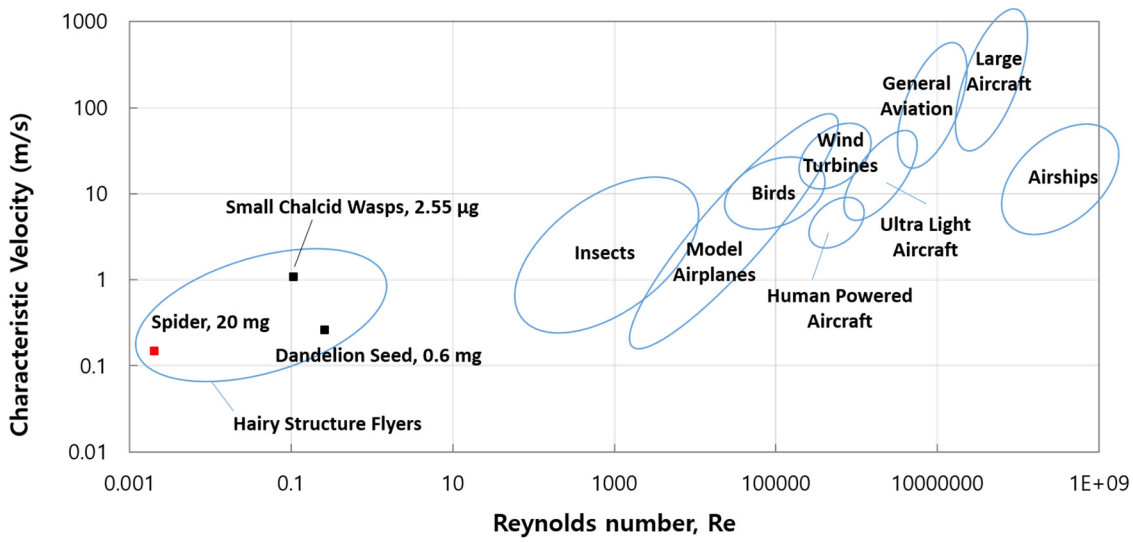

Figure 6.1 Reynolds number spectrum of flying organisms and aerodynamic machines, redrawn and modified from Lissaman (1983). The settling speeds of a spider and a dandelion seed are used as the characteristic velocity. The tip-speed of the outer wing is used for the characteristic velocity of a small chalcid wasp. The flight speeds are used for the other organisms and flying machines as the characteristic velocity. The thicknesses (diameters) of the spider silk, pappus and setae are used as the characteristic length.

6.3. Nanoscale Spider Silk and Continuity of a Medium

The nanoscale of ballooning silk raises the question of whether or not the continuity of the air is still valid on such a small object scale (Gad-el-Hak 2006). This is important because it determines the validity of the classical fluid dynamics applied to this problem. Air is different from liquid water, as it has more sparse molecules; this can be parameterised through a comparison to the mean free path of the molecules, which is defined as the average travel distance of a moving particle. While liquid water has a very small mean free path of 0.3 nm, the mean free path of the air is 65.44 nm (Jennings 1988, Marable et al. 2017). The ratio of the mean free path to the scale of an object, which is known as the Knudsen number ($Kn = 2\lambda/d_L$; the radius is the characteristic length in the case of fibrous structure; Brown 1993, Beskok et al. 2001, Zhao and Povitsky 2013, Zhao et al. 2016), decides whether or not the continuity of a medium is valid on their dynamics (Sun and Boyd 2004, Liu and Aono 2009, Santhanakrishnan et al. 2014).

The fluid states, both in Micro-Electro-Mechanical-Systems (MEMS) and in the rarefied gas environment, can be categorised into four flows: (i) continuum; (ii) slip; (iii) transition; and (iv) free molecule flows (Karniadakis et al. 2005, Gad-el-Hak 2006, Pitakarnnop 2014). If $Kn < 0.001$, the flow is regarded as a continuum, such that the no-slip condition is validated on the surface of the object. For $0.001 \leq Kn < 0.1$, it is still regarded as a continuum, but the slip boundary condition should be applied. The regime of Knudsen numbers $0.1 \leq Kn < 10$ is moderately rarefied. This regime is defined as the transition regime, in which the state changes from the continuum state to the highly rarefied state. Moreover, the regime of $10 \leq Kn$ is defined as the free molecule regime, in which the molecules can move relatively freely with decreased frequency of collisions with the object (Gad-el-Hak 2006, Tian et al. 2017). While most micro-swimmers in liquid and plumed aerial seeds in the air remain in the continuum or the near-slip regimes of the flow (the Knudsen number ranges from 10^{-4} to 10^{-2}), a ballooning silk in the air and a DNA molecule in a liquid solution are categorised as part of the transition regime, as the Knudsen numbers of both are large at 0.65 and 0.25 respectively (see Table 6.1). Therefore, the rarefaction effect of the air should be investigated.

The correction of the Stokes drag of a spherical particle for the rarefaction of a fluid medium was established by Cunningham (1910) and Millikan (1923b). Later, the modelling of the influence of the transition regime on a non-spherical particle was developed by smoothening the resistance from the continuum to the free molecular regimes (Danhneke 1973b, Tian et al. 2017). The drag anisotropy is modelled by adjusting the diameter of the spherical particle, an 'adjusted sphere' method. The Cunningham correction is applied to the drag of the non-spherical particle so as to introduce the effect of the slip condition (Dahneke 1973b, Tian et al. 2017). In this way, the anisotropic drag of the non-spherical particle in high Knudsen number cases can be investigated (see Appendix B (B. 1)-(B. 20)). Figure 6.2A shows the resistance forces of a 3.22 m long elongated ellipsoid according to the Knudsen number as the thickness of the ellipsoid is varied, while Figure 6.2B expresses the resistance force with the dimensionless resistance coefficient. The results are very remarkable: the drag forces begin to split from the estimated drags of the continuum-assumed cases at $Kn = 0.065$ and fall drastically after $Kn = 0.65$ (see Figure 6.2AB). From this, it can be concluded that the thickness of ballooning silk, at 200 nm, may be the lower boundary where the drag force of a continuum is valid. Spider silks that were thinner could not efficiently produce drag forces using the air flows.

This phenomenon can be checked with Cunningham correction factors (see Figure 6.3A). Below a Knudsen number of 0.65, the Cunningham correction factors are around 1 ($Cc \approx 1$). When the Knudsen number is larger than 0.65, the Cunningham correction factors are greater than 1 ($Cc > 1$); this means that the drag forces on the object may decrease due to the rarefaction effect. Figure 6.3B presents the plot of the drag anisotropy (the drag ratio) versus the Knudsen number. At a Knudsen number above 0.65, the ratio does not converge to the factor 2, which is the expected factor in the low Reynolds number flow (Stokes flow), but rather becomes greater than the factor 2 as the thickness of the spider silk becomes thinner than 200 nm. The larger drag ratio, $\xi_{\perp}/\xi_{\parallel} > 2$, is also observed in the moderate or high Reynolds number flow where the inertial force of the flow is dominant. A larger drag ratio means that the magnitude of the normal drag is greater than that of the tangential drag. As the drag ratio is around factor 2 at the 200 nm thickness of the ballooning silk, the tangential drag on the spider silk can be considered as an important factor in spider flight.

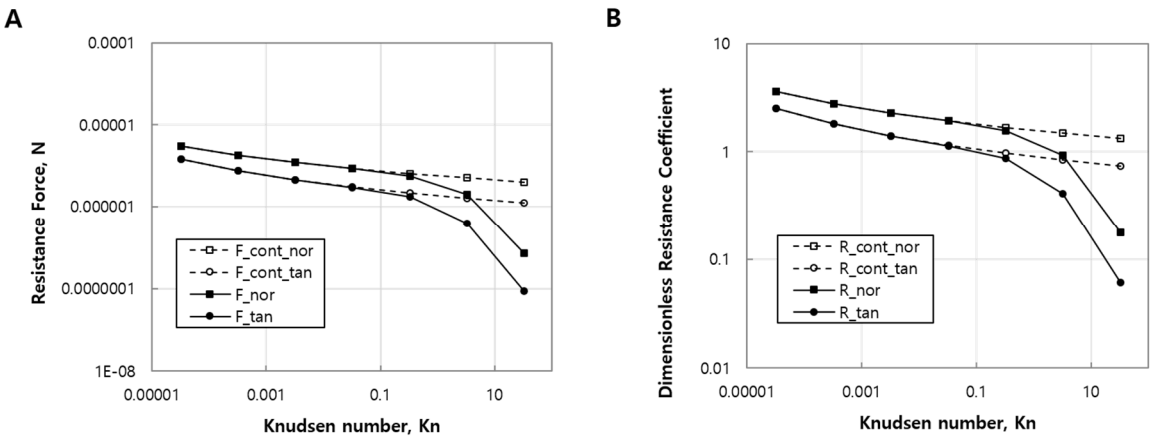

Figure 6.2 (A) The resistance forces on a 3.22 m long elongated ellipsoid versus the Knudsen number as the thickness of the ellipsoid is varied. The uniform flow is fixed at 0.1 m/s, which is in the range of the expected settling speed of a spider discussed in Chapter 4. Square markers indicate the normal drag on the ellipsoid, such that the direction of the force is normal to the axis of the ellipsoid. Circular markers indicate tangential drag on the ellipsoid, such that the direction of the force is parallel to the axis of the ellipsoid. Dashed lines are the drag forces without considering the rarefaction effect of the air (the fluid is regarded as a continuum for the entire regime of the Knudsen number). Solid lines are the drag forces considering the rarefaction effect of the air; (B) The dimensionless resistance coefficients on a 3.22 m long elongated ellipsoid versus the Knudsen number as the thickness of the ellipsoid is varied. The meanings of the plot symbols are the same as in Figure 6.2A.

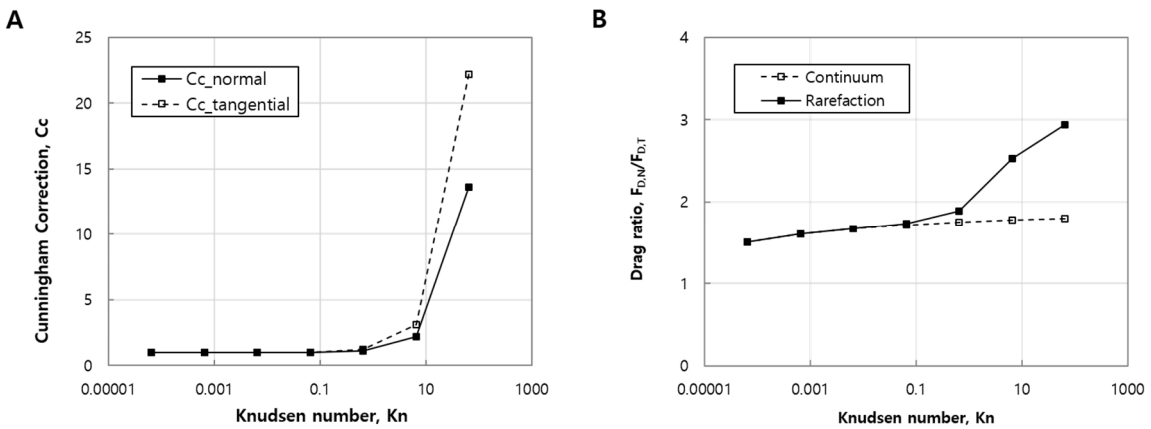

Figure 6.3 (A) Cunningham correction factors of a 3.22 m long elongated ellipsoid versus the Knudsen number as the thickness of the ellipsoid is varied. The uniform flow is fixed as 0.1 m/s, which is in the range of the expected settling speed of a spider in the Chapter 4. Solid filled square markers indicate Cunningham correction factors for the normal drag on the ellipsoid, such that the direction of the force is normal to the axis of the ellipsoid. Empty square markers indicate Cunningham correction factors for the tangential drag; (B) The drag ratio of the normal drag to the tangential drag versus the Knudsen number as the thickness of the ellipsoid is varied.

Although the Knudsen number of a ballooning silk in the air flow belongs to the regime of transition (from the continuum to the free molecule regime), the thickness of a ballooning silk exists at the lowest boundary, where the fluid-dynamic force of the continuum is still maintained as a similar value; $Cc \approx 1$. Therefore, the simulation method outlined in Chapter 5, which assumes that the ballooning structure is under a continuum condition and a low Reynolds number flow, is still valid for the simulation.

6.4. The Ballooning Number

Spiders' ballooning can be understood as a physical phenomenon in which two different physical scales are connected: the macroscopic weight of the spider, although insects of such size normally utilise a high Reynolds number flow for their flight, is sustained by the micro-fluid-dynamic forces that are harvested through the use of long thin fibres (see Figure 6.4). The physical properties of these two different scales are non-dimensionalised and expressed as the ballooning number (see Eqns. (5.32)-(5.35)). An increase in the ballooning number means that the fluid-dynamic forces exerted on a silk by the non-uniform flow become dominant compared with the force of gravity that acts on the body. Moreover, a decrease in the ballooning number means that the gravity force on the body becomes more dominant than the fluid-dynamic forces on a silk, meaning that the spider will fall like a heavy particle, cutting through the eddies of the air flow.

The characteristic velocity refers to the intensity of a non-uniform flow. In the case of the turbulent air, the root-mean-square fluctuation velocity is the characteristic velocity. If we assume that a spider flies in a 1.96 m s^{-1} mean wind speed (measured data 0.95 m above the ground), the root-mean-square fluctuation velocity is 0.41 m s^{-1} on a sunny and light breeze day. Therefore, the ballooning number for turbulence in the field may be about 7.42 in the case of a 20 mg crab spider (see Eqn. (6.2); dynamic viscosity of air: 1.837×10^{-5} kg m^{-1} s^{-1}; length of a spider silk: 3.22 m; number of silks: 60). This number belongs to the regime in which the behaviour of the ballooning structure is biased (towards slow settling in the turbulence; see Figure 5.25). The observed shapes of the ballooning silks in the field is also believed the events in the range of the ballooning number $1 < Bn_{tur} < 10$ (see Figure 4.14). The superposed shapes of these ballooning silks are compared with the results of the bead-spring model simulation (see Figure 6.5).

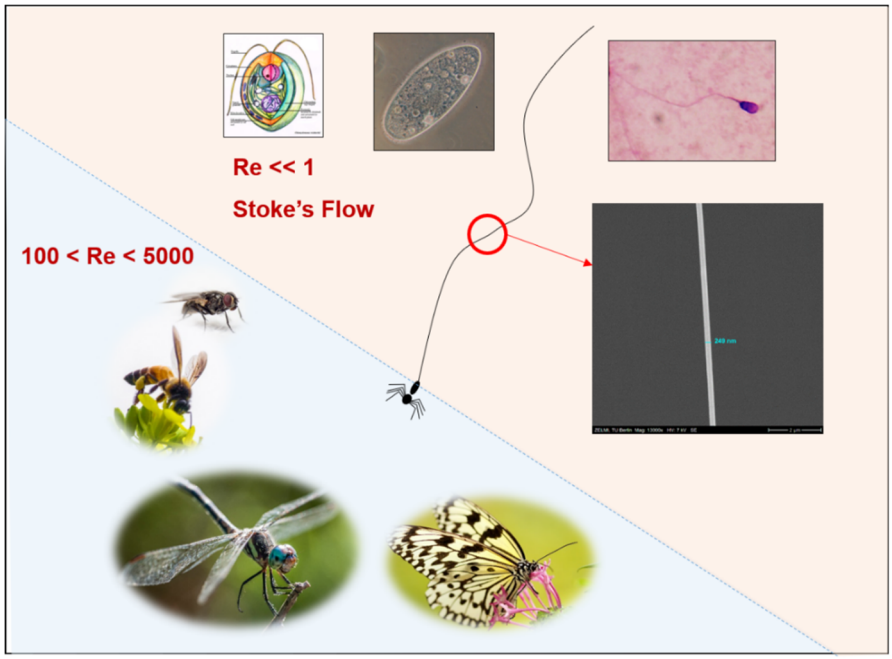

Figure 6.4 Simple schematics of two different flow regimes in animal locomotion. Although the body scale of a spider belongs to the scales of winged insects, the flow regimes around spider silks are low Reynolds number flow regimes, which can be frequently found in the locomotion of micro-organisms and cells. (Figures and photos by Ninghui Shi, Barfooz, Bobjgalindo on Wikipedia; Photos by Manlake Gabriel, Mamun Srizon, Boris Smokrovic, photostockeditor on Unsplash)

$$Bn_{tur} = \frac{\eta \sigma L}{\left({m_{spider}}/{n} \right) g} \tag{6.2}$$

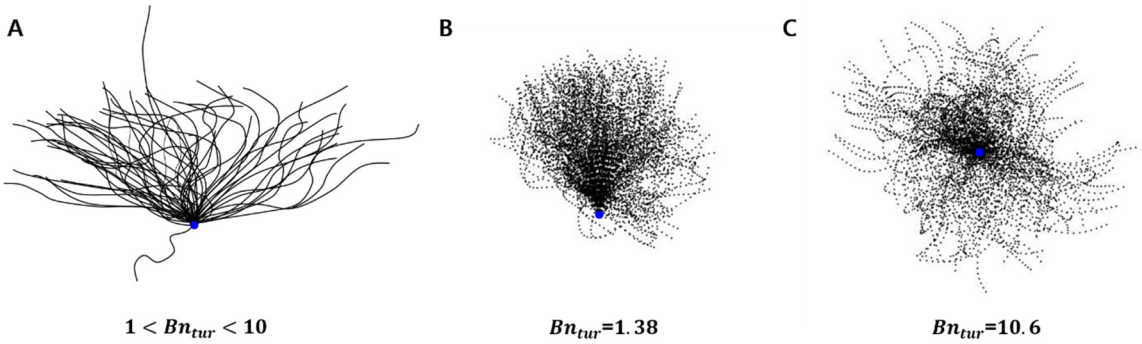

Figure 6.5 Superposed shapes of ballooning silks during the flight. The reference point is the position of its body (A) Superposed shapes of the observed ballooning events in the nature. ($1 < Bn_{tur} < 10$; see Figure 4.14) (B) Superposed shapes of the ballooning silks in the simulation ($Bn_{tur} = 1.38$; see Appendix A Figure A 27). The blue point means the position of a spider body (a point-mass). (C) Superposed shapes of the ballooning silks in the simulation ($Bn_{tur} = 10.6$; see Appendix A Figure A 24). The blue point means the position of a spider body (a point-mass).

6.5. Suspension Characteristics

The suspension characteristics of the ballooning structure were checked through the simulation. The drag anisotropy of spider silks in the low Reynolds number flow was determined as the cause of the slow settling (enhancement of floating performance) of the ballooning structure. The deformed geometry of the filament structure was the main reason behind this slow settling. The strong non-uniformity of a flow also induced the additional increase of the resistance coefficient fluid-dynamically. However, the extent to how much this mechanism works to influence the flight of spiders in nature could not be determined. The most interesting cause of the buoyancy capability of the ballooning spider may be related to the vortical structures in the turbulent wind conditions. In a periodic cellular flow, if the size of the vortex is greater than 1.2 times the length of a ballooning silk, and the ballooning number for a cellular flow, Bn_{vor}, is greater than 1.13, the ballooning structure is trapped by a two-dimensional vortex (a transverse vortex in a 3D space). The phenomenon of a heavy particle becoming trapped in a vortical flow is very interesting, as the given flow field combined with a flexible filament offers energy that prevents the heavy particle from settling down. The biased behaviour in the homogeneous turbulence proves that spiders can stay afloat longer in turbulent air for two main reasons: the anisotropic drag and being trapped in a vortical flow.

6.6. Coherent Structures in the Atmosphere

Many studies explain that the thermal buoyancy motion of the air is the cause of spiders being able to take flight (Blackwall 1827, Richter 1970, Vugts and Van Wingerden 1976, Humphrey 1987). However, the wind near the place that spiders use to take off is unsteady and fluctuates over time (Suter 1999; see Figure 4.19). Studying the structure of wind in detail may offer some clues to support a more

precise explanation for spiders' ballooning. Greenstone (1990) has already proposed that the vertical velocity gradient of windspeed on the ground may be an important factor. Moreover, Suter (1999) and Reynolds et al. (2006) suggested that the turbulent wind may be deeply related with the ballooning phenomenon. Independent of this, a vast number of studies on the detailed structure of turbulent flow have been conducted in the field of fluid dynamics over the past few decades (e.g. Theodorsen 1952, Grass 1971, Willmarth and Lu 1972, Lu and Willmarth 1973, Adrian et al. 2000, Hunt and Morrison 2000, Hommema and Adrian 2003, McNaughton 2004, Adrian 2007, Zhu et al. 2007, Finnigan et. al 2009, Steiner et al. 2011, Dennis 2015, Harun and Reda Lofty 2018). These studies show that turbulent flow is not random motion, but that there rather exist organised motions within the irregular background motions. These organised motions are called 'turbulent coherent structures' (Harun and Reda Lofty 2018). In the channel flow or on the ground, which has various surface conditions, these coherent structures exist as horseshoe vortices or hairpin vortices and play important roles in exchanging mass, momentum and heat between the layers in the boundary layer (Lu and Fitzjarrald 1994, Raupach et al. 1996, Brunet and Irvine 2000, Finnigan 2000, Ganapathissubramani et al. 2002, Thomas and Foken 2007, Finnigan et al. 2009, Steiner et al. 2011, Damian 2016, Harun and Reda Lofty 2018). Here, we discuss the relationship between these coherent structures and the mechanism of spiders' aerial dispersal.

6.6.1. Take-off Phase

In the near-surface atmospheric boundary layer, a few metres from the ground surface, the updraft is not purely initiated by thermal buoyancy forces; it is also initiated by vortical flows, which are generated by the vertical velocity gradient of wind speed (Hunt and Morrison 2000, McNaughton 2003). Figure 6.6 presents a simple explanation of this phenomenon in two dimensions. First, the wind gradient caused by the friction of the ground generates vortical flows (surface eddies, which develop from the ground and grow stronger as they move backward and upwards; Adrian et al. 2000, Hunt and Morrison 2000, Hommema and Adrian 2003, Adrian 2007, Finnigan et. al 2009) on the ground (see Figure 6.6A). On the upwind side of the vortical flow, the upcoming wind involves updraft; on the downwind side, the upcoming wind usually includes downdraft because of the streamwise rotation of the vortex (see Figure 6.6B). Because both flow regions drift with the vortex in the downwind direction, the updraft usually shows a low wind speed from the viewpoint of ground reference, while the downdraft shows high wind speed (see Figure 6.6C). Spiders are exposed to these two representative flows in the turbulent wind conditions (see Figure 6.6D). The updraft component may likely be used by a spider for their take-off in the air. The correlation of this updraft with low wind speeds may also answer the question of why spiders prefer a low wind speed regime (under 3m/s) when embarking on their flight (Richter 1970, 1971, van Wingerden and Vugt 1974, Vugt and van Wingerden 1976, Salmon and Horner 1977, Tolbert 1977, Greenstone 1990, Lee and Kuntner 2015).

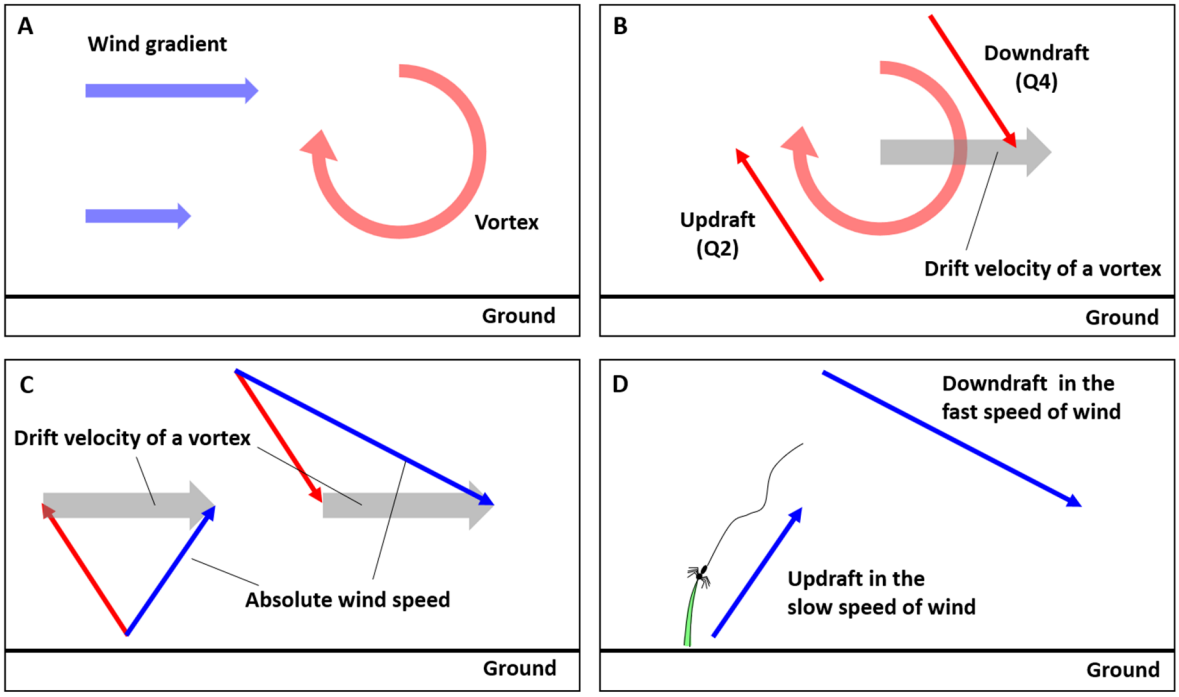

Figure 6.6 Simple schematic explanation using a single vortex on the ground. (A) Production of a vortical flow on the ground; (B) Presence of an updraft and a downdraft near the vortical flow; (C) Transformation of the relative wind speeds to the ground wind speeds; (D) Two representative flows in the turbulent wind conditions.

These low wind speed regimes, which have updraft components, are generated not only by a spanwise surface eddy (as in Figure 6.6), but also by different shapes of vortical flows in three dimensions; for example, by streamwise vortices (possibly the legs of hairpin vortices; Robinson 1991, Panton 2001, Schoppa and Hussain 1998, 2002, Jimmenez and Pinelli 1999, Eitel-Amor et al. 2015), a hairpin vortex (Theodorsen 1952, Head and Bandyopadyay 1981, Brooke and Hanratty 1993, McNaughton and Blundell 2002, Adrian 2007) or a series of hairpin vortices (a hairpin vortex packet) (Head and Bandyopadyay 1981, Smith 1984, Adrian et al. 2000). The validity of this model in the atmospheric boundary layer has been confirmed by a few experiments in the region at a few metres in height from the ground (Hommema and Adrian 2003, Maurusic and Heuer 2007, Morris et al. 2007). In the near-ground atmospheric boundary layer, the structures can be seen as the wedge-shaped first or second (I or II) generation of hairpin vortex packets (Adrian et al. 2000, Adrian 2007). This wedge-shaped vortex packet can be visualised by seeding smoke with the smoke generating devices near the ground. Figure 6.7 shows the visualised vortex packet during daytime, to which an image processing technique has been applied, in the range of a few metres above the ground. The faint smokes are recognised by comparing the RGB vectors with that of the background and amplified. The recognised smokes are negatively visualised as the colour of white. The figure shows the upward development of the packet as it drifts in the downwind direction (see Figure 6.7A-D and Figure 6.7 E-H). These packet structures can be used by passive flyers, such as spiders, for their aerial dispersal in their take-off phase. Figure 6.8 shows the schematic of the vortex packets near the ground, and how these can be used in the take-off phase of the spiders' ballooning.

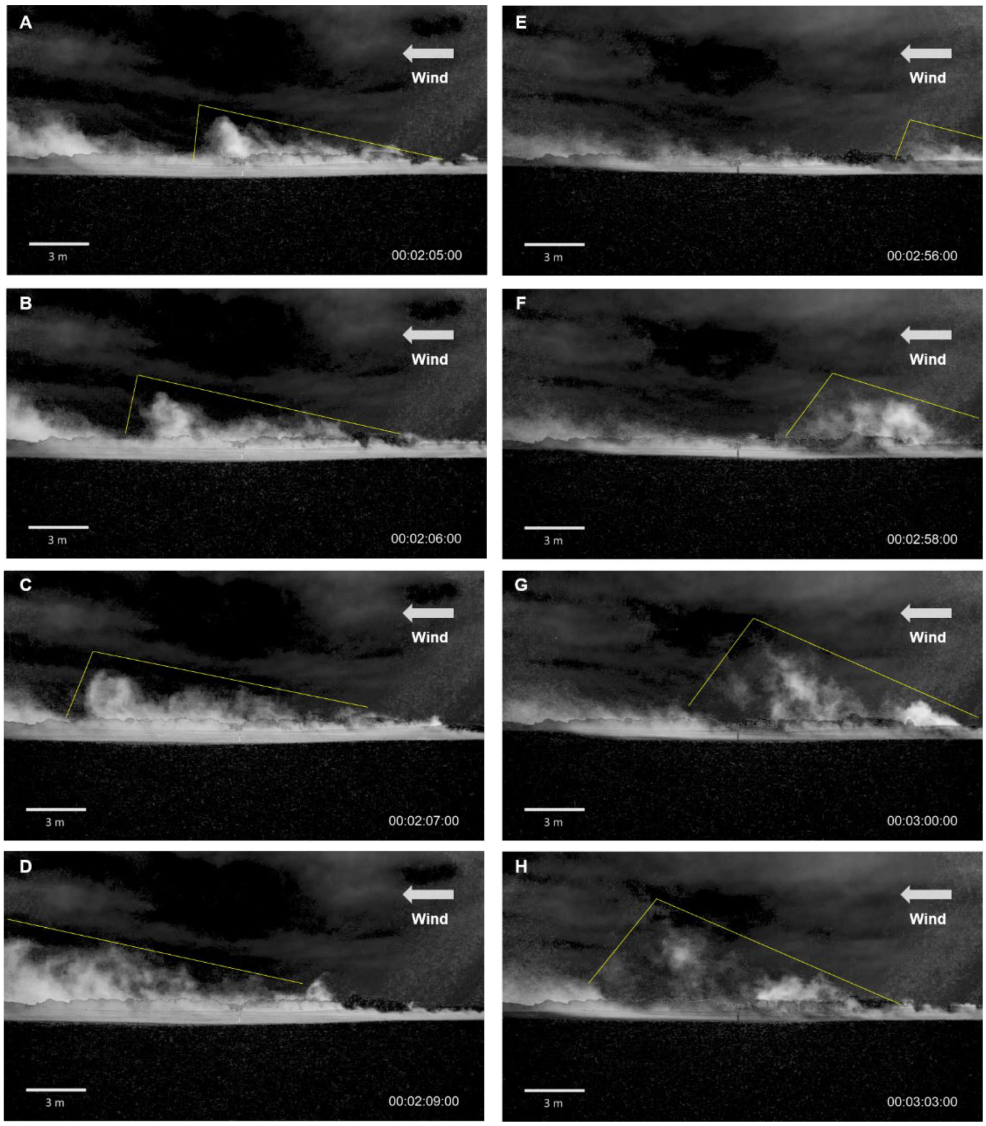

Figure 6.7 Visualisation of hairpin vortex packets in the near-ground atmospheric boundary layer during daytime. (Mean wind speed: 1.96 m s^{-1} at 0.95m above the ground) (A) A wedge-shaped hairpin vortex packet; (B-D) Sequential upward development of the hairpin vortex packet in Figure 6.7A; (E) Before the generation of the hairpin vortex packets; (F-H) Sequential upward development of the hairpin vortex packet in Figure 6.7E (from the author's experiment in the grass field). [Scan the right QR code or click the text to connect to the video]

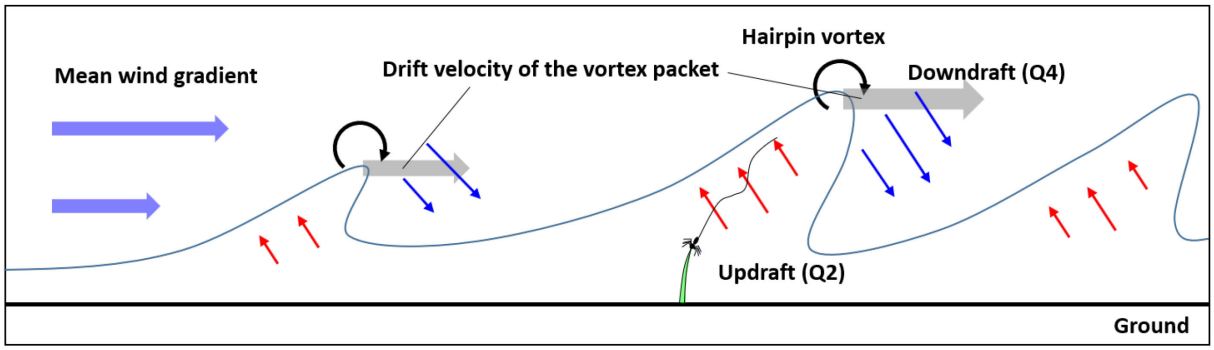

Figure 6.8 Schematic of vortex packets near the ground. Red and blue arrows are the relative wind velocities to the drift velocity of the coherent structure.

6.6.2. Suspension and Dispersal Phase

Results in Chapter 5 show that the non-uniform (horizontal shear flow, transverse 2D vortex) flows around the ballooning structure increase the buoyancy capability in the turbulent atmospheric boundary layer. The horizontally stretched fibre exhibits an increase of its vertical resistance coefficient and a vortical flow field traps the ballooning structure in or near the eddy. One of the interesting features in the near-ground boundary layer is that its ground is blocked mechanically by the ground surface. Therefore, the coherent structures (hairpin packets) are born at the surface and expand only upwards as they drift in the streamwise direction. According to studies of coherent structures in the atmospheric boundary layer, during their development, the size of the vortices becomes larger but weaker; however, once they merge together, they become larger and stronger vortices (Perry et al. 1986, McNaughton 2003, Harun and Lofty 2018). Once spiders take off using local updrafts, which are induced by vortical flows, the latter phase of spiders' aerial dispersal via ballooning may be intimately related with the development and existence of these coherent structures.

This intimate relationship can be qualitatively supported by statistical data on ballooners in the atmosphere. Meaningful information can be extracted from the data, which were collected over five years in the early 1930s by biplanes (Glick 1939). The data, which were gathered over 12 hours of flying time, were considered in order to make the plots. Figure 2.3 and Figure 2.4 present the vertical density plots of the wingless arthropods and the winged insects. While the highest population densities for winged insects are at 20 feet (about 6 m) above the ground, the lowest sampling altitude by airplane (see Figure 2.4), the highest population densities for wingless arthropods (passive flyers) are at 200 feet (about 60 m), which is not the lowest sampling altitude (see Figure 2.3). These population density distributions are very similar to the vertical distributions of vertical Reynolds stress, $\overline{w'w'}$, in the turbulent boundary layers (see the distribution of velocity variance $\overline{w^2}$ in Figure 6.9; Lenschow et al. 1980, Moeng and Sullivan 1994). The vertical Reynolds stress represents the mixing activity of mass fluxes between the layers in the boundary layer (Loureiro and Silva Freire 2005, Lamberti et al. 2018). In this way, we may understand that the aerial dispersal of wingless arthropods is related to turbulent structures in the atmospheric boundary layer. The main contribution to the Reynolds stress is made by the coherent structures. For example, although the coherent structures occupy less than 4 % of the total area, they contribute more than 25 % to $-\overline{u'w'}$ (Ganapathissubramani et al. 2002). Therefore, it can be deduced that the coherent structures in the atmospheric boundary layer may play an important role in the flight of spiders.

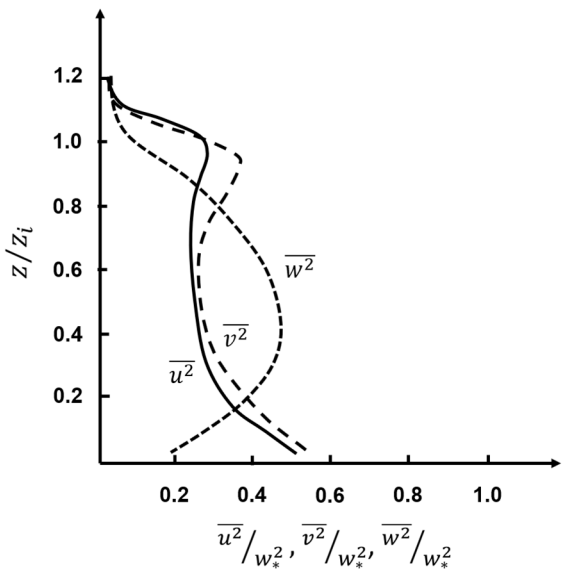

Figure 6.9 Vertical distributions of the velocity variances for the convective atmospheric boundary layer (redrawn from Moeng and Sullivan 1994, see also Lenschow et al. 1980). Here, we assume that $w = w'$, because $\overline{w} \approx 0$.

The highest altitude that spiders can reach may be limited by the atmospheric boundary layer, as the dispersal of aeroplanktons may be limited by the capping inversion (Rio and Hourdin 2007, Stull 1988, 2017). The thickness of the atmospheric boundary layer varies based on weather conditions and the diurnal cycle. During the day, the thickness of the layer is around 1-2 km, while it shrinks to only a few hundreds of meters thick during the night. The thickness extends up to 4-5 km in the case of highly heated ground (for example, the atmosphere over a desert). While the highest altitude at which a ballooning spider has been captured is 4.5 km, the spatial population between 0 and 2 km comprises 75 % of the whole population (between 0 and 4 km) based on the recalculation from Glick's collected data (Glick 1939). These two facts support the theory that spiders disperse using convection flows in the atmospheric boundary layer. The positive correlation between atmospheric instability (which is usually represented as a Richardson number) and ballooning frequency is well shown by previous studies (Thomas et al. 2003). Here, I would like to add the further detailed explanation that coherent structures in the atmospheric boundary layer may play an important role in the spiders' dispersal.

7. Conclusions

The physical flight mechanism underpinning the ballooning of spiders has been poorly understood for some time. The primary difficulty associated with research on this topic is caused by the invisible ballooning silks during the ballooning process. In the present research, observational studies in the field and laboratory first revealed the physical properties of the ballooning fibres and identified the types of silks involved. The crab spider, 20-25 mg in weight, spins 50-60 fibres of nano-scale ballooning silks, the thicknesses of which range from 121 to 323 nm. The lengths of these silks are about 3 m on average, varying from 1 to 6 m. The amount of the ballooning fibres is sufficient for even large spiders (3-150 mg in weight, 20-25 mg in this experiment) to balloon with a very light updraft of 0.1-0.5 m/s (vertical wind velocity). Previously, the drag line was known as a ballooning line. However, the present observations show that ballooning spiders use aciniform gland silks for their flight; these fibres are also used by other settling spiders when they wrap their prey.

Accordingly, new interpretations are introduced in the present research. Spiders are organisms that utilise filament-like structures for their aerial dispersal, unlike other winged flying insects. This kind of trait used to be found in plant seeds such as those of the dandelion and thistle; however, examples of this in the animal world are few. Thrips and very small chalcid wasps use wings consisting of many 200–300-μm-long stiff setae. Spiders, however, use tens of highly flexible fibres to produce aerodynamic drag. The most interesting point here is that the spider is the heaviest among these kinds of organisms. Spiders' ballooning is made possible because of the multiple, thin and long spider silks that enabled by its extreme strength. The meaning of filament-like structure in organisms, which locomote with it actively or passively is because those structures are materially efficient geometry to obtain fluid dynamic force in the low Reynold number flow (viscous dominant flow). In other words, they enable the large gain of the fluid dynamic force with the filament-like structures by investing the protein as small as possible.

The nano-scale silks also lead to another highly interesting fact. When considering the mean free path of the air molecules, which is about 65 nm, the thickness of the ballooning silks at 200 nm (averaged value; N=20), is slightly larger than the mean path length, but has the same order of magnitude. This flow condition $Kn = 0.65$ belongs to a relatively high Knudsen number, categorised as part of the transition regime ($0.1 \leq Kn < 10$) from the continuum regime to the free molecule regime. In rarefied gas dynamics, such a high Knudsen number normally leads to a reduction of drag on the object. Using the Cunningham correction for the non-spherical particle, it is revealed that the thickness of the ballooning silks is set at the lower limit in order to produce efficient drag, which has a Cunningham correction number of around 1. Therefore, 200 nm may be the smallest scale that the organism can utilise to effectively produce drag force using filament-like structures.

The experimental simulation of the ballooning structure in the horizontal shear flow and the homogeneous turbulence highlights the biased motion of the ballooner, which falls slower than the structure would in still air. The reduction of the settling speed is caused by the anisotropic drag of the filament structure, which is flexibly distorted and adapts in non-uniform flows. Normally, in particle dynamics, the non-linearity of particle motion is caused by (i) nonlinear drag (in the transition regime between low and moderate Reynolds number flows) and (ii) inertia (preferential sweeping) during their sediment process. In the case of spiders' ballooning, the anisotropic drag of the flexible filament produces this nonlinearity. In the vortical flow, the structure is trapped by a horizontal (transverse) vortex. This can be regarded as an energy extraction, because the object, which is heavier than air,

remains at the same height by means of passive motion. This may be the reason why the filament-like ballooner has a larger buoyancy capability than that of a point-like ballooner (e.g. aerial seeds).

By introducing the previous research on turbulent flows conducted over the past few decades, the author explains and hypothesises that the coherent structure in the atmospheric boundary layer plays an important role in the aerial dispersal of spiders. The updrafts induced by the coherent structures are highly correlated with low rather than high wind speed regimes in turbulent wind. This may be one of the reasons why spiders prefer a low windspeed regime (usually under 3 m s^{-1}) for their aerial dispersal.

The present research studied the spiders' ballooning from the viewpoint of fluid dynamics. Accordingly, this study may be interesting not only from the perspective of biology, but also from those of physics and engineering. Two different flow dynamics—the low Reynolds number flow and turbulent flow (a representative flow phenomenon in high Reynolds number flow)—are involved in a single ballooning phenomenon. This is because the silk has two different length scales, hundreds of nm for the thickness and a few metres for the length. The fact that the filament is asymmetrically constrained during its suspension in the turbulent air flow because of the weight (body) at the end of the filament shows another its unique feature. All these assumptions result in the ballooning structure having a biased characteristic in the turbulent flow, which is advantageous for longer flight times. Therefore, this phenomenon may be of interest for the sediment control of particles in a fluid flow, and additionally have an impact in the field of aerial exploration by upscaling the structure in the fierce environment—not only in the Earth's atmosphere, but also in extra-terrestrial atmospheres, in which the weather circumstances are violent and not well-known. Under these circumstances, the passive flight mechanism of the spiders' ballooning may be particularly useful.

8. Outlook

The present study has explored various fields in science through the lens of ballooning flight: (i) spiders' behaviour, (ii) fibre dynamics in a low Reynolds number flow, (iii) rarefied gas dynamics in MEMS, and (iv) coherent structures in the atmospheric boundary layer.

From the observational study, the physical traits of ballooning silks were first unveiled. The thickness of each ballooning silk is at the scale of 200 nm. This size is so extremely thin that we were required to consider the rarefaction effect of air molecules. The previously established model shows that this scale of fibre may be the lower boundary of the scale that can practically produce the drag force under the conditions of the air continuum. When a spider spins thinner and multiple silks, it can effectively produce drag force and thus preserve the finite resource of her silk dope. This strategy is cost-effective. Accordingly, the author suggests that the scale of 200 nm may have been optimised throughout the long history of spiders' evolution. This should be studied further in future work.

To extract important parameters in spiders' ballooning, simulations were implemented under a few assumptions: (i) a single silk ballooner, (ii) no consideration of a spider's body size, and (iii) ignorance of the inertia effect of a spider's body. As large spiders use multiple silks, the dynamics of multiple filaments may be an interesting aspect of this phenomenon. The modelling of hydrodynamic interactions between multiple fibres would also be a challenge in the simulation. In real spiders' flights occurring in nature, the drag force of silks is proportional to the relative wind speed; however, the drag force on a spider's body is in the transition region ($30 < Re < 330$) between the low Reynolds number- and the high Reynolds number flows. A study of this nonlinearity may also be interesting for future work. Moreover, the large size of a spider's body compared to the extreme thinness of a spider's silk suggests that the inertial effect of a spider's body should be considered in future modelling.

The possible correlation of spiders' ballooning take-offs to the coherent structure in the near-surface atmospheric boundary layer should be also studied in the field to confirm the hypothesis. Recently, the possible relationship between Earth's electric field and spiders' ballooning flight has attracted some attention as a possible explanation of the mechanisms behind spiders' ballooning. The electric properties of ballooning silks against an electric field, whether or not the ballooning silks are charged during the take-off phase, and the potential charging mechanisms of ballooning silks are not well understood, and could thus constitute interesting studies in the future.

Although a spider's ballooning flight appears to be a purely scientific question in the field of biology, its study involves extensive potentialities regarding its technical application. The spinning process of ballooning fibres in the air can give us insight into possible ways of humans spinning artificial spider silk in the future. The nonlinearity of a flexible fibre in a non-uniform flow provides the control mechanism of particle sedimentation in rheology and the passive control of an artificial micro-swimmer in medical science. Furthermore, the study of wind structure in the atmosphere sets us thinking about a micro-size air vehicle achieving efficient flight during its operation. Lastly, if we recall the fact that the passive flight of a spider is a very effective means of migration to new and unknown regions due to its passive mechanism, the passive flight of a spider could be an effective means of exploration of unknown new environments; for example, the exploration of hazardous weather conditions in which active unmanned aerial vehicles cannot initially be deployed. Moreover, the usage would not be limited to atmospheric circumstances such as hurricanes or typhoons, but could also be extended to the exploration of the extra-terrestrial atmospheres of gaseous planets such as Saturn or Jupiter.

9. References

1. Acharya T, Falgoust J, Schoegl I, Martin MJ. Measurement of Variation of Momentum Accommodation Coefficients with Molecular Mass and Structure. Journal of Thermophysics and Heat Transfer 2019; 33(3):773–8.
2. Adrian RJ. Hairpin vortex organization in wall turbulence. Physics of Fluids 2007; 19(4):41301.
3. Adrian RJ, Meinhart CD, Tomkins CD. Vortex organization in the outer region of the turbulent boundary layer. J. Fluid Mech. 2000; 422:1–54.
4. Agrawal A, Prabhu SV. Survey on measurement of tangential momentum accommodation coefficient. Journal of Vacuum Science & Technology A: Vacuum, Surfaces, and Films 2008; 26(4):634–45.
5. Antman SS, Marsden JE, Sirovich L. Microflows and Nanoflows. New York: Springer-Verlag; 2005. (vol 29).
6. Balachandar S, Eaton JK. Turbulent Dispersed Multiphase Flow. Annu. Rev. Fluid Mech. 2010; 42(1):111–33.
7. Barth F, Komarek S, Humphrey JC, Treidler B. Drop and swing dispersal behavior of a tropical wandering spider: Experiments and numerical model. J Comp Physiol A 1991; 169(3).
8. Bearman PW. Some measurements of the distortion of turbulence approaching a two-dimensional bluff body. J. Fluid Mech. 1972; 53(03):451.
9. Bell JR, Bohan DA, Shaw EM, Weyman GS. Ballooning dispersal using silk: World fauna, phylogenies, genetics and models. BER 2005; 95(02):2.
10. Bell JR, Bohan DA, Le Fevre R, Weyman GS. Can Simple Experimental Electronics Simulate the Dispersal Phase of Spider Ballooners? Journal of Arachnology 2005; 33(2):523–32.
11. Bergougnoux L, Bouchet G, Lopez D, Guazzelli É. The motion of solid spherical particles falling in a cellular flow field at low Stokes number. Physics of Fluids 2014; 26(9):93302.
12. Bishop L. Meteorological Aspects of Spider Ballooning. Environmental Entomology 1990; 19(5):1381–7.
13. Blackwall J. Observations and experiments, made with a view to ascertain the means by which the spiders that produce gossamer effect their aerial excursions. Transactions of the Linnean Society of London 1827; (15):449–59.
14. Blake J, Sleigh M, editors. Hydrodynamical Aspects of Ciliary Propulsion. New York; 1975. (vol 2).
15. Bomphrey RJ, Nakata T, Phillips N, Walker SM. Smart wing rotation and trailing-edge vortices enable high frequency mosquito flight. Nature 2017; 544(7648):92–5.
16. Boyadzhiev L. On the movement of a spherical particle in vertically oscillating liquid. J. Fluid Mech. 1973; 57(03):545.
17. Brennen C, Winet H. Fluid Mechanics of Propulsion by Cilia and Flagella. Annu. Rev. Fluid Mech. 1977; 9(1):339–98.
18. Bristowe WS. A Preliminary Note on the Spiders of Krakatau. Proceedings of the Zoological Society of London 1931; 101(4):1387–400.
19. Bristowe WS. The comity of spiders. Lymington: Pisces Conservation / Ray Society; 2004.
20. Brooke JW, Hanratty TJ. Origin of turbulence-producing eddies in a channel flow. Physics of Fluids A: Fluid Dynamics 1993; 5(4):1011–22.
21. Brouzet C, Verhille G, Le Gal P. Flexible fiber in a turbulent flow: a macroscopic polymer. Phys Rev Lett 2014; 112(7):74501.

22. Brown RC. Air filtration: An integrated approach to the theory and applications of fibrous filters. 1. ed. Oxford: Pergamon Press; 1993. Available from: URL: http://www.loc.gov/catdir/enhancements/fy0601/93010258-d.html.
23. Brunet Y, Irvine MR. The Control Of Coherent Eddies In Vegetation Canopies: Streamwise Structure Spacing, Canopy Shear Scale And Atmospheric Stability. Boundary-Layer Meteorol 2000; 94(1):139–63.
24. Burgers JM. in Second Report on Viscosity and Plasticity: Noord-Hollandsche Uitgevers-Maatschappij; 1938. (Verhandelingen der Koninklijke Akademie van Wetenschappen, Afdeeling Natuurkunde: Wiskunde, natuurkunde, scheikunde, kristallenleer, sterrenkunde, weerkunde, en ingenieurswetenschappen).
25. Burkman LJ. Characterization of Hyperactivated Motility by Human Spermatozoa During Capacitation: Comparison of Fertile and Oligozoospermic Sperm Populations. Archives of Andrology 2009; 13(2-3):153–65.
26. Bustamante C, Marko J, Siggia E, Smith S. Entropic elasticity of lambda-phage DNA. Science 1994; 265(5178):1599–600.
27. Casseau V, Croon G de, Izzo D, Pandolfi C. Morphologic and Aerodynamic Considerations Regarding the Plumed Seeds of Tragopogon pratensis and Their Implications for Seed Dispersal. PLoS ONE 2015; 10(5):e0125040.
28. Cbosby CR, Crosby, C. R. and Bishop, S. C. Aeronautic Spiders with a Description of a New Species. Journal of the New York Entomological Society 1936; 1(44):43–9. Available from: URL: http://www.jstor.org/stable/25004641.
29. Childress S. Mechanics of swimming and flying. Cambridge: Cambridge University Press; 1981. (Cambridge studies in mathematical biology; vol 2). Available from: URL: https://doi.org/10.1017/CBO9780511569593.
30. Coyle FA. Aerial dispersal by mygalomorph spiderlings (Araneae, Mygalomorphae). J. Arachnol. 1983; (11):283–6.
31. Coyle, Frederick A Greenstone, Matthew H Hultsch, Anne-Lise Morgan, Clyde E. Ballooning mygalomorphs: estimates of the masses of Sphodros and ummidia ballooners (Araneae: Atypidae, Ctenizidae). J. Arachnol. 1985; 13(3):291–6.
32. Csanady GT. Turbulent Diffusion of Heavy Particles in the Atmosphere. J. Atmos. Sci. 1963; 20(3):201–8.
33. Cummins C, Seale M, Macente A, Certini D, Mastropaolo E, Viola IM et al. A separated vortex ring underlies the flight of the dandelion. Nature 2018; 562(7727):414–8.
34. Cunningham E. On the Velocity of Steady Fall of Spherical Particles through Fluid Medium. Proceedings of the Royal Society A: Mathematical, Physical and Engineering Sciences 1910; 83(563):357–65.
35. Dahneke BE. Slip correction factors for nonspherical bodies—II free molecule flow. Journal of Aerosol Science 1973; 4(2):147–61.
36. Dahneke BE. Slip correction factors for nonspherical bodies—III the form of the general law. Journal of Aerosol Science 1973; 4(2):163–70.
37. Damian T. Coherent Structures in the Atmospheric Boundary Layer Measured by Dual Doppler Lidar.
38. Darwin C. Journal of researches into the natural history and geology of the countries visited during the voyage of H.M.S. Beagle round the world, under the Command of Capt. Fitz Roy, R.N. Second Edition. New York: JOHN MURRAY, ALBEMARLE STREET; 1845.

39. Das D, Sabhapandit S. Accurate statistics of a flexible polymer chain in shear flow. Phys Rev Lett 2008; 101(18):188301.
40. Dean DA, Sterling WL. Size and Phenology of Ballooning Spiders at Two Locations in Eastern Texas. Journal of Arachnology 1985; (13):111–20.
41. Delgado-Buscalioni R. Cyclic motion of a grafted polymer under shear flow. Phys Rev Lett 2006; 96(8):88303.
42. Delmotte B, Climent E, Plourabouê F. A general formulation of Bead Models applied to flexible fibers and active filaments at low Reynolds number. Journal of Computational Physics 2015; 286:14–37.
43. Dennis DJC. Coherent structures in wall-bounded turbulence. An Acad Bras Cienc 2015; 87(2):1161–93.
44. Dhont JKG. An introduction to dynamics of colloids. 2. impr. Amsterdam: Elsevier; 2003. (Studies in interface science; vol 2).
45. Doi M, Edwards SF. The theory of polymer dynamics. Oxford: Clarendon Press; 2007. (International series of monographs on physics; vol 73).
46. Doyle PS, Underhill PT. Brownian Dynamics Simulations of Polymers and Soft Matter. In: Yip S, editor. Handbook of materials modeling. Dordrecht: Springer; 2005. p. 2619–30.
47. Dreyfus R, Baudry J, Roper ML, Fermigier M, Stone HA, Bibette J. Microscopic artificial swimmers. Nature 2005; 437(7060):862–5.
48. Drummond IT, Duane S, Horgan RR. Scalar diffusion in simulated helical turbulence with molecular diffusivity. J. Fluid Mech. 1984; 138(-1):75.
49. Dudley R. The biomechanics of insect flight: Form, function, evolution. 2. print., 1. paperback print. Princeton, NJ: Princeton Univ. Press; 2002. (Princeton paperbacks).
50. Duffey E. Aerial Dispersal in a Known Spider Population. The Journal of Animal Ecology 1956; 1(25):85.
51. Eberhard WG. How Spiders Initiate Airborne Lines. The Journal of Arachnology 1987; 1(15):1–9.
52. Eitel-Amor G, Örlü R, Schlatter P, Flores O. Hairpin vortices in turbulent boundary layers. Physics of Fluids 2015; 27(2):25108.
53. Fan F-G, Ahmadi G. Wall Deposition of Small Ellipsoids from Turbulent Air Flows—A Brownian Dynamics Simulation. Journal of Aerosol Science 2000; 31(10):1205–29.
54. Finnigan JJ, Shaw RH, Patton EG. Turbulence structure above a vegetation canopy. J. Fluid Mech. 2009; 637:387.
55. Foelix RF. Biology of spiders. 3. ed. Oxford: Oxford Univ. Press; 2011.
56. Fung J, Vassilicos J. Two-particle dispersion in turbulent like flows. Phys. Rev. E 1998; 57(2):1677–90.
57. Fung JCH. Gravitational settling of particles and bubbles in homogeneous turbulence. J. Geophys. Res. 1993; 98(C11):20287.
58. Fung JCH. Shear flow turbulence structure and its Lagrangian statistics. Fluid Dyn. Res. 1996; 17(3):147–80.
59. Fung JCH. Effect of nonlinear drag on the settling velocity of particles in homogeneous isotropic turbulence. J. Geophys. Res. 1998; 103(C12):27905–17.
60. Fung JCH, Hunt JCR, Malik NA, Perkins RJ. Kinematic simulation of homogeneous turbulence by unsteady random Fourier modes. J. Fluid Mech. 1992; 236(-1):281.
61. Fung JCH, Perkins RJ. Dispersion modeling by kinematic simulation: Cloud dispersion model. Fluid Dyn. Res. 2008; 40(4):273–309.

62. Fung JCH, Vassilicos JC. Inertial particle segregation by turbulence. Phys Rev E Stat Nonlin Soft Matter Phys 2003; 68(4 Pt 2):46309.
63. Fung JCH. Gravitational settling of small spherical particles in unsteady cellular flow fields. Journal of Aerosol Science 1997; 28(5):753–87.
64. Fung JCH. Kinematic simulation of turbulent flow and particle motions [Apollo - University of Cambridge Repository].
65. Fung YC. Biomechanics: Motion, Flow, Stress, and Growth. New York, NY: Springer; 1990. Available from: URL: http://dx.doi.org/10.1007/978-1-4419-6856-2.
66. Gad-el-Hak M. The MEMS handbook. 2nd ed. Boca Raton, Fla., London: CRC Taylor & Francis; 2006. (Mechanical engineering series).
67. Ganapathisubramani B, Longmire EK, Marusic I. Characteristics of vortex packets in turbulent boundary layers. J. Fluid Mech. 2003; 478.
68. Gauger E, Stark H. Numerical study of a microscopic artificial swimmer. Phys Rev E Stat Nonlin Soft Matter Phys 2006; 74(2 Pt 1):21907.
69. Gerashchenko S, Steinberg V. Statistics of tumbling of a single polymer molecule in shear flow. Phys Rev Lett 2006; 96(3):38304.
70. Glick PA. The distribution of insects, spiders, and mites in the air. USDA Tech Bull 1939; (673):1–150.
71. Gorham PW. Ballooning Spiders: The Case for Electrostatic Flight 2013. Available from: URL: https://arxiv.org/abs/1309.4731v2.
72. Grass AJ. Structural features of turbulent flow over smooth and rough boundaries. J. Fluid Mech. 1971; 50(02):233.
73. Greene DF, Johnson EA. The Aerodynamics of Plumed Seeds. Functional Ecology 1990; 4(1):117.
74. Greenstone MH. Meteorological determinants of spider ballooning: the roles of thermals vs. the vertical windspeed gradient in becoming airborne. Oecologia 1990; 84(2):164–8.
75. Griswold CE. Atlas of phylogenetic data for entelegyne spiders (Araneae : Araneomorphae : Entelegynae): With comments on their phylogeny. San Francisco: California Academy of Sciences; 2005. (Proceedings of the California Academy of Sciences. Fourth Seriesvol. 56, suppl. 2).
76. Gustavsson K, Meneguz E, Reeks M, Mehlig B. Inertial-particle dynamics in turbulent flows: caustics, concentration fluctuations and random uncorrelated motion. New J. Phys. 2012; 14(11):115017.
77. Happel J, Brenner H. Low Reynolds number hydrodynamics: With special applications to particulate media. 5. printing. Dordrecht: Kluwer Acad. Publ; 1991. (Mechanics of fluids and transport processes).
78. Harris I, editor. The nature of the wind; 1971.
79. Harun Z, Reda Lotfy E. Generation, Evolution, and Characterization of Turbulence Coherent Structures.
80. Head MR, Bandyopadhyay P. New aspects of turbulent boundary-layer structure. J. Fluid Mech. 1981; 107(-1):297.
81. Hemadri V, Agrawal A, Bhandarkar UV. Determination of tangential momentum accommodation coefficient and slip coefficients for rarefied gas flow in a microchannel. Sādhanā 2018; 43(10):5.
82. Henschel JR. Dispersal Mechanisms of Stegodyphus (Eresidae): Do They Balloon? The Journal of Arachnology 1995; (23):202–4.
83. Hommema SE, Adrian RJ. Packet structure of surface eddies in the atmospheric boundary layer. Boundary-Layer Meteorology 2003; 106(1):147–70.

84. Hormiga G. Orsonwells, a new genus of giant linyphild spiders (Araneae) from the Hawaiian Islands. Invert. Systematics 2002; 16(3):369–448.
85. Humphrey JAC. Fluid mechanic constraints on spider ballooning. Oecologia 1987; 73(3):469–77.
86. Hunt JCR. A theory of turbulent flow round two-dimensional bluff bodies. J. Fluid Mech. 1973; 61(04):625.
87. Hunt JCR, Kaimal JC, Gaynor JE. Eddy structure in the convective boundary layer—new measurements and new concepts. Q.J Royal Met. Soc. 1988; 114(482):827–58.
88. Hunt JCR, Morrison JF. Eddy structure in turbulent boundary layers. European Journal of Mechanics - B/Fluids 2000; 19(5):673–94.
89. Jeffery GB. The Motion of Ellipsoidal Particles Immersed in a Viscous Fluid. Proceedings of the Royal Society A: Mathematical, Physical and Engineering Sciences 1922; 102(715):161–79.
90. Jeffrey DJ, Onishi Y. The forces and couples acting on two nearly touching spheres in low-Reynolds-number flow. Z. angew. Math. Phys. 1984; 35(5):634–41.
91. Jennings SG. The mean free path in air. Journal of Aerosol Science 1988; 19(2):159–66.
92. Jiménez J, Pinelli A. The autonomous cycle of near-wall turbulence. J. Fluid Mech. 1999; 389:335–59.
93. Jo K, Chen Y-L, Pablo JJ de, Schwartz DC. Elongation and migration of single DNA molecules in microchannels using oscillatory shear flows. Lab Chip 2009; 9(16):2348–55.
94. Karniadakis G, Aluru N, Antman SS, Beskok A, Marsden JE, Sirovich L. Microflows and Nanoflows: Fundamentals and Simulation. New York: Springer; 2005. (Interdisciplinary Applied Mathematics; vol 29).
95. Karniadakis G, Beşkök A. Micro flows: Fundamentals and simulation. New York: Springer; 2002.
96. Kimberly S. Sheldon, Longhua Zhao, Angela Chuang, Iordanka N. Panayotova, Laura A. Miller, and Lydia Bourouiba. Revisiting the Physics of Spider Ballooning. Women in Mathematical Biology 2017; 8:125–39.
97. Ko FK, Kawabata S, Inoue M, Niwa M, Fossey S, Song JW. Engineering Properties of Spider Silk. MRS Proc. 2001; 702:91.
98. Kraichnan RH. Diffusion by a Random Velocity Field. Phys. Fluids 1970; 13(1):22.
99. Kuethe AM, editor. On the mechanics of flight of small insects. New York; 1975. (vol 2).
100. Lafitte A, Le Garrec T, Bailly C, Laurendeau E. Turbulence Generation from a Sweeping-Based Stochastic Model. AIAA Journal 2014; 52(2):281–92.
101. Lamberti G, García-Sánchez C, Sousa J, Gorlé C. Optimizing turbulent inflow conditions for large-eddy simulations of the atmospheric boundary layer. Journal of Wind Engineering and Industrial Aerodynamics 2018; 177:32–44.
102. Lauga E, Powers TR. The hydrodynamics of swimming microorganisms. Rep. Prog. Phys. 2009; 72(9):96601.
103. Lee VMJ, Kuntner M, Li D. Ballooning behavior in the golden orbweb spider Nephila pilipes (Araneae: Nephilidae). Front. Ecol. Evol. 2015; 3:e86780.
104. Lenschow DH, Wyngaard JC, Pennell WT. Mean-Field and Second-Moment Budgets in a Baroclinic, Convective Boundary Layer. J. Atmos. Sci. 1980; 37(6):1313–26.
105. Lindström SB, Uesaka T. Simulation of the motion of flexible fibers in viscous fluid flow. Physics of Fluids 2007; 19(11):113307.
106. Lissaman PBS. Low-Reynolds-Number Airfoils. Annu. Rev. Fluid Mech. 1983; 15(1):223–39.
107. Liu H, Aono H. Size effects on insect hovering aerodynamics: an integrated computational study. Bioinspir Biomim 2009; 4(1):15002.

108. Loureiro JBR, Freire APS. Experimental investigation of turbulent boundary layers over steep two-dimensional elevations. J. Braz. Soc. Mech. Sci. & Eng. 2005; 27(4).
109. Lowe CP. Dynamics of filaments: modelling the dynamics of driven microfilaments. Philos Trans R Soc Lond B Biol Sci 2003; 358(1437):1543–50.
110. Lu SS, Willmarth WW. Measurements of the structure of the Reynolds stress in a turbulent boundary layer. J. Fluid Mech. 1973; 60(03):481.
111. Mandelkern M, Elias JG, Eden D, Crothers DM. The dimensions of DNA in solution. Journal of Molecular Biology 1981; 152(1):153–61.
112. Manton MJ. On the motion of a small particle in the atmosphere. Boundary-Layer Meteorol 1974; 6(3-4):487–504.
113. Marable DC, Shin S, Yousefzadi Nobakht A. Investigation into the microscopic mechanisms influencing convective heat transfer of water flow in graphene nanochannels. International Journal of Heat and Mass Transfer 2017; 109:28–39.
114. Mark J. Bonino. Material Properties of Spider Silk [the Degree of Master of Science]. Rochester, NY: The College School of Engineering and Applied Sciences; 2003.
115. Marusic I, Heuer WDC. Reynolds number invariance of the structure inclination angle in wall turbulence. Phys Rev Lett 2007; 99(11):114504.
116. Matthew H. Greenstone, Clyde E. Morgan, Anne-Lise Hultsch, Roger A. Farrow and J. E. Dowse. Ballooning Spiders in Missouri, USA, and New South Wales, Australia: Family and Mass Distributions. Journal of Arachnology 1987; 15(2):163–70.
117. Maxey MR. The gravitational settling of aerosol particles in homogeneous turbulence and random flow fields. J. Fluid Mech. 1987; 174(1):441.
118. Maxey MR. The motion of small spherical particles in a cellular flow field. Phys. Fluids 1987; 30(7):1915.
119. Maxey MR, Corrsin S. Gravitational Settling of Aerosol Particles in Randomly Oriented Cellular Flow Fields. J. Atmos. Sci. 1986; 43(11):1112–34.
120. McCook HC. American spiders and their spinning work: A natural history of the orb weaving spiders of the United States: with special regard to their industry and habits. Landisville, PA: Coachwhip Publications; 2006.
121. McNaughton KG. Turbulence Structure of the Unstable Atmospheric Surface Layer and Transition to the Outer Layer. Boundary-Layer Meteorology 2003; 112(2):199–221.
122. McNaughton KG, Blundell RE. A Model of the Large-Scale Ramp Structures Observed in the Atmospheric Surface Layer. Wageningen; 2002. (15th Symp. Boundary Layers and Turbulence).
123. Merriam-Webster.com. Turbulent flow; 2019 [cited 2019 Jan 30]. Available from: URL: https://www.merriam-webster.com.
124. Millikan RA. Coefficients of Slip in Gases and the Law of Reflection of Molecules from the Surfaces of Solids and Liquids. Phys. Rev. 1923; 21(3):217–38.
125. Millikan RA. The General Law of Fall of a Small Spherical Body through a Gas, and its Bearing upon the Nature of Molecular Reflection from Surfaces. Phys. Rev. 1923; 22(1):1–23.
126. Minami S, Azuma A. Various flying modes of wind-dispersal seeds. Journal of Theoretical Biology 2003; 225(1):1–14.
127. Moeng C-H, Sullivan PP. A Comparison of Shear- and Buoyancy-Driven Planetary Boundary Layer Flows. J. Atmos. Sci. 1994; 51(7):999–1022.
128. Monin AS, Yaglom AM, Ablow CM. StatisticalFluidMechanics: TheMechanicsofTurbulence. American Journal of Physics 1977; 45(10):1010.

129. Moon M-J, An J-S. Spinneret Microstructure of the Silk Spinning Apparatus in the Crab Spider, Misumenops tricuspidatus (Araneae: Thomisidae). Entomol Research 2005; 35(1):67–74.
130. Morley EL, Robert D. Electric Fields Elicit Ballooning in Spiders. Curr Biol 2018; 28(14):2324-2330.e2.
131. Morris SC, Stolpa SR, Slaboch PE, Klewicki JC. Near-surface particle image velocimetry measurements in a transitionally rough-wall atmospheric boundary layer. J. Fluid Mech. 2007; 580:319.
132. Morse DH. Dispersal of the Spiderlings of Xysticus Emertoni (Araneae, Thomisidae), A Litter-Dwelling Crab Spider. The Journal of Arachnology 1992; (20):217–221.
133. Murugesh Babu K. Silk: Processing, properties and applications. Cambridge, UK: Woodhead Publishing in association with the Textile Institute; 2013. (Woodhead publishing series in textilesno. 149).
134. Ning Z, Melrose JR. A numerical model for simulating mechanical behavior of flexible fibers. The Journal of Chemical Physics 1999; 111(23):10717–26.
135. Osaki S. Is the mechanical strength of spider's drag-lines reasonable as lifeline? International Journal of Biological Macromolecules 1999; 24(2-3):283–7.
136. Palmgren P. Experimentelle Untersuchungen fiber die Funktion der Trichobothrien bei Tegenaria Derhami. Soc. Acta Zool. Fenn. 1936; (19):3–28.
137. Panton RL. Overview of the self-sustaining mechanisms of wall turbulence. Progress in Aerospace Sciences 2001; 37(4):341–83.
138. Pelegrini MF, Vieira EDR, editors. Flow Past a Sphere at Moderate Reynolds Numbers; 2003.
139. Perkins T, Quake, Smith D, Chu S. Relaxation of a single DNA molecule observed by optical microscopy. Science 1994; 264(5160):822–6.
140. Perkins T, Smith D, Larson R, Chu S. Stretching of a single tethered polymer in a uniform flow. Science 1995; 268(5207):83–7.
141. Perry AE, Henbest S, Chong MS. A theoretical and experimental study of wall turbulence. J. Fluid Mech. 1986; 165(-1):163.
142. Pitakarnnop J. Rarefied gas flow in pressure and vacuum measurements. ACTA IMEKO 2014; 3(2):60.
143. Purcell EM. Life at low Reynolds number. American Journal of Physics 1977; 45(1):3–11.
144. Qiu T, Lee T-C, Mark AG, Morozov KI, Münster R, Mierka O et al. Swimming by reciprocal motion at low Reynolds number. Nat Commun 2014; 5:5119.
145. Raupach MR, Finnigan JJ, Brunei Y. Coherent eddies and turbulence in vegetation canopies: The mixing-layer analogy. Boundary-Layer Meteorol 1996; 78(3-4):351–82.
146. Reeks MW. On the dispersion of small particles suspended in an isotropic turbulent fluid. J. Fluid Mech. 1977; 83(03):529.
147. Reynolds AM, Bohan DA, Bell JR. Ballooning dispersal in arthropod taxa with convergent behaviours: dynamic properties of ballooning silk in turbulent flows. Biol Lett 2006; 2(3):371–3.
148. Reynolds O. XXIX. An experimental investigation of the circumstances which determine whether the motion of water shall be direct or sinuous, and of the law of resistance in parallel channels. Phil. Trans. R. Soc. Lon 1883; 174:935–82.
149. Richter CJJ. Some Aspects of Aerial Dispersal in Different Populations of Wolf Spiders, with Particular Reference to Pardosa Amentata (Araneae Lycosidae). Miscellaneous Papers, Landbouwhogeschool, Wageningen 1971; (8):77–88.
150. Richter CJJ. Aerial dispersal in relation to habitat in eight wolf spider species (Pardosa, Araneae, Lycosidae). Oecologia 1970; 5(3):200–14.

151. Riley JJ. Diffusion experiments with numerically integrated isotropic turbulence. Phys. Fluids 1974; 17(2):292.
152. Rio C, Hourdin F. A Thermal Plume Model for the Convective Boundary Layer: Representation of Cumulus Clouds. J. Atmos. Sci. 2008; 65(2):407–25.
153. Robinson SK. Coherent Motions in the Turbulent Boundary Layer. Annu. Rev. Fluid Mech. 1991; 23(1):601–39.
154. Roos FW, Willmarth WW. Some experimental results on sphere and disk drag. AIAA Journal 1971; 9(2):285–91.
155. Rossi R, Philips DA, Iaccarino G. A numerical study of scalar dispersion downstream of a wall-mounted cube using direct simulations and algebraic flux models. International Journal of Heat and Fluid Flow 2010; 31(5):805–19.
156. Rosti ME, Banaei AA, Brandt L, Mazzino A. Flexible Fiber Reveals the Two-Point Statistical Properties of Turbulence. Phys Rev Lett 2018; 121(4):44501.
157. Rotne J, Prager S. Variational Treatment of Hydrodynamic Interaction in Polymers. The Journal of Chemical Physics 1969; 50(11):4831–7.
158. Rott N. Note on the History of the Reynolds Number. Annu. Rev. Fluid Mech. 1990; 22(1):1–12.
159. Rouse PE. A Theory of the Linear Viscoelastic Properties of Dilute Solutions of Coiling Polymers. The Journal of Chemical Physics 1953; 21(7):1272–80.
160. Sakai Y, Hunt JCR, Fung JCH, Pedrizetti G, Perkins RJ. Modelling of the diffusion of fluid particles in turbulent flows approaching a circular cylinder by random Fourier modes and random flight. Appl. Sci. Res. 1993; 51(1-2):547–53.
161. Salmon JT, Horner NV. Aerial Dispersion of Spiders in North Central Texas. The Journal of Arachnology 1977; 5(2):153–7.
162. Sane SP. The aerodynamics of insect flight. Journal of Experimental Biology 2003; 206(23):4191–208.
163. Santhanakrishnan A, Robinson AK, Jones S, Low AA, Gadi S, Hedrick TL et al. Clap and fling mechanism with interacting porous wings in tiny insect flight. J Exp Biol 2014; 217(Pt 21):3898–909.
164. Schneider JM, Roos J, Lubin Y, Henschel JR. Dispersal of Stegodyphus Dumicola (Araneae, Eresidae): They Do Balloon After All! 2001; (29):114–6.
165. Schoppa W, Hussain F. Genesis of Longitudinal Vortices in Near-Wall Turbulence. Meccanica 1998; 33(5):489–501.
166. Schroeder CM, Teixeira RE, Shaqfeh ESG, Chu S. Characteristic periodic motion of polymers in shear flow. Phys Rev Lett 2005; 95(1):18301.
167. Simonneau M, Courtial C, Pétillon J. Phenological and meteorological determinants of spider ballooning in an agricultural landscape. C R Biol 2016; 339(9-10):408–16.
168. Smith CR, Patterson GK, Zakin JL. A synthesized model of the near-wall behavior in turbulent boundary layers. Rolla, Mo.; 1984. (the 8th Symp. on Turbulence).
169. Smith DJ, Gaffney EA, Blake JR, Kirkman-Brown JC. Human sperm accumulation near surfaces: A simulation study. J. Fluid Mech. 2009; 621:289.
170. Snyder WH, Lumley JL. Some measurements of particle velocity autocorrelation functions in a turbulent flow. J. Fluid Mech. 1971; 48(01):41.
171. Squires KD, Eaton JK. Particle response and turbulence modification in isotropic turbulence. Physics of Fluids A: Fluid Dynamics 1990; 2(7):1191–203.
172. Squires KD, Eaton JK. Preferential concentration of particles by turbulence. Physics of Fluids A: Fluid Dynamics 1991; 3(5):1169–78.

173. Steiner AL, Pressley SN, Botros A, Jones E, Chung SH, Edburg SL. Analysis of coherent structures and atmosphere-canopy coupling strength during the CABINEX field campaign. Atmos. Chem. Phys. 2011; 11(23):11921–36.
174. Stokes GG, editor. Mathematical and Physical Papers. Cambridge: Cambridge University Press; 2009. (Cambridge Library Collection - Mathematics).
175. Stokes GG. On the Effect of the Internal Friction of Fluids on the Motion of Pendulums. In: Stokes GG, editor. Mathematical and Physical Papers. Cambridge: Cambridge University Press; 2009. p. 1–10 (Cambridge Library Collection - Mathematics).
176. Stommel H. Horizontal Diffusion Due to Oceanic Turbulence. J. Marine Res. 1949; 8(3):199–225.
177. Stommel H. Trajectories of small bodies sinking slowly through convection cells. J. Mar. Res. 1949; 8:24–9.
178. Stout JE, Arya SP, Genikhovich EL. The Effect of Nonlinear Drag on the Motion and Settling Velocity of Heavy Particles. J. Atmos. Sci. 1995; 52(22):3836–48.
179. Stull RB. An Introduction to Boundary Layer Meteorology. Dordrecht: Springer; 1988. (Atmospheric Sciences Library; vol 13).
180. Stull RB. Practical meteorology: An algebra-based survey of atmospheric science. Version 1.02b. Vancouver, BC, Canada: University of British Columbia; 2017.
181. Sudo S, Matsui N, Tsuyuki K, Yano T, editors. Morphological Design of Dandelion; 2008.
182. Sun Q, Boyd ID. Flat-plate aerodynamics at very low Reynolds number. J. Fluid Mech. 1999; 502:199–206.
183. Suter RB. Ballooning in spiders: Results of wind tunnel experiments. Ethology Ecology & Evolution 1991; 3(1):13–25.
184. Suter RB. Ballooning: Data from Spiders in Freefall Indicate the Importance of Posture. The Journal of Arachnology 1992; 2(20):107–13.
185. Suter RB. An Aerial Lottery: The Physics of Ballooning in a Chaotic Atmosphere. The Journal of Arachnology 1999; 1(27):281–93.
186. Suzuki T, Sakai Y. Numerical Simulation of Reactive Turbulent Scalar Mixing Layer by Fourier Modes and Lagrangian Molecular Mixing Model. The Proceedings of the Fluids engineering conference 2003; 2003(0):112.
187. Taylor, Geoffrey Ingram and Green, Albert Edward. Mechanism of the production of small eddies from large ones. Proc. R. Soc. Lond. A 1937; 158(895):499–521.
188. Theodorsen T. Mechanism of turbulence. In Proc. Midwestern Conf. Fluid Dyn., Ohio State University, Columbus, Ohio. 1952.
189. Thomas CFG, Brain P, Jepson PC. Aerial activity of linyphiid spiders: modelling dispersal distances from meteorology and behaviour. Journal of Applied Ecology 2003; 40(5):912–27.
190. Tian L, Ahmadi G, Tu J. Mobility of nanofiber, nanorod, and straight-chain nanoparticles in gases. Aerosol Science and Technology 2017; 51(5):587–601.
191. Tolbert WW. Aerial Dispersal Behavior of Two Orb Weaving Spiders. Psyche: A Journal of Entomology 1977; 84(1):13–27.
192. Torkel Weis-Fogh. Quick Estimates of Flight Fitness in Hovering Animals, Including Novel Mechanisms for Lift Production. Journal of Experimental Biology 1973; (59):169–230.
193. Toschi F, Bodenschatz E. Lagrangian Properties of Particles in Turbulence. Annu. Rev. Fluid Mech. 2009; 41(1):375–404.
194. Träumner K, Damian T, Stawiarski C, Wieser A. Turbulent Structures and Coherence in the Atmospheric Surface Layer. Boundary-Layer Meteorol 2015; 154(1):1–25.

195. Turfus C. Stochastic Modelling of Turbulent Dispersion Near Surfaces: University of Cambridge; 1985.
196. Van Wingerden, W.K.R.E., Vugts, H.F. Factors influencing aeronautic behaviour of spiders. Bulletin of the British Arachnological Society 1974; 3(1):6–10.
197. Vassilicos JC, Fung JCH. The self-similar topology of passive interfaces advected by two-dimensional turbulent-like flows. Physics of Fluids 1995; 7(8):1970–98.
198. Verhille G, Bartoli A. 3D conformation of a flexible fiber in a turbulent flow. Exp Fluids 2016; 57(7):74501.
199. Vollrath F. Strength and structure of spiders' silks. Reviews in Molecular Biotechnology 2000; 74(2):67–83.
200. Vugts HF, van Wingerden WKRE. Meteorological Aspects of Aeronautic Behaviour of Spiders. Oikos 1976; 27(3):433.
201. Wang L-P, Maxey MR. Settling velocity and concentration distribution of heavy particles in homogeneous isotropic turbulence. J. Fluid Mech. 1993; 256(-1):27.
202. Wang L-P, Maxey MR. The motion of microbubbles in a forced isotropic and homogeneous turbulence. Appl. Sci. Res. 1993; 51(1-2):291–6.
203. Washburn JO, Washburn L. Active aerial dispersal of minute wingless arthropods: exploitation of boundary-layer velocity gradients. Science 1984; 223(4640):1088–9.
204. Wells MR, Stock DE. The effects of crossing trajectories on the dispersion of particles in a turbulent flow. J. Fluid Mech. 1983; 136(-1):31.
205. Weyman GS. A review of the possible causative factors and significance of ballooning in spiders. Ethology Ecology & Evolution 1993; 5(3):279–91.
206. Wickler W, Seibt U. Aerial dispersal by ballooning in adult Stegodyphus mimosarum. Naturwissenschaften 1986; 73(10):628–9.
207. Willmarth WW, Lu SS. Structure of the Reynolds stress near the wall. J. Fluid Mech. 1972; 55(01):65.
208. Winkler RG. Semiflexible polymers in shear flow. Phys Rev Lett 2006; 97(12):128301.
209. Woolley DM. Motility of spermatozoa at surfaces. Reproduction 2003; 126(2):259–70.
210. Wu TY-T, Brokaw CJ, Brennen C. Swimming and Flying in Nature. Boston, MA: Springer US; 1975.
211. Yamaguchi H, Hanawa T, Yamamoto O, Matsuda Y, Egami Y, Niimi T. Experimental measurement on tangential momentum accommodation coefficient in a single microtube. Microfluid Nanofluid 2011; 11(1):57–64.
212. Yamamoto S, Matsuoka T. A method for dynamic simulation of rigid and flexible fibers in a flow field. The Journal of Chemical Physics 1993; 98(1):644–50.
213. Yip S, editor. Handbook of materials modeling. Dordrecht: Springer; 2005.
214. Yudine MI. Physical Considerations on Heavy-Particle Diffusion. In: Advances in Geophysics Volume 6: Elsevier; 1959. p. 185–91 (Advances in Geophysics).
215. Zhao L, Panayotova LN, Chuang A, Sheldon KS, Bourouiba L, Miller LA. Flying Spiders: Simulating and Modeling the Dynamics of Ballooning. In: Layton AT, Miller LA, editors. Women in Mathematical Biology. Cham: Springer International Publishing; 2017. p. 179–210 (Association for Women in Mathematics Series).
216. Zhao S, Povitsky A. Coupled continuum and molecular model of flow through fibrous filter. Physics of Fluids 2013; 25(11):112002.
217. Zhao X, Wang S, Yin X, Yu J, Ding B. Slip-Effect Functional Air Filter for Efficient Purification of PM2.5. Sci Rep 2016; 6:35472.

218. Zhu W, van Hout R, Katz J. PIV Measurements in the Atmospheric Boundary Layer within and above a Mature Corn Canopy. Part II: Quadrant-Hole Analysis. J. Atmos. Sci. 2007; 64(8):2825–38.

10. Theses

1. Spiders use multiple types of silk from different silk glands and ballooning silks are first identified and quantified. Spiders use the drag line to anchor themselves on a ground object. The spiders produce tens of fine aciniform gland silks in the winds to disperse aerially (the aciniform gland silks are generally used by other species as wrapping silks.

2. A crab spider (18-20 mg) spun 50-60 separated ballooning fibers. Their thickness ranged 121-323 nm with an average of 211.7 nm. Their averaged length of silks was 3.22 m (max 6.2 m). The amount of ballooning silks enables even large spiders, 5-150 mg, can balloon with the help of light upward air current, the vertical wind speeds of 0.1-0.5 m/s.

3. The meaning of a filament-like structure in the organisms, which locomote with it actively or passively, is due to their materially efficient geometry in producing or gaining fluid dynamic forces in the viscous fluid environment. The structure enables that the organisms achieve appropriate fluid dynamic forces investing small amount of protein.

4. Spinning multiple thin fibres produces aerodynamic drag force more efficiently, not only from the structural viewpoint but also from the material viewpoint, than spinning a single and long silk. It's because, first, the short (relative to the length of a equivalent single silk) multiple silks can distribute their aerodynamic loads, while a single long silk should carry the whole aerodynamic drag. Second, multiple thin silks can produce multiple times of a drag force in comparison with a single thick silk which is produced with the same amount of silk dope.

5. The thickness of 100-300 nm may be the lowest boundary of the scale which can produce aerodynamic force by the physical structure. The rarefaction effect of the air increases below the scale of 100 nm. Therefore, the filament structure under 100 nm cannot produce Stoke' drag not anymore.

6. Among the organisms, which utilize hairy structures for their passive flight, spiders are the heaviest animal. Dandelion and thistle seeds also use thin pappus for their aerial dispersal. Among these passive flyers, a spider is the heaviest organism.

7. It is suggested that the ballooning behaviour of spiders may related to the coherent structure in the atmospheric boundary layer. The coherent structure builds the regions of low-speed/upward and high-speed/downward currents. This may be the reason why spiders prefer the condition of low wind speed for their take off.

8. Ballooning number is first introduced to quantify the influence of non-uniform flow on the sedimentation of a filament which has a weight at its end. The number is defined as the ratio of fluid dynamic force (low Reynolds number flow) by non-uniform flow on a filament structure to the gravity force on the weight. This number enables the nondimensional analysis of the ballooning structure in different scales.

9. As the strength of non-uniform flow becomes greater, the ballooning structure shows biased tendency of slow falling compared with its sedimentation in the still condition. One of the main causes of this biased behaviour is cause by anisotropic drag of a filament structure in a fluid flow. Trapping phenomenon of the ballooning structure in a vortex may the second cause of the biased behaviour.

10. Because of the anisotropic character of a filament and its trapping behaviour in a vortex, a filament-like ballooner has better buoyant capability compared with a point-like ballooner.

11. The coherent structure in the atmospheric boundary layer develops always from the ground surface to the upper atmosphere, this asymmetric environment can be also used in the spiders' ballooning.

12. If we account the fact that spiders are the first immigrants on the new-born volcanic island and the adaptability of the flexible filament and the robustness of the passive flight in the turbulence (from the viewpoint of stability and control), the passive flight of a spider can be used by the human for the exploration of the unknown new environment, like the exploration of hazardous weather condition which can be found in a hurricane, typhoon or extraterrestrial atmosphere like the atmosphere in Saturn or Jupiter.

Publications

I

PLOS | BIOLOGY

RESEARCH ARTICLE

An observational study of ballooning in large spiders: Nanoscale multifibers enable large spiders' soaring flight

Moonsung Cho[1,2]*, Peter Neubauer[2], Christoph Fahrenson[3], Ingo Rechenberg[1]

1 Technische Universität Berlin, Institut für Bionik und Evolutionstechnik, Berlin, Germany, **2** Technische Universität Berlin, Institut für Biotechnologie, Berlin, Germany, **3** Technische Universität Berlin, Zentraleinrichtung Elektronenmikroskopie, Berlin, Germany

* m.cho@campus.tu-berlin.de

Check for updates

OPEN ACCESS

Citation: Cho M, Neubauer P, Fahrenson C, Rechenberg I (2018) An observational study of ballooning in large spiders: Nanoscale multifibers enable large spiders' soaring flight. PLoS Biol 16(6): e2004405. https://doi.org/10.1371/journal.pbio.2004405

Academic Editor: Laura Miller, University of North Carolina at Chapel Hill, United States of America

Received: October 3, 2017

Accepted: May 10, 2018

Published: June 14, 2018

Copyright: © 2018 Cho et al. This is an open access article distributed under the terms of the Creative Commons Attribution License, which permits unrestricted use, distribution, and reproduction in any medium, provided the original author and source are credited.

Data Availability Statement: All relevant data are within the paper and its Supporting Information files.

Funding: Elsa-Neumann-Scholarship http://www.fu-berlin.de/sites/promovieren/drs/nachwuchs/nachwuchs/nafoeg.html (grant number T61004). The funder had no role in study design, data collection and analysis, decision to publish, or preparation of the manuscript.

Competing interests: The authors have declared that no competing interests exist.

Abstract

The physical mechanism of aerial dispersal of spiders, "ballooning behavior," is still unclear because of the lack of serious scientific observations and experiments. Therefore, as a first step in clarifying the phenomenon, we studied the ballooning behavior of relatively large spiders (heavier than 5 mg) in nature. Additional wind tunnel tests to identify ballooning silks were implemented in the laboratory. From our observation, it seems obvious that spiders actively evaluate the condition of the wind with their front leg (leg I) and wait for the preferable wind condition for their ballooning takeoff. In the wind tunnel tests, as-yet-unknown physical properties of ballooning fibers (length, thickness, and number of fibers) were identified. Large spiders, 16–20 mg *Xysticus* spp., spun 50–60 nanoscale fibers, with a diameter of 121–323 nm. The length of these threads was 3.22 ± 1.31 m ($N = 22$). These physical properties of ballooning fibers can explain the ballooning of large spiders with relatively light updrafts, 0.1–0.5 m s^{-1}, which exist in a light breeze of 1.5–3.3 m s^{-1}. Additionally, in line with previous research on turbulence in atmospheric boundary layers and from our wind measurements, it is hypothesized that spiders use the ascending air current for their aerial dispersal, the "ejection" regime, which is induced by hairpin vortices in the atmospheric boundary layer turbulence. This regime is highly correlated with lower wind speeds. This coincides well with the fact that spiders usually balloon when the wind speed is lower than 3 m s^{-1}.

Author summary

Aerial dispersal of spiders, which is known as "ballooning," enables spiders' wide range of dissemination—sometimes transoceanic. However, little is known about the ballooning mechanism of spiders, due to the difficulty of observing the ballooning silks and little awareness of spiders' ballooning flight itself. From our observations in the field and in the laboratory using a wind tunnel, we have characterized the heretofore unknown physical properties of spiders' ballooning silks. These quantitative values can explain large spiders' ballooning behaviors. Crab spiders use tens of nanoscale fibers for their aerial dispersal. In

the air current, these nanoscale fibers are governed by low Reynolds number fluid dynamics, which means that the viscous force of the air is much more dominant than the inertial force of the air. Using this nano/microscale fluid dynamics, spiders can become airborne with a light updraft. From our wind measurements, we suggest that spiders use the organized updraft current in the turbulent wind. This may explain why spiders show the ballooning behavior at a low wind speed, as the updraft frequently exists in the low-speed regime of the fluctuating wind flows. This work represents the most rigorous investigation of spider ballooning to date and will inspire future research on the subject.

Introduction

Some spiders from different families, such as Linyphiidae (sheet-weaver spiders), Araneidae (orb-weaving spiders), Lycosidae (wolf spiders), and Thomisidae (crab spiders), can disperse aerially with the help of their silks, which is usually called ballooning behavior [1–6]. There are 2 representative takeoff methods in ballooning flight: "tiptoe" and "rafting" [7–10]. If spiders perceive appropriate weather conditions for ballooning, they climb up to the highest position of a blade of grass or a branch of a tree and raise their abdomen as if standing on their tiptoes, in order to position the abdomen at the highest level, before spinning the ballooning lines. They release a single or a number of silks in the wind current and wait until a sufficient updraft draws their body up in the air. This is known as a "tiptoe" takeoff [9,10] (see S1 and S2 Figs). Another takeoff method is called "rafting," in which spiders release the ballooning lines from a hanging position, relying on their drag line [7,8,10] (see S3 Fig). In these ways, some spiders can travel passively hundreds of kilometers and can reach as high as 4.5 km above sea level [11,12]. For example, one of the first immigrant species on new-born volcanic islands are known to be spiders [13–15]. Aerial dispersal of spiders is an influential factor on agricultural economy and ecology because spiders are highly ranked predators in arthropods and impact on a prey's population [16]. Due to the spider's incredible aerial dispersal ability, the physical mechanism of a spider's flight has been questioned for a long time, not only in public media but also in scientific research [16–23].

Ballooning dispersal is efficiently used by spiderlings (young spiders, just a few days after eclosion from their eggs) to avoid cannibalism at their birth sites, which are densely populated by hundreds of young spiders, and to reduce competition for resources [23,24]. Some adult female spiders balloon to find a place for a new colony [4,25,26], and others balloon to search for food and mates [4,27]. Most of the ballooning spiders were spiderlings and spiders under 3 mm in length and 0.2–2 mg in mass [1–5,28,29]. Nevertheless, there are only a few reports on the ballooning of large spiders (over 3 mm in length, over 5 mg in mass) [4,5,25,26].

Spiders balloon most frequently during late spring and autumn seasons [2,4,30]. The influences of microclimates on ballooning—such as temperature, humidity, and wind conditions—have been extensively studied: (i) Many studies agree on a positive correlation of temperature [1,3,31] or a rapid increase in temperature [31–34]; (ii) low humidity is favorable for spiders to balloon [1,32,34]; (iii) for small spiders, 0.2–2 mm in length, the favorable mean wind speed is limited to 3 m s^{-1} at a level of 2 m [30,31,35]. The local favorable wind speeds were 0.35–1.7 m s^{-1} in experiments and 0.55–0.75 m s^{-1} in nature [1,3]. These values, however, differ for spiders of different sizes (between 0.78–1.21 mm) [1,36]. Recently, Lee and colleagues showed that not only the mean wind speed at a level of 2 m but also the local wind speed can be limited by a wind speed of 3 m s^{-1} for spiderlings [37]. Instability of atmosphere was pointed out as an

influential factor [30,31,35]. Suter and Reynolds suggested a possible relation of spiders' ballooning behavior with atmospheric turbulent flow [16,20].

There have been a number of models that have tried to explain spiders' high buoyant capability (aerial dispersal capability): a fluid-dynamic lollipop model [17], a flexible filament model in turbulence [16], and an electrostatic flight model [22]. Recently, Zhao and colleagues implemented the 2-dimensional numerical simulation using an immersed boundary method, which can simulate the ballooning dynamics in more detail [38]. The result shows that the atmospheric instability enables longer suspension of a ballooner in the air, which agrees with the result of Reynolds's simulation and suggests that a spider may sense the vibration of vortex shedding on the spider silk through their silk [16,38], which is an interesting hypothesis.

In spite of the abovementioned models and studies, dynamics in spiders ballooning are still not well understood, because of a lack of serious scientific observation studies and specific experiments. Many of the ballooning spiders are very small, with weights of 0.2–2 mg, which are difficult to study [1,3,36,37]. Many described experiments were not focusing on the spider's ballooning behavior itself but assumed that spiders use a certain length of the drag line [18,19,21]. The ballooning of large spiders is also a struggle because (i) the observed physical properties of ballooning silks and spider size (60–80 cm long and 3–4 silk threads, 85–150 mg body weight) of an adult of *Stegodyphus mimosarum* seemed to be unrealistic for ballooning [25], because the required vertical speed of wind was 9.2–21.6 m s^{-1}, according to Henschel's calculation [18,39]; (ii) Humphrey's model cannot explain the ballooning flight of spiders with a weight of over 9 mg, because of the mechanical properties of a spider silk [17]. The following questions are still to be answered: (i) How many and how long are the silk fibers needed for ballooning, especially in the case of large spiders with weights over 5 mg? (ii) Which silk fibers and glands are used for ballooning? (iii) How do ballooning silks shape during the flight? (iv) Do spiders control the buoyant capability by changing the length of silks or their pose during the flight? (v) Why do spiders usually balloon at a low wind speed (below 3 m s^{-1})?

The aim of this paper is to offer behavioral clues and quantitative data in ballooning flight that may answer these questions. Therefore, we investigated the ballooning behavior of adult and subadult crab spiders (*Xysticus* spp., Thomisidae) that had a size of 3–6 mm and a weight of 6–25 mg. This observation of large spiders could provide a good basis for the physical characterization of ballooning. Additional experiments were performed in a wind tunnel for a precise documentation of ballooning silks and to analyze the details of ballooning behavior. Also, the aerodynamic environment on a flat grass field was measured to investigate the usable updraft for a ballooning flight.

Materials and methods

Ethics statement

The species used in the experiments (*Xysticus* genus) are not endangered or protected species. No specific permissions were required. All applicable international, national, and institutional guidelines for the care and use of animals were followed. No permission was required to collect insects from the collection site, the Lilienthal Park and the Teltow Canal. These sites are within the province of Steglitz-Zehlendorf.

Animal care

The collected adult and subadult crab spiders (*Xysticus* genus) were raised separately in a plastic box (length × width × height: 13 × 13 × 7 cm), which has ventilation holes. Once a week, the spiders were fed a mealworm, *Tenebrio molitor*, and moisture was provided with a water spray.

Field observations

Crab spiders *(Xysticus cristatus*, *X. audax*, etc.) were collected at Lilienthal Park and along the Teltow Canal in the Berlin area, Germany, and observed each autumn, especially during October, from 2014 to 2016. Lilienthal Park was selected for the observation of preballooning behavior because the ballooning phenomenon of adult and subadult crab spiders is frequently observed in this region.

Takeoff. On sunny and partly cloudy days in autumn, 14 crab spiders (8 females, 2 males, and 4 not identified; adult or subadults) were collected at Lilienthal Park. These spiders were released in the same place on a self-built artificial mushroom-like platform (a 5.5 cm diameter half sphere, 1.2 m above a ground surface, gypsum material). This platform was intended to stimulate tiptoe preballooning behavior. Because of its convex surface (half sphere), spiders can easily recognize that the top of the convex surface is the highest position that may promote tiptoe behavior. The white color of this platform allowed the visual clarity of the spider's behavior. During the observation, the ballooning behaviors were recorded by digital camera. Additionally, titanium tetrachloride was used for the flow visualization of the wind. The local wind speed and temperature were not measured directly, but the values from the Dahlem weather station (4.5 km distance from the observation site, the anemometer is installed 36 m above the ground in the 20 m-high forest canopy) may provide approximate conditions.

Statistical analysis of preballooning behaviors. The 14 crab spiders were set a total of 27 times onto the mushroom-shaped platform in natural weather. The detailed preballooning behaviors in "takeoff" observation were analyzed statistically: (i) active sensing motion, (ii) tiptoe motion, (iii) tiptoe takeoff, (iv) drop down, and (v) rafting takeoff (see "Takeoff" in the Results section). If they did not tend to balloon or hid for about 5 min, they were recollected. Once a spider raised 1 or both front legs (leg I) and then put them back again on the platform, this was considered to be an active sensing motion and was counted as 1 behavior. Tiptoe motion, raising the abdomen and putting it down again, was also counted as 1 motion. The transitions between behaviors were also counted. These numbers were first expressed as percentage frequency by normalizing with the total number of transitions (see Eq [1], $f_{i,j}$ is a normalized frequency of the transition from i-th to j-th behavior. $n_{i,j}$ is the number of the transition from i-th to j-th. m is the number of categorized behaviors). The probability from one behavior to next behavior is expressed by normalizing with the total number of previous behaviors (see Eq [2], $p_{i,j}$ is the probability of the transition from i-th to j-th behavior).

$$f_{i,j} = \frac{n_{i,j}}{\sum_{i=1}^{m}\sum_{j=1}^{m} n_{i,j}}, \ \sum_{i=1}^{m}\sum_{j=1}^{m} f_{i,j} = 1 \tag{1}$$

$$p_{i,j} = \frac{n_{i,j}}{\sum_{j=1}^{m} n_{i,j}}, \ \sum_{j=1}^{m} p_{i,j} = 1, \text{ where } i = 1, 2, \ldots, m \tag{2}$$

Gliding. Gliding of crab spiders was observed in the autumn along the Teltow Canal because of the ecological and topographical benefits for the observation of ballooners: (i) crab spiders frequently glide along the canal during the autumn; (ii) the angle of the sun's rays in the morning was appropriate for the detection of the ballooning silks during their flight; (iii) the dense trees on the opposite side of the canal provide a dark background, which facilitates the observation of floating silks. The shape of the threads during flight could not be photographed nor recorded as a video because only limited parts of the ballooning threads were

reflected by the sun's rays. However, the movement and shape of the threads could be recognized with the naked eye, and these shapes were quickly sketched by hand.

Identification of ballooning lines

Sampling of ballooning lines. Twelve crab spiders (9 females and 3 males, adult or subadult) were used for the wind tunnel experiment. Preballooning behavior of these spiders was induced in front of an open jet wind tunnel in which the diameter of the nozzle exit is 0.6 m (see Fig 1A). The spinning behaviors that led to the ballooning silks was observed precisely. There were no obstacles next to the wind tunnel, leaving about 9 m of free space from the nozzle to allow ballooning fibers to float horizontally without any adhesion to other objects. The wind speed and temperature were measured with a PL-135 HAN hot-wire anemometer. To

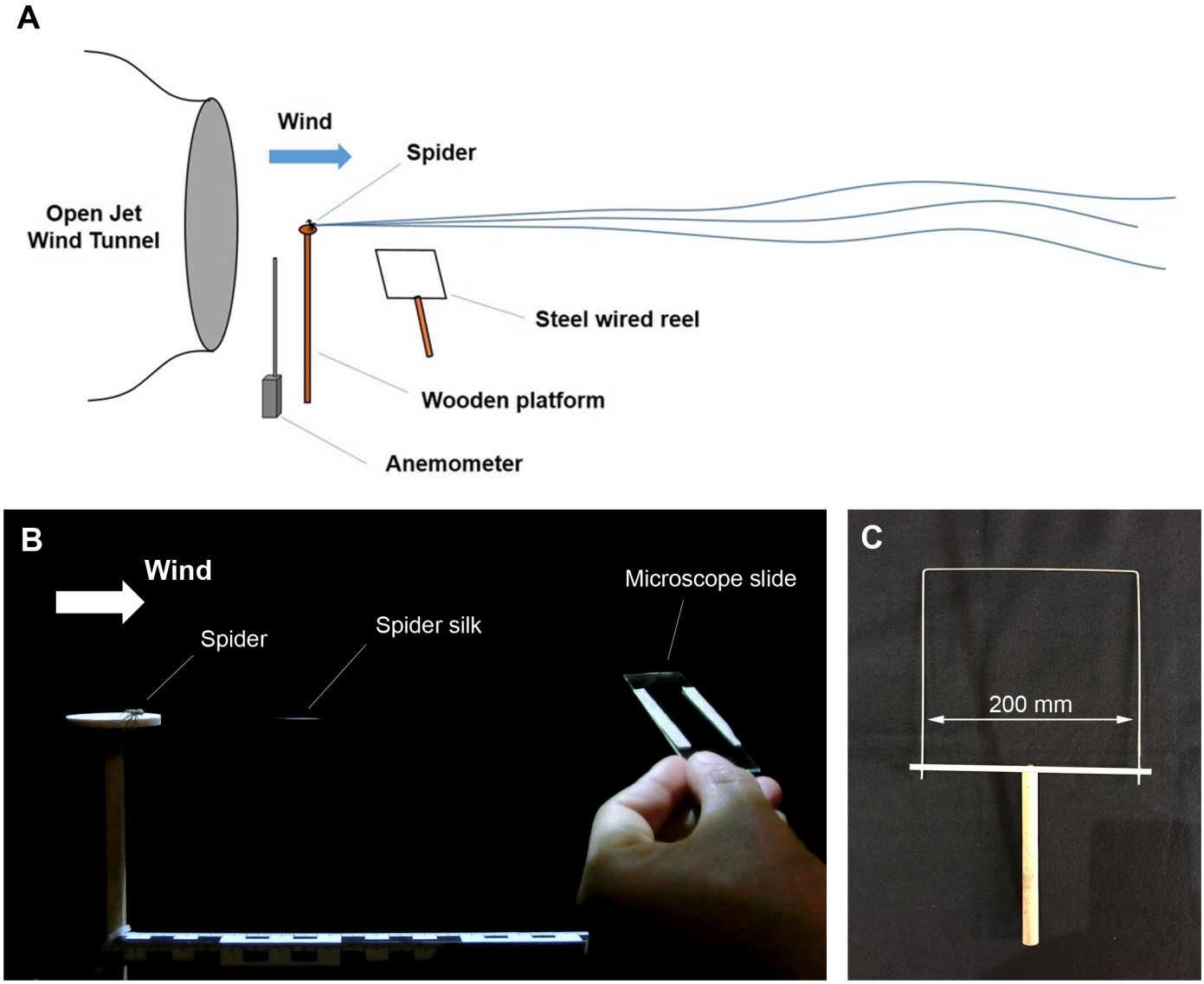

Fig 1. Experimental materials and methods for identification of ballooning lines. (A) A schematic view of wind tunnel tests. (B) Sampling of ballooning fibers in front of an open jet wind tunnel. (C) Reel with a steel wire to measure the length of ballooning silks.

https://doi.org/10.1371/journal.pbio.2004405.g001

enable sampling of the ballooning fibers, the wind speed was adjusted at 0.9 m s^{-1}, because spiders drifted downstream if the wind speed was above 1 m s^{-1}. The room temperature was 22–25 ˚C. The ballooning behavior was stimulated with a 1,000-watt hair dryer (low-wind-speed mode) that produces warm air (30–35 ˚C) and the fluctuation of wind. The hair dryer was positioned beneath the nozzle of the wind tunnel upward to avoid direct exposure to hot wind from the hair dryer (see S4 Fig). As soon as spiders showed tiptoe behavior, the hair dryer was turned off. The turbulent intensity of the wind tunnel was 1.1% (without the hair dryer) and 11.3% (when the hair dryer turned on). There was difference in temperature between the laboratory and the field. The difference can be explained as follows: first, the ballooning behavior is coupled not only with weather condition but also with biological condition, e.g., seasonal dispersal, mating, insufficient resources, etc. [2,4,26,30]. If the biological pressure for spiders to disperse is high, spiders may try to disperse even though it is low temperature. Second, the sudden increase of temperature acts on ballooning behavior as an influential factor [31–35]. If there is the sudden increase of temperature—e.g., because of sunshine in the morning—the ballooning behavior can be triggered even in low-temperature conditions. There are some reports that spiders ballooned also at relatively low temperatures, 10–20 ˚C [33,34; the author's field observation (13–19 ˚C)].

Ballooning fibers were collected on a microscope slide on which 2 narrow strips of a double-sided bonding tape were attached. The ballooning fibers were sampled near the spinnerets (see Fig 1B). A total of 11 samples were prepared from 28 spinning events of ballooning silks. In the experiment, a total of 4 spiders responded to show ballooning behavior—two of them were very active. Two samples were selected, because the other samples failed to capture all the ballooning fibers on a single microscope slide or because the fibers on the slides were deranged during the capturing process. Simultaneously, silk fibers were captured on a square wire frame and carefully wound around it in order to measure the length of ballooning threads (see Fig 1C). The length of the silks was calculated by multiplying the total number of half revolutions by the width of the square wire frame (20 cm). The successfully sampled ballooning fibers were later studied with a field emission scanning electron microscope (FESEM).

FESEM. The sampled ballooning fibers were coated with gold using a sputter coater (SCD 030, Balzers Union) and observed with a FESEM (DSM 982 Gemini, ZEISS, with 5–10 kV accelerating voltage). The number of ballooning fibers was carefully counted, and the thickness of fibers was measured. The spinnerets of a female *X. cristatus* were also observed with the FESEM. For sample preparation, the female spider was fixed in 2.5% glutaraldehyde and dehydrated in ascending concentrations of ethyl alcohol from 30% to 100% (10 min at each concentration). After dehydration, the sample was dried with a critical point dryer (CPD 030, BAL-TEC). The prepared sample was coated with gold using a sputter coater (SCD 030, Balzers Union) and observed with the FESEM (SU8030, Hitachi, with 20 kV accelerating voltage).

Investigation of the aerodynamic environment

For the investigation of the turbulent atmospheric boundary layer, ultrasonic 3-dimensional wind speed measurement took place on a grass field (53˚ 11′ 42″ N, 12˚ 09′ 40″ E, see Fig 2A and 2B). This place is also a habitat of the *Erigone* and *Xysticus* genus, which do ballooning behavior. To avoid mechanically induced updrafts by hills, trees, and rocks, a flat grass field was selected. The 3-dimensional wind speed data at 2 different mean wind speeds (1.99 m s^{-1} and 3.07 m s^{-1}) were measured on a sunny day in the autumn for 5 min with the sampling frequency of 20 Hz. In order to eliminate small-scale fluctuation in the turbulent boundary layer, a quadrant analysis was introduced [40–44] (see Eq [3]; u and w are, respectively, horizontal and vertical wind speeds. u' and w' represent, respectively, streamwise fluctuating velocity and

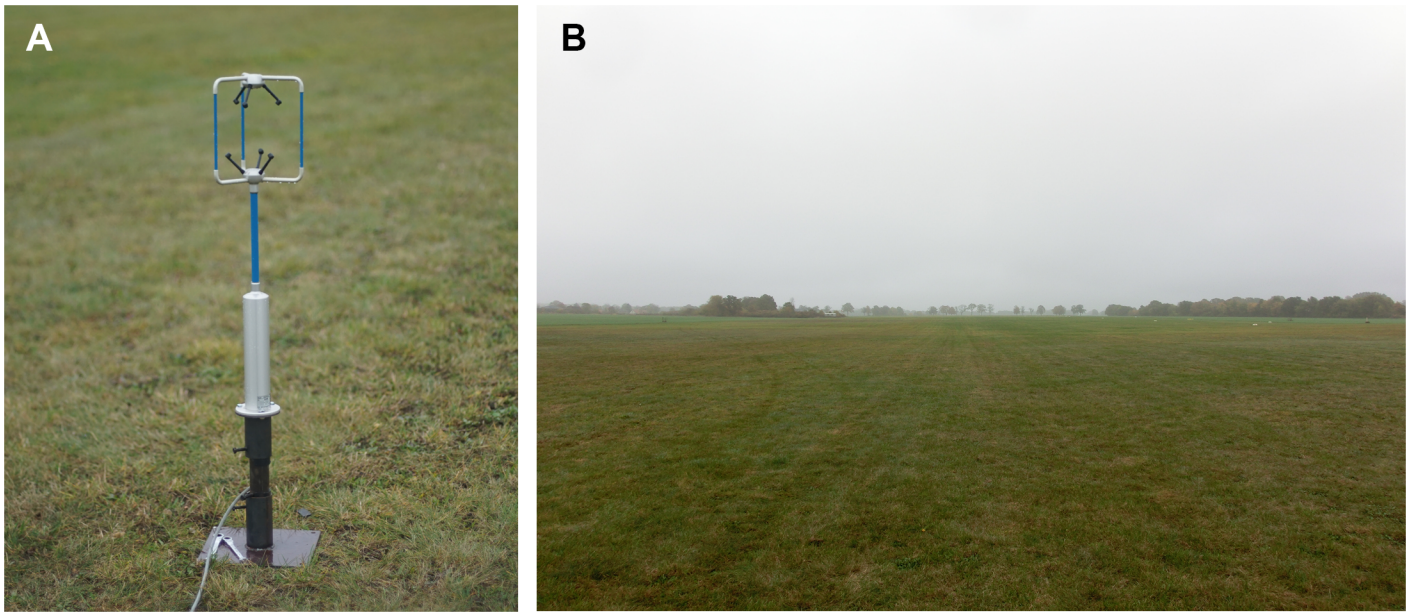

Fig 2. Experimental material and place for 3-dimensional wind velocity measurement. (A) A 3-dimensional ultrasonic anemometer (Windmaster 1590-PK-020, Gill Instruments) is installed 0.95 m above the ground. (B) The simplest conditions (i.e., a flat surface) were selected. The flat place is covered with the 6 cm short cut grass. Within a radius of 300 m, there is no obstacle object.

https://doi.org/10.1371/journal.pbio.2004405.g002

vertical fluctuating velocity. Those are equal to the subtracted values of the actual values of velocity minus the mean values of the velocity. H is the threshold parameter, which means the size of a hole. u'_{rms} and w'_{rms} indicate root mean squared fluctuation velocities).

$$u'w' \geq H(u'_{rms}w'_{rms}) \tag{3}$$

Results

Field observations

Takeoff. In the Thomisidae family, not only female but also male adult spiders showed ballooning behaviors (see S1 Fig). During the observation days, the temperature was 16–19 ˚C, and the mean wind speed was 6–7 m s^{-1} (gust 14–17 m s^{-1}), as reported by the nearest weather station in Dahlem. The sensor was installed on 36 m position above the ground. Therefore, the local wind speed at 1.2 m above the ground must be much lower than these values. Later, we checked the wind speed on a similar day, on which the mean wind speed from the weather station showed 6–7 m s^{-1}. The mean wind speed for 10 min showed 2.11 m s^{-1}.

On the experiment day, the spiders mostly showed tiptoe behavior. At the first stage of tiptoe behavior, the crab spider evaluated the wind condition not just passively through the sensory hairs on its legs but rather actively by raising 1 of its front legs (leg I), or sometimes both, and waited in this position for 5–8 s (see Fig 3A, 3B and 3C and S1 Video). This sensing behavior was often repeated a few times before the tiptoe pose. After each sensing step, the crab spider rotated its body in the direction of the wind (see Fig 3C and 3D).

If the spider decided that the wind was adequate to balloon, it raised its abdomen (already known as a tiptoe behavior, see Fig 3D) and spun its ballooning silks without any help from its legs. Before spinning ballooning silks, there was a motion of a rear leg (leg IV) (see S5 Fig), with which the spider holds its safety line that connected its spinnerets to the substrate and then puts it on the substrate (see S2A and S2B Fig and S2 Video).

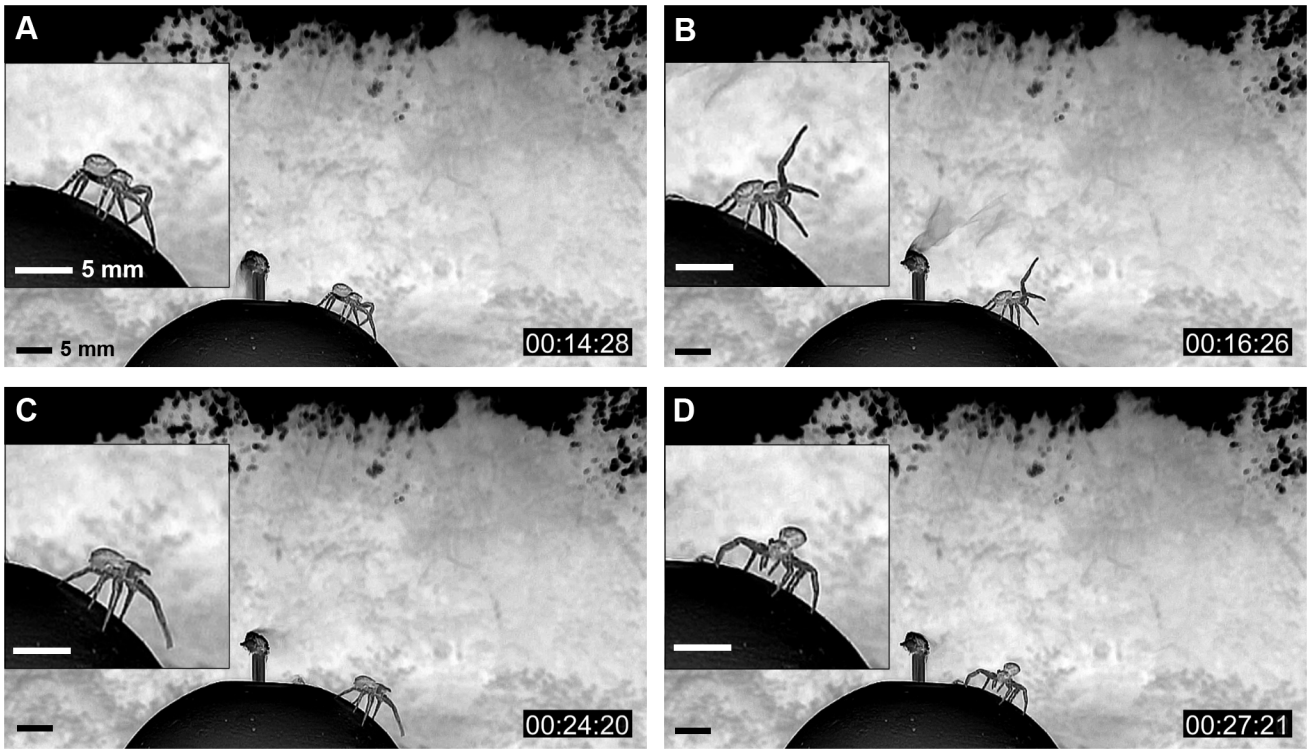

Fig 3. Sequence of active sensing motion with front leg (leg I) (negative images). (A) The spider first senses the condition of the wind current only through sensory hairs on its legs. (B) Then, if the condition seemed appropriate, the spider sensed more actively by raising leg I and keeping this pose for 8 sec. (C) If the spider decided to balloon, it altered its posture. (D) The spider rotated its body in the direction of the wind and assumed tiptoe posture.

https://doi.org/10.1371/journal.pbio.2004405.g003

The crab spider first spun a single or a few fibers and then many fibers (see Fig 4A–4G). The spun ballooning fibers were approximately 2–4 m long and formed a triangular sheet, which fluttered among the turbulent flows of the wind. The vertex angle of this triangular sheet was about 5–35˚ (see Fig 4C–4G). If the wind condition was not appropriate, the spider cut the silk fibers and spun them again. If the ballooning silks generated enough drag, the spider released the substrate and became airborne (see Fig 4H). From careful video investigation, it was observed that spiders stretched all their legs outward as soon as the spiders achieved takeoff. Many ballooned crab spiders soared diagonally upward along the wind flows. These paths had 5–20˚ inclination above the horizon. Some spiders traveled quasi-horizontally. Some spiders soared along a steep path (about 45˚). During this steep takeoff, the spiders took off with relatively slow speed. The anchored drag line (safety line) between the platform and the spider's spinneret could be seen. This anchored line endured without breaking until it became 3–5 m long. After a while, it was broken mechanically. From the wind tunnel experiment, it was found that the anchored line consists of 2 fibers.

Three new facts about ballooning were uncovered. First, the crab spider does not evaluate the wind condition passively, but actively by raising 1 of its legs I. Second, this adult ballooner anchors its drag lines on the platform not only during its rafting takeoff but also during tiptoe takeoff. Third, the crab spider postures all its legs outward and stretched, when airborne, not only at the takeoff moment but also during the gliding phase (see S6A–S6D Fig).

Rafting preballooning behavior was also observed. The local weather condition was a little bit colder and windier than that of the previous observation day of tiptoe takeoff. Crab spiders

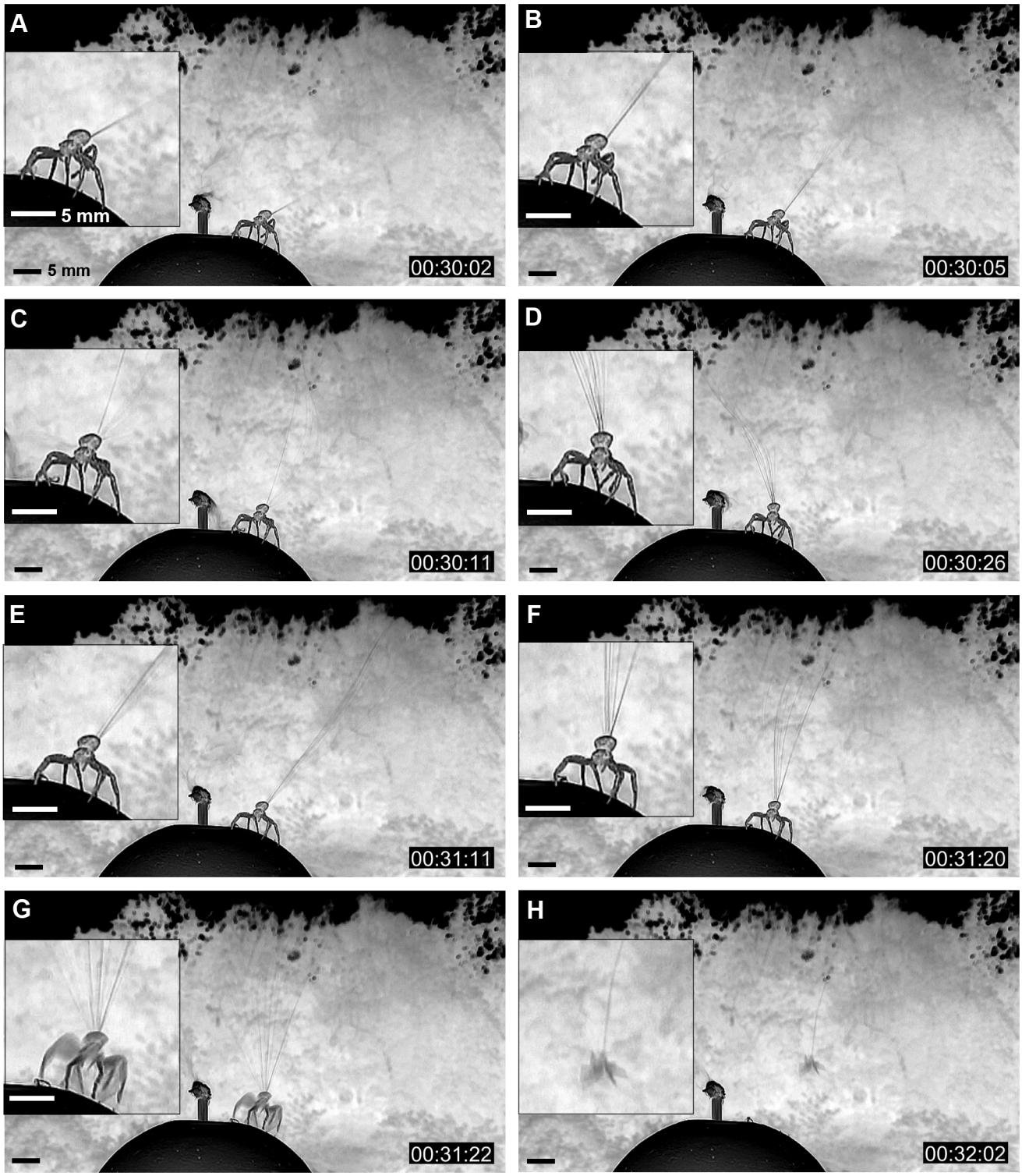

Fig 4. A crab spider's ballooning process (images were converted to negative images to visualize ballooning lines). (A, B) Initial phase of spinning ballooning lines; (C, D, E, F) Fluttering of a bundle of ballooning lines. Because of turbulent flows in wind, the ballooning threads fluttered unsteadily. (G) Takeoff moment. (H) Airborne state of a ballooning spider. (Original video: see S3 Video).

https://doi.org/10.1371/journal.pbio.2004405.g004

were not active on that day. As soon as they were set on the platform, they showed 1 of 2 behaviors. Either they hid on the opposite side of the platform to avoid the wind, or they quickly retreated downward about 0.4–1.1 m, relying on their drag lines (see S3A and S3B Fig), and spun their ballooning fibers downstream of the wind. At this time, spiders spun a single or a few fibers first and then many fibers, as they showed during the tiptoe takeoff (see S3C and S3D Fig). During this process, the spiders also postured all their front legs and second legs outward and backward so that they hung and directed their bellies in an upward direction of the wind. The backward (downstream)-spun threads slowly curved upward, and the spiders' bodies also slowly moved upward (see S3D Fig). At some point, when the threads had generated enough drag and lift, the drag lines near the spinnerets were cut, and the spider finally ballooned (see S3E and S3F Fig).

Statistical analysis of preballooning behaviors. The spiders showed 68 active sensing motions with leg I. Forty-two tiptoe preballooning motions could be observed. Six spiders had ballooned successfully after their tiptoe pose. They also dropped down 8 times, relying on their drag line. Three of them showed a rafting takeoff (see Table 1).

The initial behaviors were mostly started with sensing motion. The frequent transitions occurred between sensing motion and tiptoe motion (see Fig 5A). Spiders flew from only either the tiptoe pose or the dropping and hanging pose (see Fig 5B). The probability of the ballooning takeoff from tiptoe behavior was 9.8%. The probability of the ballooning takeoff from the rafting pose was 37.5%.

The duration of each tiptoe behavior was measured, and their frequencies were analyzed. Short-period tiptoe poses, which lasted for less than 5 s, were the most frequent. The longest tiptoe event lasted 65 s. The observed successful ballooning takeoffs were not biased in relation to tiptoe duration (see Fig 6).

Gliding. A total of 32 floating threads were observed at the Teltow Canal. Most of them were horizontally transported along the channel at about 1–8 m above the water surface. They drifted passively due to light wind but rarely fell down. Some of their silks were inclined downstream. The others were inclined upstream. Two of 32 floating threads were just threads alone without a spider. The number of observed threads was 1–5. However, as not all threads were visible with the naked eye, some may have been the multiple threads that stuck together, although they seemed to be a single thread. Some of them may not have been seen because of their inappropriate angles and positions in relation to the sun. Most of the spiders were positioned at the lower end of their threads. Although the threads showed different numbers and shapes, they were usually laid diagonally (see Fig 7).

Table 1. Ballooning behaviors on the artificial platform.

Date (2015)	Temp. (˚C)	Wind (mean /gust) (m s^{-1})	Number of specimens	Number of tests	Sensing motion	Tiptoeing		Rafting		Total ballooned spiders	Escape (fall down)
						Tried	Ballooned	Drop & climb	Ballooned		
9.24 (13:00–14:30)	19	6/17	7	14	48	30	4	1	0	4	3
9.26 (13:00–15:30)	16 ± 1	7/14	5	11	20	12	2	5	1	3	2
9.28 (12:00–12:30)	16	6/16	2	2	0	0	0	2	2	2	0
Total			14	27	68	42	6	8	3	9	5

https://doi.org/10.1371/journal.pbio.2004405.t001

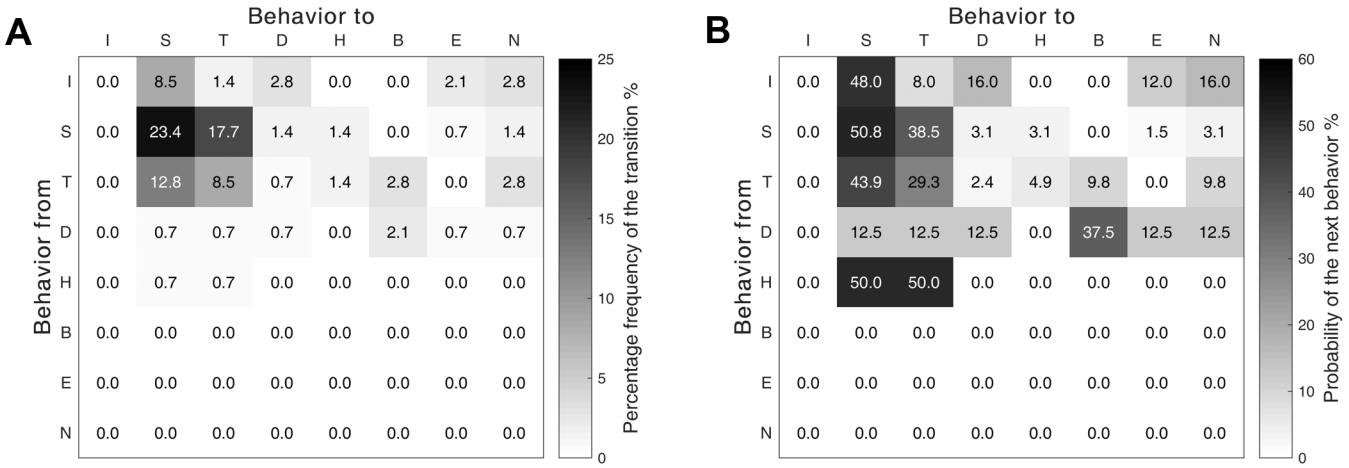

Fig 5. Sequential relations between behaviors for ballooning. (A) The percentage frequency of the behavior transition (the total number of transitions: $N = 141$). (B) The transition matrix between behaviors (the total numbers of categorized behaviors: $N_I = 25$, $N_S = 65$, $N_T = 41$, $N_D = 8$, $N_H = 2$). The corresponding underlying data can be found in S1 Data. B, takeoff; D, dropping and hanging behavior; E, escape; H, hiding motion; I, initial state; N, not flown; S, sensing motion; T, tiptoe behavior.

https://doi.org/10.1371/journal.pbio.2004405.g005

Identification of ballooning fibers

The separation of glands for a drag line and ballooning lines was observed in ballooning behaviors in the laboratory. The anchored drag line was connected to the anterior spinnerets, and ballooning fibers were spun from either 1 or both posterior and/or median spinnerets (see S5A and S5B Fig). The lengths of the ballooning fibers were measured, 3.22 ± 1.31 m ($N = 22$),

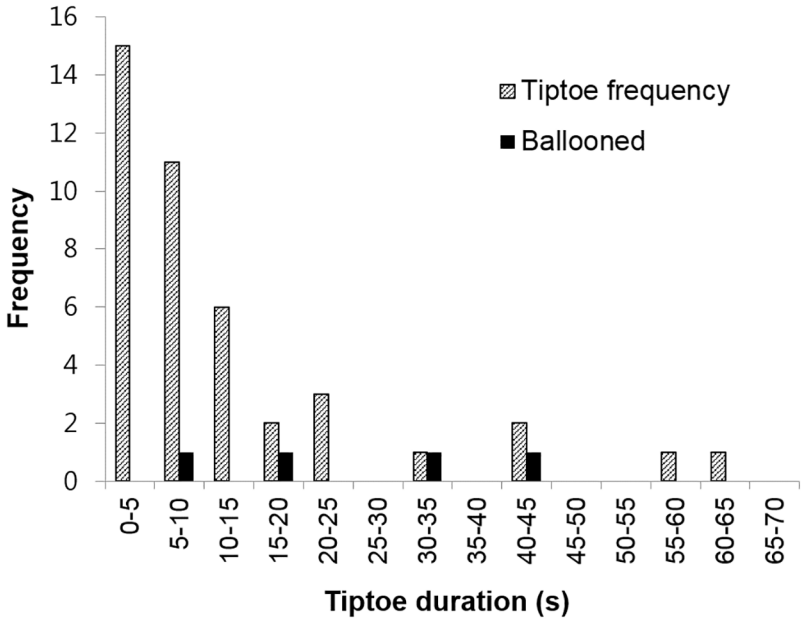

Fig 6. Frequency diagram of tiptoe behaviors according to tiptoe duration ($N = 42$). Black columns are the tiptoe behaviors that were connected to the successful ballooning takeoffs ($N = 4$). The corresponding underlying data can be found in S1 Data.

https://doi.org/10.1371/journal.pbio.2004405.g006

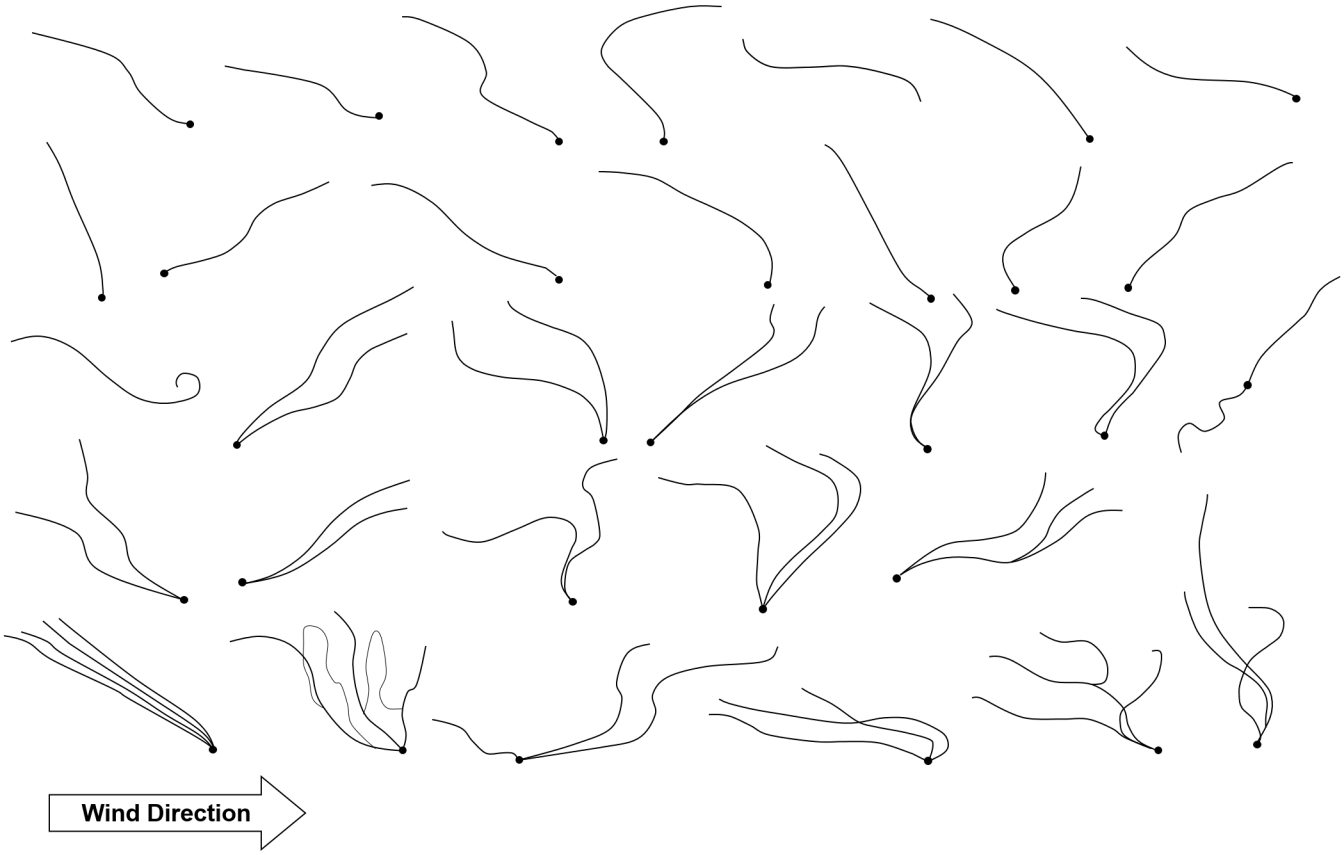

Fig 7. Sketches of ballooning structures (body + ballooning threads). These structures were observed above the water surface, at heights of 1–8 m. Wind was blowing from left to right. Therefore, these structures were transported in the same direction as the wind. Black, thick points represent the spider's body. Black lines represent ballooning threads.

https://doi.org/10.1371/journal.pbio.2004405.g007

from 22 spinning events of 2 crab spiders (16.4 and 18 mg) (see Fig 8). The maximum length of the spun ballooning lines was 6.2 m.

The successfully collected ballooning fibers of both *X. cristatus* and *Xysticus* spp. were observed with the FESEM. Ballooning fibers consisted of 2 thick nanoscale fibers that were attached together (see Fig 9B and 9C) and many thin nanoscale fibers (see Fig 9A–9D). The 2 adult spiders, *Xysticus* species, spun 48–58 thin nanofibers and 2 thick nanofibers. The thickness of the thin nanofibers ranged from 121 to 323 nm, with an average of 211.7 ± 45.2 nm ($N = 40$). The thickness of the thick nanofibers was 698–768 nm, with an average of 722.2 ± 32.5 nm ($N = 4$) (see Table 2). The spun fibers were split independently (see Fig 9A–9D).

On the other hand, drag lines consist of 1 pair of fibers (see Fig 9E) (sometimes 2 pairs, from left and right, see Fig 9F), which were spun from the major ampullate glands on the anterior spinnerets. The thickness of these major ampullate silks was about 500 to 800 nm (see Fig 9E and 9F).

Aerodynamic environment on the short-grass field

Two data sets at the different mean wind speeds (1.99 m s^{-1} and 3.07 m s^{-1}) for 5 min were collected. Usable updrafts were investigated in the turbulent atmospheric boundary layer. Each of the cases showed the vertical deviation of ±0.225 m s^{-1} and ±0.267 m s^{-1}, respectively, which

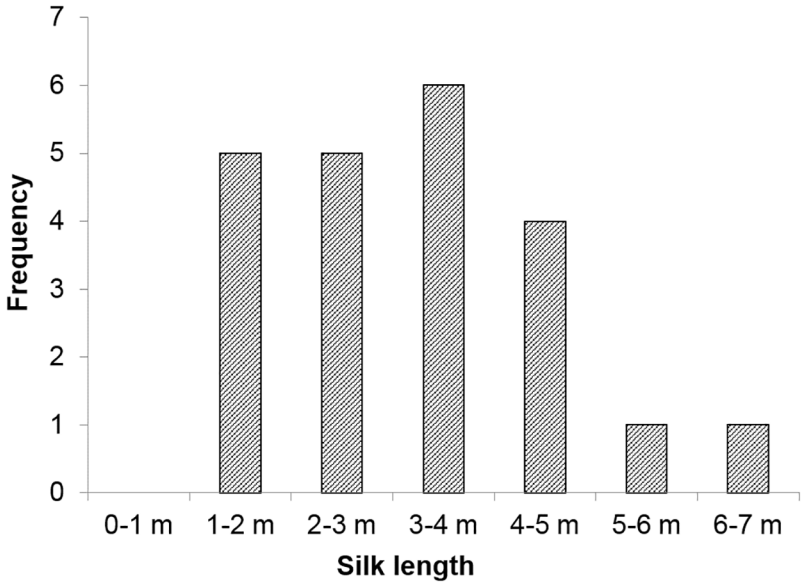

Fig 8. Distribution of the length of ballooning lines (*N* = 22). The corresponding underlying data can be found in S2 Data.

https://doi.org/10.1371/journal.pbio.2004405.g008

ranged from −0.5 to 0.5 m s^{-1} and from −0.6 to 0.7 m s^{-1} (see Fig 10A and 10B). The turbulent intensities were 21% and 23.7% in the mean wind speeds of 1.99 m s^{-1} and 3.07 m s^{-1}, respectively. The vertical wind speed of both cases is negatively correlated to the horizontal wind speed. The slopes of regression fits are −0.235 (r = −0.575r) and −0.077 (r = −0.259), respectively. The horizontal wind speeds of both Q2s are positioned below the wind speed of 3 m s^{-1}.

Discussion

From our observation, the physical properties of ballooning silks were identified together with previously undescribed behaviors during ballooning: (i) an active sensing motion of the wind, (ii) an anchoring behavior during tiptoe takeoff, (iii) a tidying-up motion of an anchor line (drag line, safety line), and (iv) an outward stretching pose during a flight. These findings provide some clues and answers that were previously unsolved in spiders' ballooning flight. The measured wind data also provide the possible mechanism from the viewpoint of the environment. We interpret as follows.

Spider's active sensing motion of the wind condition

Crab spiders showed a motion that seemed like actively evaluating the meteorological condition before their takeoff. Normally, ballooning behavior is first triggered either by a warm ambient temperature or by a rapid increase in ambient temperature [31,36]. Additionally, if they are exposed to a wind that is slower than 3 m s^{-1} (favorable in 0.35–1.7 m s^{-1} wind speed for spiderlings), they show tiptoe behavior [1,3,36,37]. Until now, it had been thought that spiders sense the wind speed passively through the sensory hair (trichobothria) on their legs [17,31,45]. However, the present observations show that spiders may sense the aerodynamic condition of wind not just passively but rather actively, raising leg I high and shaking it. Strong interactive behavior transition between sensing motion and tiptoe motion (see Fig 5A) supports that active sensing motions are related to the spiders' ballooning flight, because the tiptoe behavior is prerequisite behavior for ballooning takeoff (see Fig 11). The leg-raising behavior

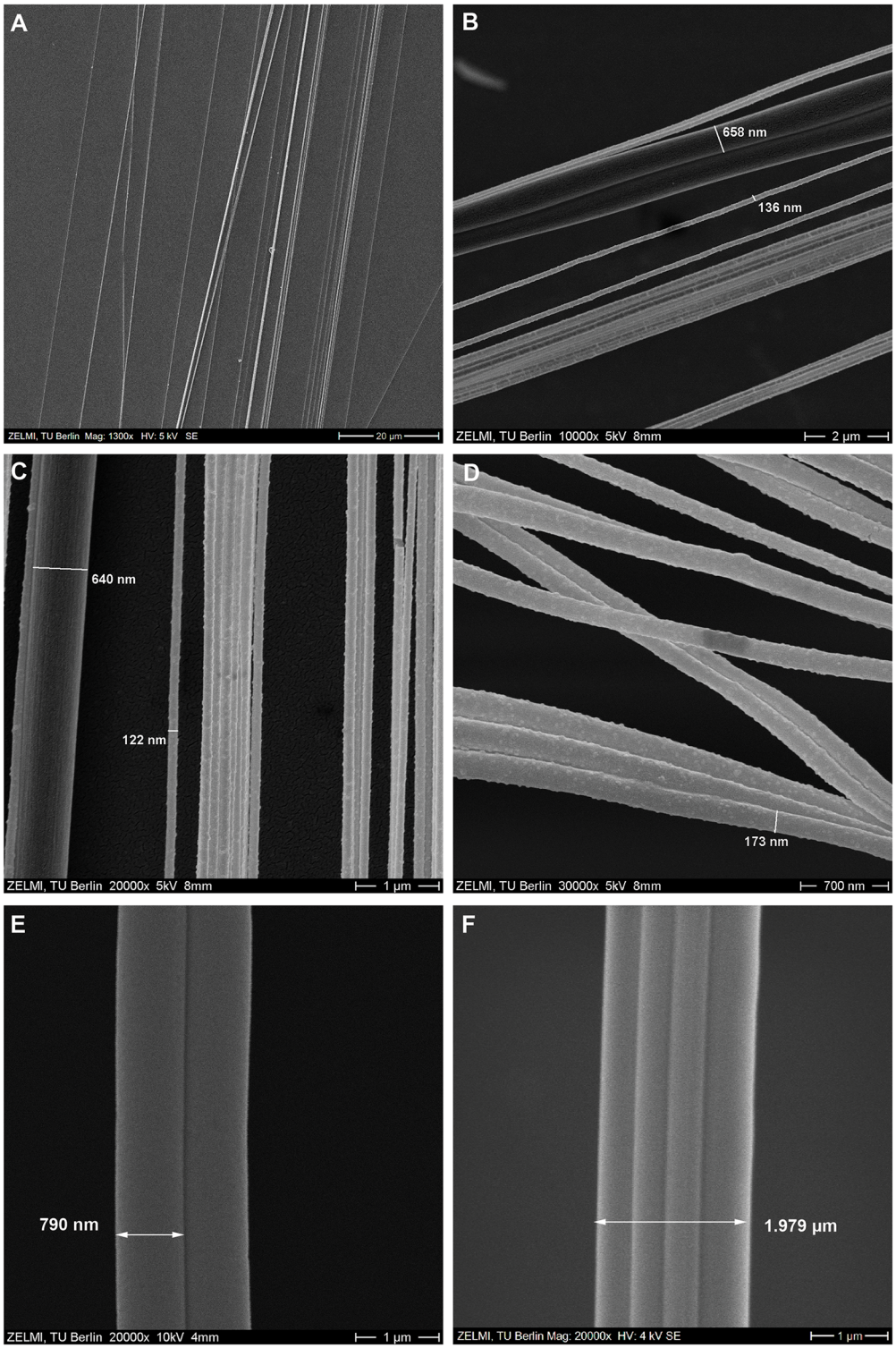

Fig 9. Scanning electron microscopic images of ballooning lines and drag lines. (A) Ballooning fibers of *X. cristatus* (1,300×). (B) Ballooning fibers of *X. audax* (10,000×). (C) Middle part of ballooning fibers of *X. audax* (20,000×). (D) Ballooning fibers of *X. cristatus* (30,000×). (E) One pair of drag fibers of *X. cristatus* (a weight of 18 mg) (20,000×). (F) Two pairs of drag fibers of *Xysticus* spp. (a weight of 15.6 mg), which attached together (20,000×).

https://doi.org/10.1371/journal.pbio.2004405.g009

Table 2. Identification of the number and thickness of ballooning fibers through FESEM.

	Species	Weight	Thin nanoscale fibers		Thick nanoscale fibers	
			Number of fibers	Thickness of fibers	Number of fibers	Thickness of fibers
Spider 1	*Xysticus* spp *(f.)*	20.8 mg	58	192.3 ± 36.3 nm ($N = 20$)	2	734.0 ± 48.1 nm ($N = 2$)
Spider 2	*X. cristatus (f.)*	18 mg	48	231.1 ± 45.6 nm ($N = 20$)	2	710.5 ± 17.7 nm ($N = 2$)
Average	-	-	53 ± 7.1 ($N = 2$)	211.7 ± 45.2 nm ($N = 40$)	2 ($N = 2$)	722.2 ± 32.5 nm ($N = 4$)

Abbreviation: FESEM, field emission scanning electron microscope

https://doi.org/10.1371/journal.pbio.2004405.t002

can be interpreted as follows: the spider enhances the sensibility of its sensory hairs by raising its legs upward in the outer region of the boundary layer, where airflows are faster than near the substrate and undisturbed by spiders' bodies themselves. The first instars of the coccid *Pulvinariella mesembryanthemi* show a similar behavior by standing on their hind legs to capitalize on higher air speed in the thin boundary layer for their aerial dispersal [46].

The spider's active sensing motion of the wind tells us two important things. First, in spiders' ballooning, aerodynamic force maybe be a dominant factor. One hypothesis claims that an electrostatic charge on ballooning silks could generate lifting forces in the earth's vertical atmospheric electrostatic field [22]. However, the leg-raising behavior indicates that, from the spider's viewpoint, airflow is an important factor for its ballooning. Second, the spiders' ballooning may not be random flight that simply relies on the random condition of the wind, but they may sense and evaluate the condition of the wind and wait for the appropriate moment to initiate ballooning. Thirty-eight percent of tiptoe behaviors lasted 10–65 s. This can be interpreted that there may be favorable wind conditions for spiders to balloon. If spiders evaluate wind conditions and wait for their aerial dispersal, this can be a distinct feature of spiders' ballooning in contrast to other passive aerial dispersal, like that of seeds or aeroplanktons. Additionally, this evaluating behavior can also save their silk dopes during their takeoff trials by reducing failure cases, for example, by avoiding unfavorable wind conditions after spinning the ballooning silks.

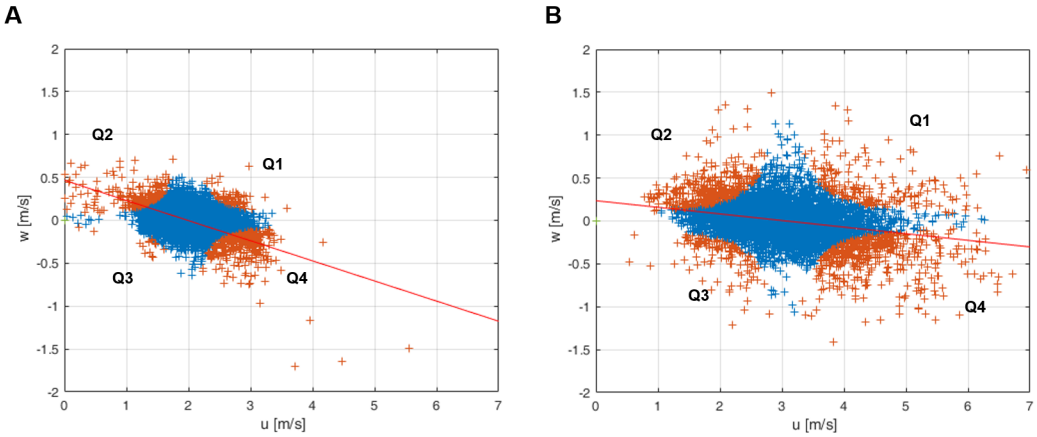

Fig 10. Horizontal and vertical components of the wind speeds for 5 min on u–w domain. (20-Hz sensing rate). (A) The case of 1.99 m s^{-1} mean wind speed (30 October 2016 12:39–12:45 LT). (B) The case of 3.07 m s^{-1} mean wind speed (29 October 2016 10:54–11:00 LT). Orange cross points: the quadrant data (Q1–Q4) of the measured wind speeds according to u′ and w′. Blue cross points: the ignored data regarding as a small-scale fluctuation ($H < 1$). Red lines are linear regression fit lines. The corresponding underlying data can be found in S3 Data.

https://doi.org/10.1371/journal.pbio.2004405.g010

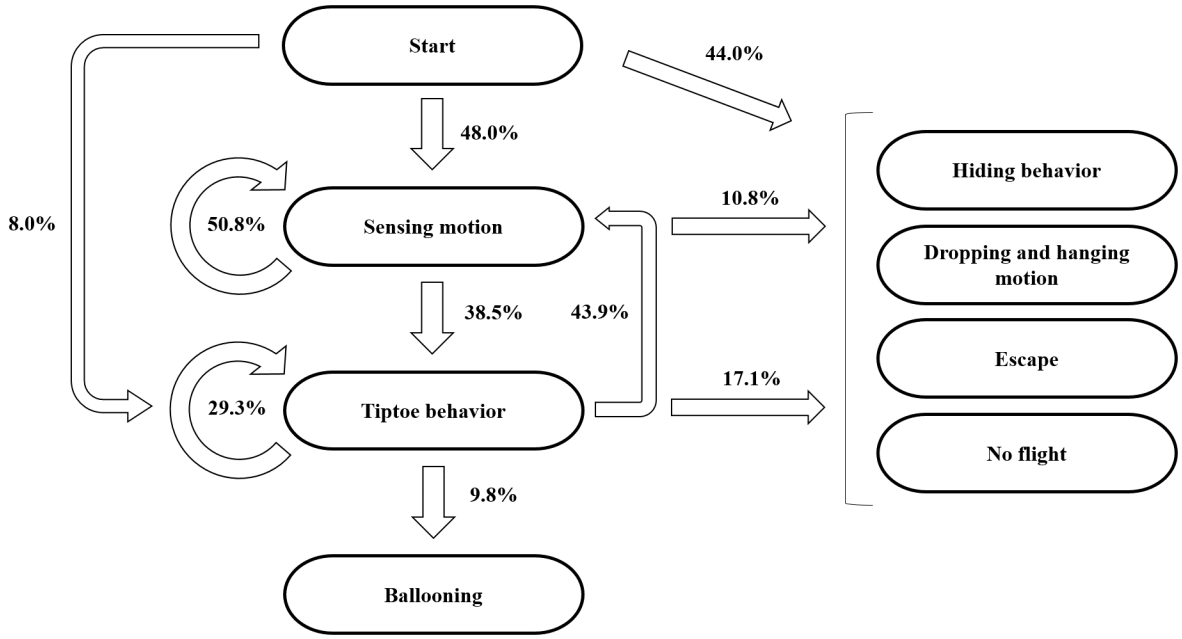

Fig 11. Takeoff process for tiptoe ballooning. The probabilities are calculated based on the total number of behaviors at each stage (see Fig 5B).

https://doi.org/10.1371/journal.pbio.2004405.g011

In the near-surface atmospheric boundary layer, the updraft is not initiated by thermal buoyancy forces but is initiated by the shear winds, which generate shear-driven turbulent flows [47,48]. The generated turbulent eddies build intermittent updraft and downdraft regions, which drift to the downwind direction. If spiders sense either this moving updraft zone directly or the appropriate wind condition that can build this moving updraft structure, indirectly, the spiders' sensing motion and timing of the decision may be helpful for their successful takeoff.

There are still other questions that can be asked. If spiders sense these wind conditions, what type of information do spiders need for their decision to balloon? From previous studies and the author's observations, we deduce several factors. (i) Wind speed: A spider does not show tiptoe behavior under conditions of high wind speed, over 3 m s^{-1} [1,3,36,37]. (ii) A vertical wind speed: Favorable condition for ballooning, usually vertical acceleration of wind, persisting only for a few seconds. Under such a condition, the spider spins its silk fibers in wind rapidly and releases its substrate [20,36]. (iii) Wind direction: From our observation, spiders rotate their body in the direction of the wind as soon as they have evaluated the wind condition. Therefore, at least, spiders perceive wind direction. (iv) Wind fluctuation: For drop and swing dispersal, spiders were particularly more active with turbulent flows [49]. This shows that spiders can perceive the fluctuation of a turbulent flow. Suter showed that the ballooning site is usually laid within chaotic air flows [20]. Reynolds showed that the chaotic motion of turbulent flow reduces the terminal speed of ballooners and that this feature enables long permanence in the air [16]. Therefore, it can be deduced that spiders may sense the fluctuation of wind.

Ballooning lines and anchored line

For crab spiders, ballooning lines were not identical with a drag line. The source of ballooning lines is not well known [3,19]. There is a report that some of primitive spiders—*Sphodros*

spiderlings and *Ummidia* spiderlings, which do not use the complex preballooning behaviors such as tiptoe and rafting—use a drag line as a ballooning line, which is known as "suspended ballooning" [10]. Spiders drop down from the end of a branch, relying on their drag line. If there is a breeze, the drag line near its point of attachment to the platform would be sheared and drift through the air [28,50]. From this context, many previous studies regarded that spiders use their drag line for ballooning dispersal [16,17,22,23,38]. Some experiments substituted a drag line for a ballooning line [18,19,21]. However, Suter guessed from Tolbert's observation that ballooning lines might be different from the drag line [3,18,20]. Our observation assures that in crab spiders, these ballooning lines are not identical with a drag line because those were spun from either or both of the median and/or posterior spinnerets (see S7A and S7B Fig). Normally, the drag line is spun from major ampullate glands in the anterior spinneret [51]. The crab spiders spun 48 to 58 thin nanofibers and 2 thick nanofibers. These thin nanoscale fibers seemed to be aciniform fibers (wrapping silk) from the median/posterior spinnerets. The thick nanoscale fibers seemed to be minor ampullate silks from the median spinnerets. Moon and An observed that one of the median spinnerets (left and right) of *Misumenops tricuspidatus* (crab spider) contains 2 pairs of ampullate glands and 20 (±3) pairs of aciniform glands, and one of its posterior spinnerets includes 50 (±5) pairs of aciniform glands [52]. Our observation in *Xysticus* spp. showed similar features to Moon and An's observation (see S7C and S7D Fig).

The anchored drag lines are possibly normal drag lines (major ampullate silks), which a spider spins constantly while it is crawling and attaching its silk fibers to the ground surface for safety purposes. The anchored line was connected to the anterior spinnerets (see S7A Fig) and consisted of 2 fibers. From Osaki's observation, drag lines are also composed of 2 fibers [53]. The anchored line can be observed in every ballooning behavior, in not only rafting takeoff [10] but also tiptoe takeoff.

Before the spinning motion of ballooning lines, there was a motion of a rear leg (leg IV) (see S5A and S5B Fig), resembling "wrap spinning," during which spiders use leg IV to initiate ballooning lines by wiping their spinnerets [54]. However, in our case, it was obvious that the spiders did use their leg IV not to initiate ballooning lines but to tidy up the unfamiliarly positioned anchored line (safety line), which might have obstructed the spinning of ballooning silks (see S2A and S2B Fig and S2 Video). During the tiptoe takeoff, this anchored line is normally cut in a short time mechanically, when a spider drifts fast either horizontally or at a small inclination. But when a spider becomes slowly airborne with a very steep inclination because of a local updraft, this line bears until it is lengthened to 3–5 m. In our opinion, it is not stretched, but a spider lengthened the safety silk by spinning an additional safety line. The reason is that the maximum elongation of spider silks is limited by about 30% [55,56]. This means that spiders control their anchored line during the steep or slow takeoff.

Nanoscale multifibers and ballooning flight

While the ballooning of small spiders, which are lighter than 2.0 mg, was investigated by calculation [17], experiments [18,21], and observation [1,3], the plausibility of a large spider's ballooning was not yet explained [17,39]. The mysterious flying behavior of large spiders can be explained by their nanoscale multifibers. From our wind tunnel test, we found that the *Xysticus* genus uses tens of nanofibers (diameters of 121 to 323 nm) for their aerial dispersal (see Fig 9A–9D). The number of ballooning fibers and their lengths were identified. Based on these measured values, the required updraft speed for the ballooning takeoff was calculated using modified Humphrey's and Suter's equations (Eqs [4–8]) [17,18]. The fluid-dynamic interaction between each fiber is not considered. The split case of fibers is calculated. For a crab spider

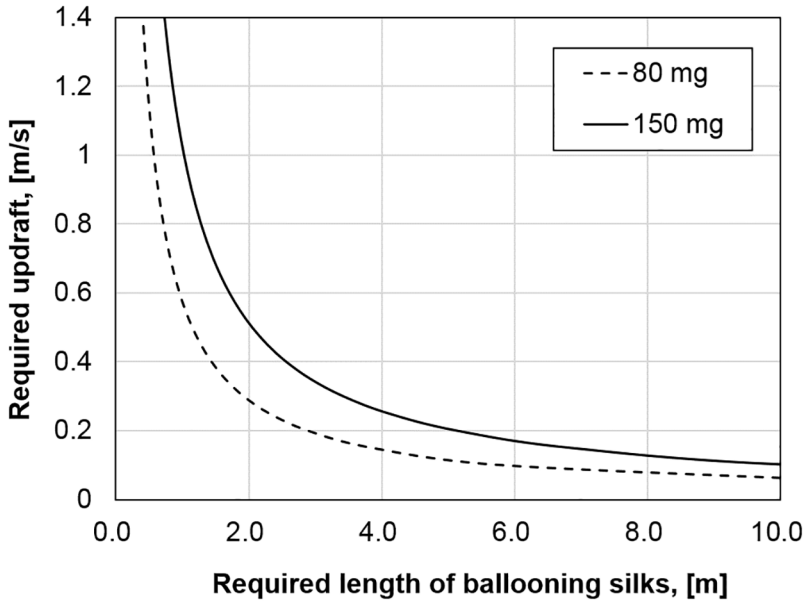

Fig 12. Required updraft wind speed and length of ballooning silks for the ballooning of 80–150 mg *Stegodyphus* spp. It is assumed that *Stegodyphus* spp. use 2 minor ampullate silks (2.1–2.9 μm thickness) and 78 aciniform silks (650–900 nm thickness) for their ballooning. The corresponding underlying data can be found in S4 Data.

https://doi.org/10.1371/journal.pbio.2004405.g012

weighing 10–25 mg, the required vertical wind velocities are, according to Humphrey's theoretical formula, 0.08–0.20 m s^{-1} and, according to Suter's empirical formula, 0.04–0.09 m s^{-1}. These values are much smaller than the values 9.2–21.6 m s^{-1}, which were calculated for *Stegodyphus* spp. [25,39]. We calculated the required length of ballooning fibers for *Stegodyphus* spp. according to the updraft air speeds (see Fig 12). Our result shows that *Stegodyphus* spp. can also balloon with relatively light updraft, 0.2–0.35 m s^{-1}, with 3 m length and a total numbering 80 ballooning fibers. These results support Schneider's observation that adult females of the *Stegodyphus* genus, 80–150 mg, balloon with at least tens to hundreds of threads [26]. In this calculation, the number of ballooning fibers for *Stegodyphus* genus is assumed conservatively that only 1 side (left or right) of the median and posterior spinnerets is used for spinning ballooning fibers. This number of fibers is estimated by counting the fiber glands of *S. mimosarum*'s spinnerets (the number of minor ampullate fibers is 2; the number of aciniform fibers is 78) [57]. This number is reasonable because *Xysticus* spp. spun a similar order of the number of fibers (2 thick fibers and 58 thin fibers, from our experiments). The thicknesses of a minor ampullate fiber and an aciniform fiber are assumed 80% and 25% of that of the major ampullate fiber, respectively. The thickness of a major ampullate fiber is estimated from Suter's body weight and silk thickness relationship (Eq [8], [18]).

$$D_H = \sum_{i=1}^{n} \frac{2\pi \cdot \mu \cdot U \cdot l_i}{ln(2l_i/d_i) - 0.72} \times 10^6 \tag{4}$$

$$D_S = \sum_{i=1}^{n} 11.5 \cdot l_i \cdot U \cdot W_{eq,i}^{0.094} \tag{5}$$

$$U_H = \frac{W}{\sum_{i=1}^{n} \frac{2\pi \cdot \mu \cdot l_i}{ln(2l_i/d_i) - 0.72} \times 10^6 + 1.94 \cdot W^{0.366}} \tag{6}$$

$$U_S = \frac{W}{\sum_{i=1}^{n} 11.5 \cdot l_i \cdot W_{eq,i}^{0.094} + 1.94 \cdot W^{0.366}} \tag{7}$$

$$W_{eq,i} = \frac{\pi (d_i \times 10^6)^2 + 0.184}{0.0277} \tag{8}$$

D_H: Drag of multiple fibers by Humphrey's equation in μN.

D_S: Drag of multiple fibers by Suter's equation in μN.

U_H: Required vertical wind speed for ballooning using Humphrey's equation in m s^{-1}. (The spider's body drag is used from the Suter's empirical relationship.)

U_S: Required vertical wind speed for ballooning using Suter's equation in m s^{-1}.

μ: Dynamic viscosity of the air at 20°C (1.837×10^{-5} kg m^{-1} s^{-1}).

U: Velocity of the air in m s^{-1}.

l_i: Length of i-th silk fiber in m.

d_i: Diameter of i-th silk fiber in m.

W: Weight of the spider body in μN.

$W_{eq,i}$: Equivalent weight of the spider body corresponding to the diameter of a ballooning fiber in μN.

n: Total number of ballooning fibers.

Low Reynolds number fluid dynamics in a spider's ballooning flight

The ballooning silks, exposed to the air, experience a low Reynolds number flow (Stokes flow, their Reynolds number is lower than 1). The upper limit of the Reynolds number is about 0.04 ($Re = \rho V d / \mu$; the air density, ρ: 1.225 kg m^{-3}; the maximum possible velocity, V: 3 m s^{-1}; the thickness of spider silk, d: 211 nm; the dynamic viscosity of air, μ: 1.837×10^{-5} kg m^{-1} s^{-1}). The maximum possible speed that the thread experiences is assumed to be 3 m s^{-1} because a spider seldom flies above this wind speed. Once a spider is airborne, the relative air speed with respect to the silk is reduced. Therefore, the Reynolds number of spiders' silks during their flight is much smaller than 0.04, and the spider's flight is dominated by low Reynolds number fluid dynamics [58]. However, a large spider's body shows much larger scales than those of a spider silk, not only in size but also in weight. In a free-fall case of a spider body without any silks, the Reynolds number is about 2,300 ($Re = \rho V_t D / \mu$; $V_t = \sqrt{2mg / (\rho A C_D)}$; a spider's body is assumed as a 5 mm diameter, D, sphere with 25 mg mass, m; the projected area of a sphere, A: 19.6 mm^2; the coefficient of a sphere, C_D: 0.43; the terminal speed, V_t: 6.2 m s^{-1}) [59]. In this Reynolds number flow regime, the drag of a body is proportional to almost the square of relative wind speed, because the Reynolds number region of $5 < Re < 3{,}000$ is categorized as moderate Reynolds numbers, in which inertial force of flow is still dominant in comparison with a viscous flow [60]. On the other hand, the drag of spider silk is proportional to relative wind speed because a viscous force is dominant in this low Reynolds number regime ($Re \ll 5$) [60]. Therefore, the macroscale spider's body, which means that a spider falls with acceleration without ballooning silks, is suspended by their high-tensile-strength nanoscale fibers that experience microscale fluid dynamics (low Reynolds number flow). This enables a spider to float in the air like a particle that experiences relatively low Reynolds number flow. The Reynolds number of a spider's body with ballooning fibers is about 30 ($Re = \rho V D / \mu$; minimum possible velocity, V: 0.09 m s^{-1} by the lowest terminal speed from modified Suter's formula). The utilization of low Reynolds number fluid dynamics in ballooning flight is different

from flight mechanics of other membranous-winged insects' flight, which mostly uses moderate or high Reynolds number aerodynamics, $10^3 < Re < 10^5$ [61–63]. The low Reynolds number flight, which use a hairy structure, can also be found in that of thrips and parasitoid wasps [64–66]. While they produce drag during passive flight mode (parachuting) by using 200–300-μm-long stiff stae, spiders use about 3 m long flexible multifibers for ballooning flight. This scale difference (10^4) enables large spiders' ballooning (the weight of *Xysticus* spp. is 25 mg; the weight of *Encarsia formosa* [Chalcid wasp] is 2.55 μg) [64].

Low wind speed and turbulence

The measured vertical wind speeds of updrafts ranged 0–0.5 m s^{-1} at the mean wind speed of 1.99 m s^{-1} and 0–0.7 m s^{-1} at the mean wind speed of 3.07 m s^{-1}. These values are enough for spiders' ballooning, the required vertical wind speeds of which were 0.04–0.2 m s^{-1} for 10–25 mg *Xysticus* spp. and 0.2–0.35 m s^{-1} for 80–150 mg *Stegodyphus* spp. The observed negative correlation between vertical wind speed and horizontal wind speed in the turbulent boundary layer, which has been also studied in the fields of fluid dynamics and meteorology [42–44], suggests to us that the reason spiders show their preballooning behavior at a low-wind-speed regime (smaller than 3 m s^{-1}) is because they may use the "ejection" regimes in turbulent flow, which contain updraft components and are induced by a "coherent structure" near the surface boundary layer. A shear wind on a planted field, a meadow, or relatively short plants form an organized structure called the "coherent structure" (possibly "hairpin vortex" or "horseshoe vortex," see Fig 13A and 13B; "hairpin vortex packets" over relatively short plants and "dual hairpin vortex structures" over planted field [see Fig 13C and 13D]) [42,67–71]. These structures intermittently produce up- and downdrafts [42,68,70]. The interesting point is that these updrafts are highly correlated with a decrease in wind speed, which is categorized as Q2 ($u' < 0$ and $v' > 0$), an "ejection" region in a quadrant analysis [42–44] (see Fig 10). Therefore, the phenomenon of spiders usually ballooning in the low-wind-speed regime (lower than 3 m s^{-1}) could be explained with this organized structure in the atmospheric turbulent flows above the ground. However, the frequency and duration of these updrafts are not well known.

Shear flow and the spider's posture

While Reynolds postulated the tangled shape of ballooning fibers in his simulation, the diagonally lying shape of the spider's ballooning fibers was observed in our field observations in the Teltow Canal (see Fig 7) [16]. The difference between our observation and Reynolds' simulation is caused by the fact that while Reynolds introduced homogeneous turbulence in his simulation, the real turbulence near the surface boundary layer includes instantaneous horizontal wind shears that are mostly induced by vertical differences in wind speed [71,72]. This diagonally stretched shape of ballooning fibers may be caused by the shear wind in the atmospheric boundary layer. We think that this may be helpful for long-endurance ballooning flight because horizontally stretched silks produce more drag, up to a factor of 2, than vertically distributed shapes of silk, because of an anisotropic drag of silks in a low Reynolds number flow [73] (see S8A–S8C Fig).

The observed fact, that spiders outstretch all legs during their flight, is puzzling because of its small drag ratio compared to the drag of a spider's ballooning silks. Suter concluded that when a spider uses a relatively short length of silk, the influence of posture on its terminal speed is greater than when the silk is very long [19]. However, our observation shows that spiders spin abundant ballooning fibers. From Suter's empirical formula, spiders' (weighing 10 to 25 mg) body drags per unit velocity, which are 10.4–14.5 μN m^{-1} s, are just 0.4–0.56% of the whole drag (silks + body) per unit velocity, 2576.5–2580.5 μN m^{-1} s. Even if a spider stretches

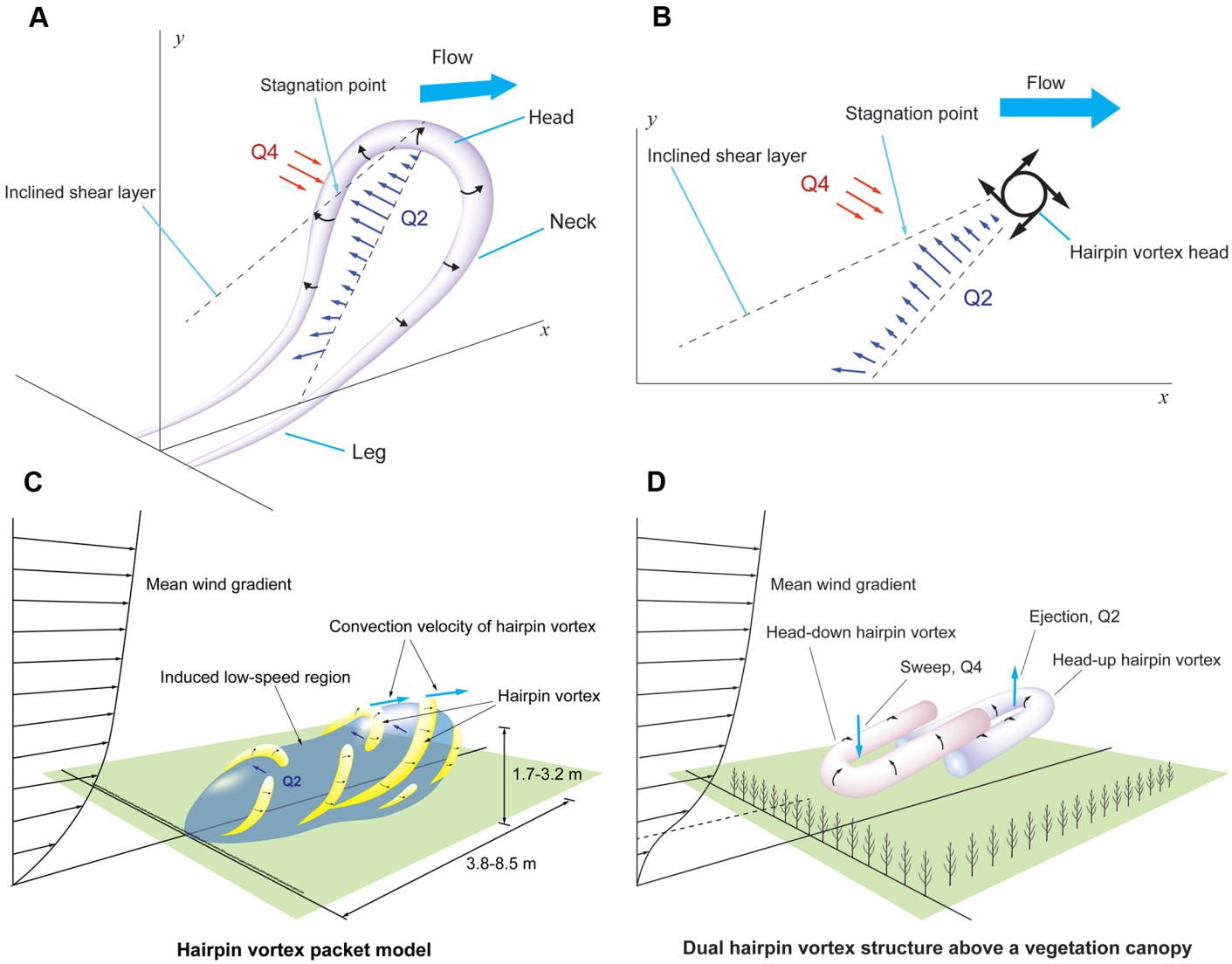

Fig 13. Schematic diagram of updraft generation by a vortex and vortices in near-surface atmospheric boundary layer. (A) Schematic diagram of a single hairpin vortex in the wall boundary layer. Q2 is an "ejection" region whose velocity vectors are $u' < 0$ and $v' > 0$. Q4 is a "sweep" region whose velocity vectors are $u' > 0$ and $v' < 0$. (B) Cross-section of the x-y plane of the hairpin vortex. (C) Schematic diagram of the hairpin vortex packet. Yellow colors mean hairpins or cane-type vortices. Blue region means low momentum region, which contains upward air currents. (D) Coherent structure, "dual hairpin vortex," on the plant field. Head-down hairpin vortex produces "sweep" event. Head-up hairpin vortex produces "ejection" event. (A, B) Redrawn from [68]. (C) Redrawn from [68, 69]. (D) Redrawn from [70].

https://doi.org/10.1371/journal.pbio.2004405.g013

its legs outward, the percentage of body drag is still 2.0–2.8% (5-fold change is applied, from Suter's research) [18,19]. Despite such a small drag effect of spiders' posture, spiders stretch their legs outward during flight (see S6C and S6D Fig). Then the question arises, What role do the stretched legs play in ballooning flight? These should be studied as a future work.

Conclusion and outlook

Studying ballooning mechanics in spiders can be helpful for understanding not only the ecological influence of spiders' dispersal but also efficient passive transport of particles using air or oceanic currents.

By observing the ballooning behavior in relatively large spiders (10–25 mg *Xysticus* spp.) in the field and in the laboratory, we have revealed that the large spiders' ballooning, even that of

80–150 mg *Stegodyphus* spp., is possible with the help of tens of multiple nanoscale fibers. The observed ballooning lines were not identical to the drag line, which has been regarded as a ballooning line. From the observation of spinning behaviors and morphological dimensions of fibers, we concluded that these ballooning silks are pairs of minor ampullate silks and multiple aciniform silks, which are usually used in other species as wrapping silks. *Xysticus* spp., however, used these silks for their aerial dispersal. Spiders also showed an interesting behavior (active sensing motion) such as evaluating the wind conditions before their ballooning behavior. This behavior may save spiders' silk dopes, which can be consumed during their takeoff trials.

Two major features in the physics of ballooning are suggested from the study. First, atmospheric shear flow, which is a major part of the flow structure in the turbulent boundary layer, may be helpful for the high buoyant capability of a ballooning structure because horizontally/diagonally stretched silks produce more drag than vertically distributed shapes of silks. Second, spiders may use the updrafts that are induced by "coherent structures" in the turbulent atmospheric boundary layer. From the measured wind data, we showed that these updrafts are correlated with lower wind speeds. Therefore, this hypothesis is expected to explain why spiders usually balloon when the wind speed is lower than 3 m s^{-1}. However, these suggestions should be studied further for theoretical firmness.

Whether or not vertical wind speed and fluctuation of wind influence on spiders' evaluation processes for ballooning, how multiple fibers form a triangular sheet without entanglement during the takeoff phase (do any electrostatic forces act between fibers [11, 22, 26], or can the bundle of fibers be unfolded only with the help of wind fluctuation?), and why spiders stretch their legs outward during their flight are questions that still remain. These could be interesting topics for future research.

Supporting information

S1 Fig. Ballooning behavior of a male crab spider. The spider shows the tiptoe behavior and spins ballooning silks.
(TIF)

S2 Fig. Sequential sketches of "tiptoe" takeoff in the field experiment. Red lines: an anchored line (a drag line). Blue lines: ballooning lines. (A) A spider, *Xysticus* spp., tries to hold the anchored line with 1 of legs IV. (B) The spider holds the anchored line and then puts it on the substrate. (C) The spider first spins a single or a few fibers. (D) And then, the spider spins many split fibers. (E) If the wind condition is appropriate, the spider releases the substrate. (F) In a very short time, the anchored line is cut. The crab spider becomes airborne.
(TIF)

S3 Fig. Sequential sketches of "rafting" takeoff in the field experiment. Red lines: an anchored line (a drag line). Blue lines: ballooning lines. (A)(B) A spider, *Xysticus* spp., drops down about 0.4–1.1 m, relying on its anchored line (a drag line). (C) The spider first spins a single or a few fibers downstream of the wind. (D) And then, the spider spins many fibers continuously. (E)(F) The spun ballooning lines slowly curved upward. At some point, the anchored line near the spinnerets is cut, and the spider balloons.
(TIF)

S4 Fig. The sketch describes the position of the hair dryer. The mixed air zone generates 28–33 ˚C warm air and fluctuating updraft (horizontal mean wind speed: 0.58 m s^{-1}, vertical mean wind speed: 0.40 m s^{-1}).
(TIF)

S5 Fig. Tidying-up motion of safety line (anchored line) with leg IV. Two independent events; a front view (A), a side view (B). Both spiders hold their safety line and then put it on the substrate before spinning of ballooning lines.
(TIF)

S6 Fig. Spiders' posture in takeoff and flight. (A, B) An anchored line was found during a tiptoe takeoff. As soon as spiders were airborne, they stretched the legs outward. (C) To ensure the behavior of outstretched legs during flight, the pose of a spider was observed during its gliding phase. (D) The spider kept its legs outstretched.
(TIF)

S7 Fig. Spinning behavior for ballooning and scanning electron microscopic images of spinnerets. (A) Spinning motion of ballooning silks in front of the open jet wind tunnel. Ballooning lines were spun from either or both of the median or/and posterior spinnerets. (B) Spinnerets of *X. cristatus* through FESEM. (C) Median spinneret of *Xysticus* spp. Two minor ampullate glands and 10 aciniform glands are distributed on the median spinneret. (D) A number of aciniform glands on the posterior spinneret. FESEM, field emission scanning electron microscope.
(TIF)

S8 Fig. Schematic diagrams of the ballooning structure in a shear flow. (A) Ballooning structure in a shear flow. (B) Drift of a ballooning structure along with wind. The upper and lower parts of the silk are exposed to the flow fields, which exert to the other directions. (C) The ballooning structure exposed in a shear flow is stretched horizontally. $\boldsymbol{D_S}$, horizontal component of drag on the spider's body; $\boldsymbol{h}$, height; $\boldsymbol{V_D}$, drift speed of a ballooning structure; $\boldsymbol{V_{wG}}$, wind speed profile relative to ground; $\boldsymbol{V_{wR}}$, wind speed profile relative to a ballooning structure.
(TIF)

S1 Video. Sensing motion of a crab spider before tiptoe motion.
(MP4)

S2 Video. Tidying-up motion of an anchored line before spinning ballooning lines.
(MP4)

S3 Video. A preballooning behavior of a crab spider, *Xysticus* spp.
(MP4)

S1 Data. Statistical data of preballooning behaviors.
(XLSX)

S2 Data. Physical properties of ballooning fibers.
(XLSX)

S3 Data. Three-dimensional wind velocity data on a flat grass field.
(XLSX)

S4 Data. Required vertical airspeed for ballooning.
(XLSX)

Acknowledgments

We would like to thank Jason Dunlop of the Naturkundemuseum Berlin for advice on spider identification. Many thanks to Robert B. Suter for the detailed explanation of his research. We

thank Iván Santibáñez Koref and Wladyslaw Chrusciel for the scientific discussions. We also thank Susi Koref, who improved the English in this manuscript. Many thanks to Akaflieg Berlin and Enerkite members, who offered facilities during the wind measurements.

Author Contributions

Conceptualization: Moonsung Cho, Peter Neubauer, Ingo Rechenberg.

Data curation: Moonsung Cho.

Formal analysis: Moonsung Cho.

Funding acquisition: Peter Neubauer.

Investigation: Moonsung Cho, Peter Neubauer, Christoph Fahrenson, Ingo Rechenberg.

Methodology: Moonsung Cho, Christoph Fahrenson.

Project administration: Ingo Rechenberg.

Resources: Peter Neubauer.

Supervision: Peter Neubauer, Ingo Rechenberg.

Validation: Moonsung Cho, Ingo Rechenberg.

Visualization: Moonsung Cho, Christoph Fahrenson.

Writing – original draft: Moonsung Cho.

Writing – review & editing: Peter Neubauer.

References

1. Richter CJJ. Aerial dispersal in relation to habitat in eight wolf spider species (Pardosa, Araneae, Lycosidae). *Oecologia* 1970; 5(3):200–14. https://doi.org/10.1007/BF00344884 PMID: 28309820
2. Salmon JT, Horner NV. Aerial dispersion of spiders in North Central Texas. *The J. Arachnol.* 1977; 5 (2):153–7.
3. Tolbert WW. Aerial dispersal behavior of two orb weaving spiders. *Psyche*: *A Journal of Entomology* 1977; 84(1):13–27.
4. Dean D.A, Sterling WL. Size and phenology of ballooning spiders at two locations in eastern Texas. *J. Arachnol.* 1985;(13):111–20.
5. Greenstone MH, Morgan CE, Hultsch AL, Farrow RA, Dowse JE. Ballooning spiders in Missouri, USA, and New South Wales, Australia: Family and mass distributions. *J. Arachnol.* 1987; 15(2):163–70.
6. Morse DH. Dispersal of the spiderlings of *Xysticus Emertonu* (Araneae, Thomisidae), a litter-dwelling crab spider. *J. Arachnol.* 1992;(20):217–221.
7. Cbosby CR, Crosby C. R. and Bishop S. C. Aeronautic spiders with a description of a new species. *Journal of the New York Entomological Society* 1936; 1(44):43–9.
8. McCook HC. American spiders and their spinning work: A natural history of the orbweaving spiders of the United States: with special regard to their industry and habits. Landisville, PA: Coachwhip Publications;2006.
9. Blackwall J. Observations and experiments, made with a view to ascertain the means by which the spiders that produce gossamer effect their aerial excursions. *Transactions of the Linnean Society of London* 1827;(15):449–59.
10. Bell JR, Bohan DA, Shaw EM, Weyman GS. Ballooning dispersal using silk: World fauna, phylogenies, genetics and models. BER 2005; 95(02):2.
11. Darwin C. Journal of researches into the natural history and geology of the countries visited during the voyage of H.M.S. Beagle round the world, under the Command of Capt. Fitz Roy R.N. 2nd ed. New York: John Murray, Albemarle Street;1845.
12. Glick PA. The distribution of insects, spiders, and mites in the air. *USDA Tech Bull* 1939;(673):1–150.

13. Bilsing SW. Quantitative studies in the food of spiders. *The Ohio Journal of Science* 1920; 20(7):215–60.
14. Bristowe WS. A Preliminary Note on the Spiders of Krakatau. Proceedings of the Zoological Society of London 1931; 101(4):1387–400.
15. Hormiga G. Orsonwells, A new genus of giant linyphild spiders (Araneae) from the Hawaiian Islands. *Invert. Systematics* 2002; 16(3):369–448.
16. Reynolds AM, Bohan DA, Bell JR. Ballooning dispersal in arthropod taxa with convergent behaviours: dynamic properties of ballooning silk in turbulent flows. *Biol Lett* 2006; 2(3):371–3. https://doi.org/10.1098/rsbl.2006.0486 PMID: 17148406
17. Humphrey JAC. Fluid mechanic constraints on spider ballooning. *Oecologia* 1987; 73(3):469–77. https://doi.org/10.1007/BF00385267 PMID: 28311532
18. Suter RB. Ballooning in spiders: Results of wind tunnel experiments. *Ethology Ecology & Evolution* 1991; 3(1):13–25.
19. Suter RB. Ballooning: Data from spiders in freefall indicate the importance of posture. *J. Arachnol.* 1992; 2(20):107–13.
20. Suter RB. An aerial lottery: The physics of ballooning in a chaotic atmosphere *J. Arachnol.* 1999; 1 (27):281–93.
21. Bell JR, Bohan DA, Le Fevre R, Weyman GS. Can simple experimental electronics simulate the dispersal phase of spider ballooners? *J. Arachnol.* 2005; 33(2):523–32.
22. Gorham PW. Ballooning Spiders: The Case for Electrostatic Flight 2013. https://arxiv.org/abs/1309.4731v2 [cited 2014 Sep 2]
23. Sheldon KS, Zhao L, Chuang A, Panayotova IN, Miller LA, Bourouiba L. Revisiting the physics of spider ballooning. *Women in Mathematical Biology* 2017; 8:125–39.
24. Weyman GS. A review of the possible causative factors and significance of ballooning in spiders. *Ethology Ecology & Evolution* 1993; 5(3):279–91.
25. Wickler W, Seibt U. Aerial dispersal by ballooning in adult *Stegodyphus mimosarum*. *Naturwissenschaften* 1986; 73(10):628–9.
26. Schneider JM, Roos J, Lubin Y, Henschel JR. Dispersal of Stegodyphus Dumicola (Araneae, Eresidae): They Do balloon after all! *J. Arachnol.* 2001;(29):114–6.
27. Simonneau M, Courtial C, Pétillon J. Phenological and meteorological determinants of spider ballooning in an agricultural landscape. *C R Biol* 2016; 339(9–10):408–16. https://doi.org/10.1016/j.crvi.2016.06.007 PMID: 27527898
28. Coyle FA, Greenstone MH, Hultsch AL, Morgan CE. Ballooning mygalomorphs: estimates of the masses of Sphodros and ummidia ballooners (Araneae: Atypidae, Ctenizidae). J. Arachnol. 1985; 13 (3):291–6.
29. Greenstone MH, Morgan CE, Hultsch AL. Spider ballooning: development and evaluation of field trapping methods. *J. Arachnol.* 1985; 13(3):337–45.
30. Greenstone MH. Meteorological determinants of spider ballooning: the roles of thermals vs. the vertical windspeed gradient in becoming airborne. *Oecologia* 1990; 84(2):164–8. https://doi.org/10.1007/BF00318267 PMID: 28312748
31. Vugts HF, Van Wingerden WKRE. Meteorological aspects of aeronautic behaviour of spiders. *Oikos* 1976; 27(3):433.
32. Bristowe WS. The comity of spiders. Lymington: Pisces Conservation/Ray Society;2004.
33. Duffey E. Aerial dispersal in a known spider population. *The Journal of Animal Ecology* 1956; 1(25):85.
34. Bishop L. Meteorological aspects of spider ballooning. *Environmental Entomology* 1990; 19(5):1381–7.
35. Van Wingerden WKRE, Vugts HF. Factors influencing aeronautic behaviour of spiders. *Bulletin of the British Arachnological Society* 1974; 3(1):6–10
36. Richter C. Some aspects of aerial dispersal in different populations of wolf spiders, with particular reference to Pardosa Amentata (Araneae Lycosidae). Miscellaneous Papers, Landbouwhogeschool, Wageningen 1971;(8):77–88.
37. Lee VMJ, Kuntner M, Li D. Ballooning behavior in the golden orb web spider Nephila pilipes (Araneae: Nephilidae). *Front. Ecol. Evol.* 2015; 3:e86780.
38. Zhao L, Panayotova IN, Chuang A, Sheldon KS, Bourouiba L, Miller LA. Flying spiders: Simulating and modeling the dynamics of ballooning. *Women in Mathematical Biology* 2017; 8:179–210.
39. Henschel JR. Dispersal mechanisms of Stegodyphus (Eresidae): Do they balloon? *J. Arachnol.* 1995; (23):202–4.

40. Willmarth WW, Lu SS. Structure of the Reynolds stress near the wall. *J. Fluid Mech*. 1972; 55(01):65.

41. Lu SS, Willmarth WW. Measurements of the structure of the Reynolds stress in a turbulent boundary layer. *J. Fluid Mech*. 1973; 60(03):481.

42. Adrian RJ. Hairpin vortex organization in wall turbulence. *Physics of Fluids* 2007; 19(4):041301.

43. Zhu W, van Hout R, Katz J. PIV Measurements in the atmospheric boundary layer within and above a mature corn canopy. Part II: Quadrant-hole analysis. *J. Atmos. Sci*. 2007; 64(8):2825–38.

44. Steiner AL, Pressley SN, Botros A, Jones E, Chung SH, Edburg SL. Analysis of coherent structures and atmosphere-canopy coupling strength during the CABINEX field campaign. *Atmos. Chem. Phys*. 2011; 11(23):11921–36.

45. Palmgren P. Experimentelle Untersuchungen Fiber die Funktion der Trichobothrien bei Tegenaria Derhami. *Soc. Acta Zool. Fenn*. 1936;(19):3–28.

46. Washburn JO, Washburn L. Active aerial dispersal of minute wingless arthropods: exploitation of boundary-layer velocity gradients. *Science* 1984; 223(4640):1088–9. https://doi.org/10.1126/science.223.4640.1088 PMID: 17830156

47. Hunt JC, Morrison JF. Eddy structure in turbulent boundary layers. *European Journal of Mechanics—B/Fluids* 2000; 19(5):673–94.

48. McNaughton KG. Turbulence structure of the unstable atmospheric surface layer and transition to the outer layer. *Boundary-Layer Meteorology* 2004; 112(2):199–221.

49. Barth F, Komarek S, Humphrey J, Treidler B. Drop and swing dispersal behavior of a tropical wandering spider: Experiments and numerical model. *J Comp Physiol A* 1991; 169(3).

50. Coyle FA. Aerial dispersal by mygalomorph spiderlings (Araneae, Mygalomorphae). *J. Arachnol*. 1983; (11):283–6.

51. Vollrath F. Strength and structure of spiders' silks. *Journal of Biotechnology* 2000; 74(2):67–83. PMID: 11763504

52. Moon MJ, An JS. Spinneret Microstructure of the Silk Spinning Apparatus in the Crab Spider, Misumenops tricuspidatus (Araneae: Thomisidae). *Entomol Research* 2005; 35(1):67–74.

53. Osaki S. Is the mechanical strength of spider's drag-lines reasonable as lifeline? *International Journal of Biological Macromolecules* 1999; 24(2–3):283–7. PMID: 10342776

54. Eberhard WG. How spiders initiate airborne lines. *J. Arachnol*. 1987; 1(15):1–9.

55. Ko FK, Kawabata S, Inoue M, Niwa M, Fossey S, Song JW. Engineering properties of spider silk. *MRS Proc*. 2001; 702:91.

56. Bonino MJ. Material Properties of Spider Silk. dissertation. Rochester, NY: The College School of Engineering and Applied Sciences;2003.

57. Griswold CE. Atlas of phylogenetic data for entelegyne spiders (Araneae: Araneomorphae: Entelegynae): With comments on their phylogeny. In: Proceedings of the California Academy of Sciences, 4th series (Vol. 56, Suppl. 2) San Francisco: California Academy of Sciences;2005.

58. Purcell EM. Life at low Reynolds number. *Am. J. Phys*. 1977; 45:3–11.

59. Roos FW, Willmarth WW. Some experimental results on sphere and disk drag. *AIAA Journal* 1971; 9 (2):285–91.

60. Pelegrini MF, Vieira EDR. Flow past a sphere moderate Reynolds numbers. 17th International Congress of Mechanical Engineering, November 10–14, 2003, São Paulo, SP.

61. Dudley R. The biomechanics of insect flight: Form, function, evolution. Princeton, NJ: Princeton Univ. Press;2002.

62. Sane SP. The aerodynamics of insect flight. *Journal of Experimental Biology* 2003; 206(23):4191–208.

63. Bomphrey RJ, Nakata T, Phillips N, Walker SM. Smart wing rotation and trailing-edge vortices enable high frequency mosquito flight. *Nature* 2017; 544(7648):92–5. https://doi.org/10.1038/nature21727 PMID: 28355184

64. Weis-Fogh T. Quick Estimates of Flight Fitness in Hovering Animals, Including Novel Mechanisms for Lift Production. *J. Exp. Biol*. 1973; (59):169–230.

65. Kuethe AM. On the mechanics of flight of small insects. Swimming and Flying in Nature. New York: Wu TY, Brokaw CI, Brennan C, editor; 1975. (vol 2).

66. Santhanakrishnan A, Robinson AK, Jones S, Low AA, Gadi S, Hedrick TL, Miller A. Clap and fling mechanism with interacting porous wings in tiny insect flight. *J. Exp. Biol*. 2014; 217(Pt 21):3898–909. https://doi.org/10.1242/jeb.084897 PMID: 25189374

67. Theodorsen T. Mechanism of turbulence. In Proc. Midwestern Conf. Fluid Dyn., Ohio State University, Columbus, Ohio. 1952.

68. Adrian RJ, Meinhart CD, Tomkins CD. Vortex organization in the outer region of the turbulent boundary layer. *J. Fluid Mech*. 2000; 422:1–54.

69. Hommema SE, Adrian RJ. Packet structure of surface eddies in the atmospheric boundary layer. *Boundary-Layer Meteorology* 2003; 106(1):147–70.

70. Finnigan JJ, Shaw RH, Patton EG. Turbulence structure above a vegetation canopy. *J. Fluid Mech*. 2009; 637:387.

71. Dennis DJC. Coherent structures in wall-bounded turbulence. *An Acad Bras Cienc* 2015; 87(2):1161–93. https://doi.org/10.1590/0001-3765201520140622 PMID: 26062112

72. Grass AJ. Structural features of turbulent flow over smooth and rough boundaries. *J. Fluid Mech*. 1971; 50:233.

73. Childress S. Mechanics of swimming and flying. In: Cambridge studies in mathematical biology, vol. 2.: Cambridge University Press;1981.

II

Spiders' Ballooning Flight as a Model for the Exploration of Hazardous Atmospheric Weather Conditions

Moonsung Cho[1,2](✉), Klaus Affeld[3], Peter Neubauer[1], and Ingo Rechenberg[2]

[1] Technical University of Berlin, Institute of Biotechnology, Ackerstraße 76/ACK 24, 13355 Berlin, Germany
m.cho@campus.tu-berlin.de

[2] Technical University of Berlin, Institute of Bionics and Evolution Technique, Ackerstraße 76/ACK 1, 13355 Berlin, Germany

[3] Charité – Universitätsmedizin Berlin, Biofluid Mechanics Lab, Augustenburger Platz 1, 13353 Berlin, Germany

Abstract. Passive flight in living things, such as in maple or dandelion seeds, is one of the most primitive methods of aerial dispersal. This mechanism is robust and efficient, as it utilizes the present wind conditions. Passive flight is used not only by plant seeds but also by some animals. Spiders use fine, flexible silk filaments to fly, a behavior known as ballooning. This capability is distinct from that of other winged insects, as some ballooning spiders can travel hundreds of kilometers, reaching as high as 4.5 km above sea level. Various hypotheses explain the physical mechanism of ballooning flight. Some studies have shown that turbulent flow in the atmospheric boundary layer enhances spiders' flight endurance. This mechanism may be usefully applied in the exploration of hazardous weather conditions, such as severe storms, tornadoes, and clear-air turbulence, in the atmosphere, if we scale them up. In this paper, the authors briefly introduce the flight characteristics of the ballooning structure (i.e., the spider body and silk filaments), which were revealed in a simulation using a bead-spring model, and examine the possibility of scaling up ballooning flight from 25 mg to 1–2.5 kg for the exploration of hazardous weather conditions in the atmosphere.

Keywords: Ballooning spider · Passive flight · Hurricane · Clear-air turbulence Atmospheric boundary layer

1 Introduction

The study of hazardous weather conditions in the atmosphere is important for public safety. Hurricanes, typhoons, tornadoes, and severe storms can threaten life and property [1]. Clear-air turbulence may cause unsafety in aircraft operation [2]. These hazardous phenomena have been studied and measured via radar, satellite, and stationary instruments. Recently, more direct methods have been employed, such as the National Oceanic and Atmospheric Administration's (NOAA's) deployment of dropsondes from a highly

© Springer International Publishing AG, part of Springer Nature 2018
V. Vouloutsi et al. (Eds.): Living Machines 2018, LNAI 10928, pp. 110–114, 2018.
https://doi.org/10.1007/978-3-319-95972-6_12

instrumented aircraft and the Taiwan Aerosonde Team's (TAT's) operation of an aerosonde (unmanned air vehicle) to acquire more accurate data [3, 4]. However, these methods are risky and relatively expensive and require highly experienced personnel [4].

In researching severe and unknown weather conditions, the passive flight mechanism may be useful due to its adaptability and high robustness [5]. For many years, the authors have studied passive flight in spiders utilizing fine, flexible silk filaments for aerial dispersal. The authors hypothesized that shear flow and vorticity (i.e., coherent structure) in atmospheric turbulence enhance the spiders' buoyancy and allow them to achieve long-range dispersal [6]. In this paper, we propose a macroscopic model for ballooning flight at the kilogram scale. This model can be used to research clear-air turbulence, hurricanes, typhoons, and tornadoes.

2 Characteristics of a Spider's Ballooning Structure

In a recent study, Cho et al. [6] showed how spiders use abundant nanoscale multi-fibers for aerial dispersal. These flexible silk filaments adapt to turbulent airflow, enhancing the buoyancy of the spider [6–8] (Fig. 1). Cho et al. explained that low-Reynolds-number fluid dynamics—in which the viscous force of the air is much more dominant than the inertial force of the air, —plays a vital role in ballooning flight. The low-Reynolds-number fluid dynamics in spider ballooning is characterized firstly by the large drag coefficient of a filament, because of the dominant viscous flow, and secondly by the anisotropic drag of a filament, which means that the drag of a filament changes according to the direction of the fluid flow [9, 10].

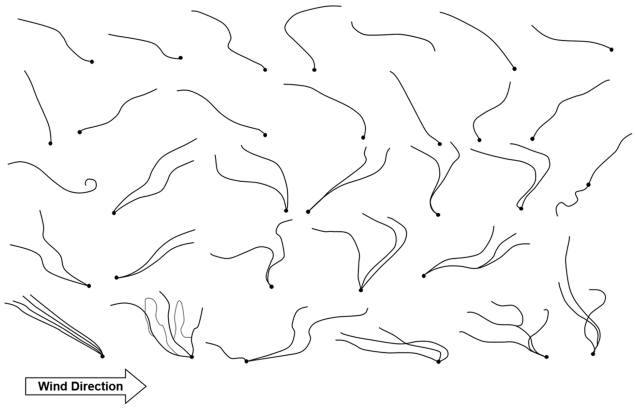

Fig. 1. Sketches of the ballooning structure (i.e., spider body and silk filaments) affected by turbulence in the atmospheric boundary layer [6].

The characteristics of a spider's ballooning structure can be summarized as follows:

1. The filament should generate enough aerodynamic drag to counteract its weight.
2. The ratio of normal drag to tangential drag should be about 2:1.

3. The filament should be highly flexible.
4. Most of the weight should be located at one end of the filament.

Our simulation used a bead-spring model, which is frequently employed in investigating the dynamics of microswimmers and in polymer physics [11]; it revealed that the settling speed of the ballooning structure in low-Reynolds-number shear flow decreases as the shear rate increases (Fig. 2). This reduction in the settling speed is caused firstly by the geometrical shape of the ballooning structure and secondly by the generation of fluid-dynamic forces in nonuniform flows. Additionally, we found that the ballooning structure could become trapped in a vortex flow.

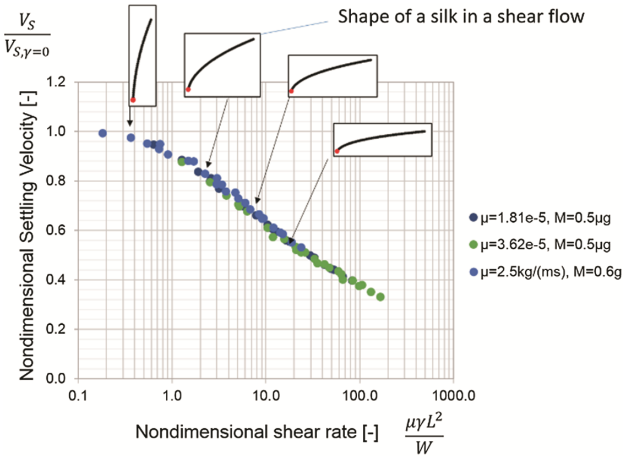

Fig. 2. Influence of shear flow on the ballooning structure simulated using a bead-spring model. V_S: settling speed, $V_{S,\gamma=0}$: settling speed at a shear rate of zero, μ: dynamic viscosity of the fluid, L: length of the filament, W: weight of the body.

3 Design and Fabrication of the Ballooning Structure

Spiders' ballooning flight is dominated by low-Reynolds-number flow (i.e., Stokes flow, which has a Reynolds number lower than 1) due to their extremely thin ballooning filaments (about 200 nm wide). In this flow regime, the drag coefficient of a certain object is tens to hundreds of times greater than that of objects in high-Reynolds-number flow [10]. The scaling up of this mechanism is problematic because the structure loses the characteristics of low-Reynolds-number flow as it becomes large. There is an over 10^4-scale difference in weight between the spider system and a payload system; the weight of *Xysticus* spp. is 25 mg, while the weight of a payload is about 1–2.5 kg. To mimic the ballooning dynamics of spiders, we designed an ultralight membranous structure. The basic unit of the structure is a three-dimensional quasi-isotropic membrane structure, the drag of which is quasi-independent of the flow direction (Fig. 3A). This single structure is called an isotropic kite, and it is possible to create a chain of kites.

The drag of the chain then becomes anisotropic, similar to that of a thin filament in low-Reynolds-number flow (Fig. 3B, C). Large ballooning spiders utilize multiple fine fibers; however, here, we use the single-silk case to experimentally identify the characteristics of the structure. In the experimental stage, the structure will first be launched with the help of a weather balloon and then released at a suitable altitude. If this chain-like structure is positioned within suitable turbulent flows, we expect that it will maintain buoyancy for long periods.

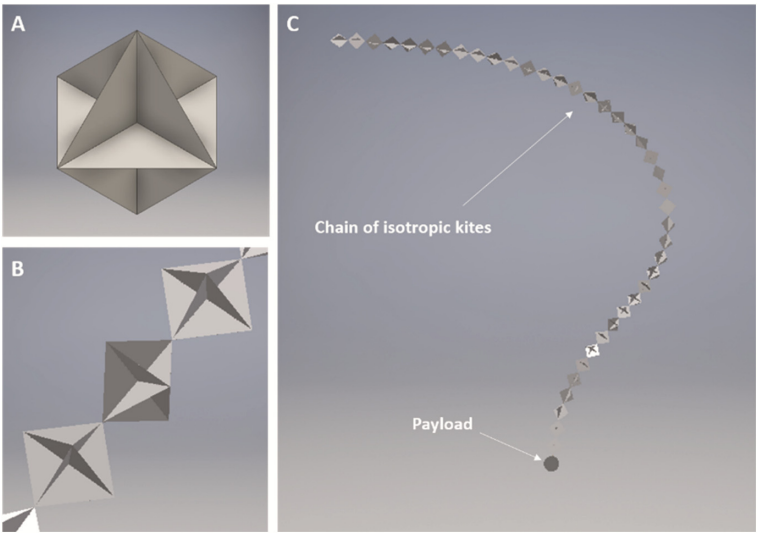

Fig. 3. (A) An isotropic kite. (B) A chain of isotropic kites. (C) A ballooning structure for weather-monitoring missions. The payload can transmit data (e.g., GPS, triple-axis acceleration, pressure, temperature, relative humidity, wind speed, wind direction, etc.) back to the operator directly or via satellites.

Each isotropic kite is designed to be constructed from polyethylene film and a 1-mm-thick carbon rod, and the kites can be connected to one another. At first, the diameter of each isotropic kite will be assumed to be about 40 cm. For a prototype of the ballooning structure, the length of the chain and the maximum weight of the payload will be determined based on wind-tunnel test results.

4 Conclusions and Future Work

To explore severe weather phenomena such as hurricanes, typhoons, tornadoes, and clear-air turbulence, we propose a passive flight structure inspired by spiders' ballooning flight. The structure consists of a chain of multiple quasi-isotropic, membranous kites and a payload at the end of the chain. The chain is highly flexible so that it can adapt to turbulent flow. Passive flight reduces the aerodynamic load on the structure due to its adaptability, decreasing the cost of stabilizing the flying object in turbulence. As the

optimum dimensions for the prototype have not yet been determined, future research will implement wind-tunnel and drop testing.

Acknowledgments. MS.C. was supported by the state of Berlin's Elsa Neumann Scholarship (T61004) during this study.

References

1. Pielke, R.A., Gratz, J., Landsea, C.W., Collins, D., Saunders, M.A., Musulin, R.: Normalized hurricane damage in the United States: 1900–2005. Nat. Hazards Rev. **9**(1), 29–42 (2008). https://doi.org/10.1061/(asce)1527-6988(2008)9:1(29)
2. Golding, W.L.: Turbulence and its impact on commercial aviation. J. Aviat./Aerosp. Educ. Res. **11**(2), 19–29 (2000)
3. Collins, J., Flaherty, P.: The NOAA hurricane hunters: a historical and mission perspective. Fla. Geogr. **45**, 14–27 (2014)
4. Lin, P.H., Lee, C.S.: The eyewall-penetration reconnaissance observation of Typhoon Longwang (2005) with unmanned aerial vehicle, aerosonde. J. Atmos. Oceanic Technol. **25**(1), 15–25 (2008). https://doi.org/10.1175/2007JTECHA914.1
5. Pandolfi, C., Izzo, D.: Biomimetics on seed dispersal: survey and insights for space exploration. Bioinspir. Biomim. **8**(2), 25003 (2013). https://doi.org/10.1088/1748-3182/8/2/025003
6. Cho, M.S., Neubauer, P., Fahrenson, C., Rechenberg, I.: An observational study of ballooning in large spiders: nanoscale multifibers enable large spiders' soaring flight. PLoS bio. **16**(6), e2004405 (2018). http://doi.org/10.1371/journal.pbio.2004405
7. Reynolds, A.M., Bohan, D.A., Bell, J.R.: Ballooning dispersal in arthropod taxa with convergent behaviours: dynamic properties of ballooning silk in turbulent flows. Biol. Lett. **2**(3), 371–373 (2006). https://doi.org/10.1098/rsbl.2006.0486
8. Zhao, L., et al.: Flying spiders: simulating and modeling the dynamics of ballooning. In: Layton, A., Miller, L. (eds.) Women in Mathematical Biology. AWMS, vol. 8, pp. 179–210. Springer, Cham (2017). https://doi.org/10.1007/978-3-319-60304-9_10
9. Childress, S.: Mechanics of Swimming and Flying (Cambridge Studies in Mathematical Biology, 2). Cambridge University Press, Cambridge (1981). https://doi.org/10.1017/cbo9780511569593
10. Tritton, D.J.: Experiments on the flow past a circular cylinder at low Reynolds numbers. J. Fluid Mech. **6**(4), 547 (1959). https://doi.org/10.1017/S0022112059000829
11. Gauger, E., Stark, H.: Numerical study of a microscopic artificial swimmer. Phys. Rev. E. Stat. Nonlin. Soft Matter Phys. **74(2 Pt. 1)**(2), 21907 (2006)

III

CC BY SA

February 25, 2019

Evolution & Behavior

How Spiders Catch the Air for Their Flight

by Moonsung Cho [1] | PhD student

[1]: Technische Universität Berlin, Institut für Bionik und Evolutionstechnik, Berlin, Germany

This Break was edited by Beata Kusmider, *Scientific Editor* - TheScienceBreaker

ABSTRACT

Though most spiders crawl from one location to another, some families of spiders travel through the air. This is known as ballooning. To better understand ballooning, we observed the flying spiders in nature and measured the properties of their ballooning silks in the laboratory.

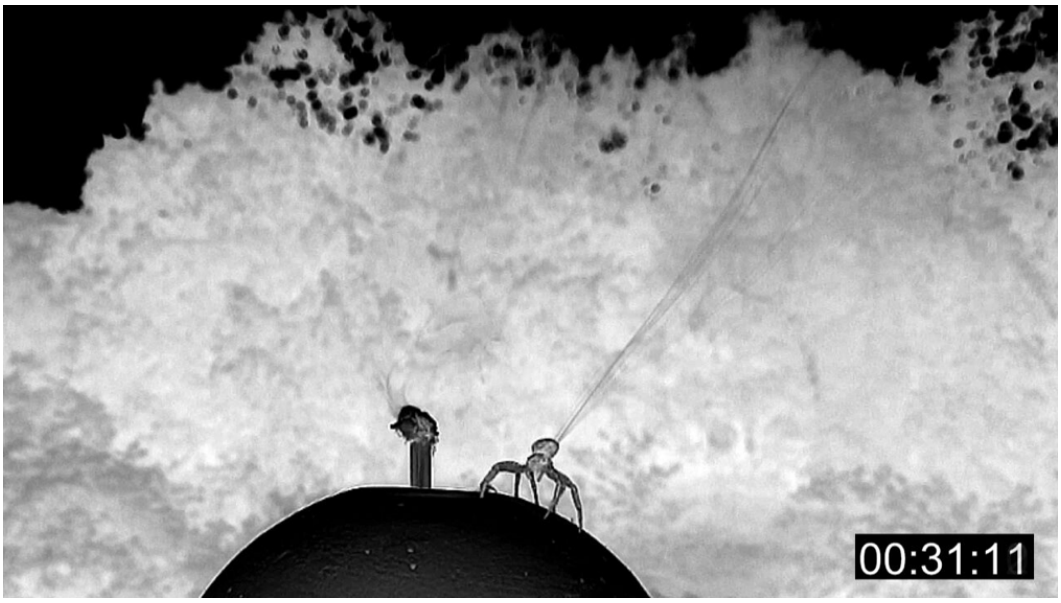

Image credits: Moonsung Cho ©

Bacteria or sperm cells can swim using a hair-like structure. Other organisms use similar structures to fly, like dandelion and thistle seeds with their parachute hairs. But this mode of flying is not limited to plant seeds. One weird aviator is the spider. Using their fine silks, spiders can travel through the air from over tens of meters to hundreds of kilometers. Some spiders were caught in the air at a height of a few kilometers above the ground! This flying behavior of spiders is called ballooning.

Most ballooning spiders are young or small adult spiders, less than 2 mm in length and 2 mg in weight, the size and mass of a millet seed. The young spiders take to the air to escape cannibalism just a few days after birth. Some adult spiders balloon to find a place for a new colony, food and mates. Small spiders become airborne even with light upward wind by producing a single or a few fine silks. These silks are however not enough for the larger ballooning spiders (10 to 150 mg, comparable with the size and mass of a small pill). To understand how spiders - especially the large ones - fly, we recorded and analyzed how spiders prepare and take to the air in nature. We also counted and measured the ballooning silks by inducing spiders to produce them and fly in a wind tunnel.

We selected crab spiders, which are among the relatively large spiders that balloon. We first observed their ballooning in the field, which revealed a couple of new facts. Spiders evaluated the wind

CC BY SA

conditions before taking off by raising their front leg for a few seconds. Spiders produce their silks in specialized glands. A single spider has many different silk glands and spins multiple types of silk. Previously, scientists thought that spiders fly using a thick silk named dragline. We found that crab spiders use the dragline to anchor themselves for safety in the case of failed takeoff. To fly, the spiders produce tens of fine wrapping silks.

After that, we placed spiders in front of a wind tunnel to get samples of the ballooning silks. Measuring the nanoscopically thin ballooning silks in the tunnel is not possible because they flutter in the wind. We had to collect the samples on a glass slide covered with a double-sided adhesive tape. Later, we observed the fibers with a scanning electron microscope, which allows the imaging of very small objects. Crab spiders spin 50 to 60 thin fibers for their flight. The thickness of these fibers is about 200 nm. This is smaller than the wavelength of visible light, 400 to 700 nm. This is why we could not use an optical microscope - visible light passes through this extremely thin silk. We also measured the length of the ballooning silks by winding them on a reel. The ballooning fibers measured 3 meters on average, with the longest reaching 6 meters.

Unlike other flying insects and birds which use their wings, spiders fly by spinning ballooning silks. Although the silks are nanoscopically thin, their length and their number are enough for the spiders to soar up even with a light upward wind. We may question how spiders catch the air with this extremely thin silk. In the macro-world, fluid force acting on an object is proportional to the projected area of that object (like bird wings). In the micro-world, this force is not proportional to the projected area of the object, but to the length of it. The thinness of spider silks keeps the fluid-dynamic character in the micro-world and the length enlarges the fluid force acting on this thin fiber. This is how spiders utilize micro-world dynamics to their advantage.

Similarly to dandelion and thistle seeds, we find hair-like structures in spiders' ballooning. In a microscopic world, this hair-like structure is an efficient structure to produce resistance force in the air. The interesting fact is that spiders are the heaviest organisms using this type of mechanics for their flight. This is possible because spiders produce uniquely thin and strong silks.

Appendix A

Dynamic Motions in a Periodic Cellular Flow

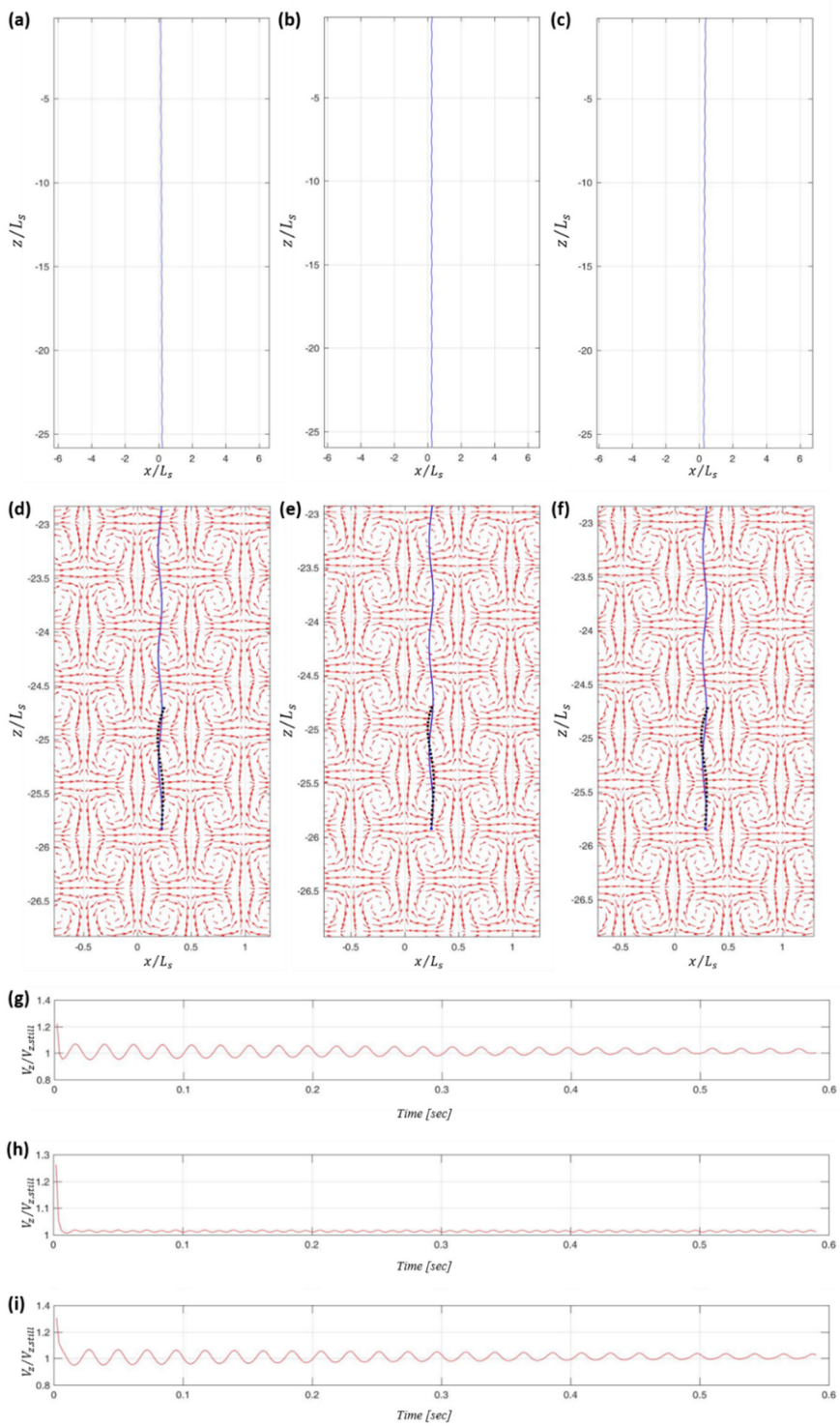

Figure A 1 Eddy crossing $\langle V_z \rangle / V_{z,still} = 1.014$; (a)-(c): Trace plots of a point mass (spider body). (d)-(f): Flow fields and the bead-spring model. (blue lines: trajectory plots). (g)-(i): Nondimensionalised settling speeds over time. $Bn_{vor} = 0.13$ (the number of beads: 30, length: 4.45 m, mass: 1 kg, viscosity: 0.5 kg/ms, vortex velocity: $U_0 = 0.5\, m/s$, size of the vortex cell: $L_c/L_s = 0.5$; (a),(d),(g): $x_0/L_c = 0.25$; (b),(e),(h): $x_0/L_c = 0.5$; (c),(f),(i): $x_0/L_c = 0.75$)

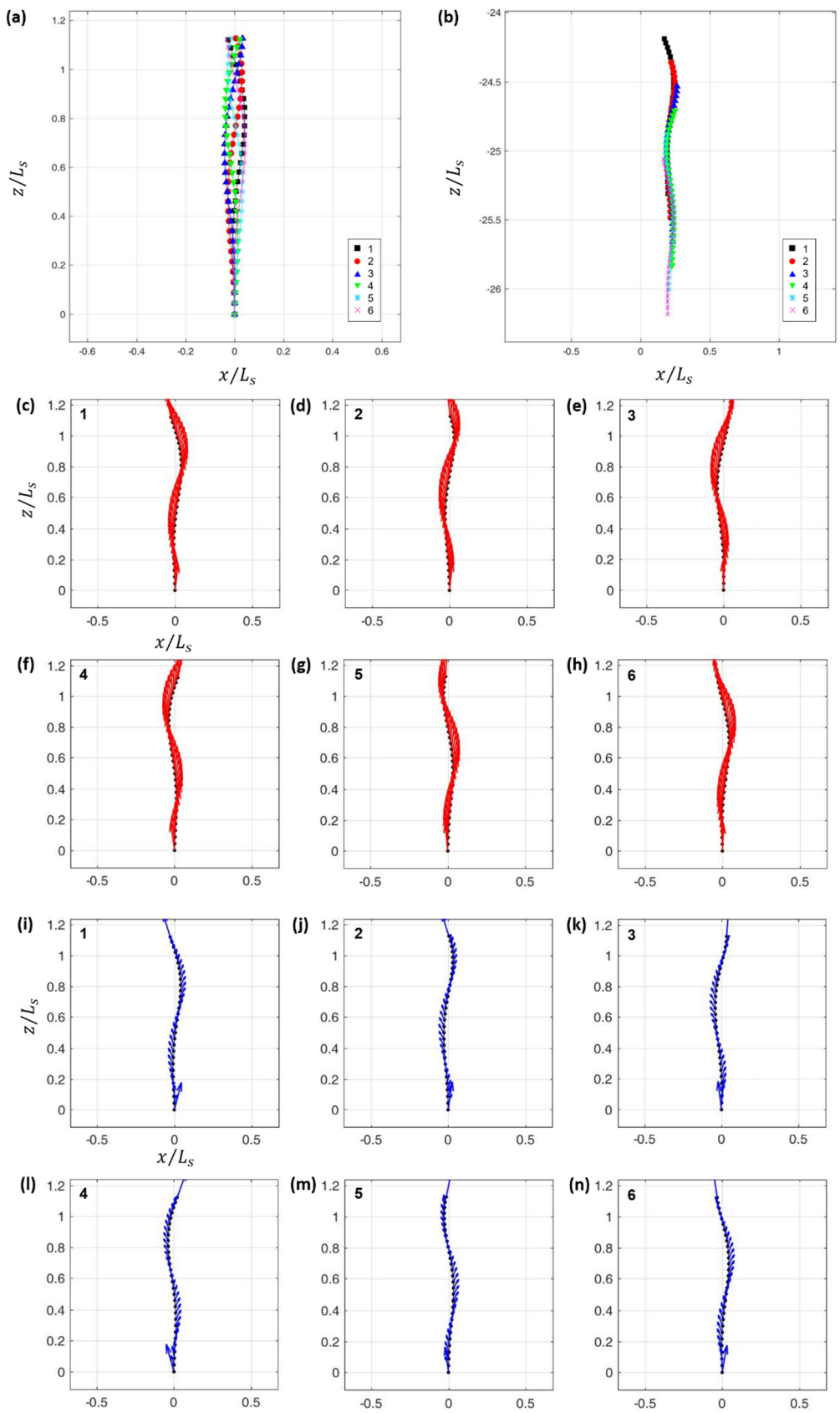

Figure A 2 Eddy crossing $\langle V_z \rangle / V_{z,still} = 1.014$; (a) Shape of a filament during sedimentation in relative coordinate of the lower end. (b) Shape of a filament during sedimentation in absolute coordinate. (c)-(h): Distribution of the relative velocity vectors of the flow. (i)-(n): Distribution of the force vectors by the flow. $Bn_{vor} = 0.13$ (the number of beads: 30, length: 4.45 m, mass: 1 kg, viscosity: 0.5 kg/ms, vortex velocity: $U_0 = 0.5\ m/s$, size of the vortex cell: $L_c/L_s = 0.5$)

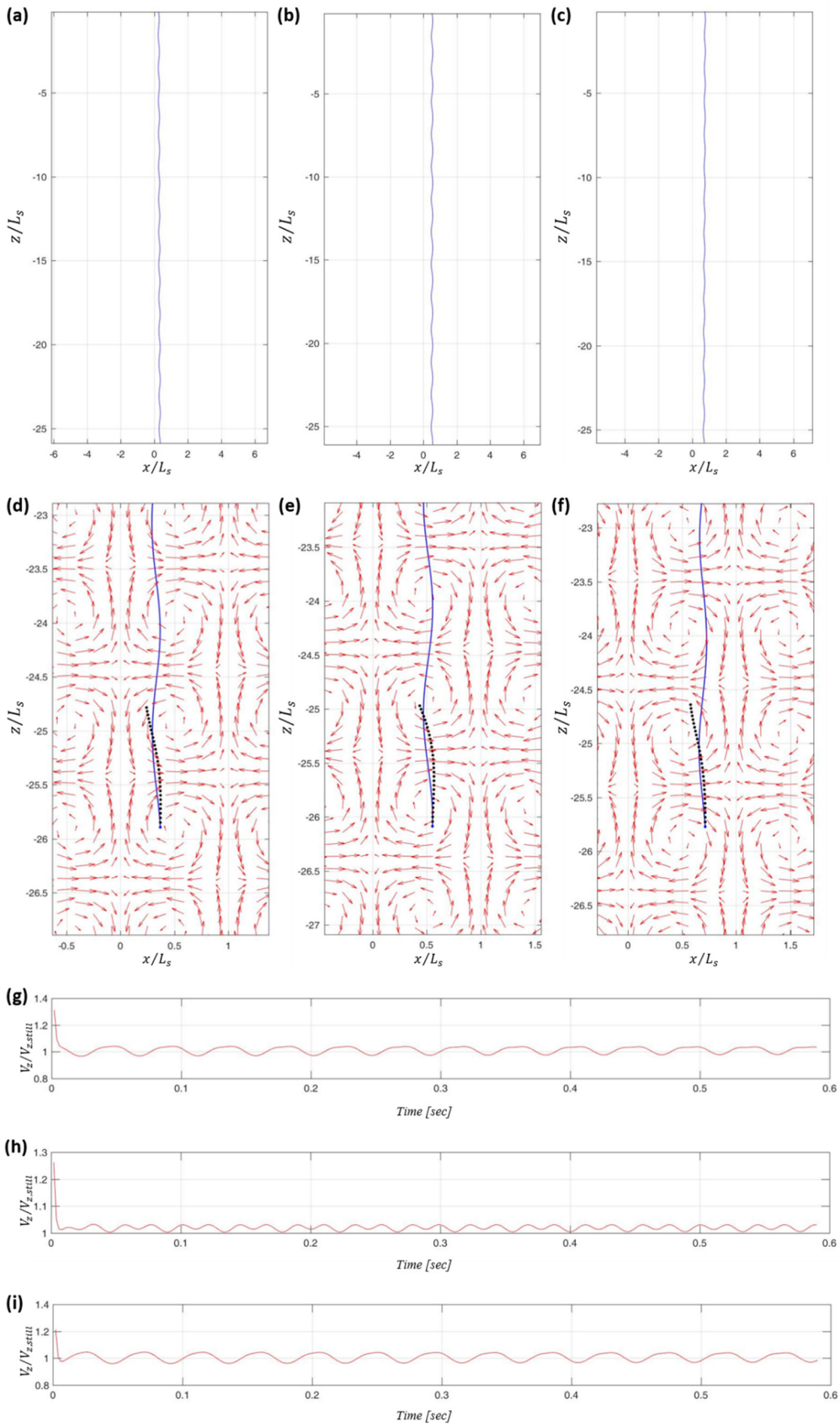

Figure A 3 Eddy crossing $\langle V_z \rangle / V_{z,still} = 1.015$; (a)-(c): Trace plots of a point mass (spider body). (d)-(f): Flow fields and the bead-spring model. (blue lines: trajectory plots). (g)-(i): Nondimensionalised settling speeds over time. $Bn_{vor} = 0.13$ (the number of beads: 30, length: 4.45 m, mass: 1 kg, viscosity: 0.5 kg/ms, vortex velocity: $U_0 = 0.5\ m/s$, size of the vortex cell: $L_c/L_s = 1$; (a),(d),(g): $x_0/L_c = 0.25$; (b),(e),(h): $x_0/L_c = 0.5$; (c),(f),(i): $x_0/L_c = 0.75$)

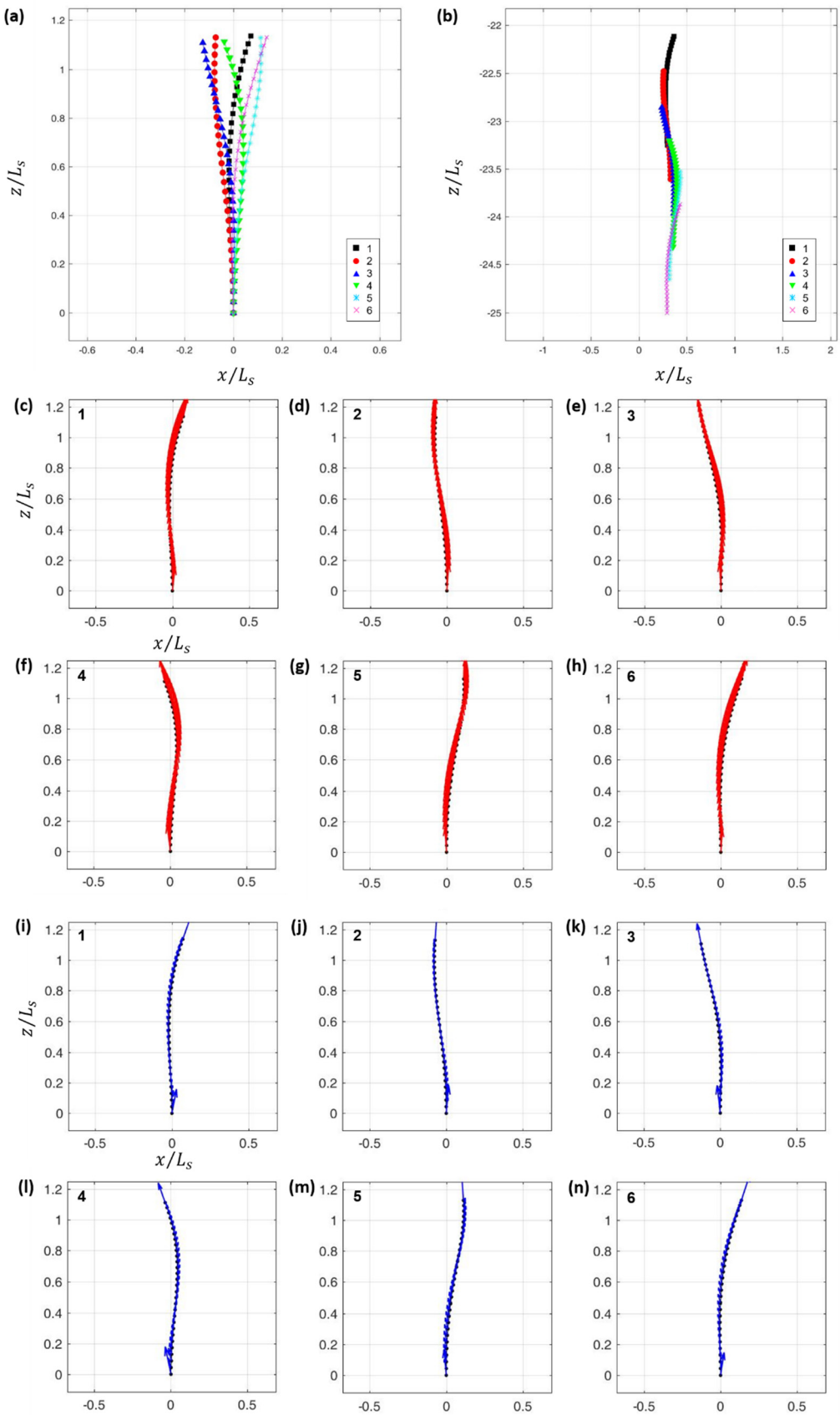

Figure A 4 Eddy crossing $\langle V_z \rangle / V_{z,still} = 1.015$; (a) Shape of a filament during sedimentation in relative coordinate of the lower end. (b) Shape of a filament during sedimentation in absolute coordinate. (c)-(h): Distribution of the relative velocity vectors of the flow. (i)-(n): Distribution of the force vectors by the flow. $Bn_{vor} = 0.13$ (the number of beads: 30, length: 4.45 m, mass: 1 kg, viscosity: 0.5 kg/ms, vortex velocity: $U_0 = 0.5\ m/s$, size of the vortex cell: $L_c/L_s = 1$)

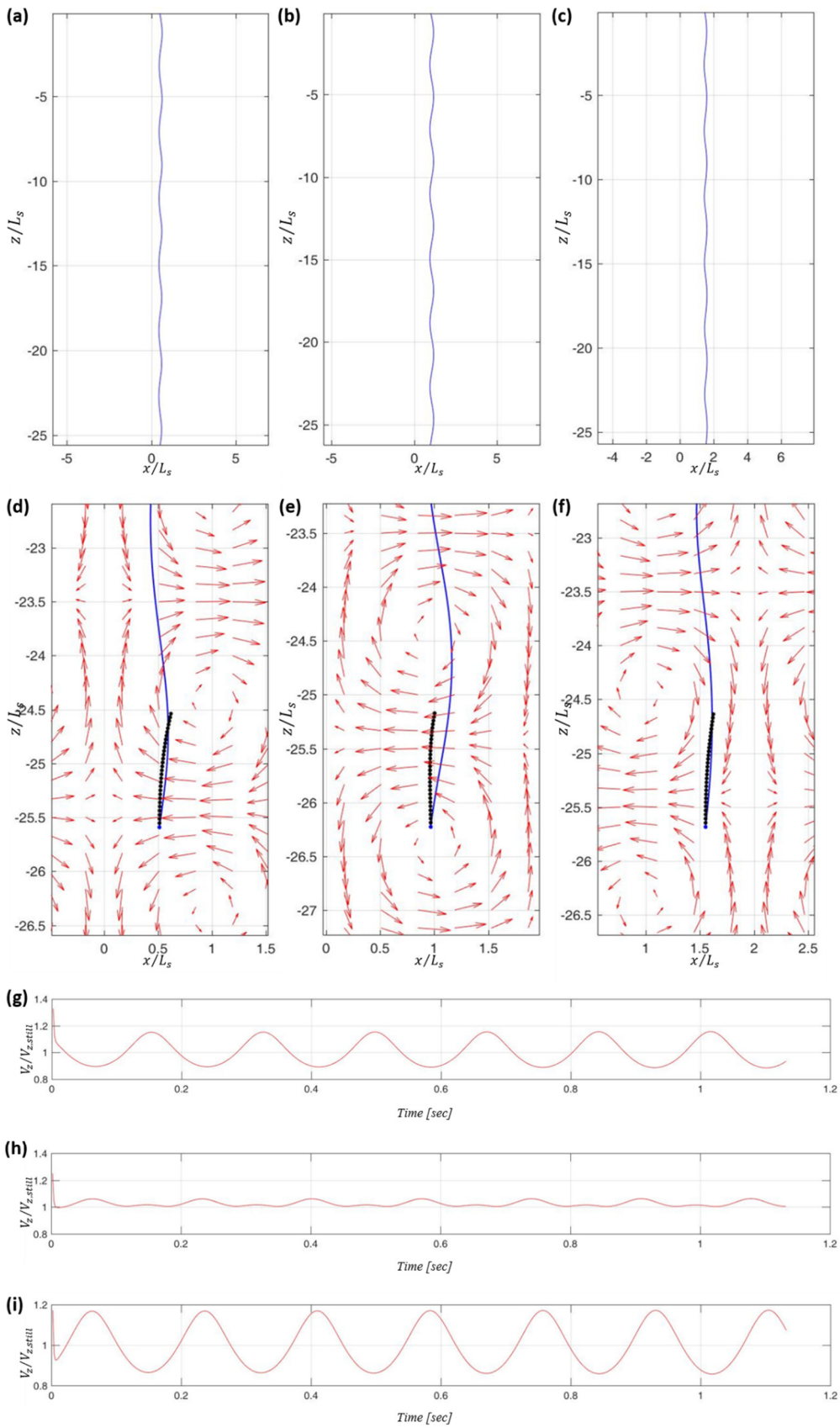

Figure A 5 Eddy crossing $\langle V_z \rangle / V_{z,still} = 1.001$; (a)-(c): Trace plots of a point mass (spider body). (d)-(f): Flow fields and the bead-spring model. (blue lines: trajectory plots). (g)-(i): Nondimensionalised settling speeds over time. $Bn_{vor} = 0.13$ (the number of beads: 30, length: 4.45 m, mass: 1 kg, viscosity: 0.5 kg/ms, vortex velocity: $U_0 = 0.5\ m/s$, size of the vortex cell: $L_c/L_s = 2$; (a),(d),(g): $x_0/L_c = 0.25$; (b),(e),(h): $x_0/L_c = 0.5$; (c),(f),(i): $x_0/L_c = 0.75$)

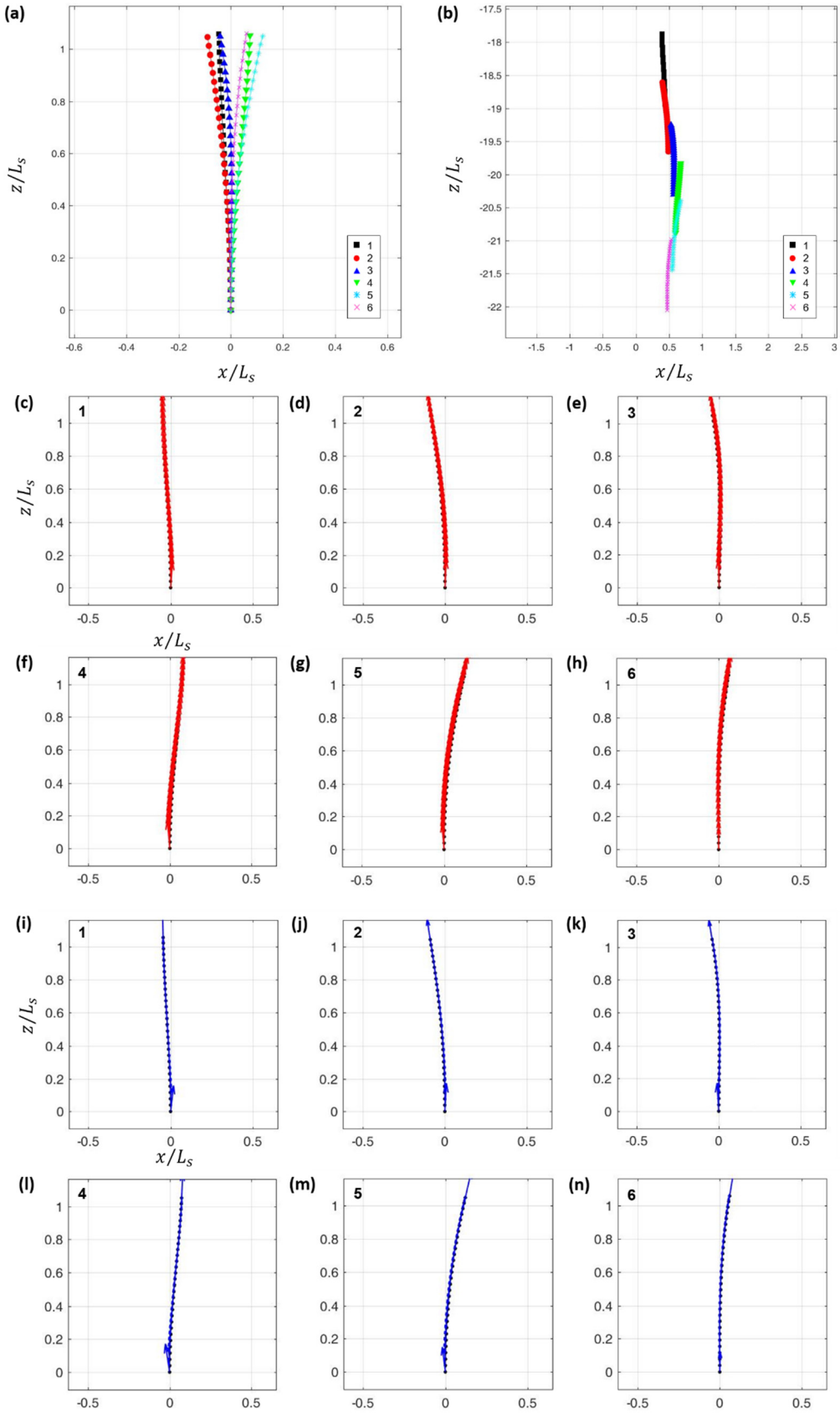

Figure A 6 Eddy crossing $\langle V_z \rangle / V_{z,still} = 1.001$; (a) Shape of a filament during sedimentation in relative coordinate of the lower end. (b) Shape of a filament during sedimentation in absolute coordinate. (c)-(h): Distribution of the relative velocity vectors of the flow. (i)-(n): Distribution of the force vectors by the flow. $Bn_{vor} = 0.13$ (the number of beads: 30, length: 4.45 m, mass: 1 kg, viscosity: 0.5 kg/ms, vortex velocity: $U_0 = 0.5\ m/s$, size of the vortex cell: $L_c/L_s = 2$)

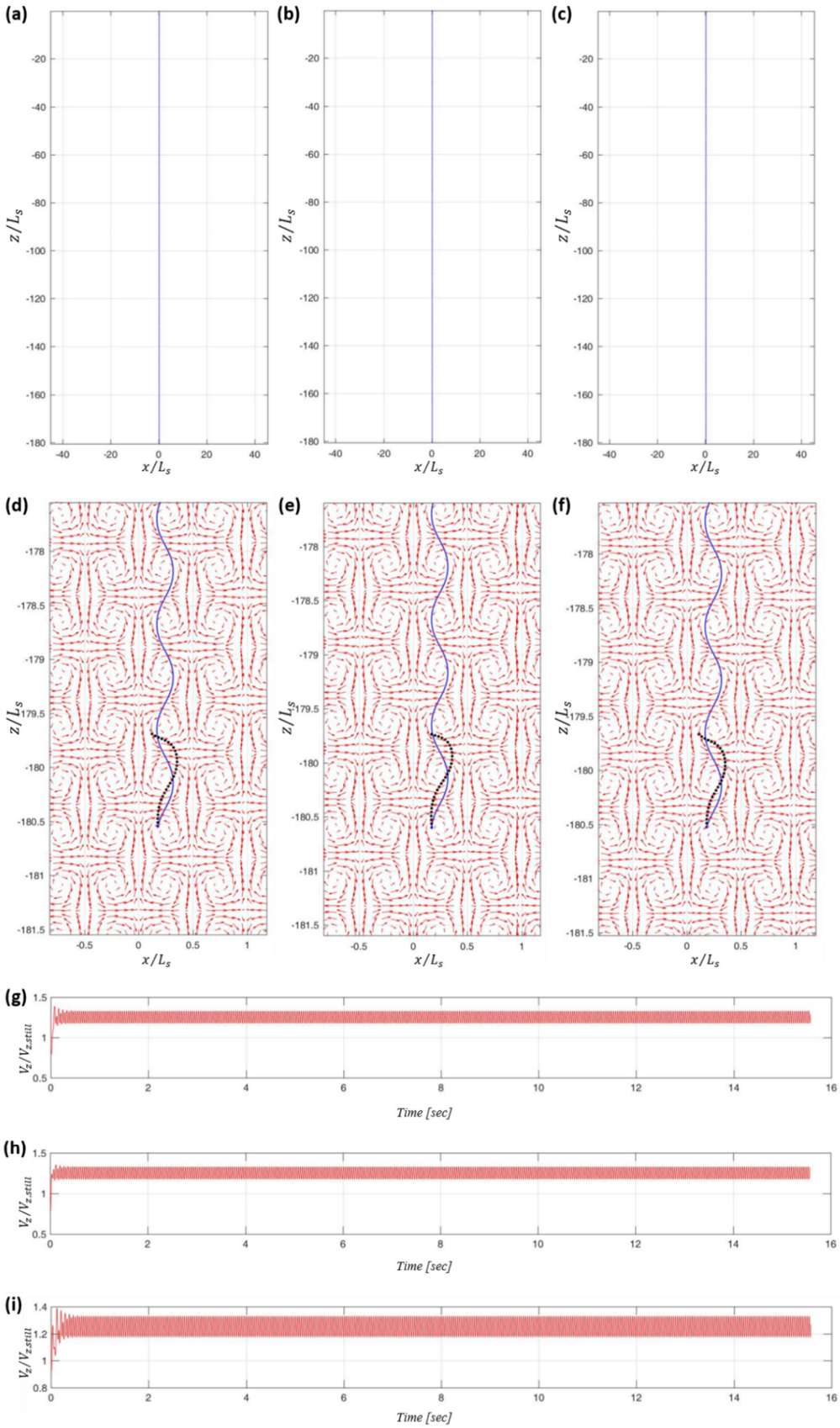

Figure A 7 Fast settling $\langle V_z \rangle / V_{z,still} = 1.251$; (a)-(c): Trace plots of a point mass (spider body). (d)-(f): Flow fields and the bead-spring model. (blue lines: trajectory plots). (g)-(i): Nondimensionalised settling speeds over time. $Bn_{vor} = 0.58$ (the number of beads: 30, length: 4.45 m, mass: 0.2 kg, viscosity: 0.5 kg/ms, vortex velocity: $U_0 = 0.5\, m/s$, size of the vortex cell: $L_c/L_s = 0.5$; (a),(d),(g): $x_0/L_c = 0.25$; (b),(e),(h): $x_0/L_c = 0.5$; (c),(f),(i): $x_0/L_c = 0.75$)

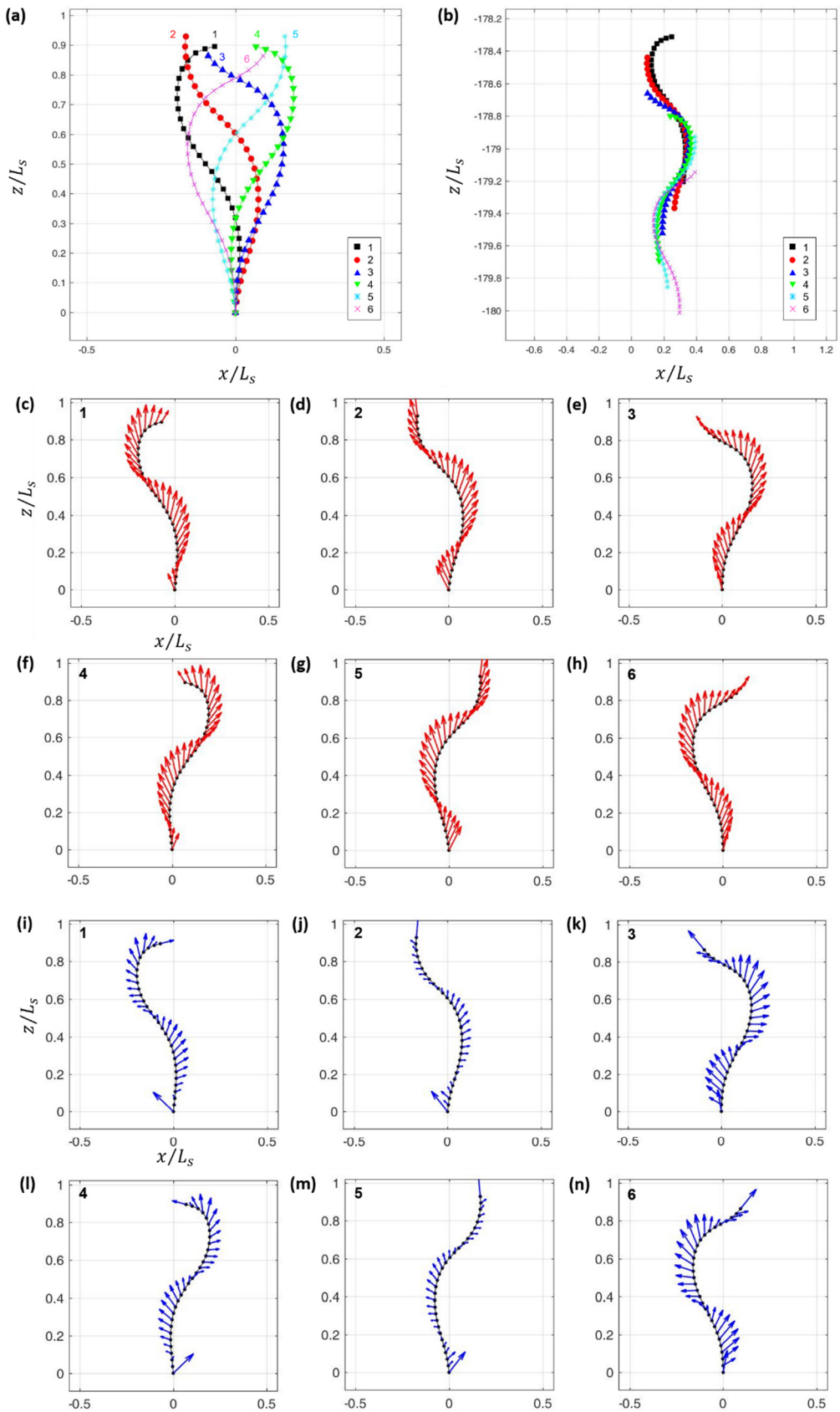

Figure A 8 Fast settling $\langle V_z \rangle / V_{z,still} = 1.251$; (a) Shape of a filament during sedimentation in relative coordinate of the lower end. (b) Shape of a filament during sedimentation in absolute coordinate. (c)-(h): Distribution of the relative velocity vectors of the flow. (i)-(n): Distribution of the force vectors by the flow. $Bn_{vor} = 0.58$ (the number of beads: 30, length: 4.45 m, mass: 0.2 kg, viscosity: 0.5 kg/ms, vortex velocity: $U_0 = 0.5\ m/s$, size of the vortex cell: $L_c/L_s = 0.5$)

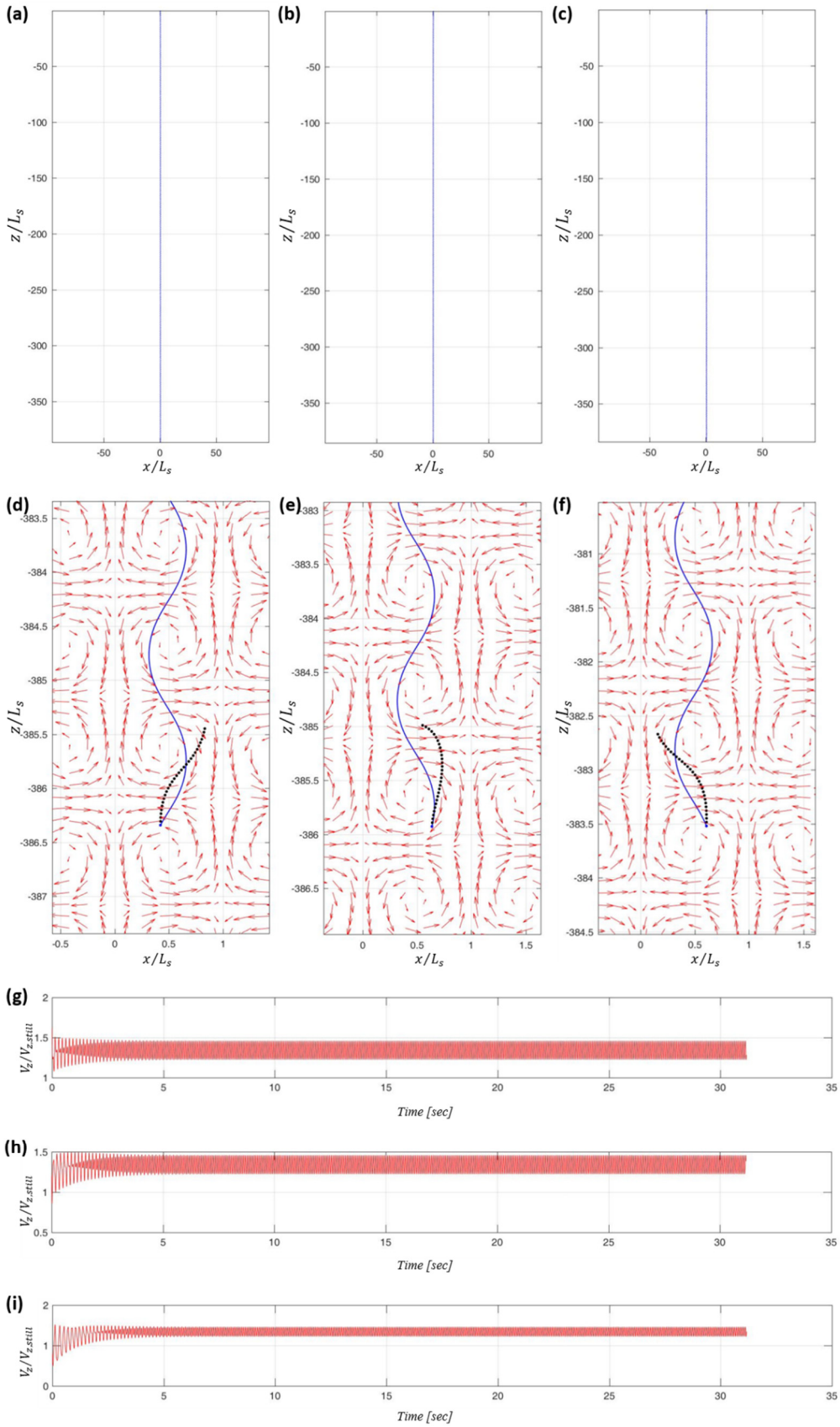

Figure A 9 Fast settling $\langle V_z \rangle / V_{z,still} = 1.328$; (a)-(c): Trace plots of a point mass (spider body). (d)-(f): Flow fields and the bead-spring model. (blue lines: trajectory plots). (g)-(i): Nondimensionalised settling speeds over time. $Bn_{vor} = 0.58$ (the number of beads: 30, length: 4.45 m, mass: 0.2 kg, viscosity: 0.5 kg/ms, vortex velocity: $U_0 = 0.5\ m/s$, size of the vortex cell: $L_c/L_s = 1$; (a),(d),(g): $x_0/L_c = 0.25$; (b),(e),(h): $x_0/L_c = 0.5$; (c),(f),(i): $x_0/L_c = 0.75$)

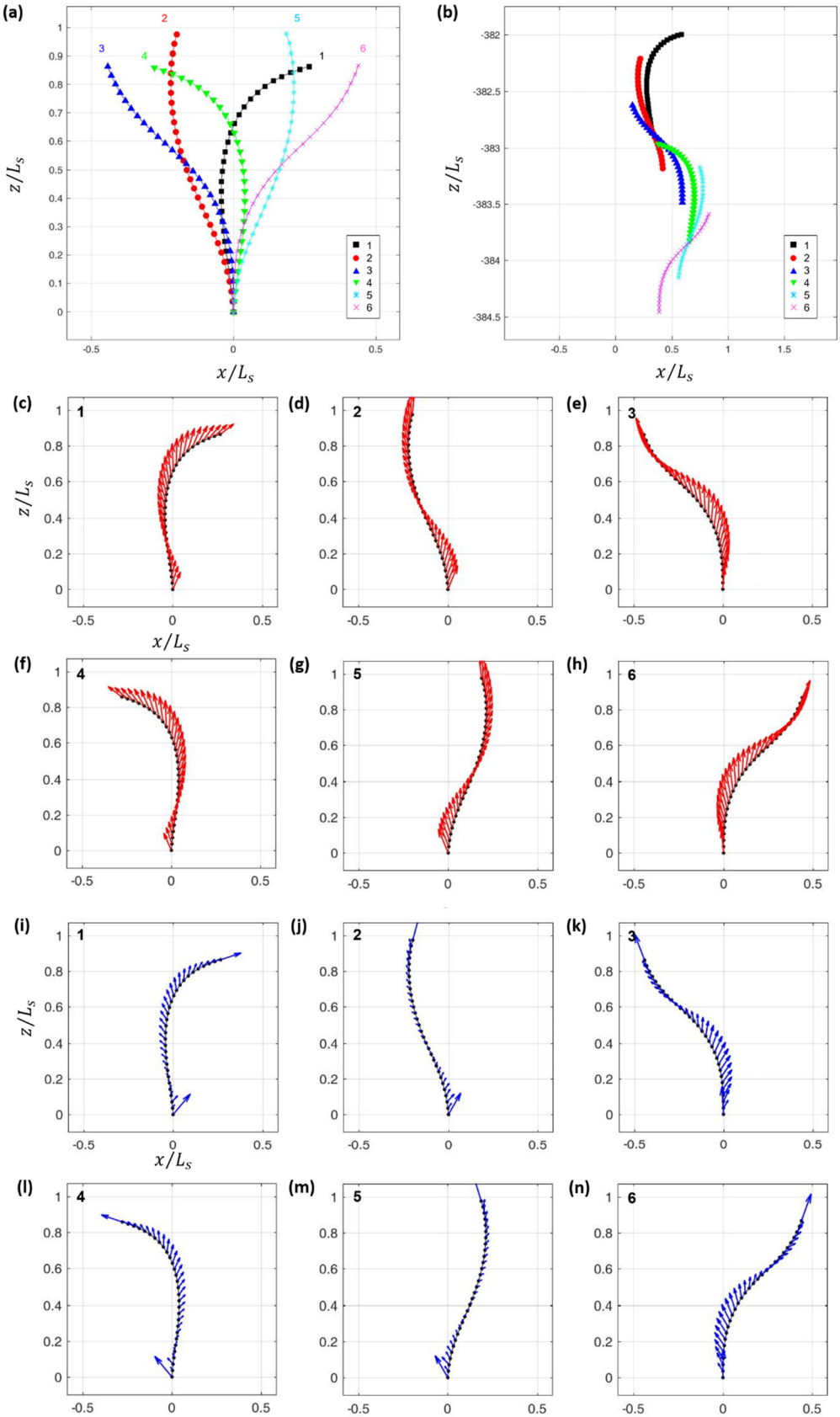

Figure A 10 Fast settling $\langle V_z \rangle / V_{z,still} = 1.328$; (a) Shape of a filament during sedimentation in relative coordinate of the lower end. (b) Shape of a filament during sedimentation in absolute coordinate. (c)-(h): Distribution of the relative velocity vectors of the flow. (i)-(n): Distribution of the force vectors by the flow. $Bn_{vor} = 0.58$ (the number of beads: 30, length: 4.45 m, mass: 0.2 kg, viscosity: 0.5 kg/ms, vortex velocity: $U_0 = 0.5\ m/s$, size of the vortex cell: $L_c/L_s = 1$)

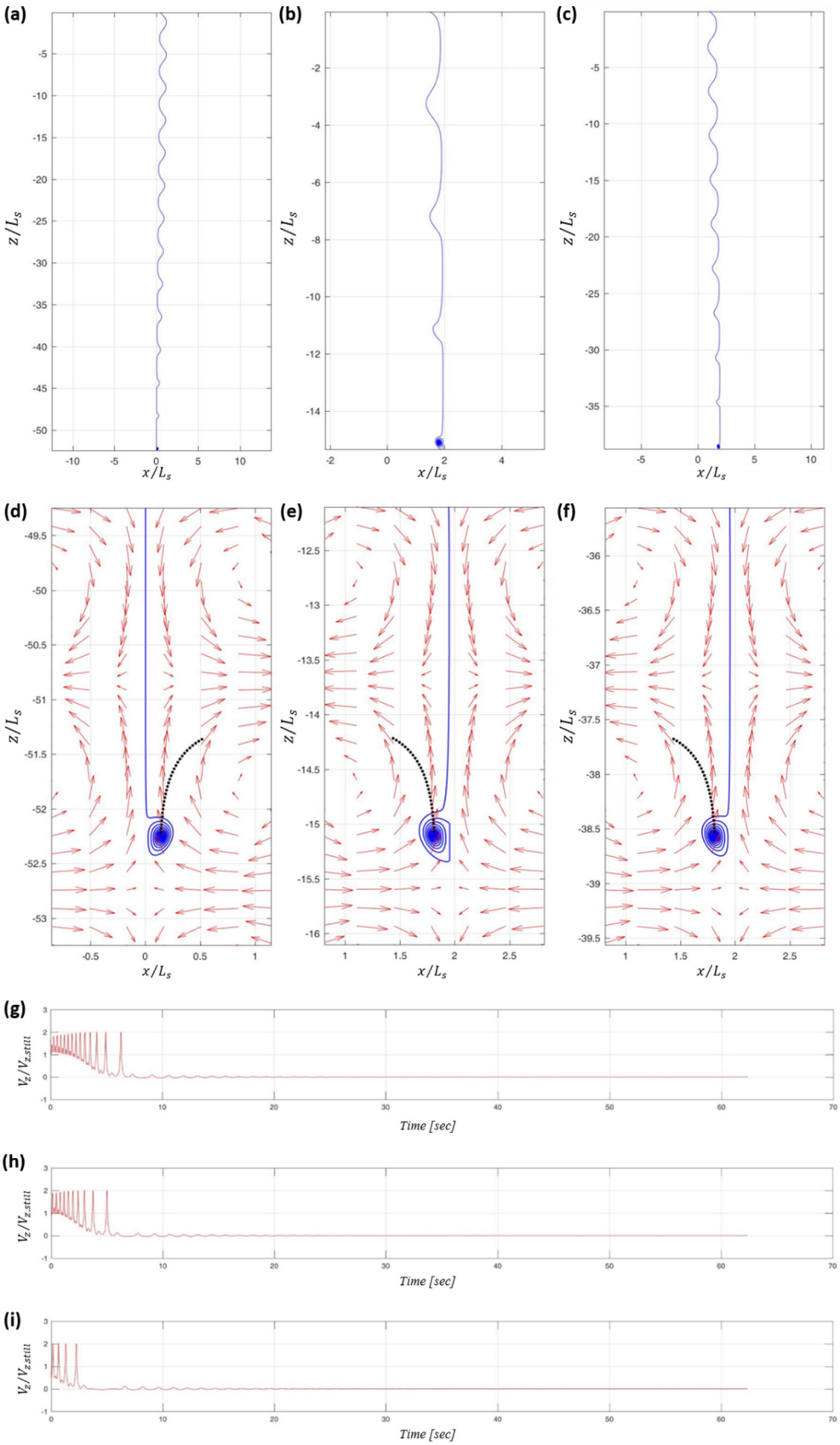

Figure A 11 Trapping $\langle V_z \rangle / V_{z,still} = 0$; (a)-(c): Trace plots of a point mass (spider body). (d)-(f): Flow fields and the bead-spring model. (blue lines: trajectory plots). (g)-(i): Nondimensionalised settling speeds over time. $Bn_{vor} = 0.58$ (the number of beads: 30, length: 4.45 m, mass: 0.2 kg, viscosity: 0.5 kg/ms, vortex velocity: $U_0 = 0.5\ m/s$, size of the vortex cell: $L_c/L_s = 2$; (a),(d),(g): $x_0/L_c = 0.25$; (b),(e),(h): $x_0/L_c = 0.5$; (c),(f),(i): $x_0/L_c = 0.75$)

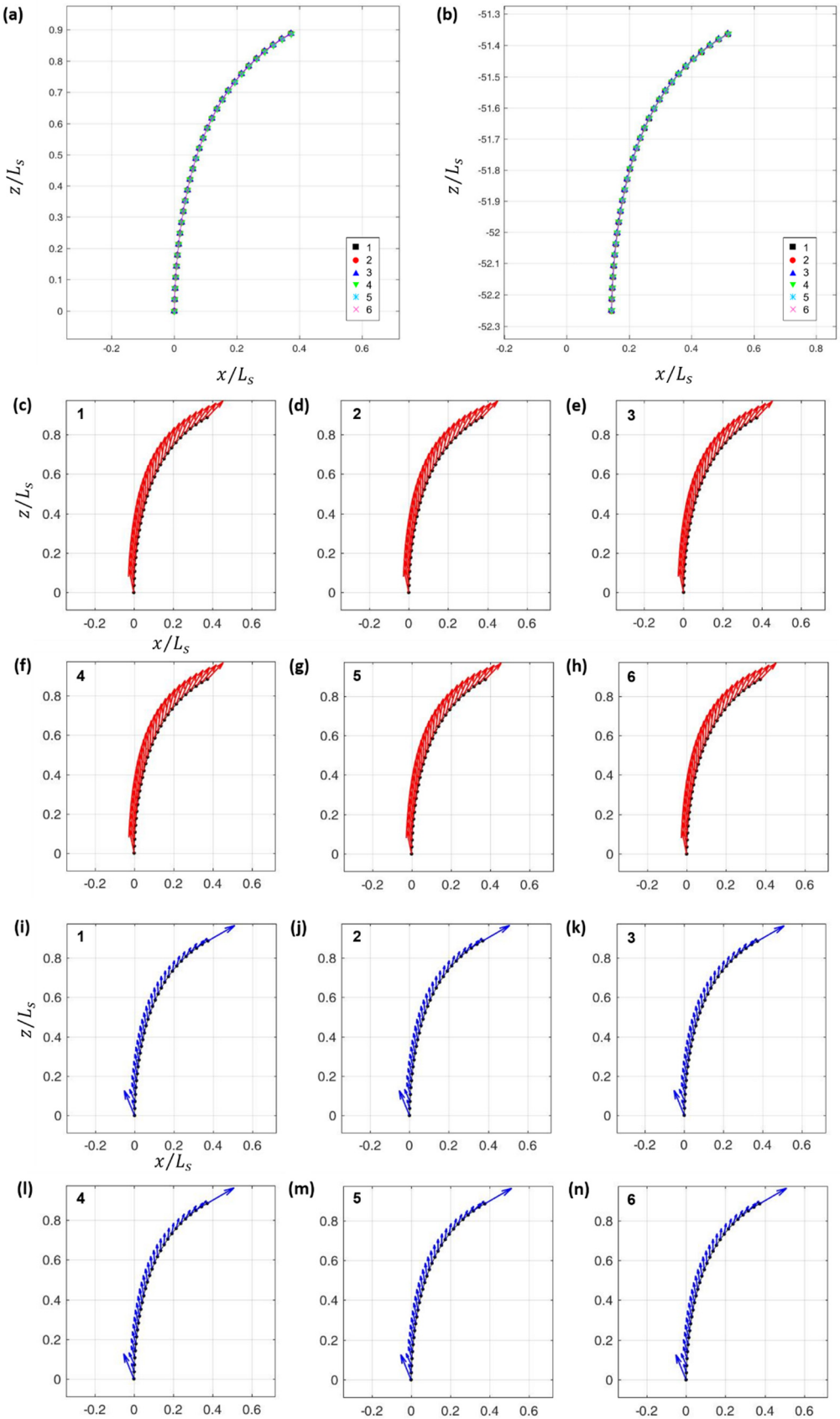

Figure A 12 Trapping $\langle V_z \rangle / V_{z,still} = 0$; (a) Shape of a filament during sedimentation in relative coordinate of the lower end. (b) Shape of a filament during sedimentation in absolute coordinate. (c)-(h): Distribution of the relative velocity vectors of the flow. (i)-(n): Distribution of the force vectors by the flow. $Bn_{vor} = 0.58$ (the number of beads: 30, length: 4.45 m, mass: 0.2 kg, viscosity: 0.5 kg/ms, vortex velocity: $U_0 = 0.5\ m/s$, size of the vortex cell: $L_c/L_s = 2$)

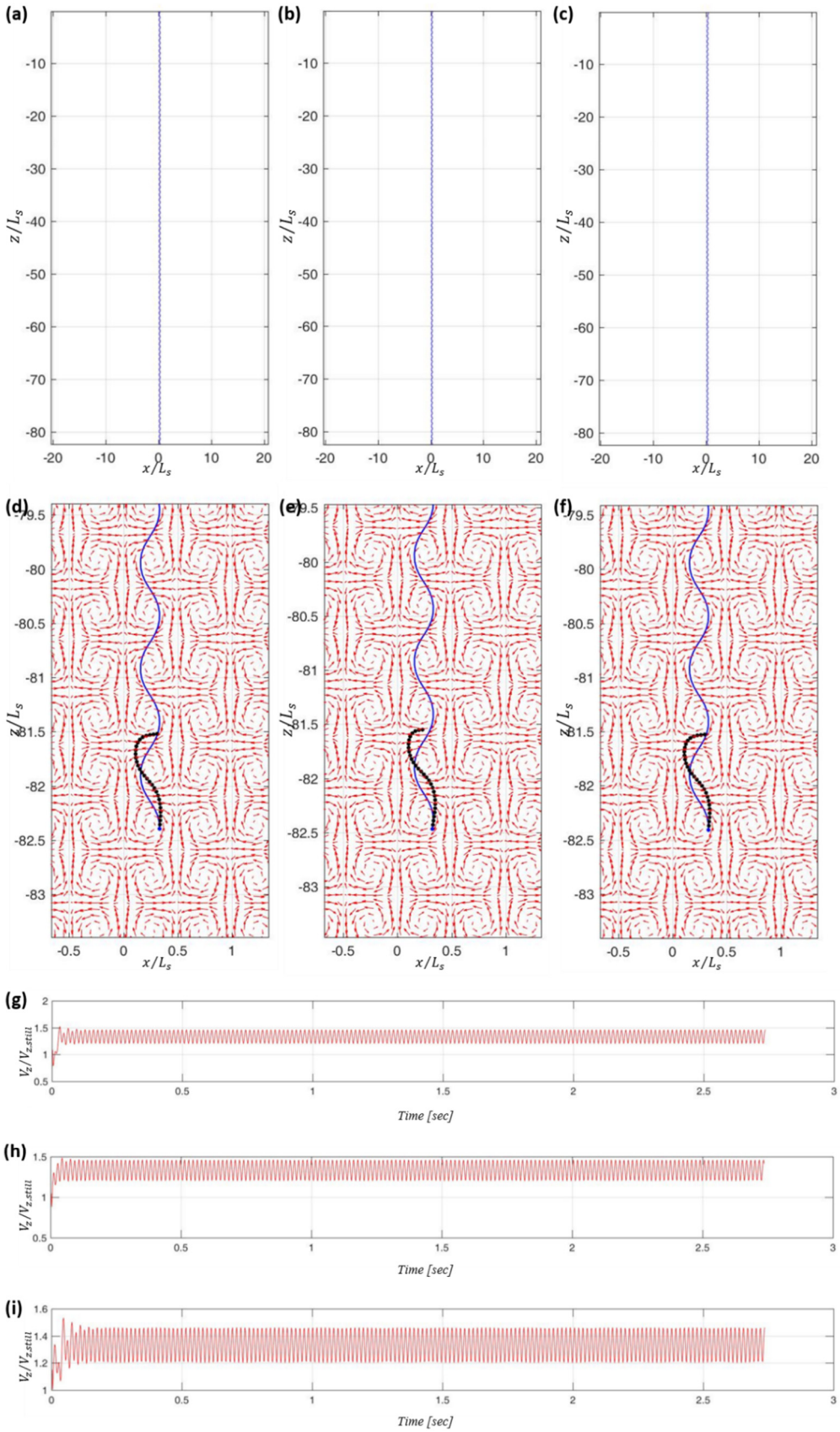

Figure A 13 Fast settling $\langle V_z \rangle / V_{z,still} = 1.335$; (a)-(c): Trace plots of a point mass (spider body). (d)-(f): Flow fields and the bead-spring model. (blue lines: trajectory plots). (g)-(i): Nondimensionalised settling speeds over time. $Bn_{vor} = 0.72$ (the number of beads: 30, length: 4.45 m, mass: 0.5 kg, viscosity: 0.5 kg/ms, vortex velocity: $U_0 = 1.5\, m/s$, size of the vortex cell: $L_c/L_s = 0.5$; (a),(d),(g): $x_0/L_c = 0.25$; (b),(e),(h): $x_0/L_c = 0.5$; (c),(f),(i): $x_0/L_c = 0.75$)

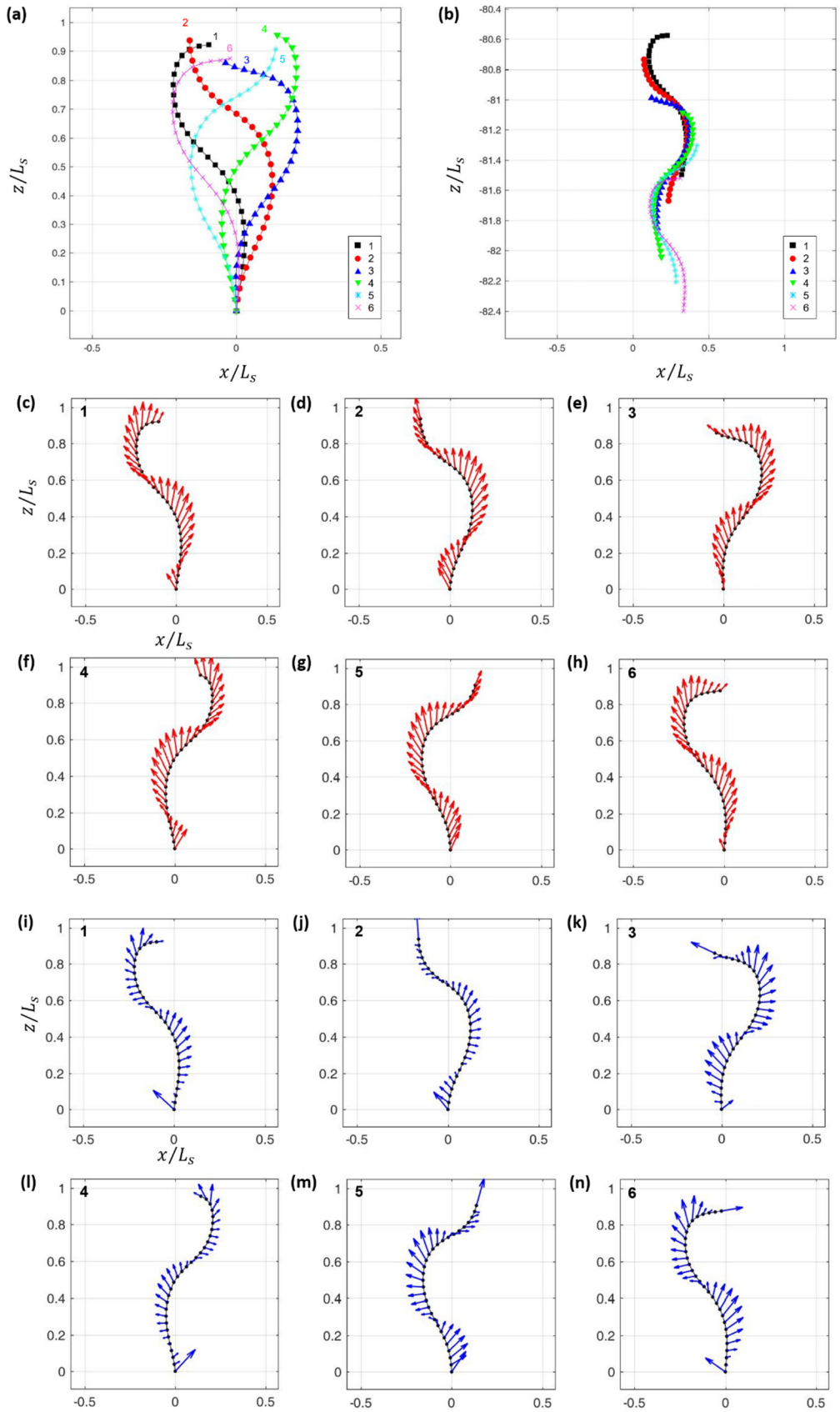

Figure A 14 Fast settling $\langle V_z \rangle / V_{z,still} = 1.335$; (a) Shape of a filament during sedimentation in relative coordinate of the lower end. (b) Shape of a filament during sedimentation in absolute coordinate. (c)-(h): Distribution of the relative velocity vectors of the flow. (i)-(n): Distribution of the force vectors by the flow. $Bn_{vor} = 0.72$ (the number of beads: 30, length: 4.45 m, mass: 0.5 kg, viscosity: 0.5 kg/ms, vortex velocity: $U_0 = 1.5\ m/s$, size of the vortex cell: $L_c/L_s = 0.5$)

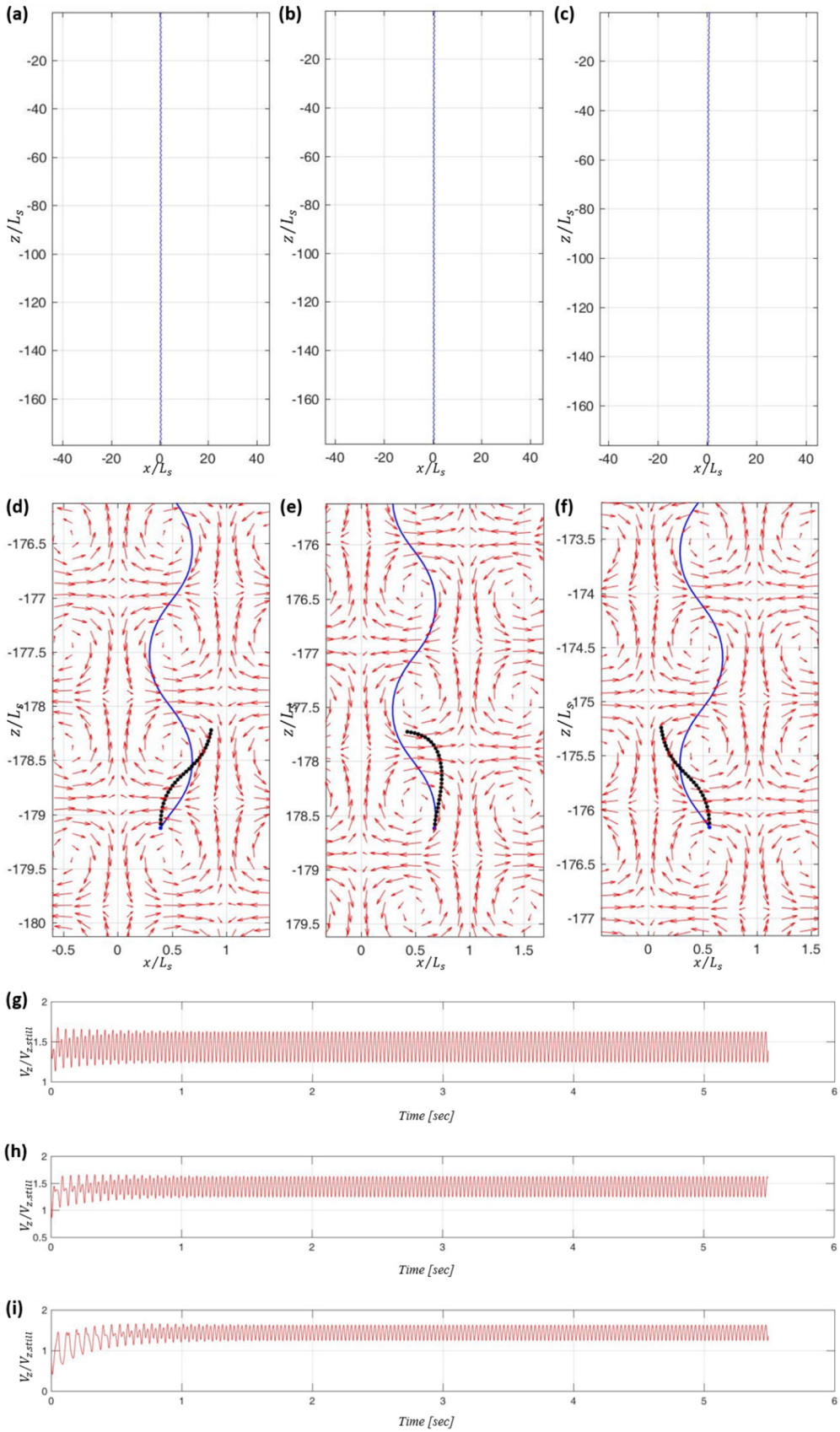

Figure A 15 Fast settling $\langle V_z \rangle / V_{z,still} = 1.446$; (a)-(c): Trace plots of a point mass (spider body). (d)-(f): Flow fields and the bead-spring model. (blue lines: trajectory plots). (g)-(i): Nondimensionalised settling speeds over time. $Bn_{vor} = 0.72$ (the number of beads: 30, length: 4.45 m, mass: 0.5 kg, viscosity: 0.5 kg/ms, vortex velocity: $U_0 = 1.5\ m/s$, size of the vortex cell: $L_c/L_s = 1$; (a),(d),(g): $x_0/L_c = 0.25$; (b),(e),(h): $x_0/L_c = 0.5$; (c),(f),(i): $x_0/L_c = 0.75$)

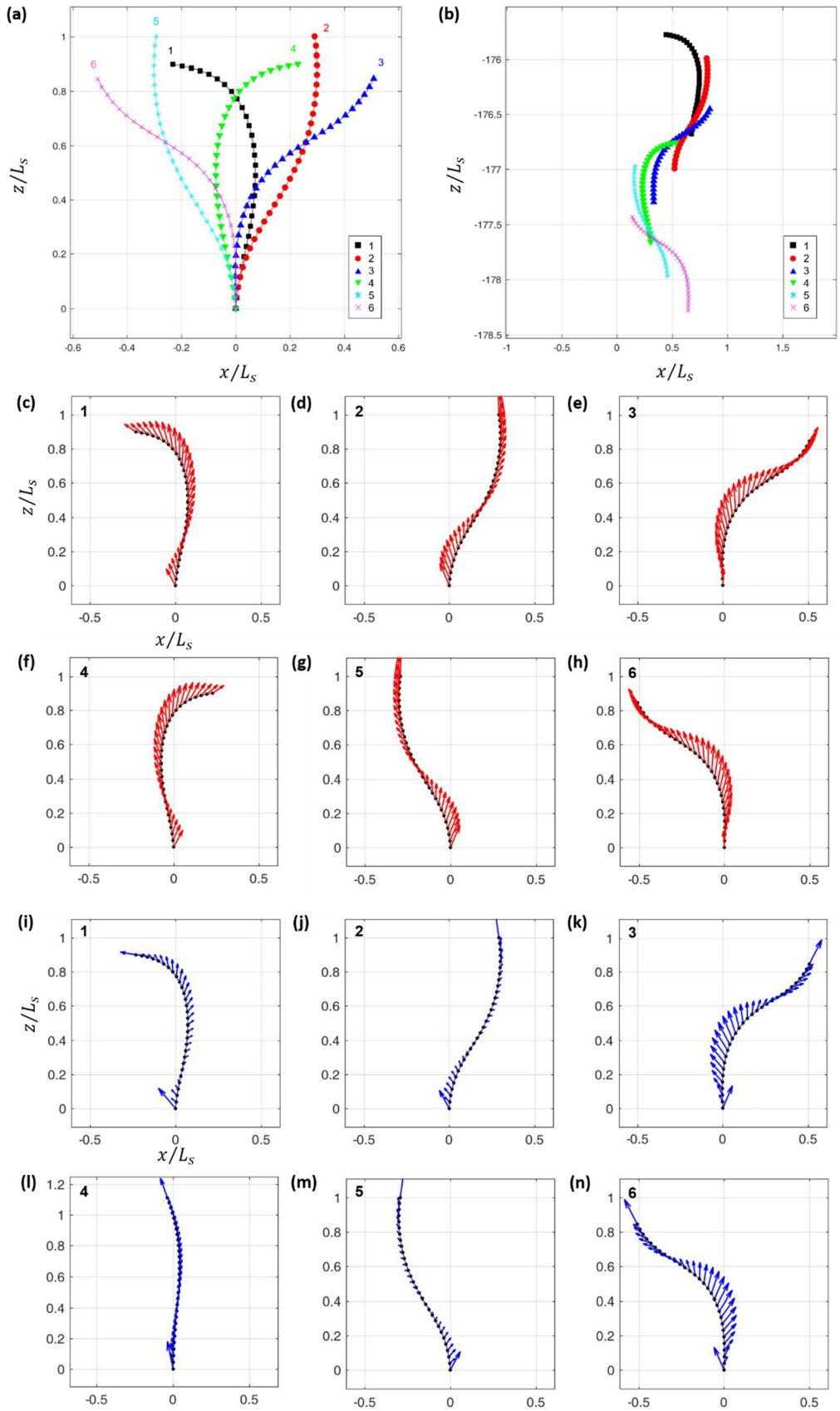

Figure A 16 Fast settling $\langle V_z \rangle / V_{z,still} = 1.446$; (a) Shape of a filament during sedimentation in relative coordinate of the lower end. (b) Shape of a filament during sedimentation in absolute coordinate. (c)-(h): Distribution of the relative velocity vectors of the flow. (i)-(n): Distribution of the force vectors by the flow. $Bn_{vor} = 0.72$ (the number of beads: 30, length: 4.45 m, mass: 0.5 kg, viscosity: 0.5 kg/ms, vortex velocity: $U_0 = 1.5\ m/s$, size of the vortex cell: $L_c/L_s = 1$)

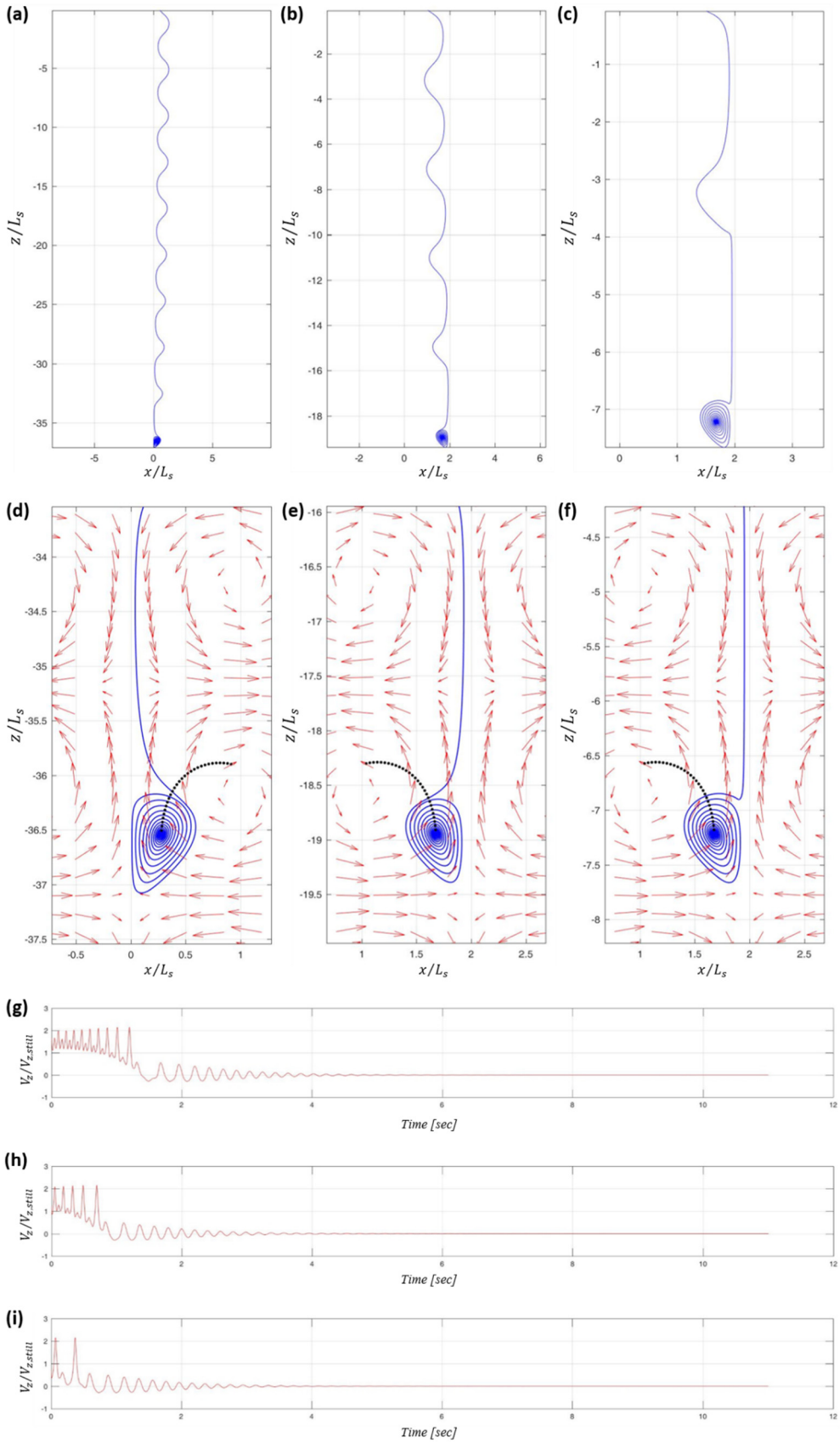

Figure A 17 Trapping $\langle V_z \rangle / V_{z,still} = 0$; (a)-(c): Trace plots of a point mass (spider body). (d)-(f): Flow fields and the bead-spring model. (blue lines: trajectory plots). (g)-(i): Nondimensionalised settling speeds over time. $Bn_{vor} = 0.72$ (the number of beads: 30, length: 4.45 m, mass: 0.5 kg, viscosity: 0.5 kg/ms, vortex velocity: $U_0 = 1.5\ m/s$, size of the vortex cell: $L_c/L_s = 2$; (a),(d),(g): $x_0/L_c = 0.25$; (b),(e),(h): $x_0/L_c = 0.5$; (c),(f),(i): $x_0/L_c = 0.75$)

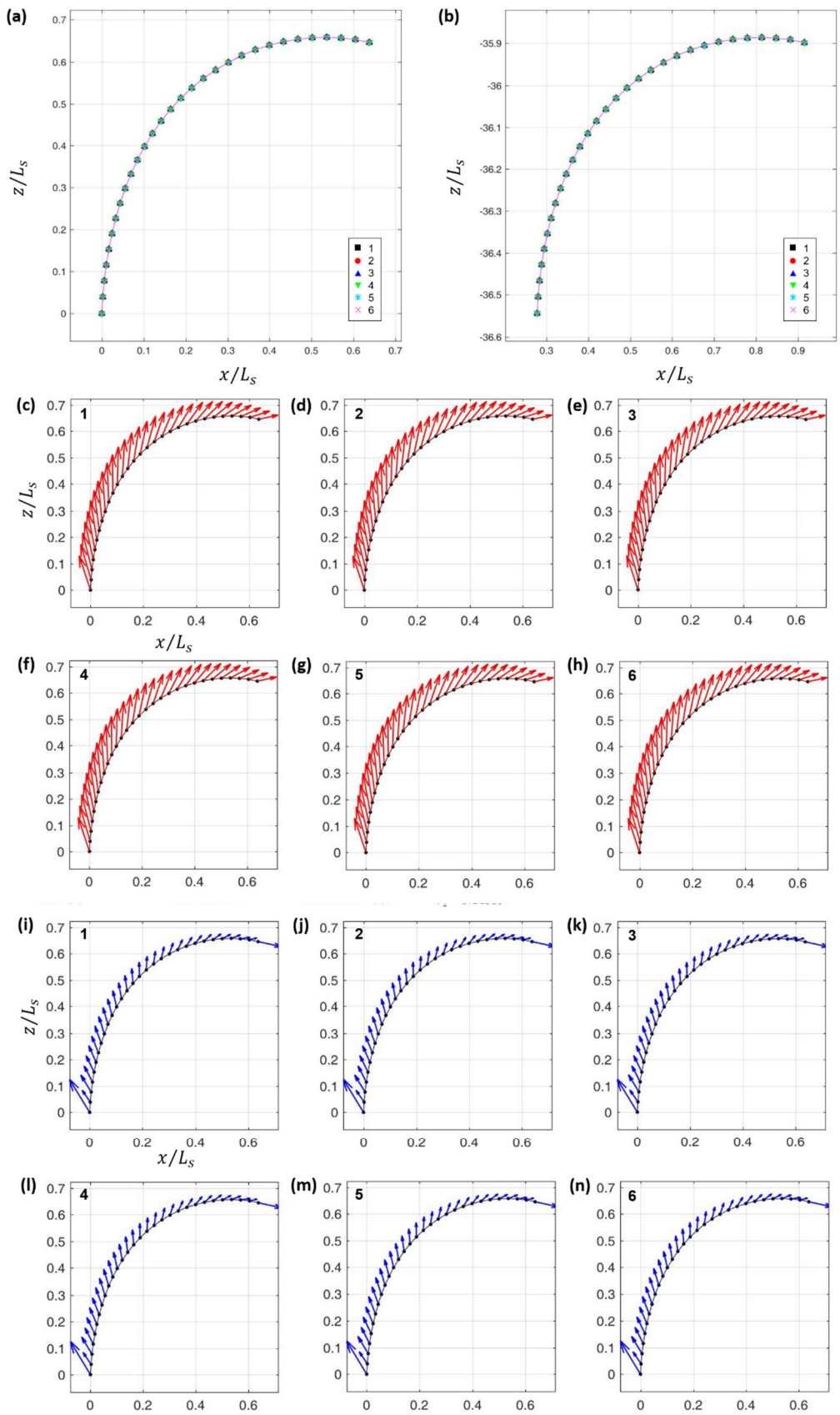

Figure A 18 Trapping $\langle V_z \rangle / V_{z,still} = 0$; (a) Shape of a filament during sedimentation in relative coordinate of the lower end. (b) Shape of a filament during sedimentation in absolute coordinate. (c)-(h): Distribution of the relative velocity vectors of the flow. (i)-(n): Distribution of the force vectors by the flow. $Bn_{vor} = 0.72$ (the number of beads: 30, length: 4.45 m, mass: 0.5 kg, viscosity: 0.5 kg/ms, vortex velocity: $U_0 = 1.5\ m/s$, size of the vortex cell: $L_c/L_s = 2$)

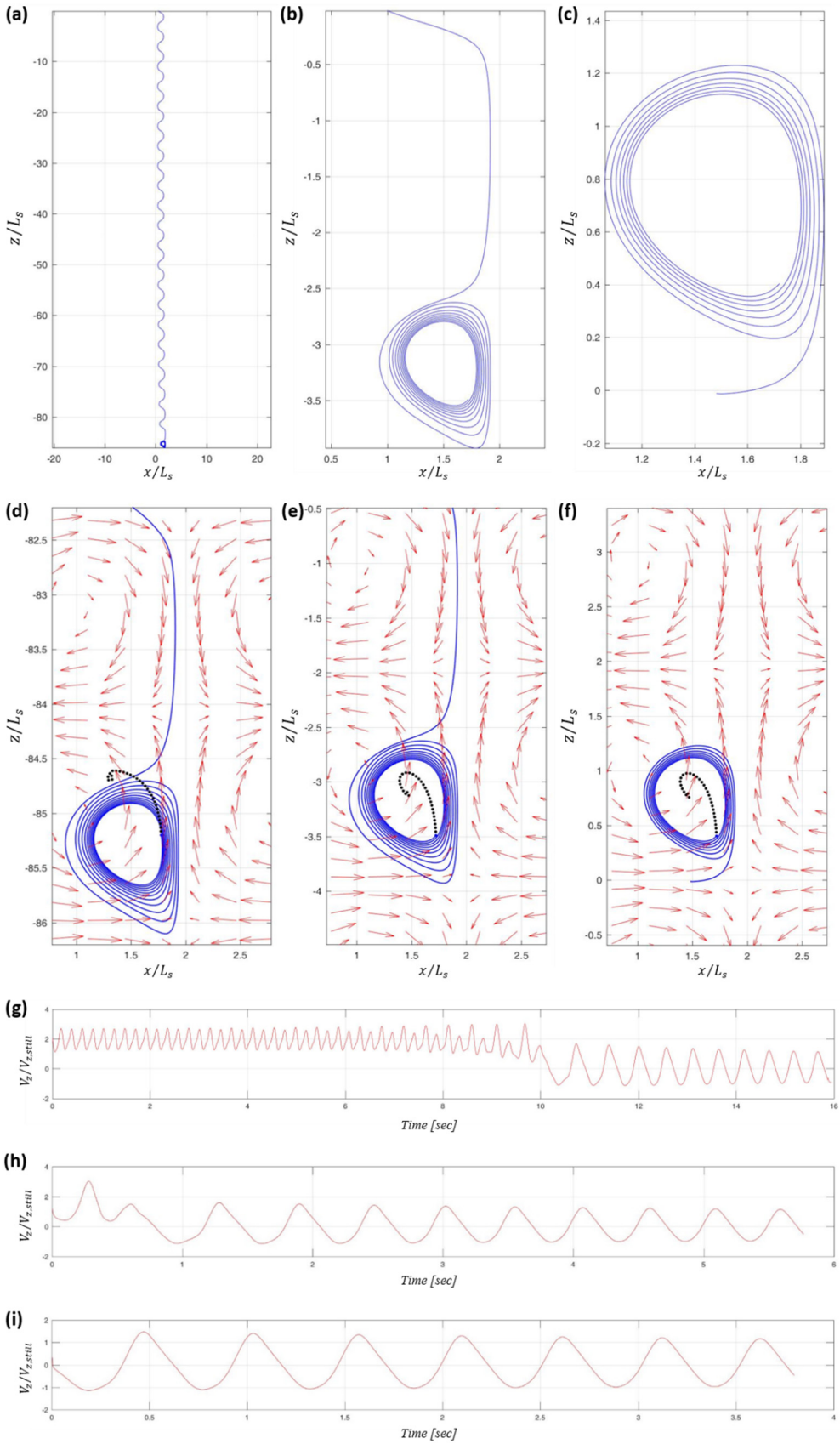

Figure A 19 Trapping $\langle V_z \rangle / V_{z,still} = 0$; (a)-(c): Trace plots of a point mass (spider body). (d)-(f): Flow fields and the bead-spring model. (blue lines: trajectory plots). (g)-(i): Nondimensionalised settling speeds over time. $Bn_{vor} = 1.13$ (the number of beads: 30, length: 4.45 m, mass: 0.1 kg, viscosity: 0.5 kg/ms, vortex velocity: $U_0 = 0.5\ m/s$, size of the vortex cell: $L_c/L_s = 2$; (a),(d),(g): $x_0/L_c = 0.25$; (b),(e),(h): $x_0/L_c = 0.5$; (c),(f),(i): $x_0/L_c = 0.75$)

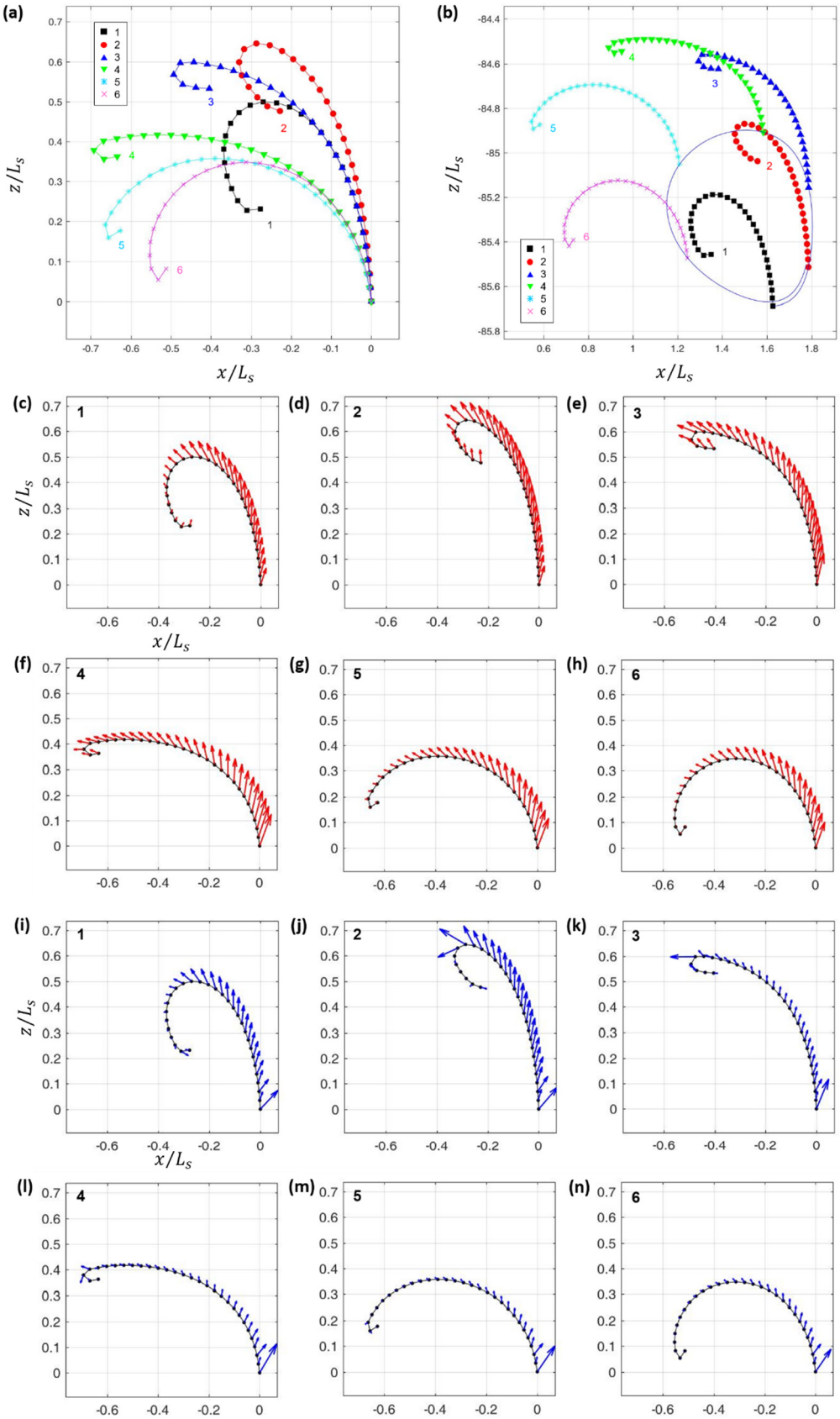

Figure A 20 Trapping $\langle V_z \rangle / V_{z,still} = 0$; (a) Shape of a filament during sedimentation in relative coordinate of the lower end. (b) Shape of a filament during sedimentation in absolute coordinate. (c)-(h): Distribution of the relative velocity vectors of the flow. (i)-(n): Distribution of the force vectors by the flow. $Bn_{vor} = 1.13$ (the number of beads: 30, length: 4.45 m, mass: 0.1 kg, viscosity: 0.5 kg/ms, vortex velocity: $U_0 = 0.5\ m/s$, size of the vortex cell: $L_c/L_s = 2$)

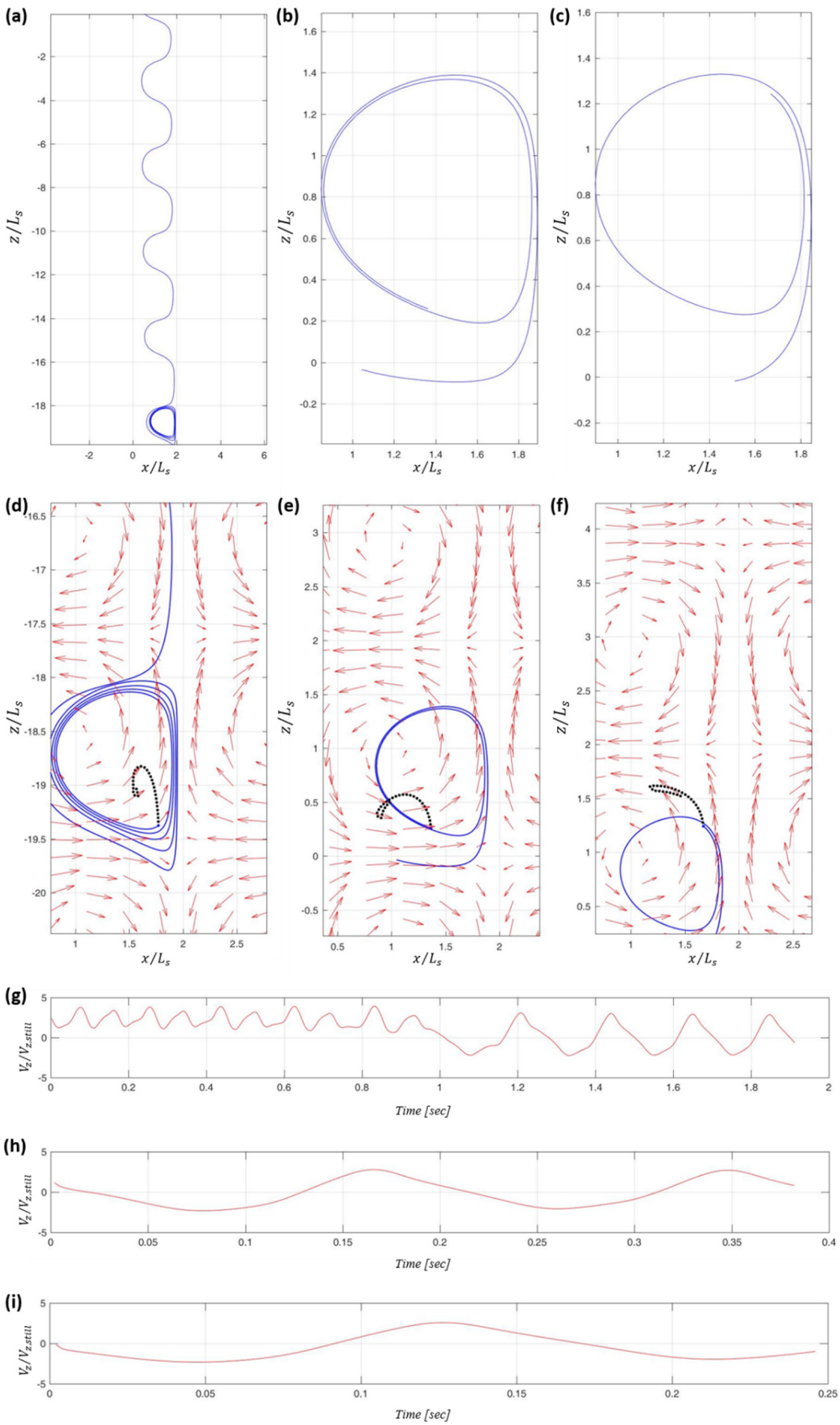

Figure A 21 Trapping $\langle V_z \rangle / V_{z,still} = 0$; (a)-(c): Trace plots of a point mass (spider body). (d)-(f): Flow fields and the bead-spring model. (blue lines: trajectory plots). (g)-(i): Nondimensionalised settling speeds over time. $Bn_{vor} = 1.72$ (the number of beads: 30, length: 4.45 m, mass: 0.2 kg, viscosity: 0.5 kg/ms, vortex velocity: $U_0 = 1.5\ m/s$, size of the vortex cell: $L_c/L_s = 2$; (a),(d),(g): $x_0/L_c = 0.25$; (b),(e),(h): $x_0/L_c = 0.5$; (c),(f),(i): $x_0/L_c = 0.75$)

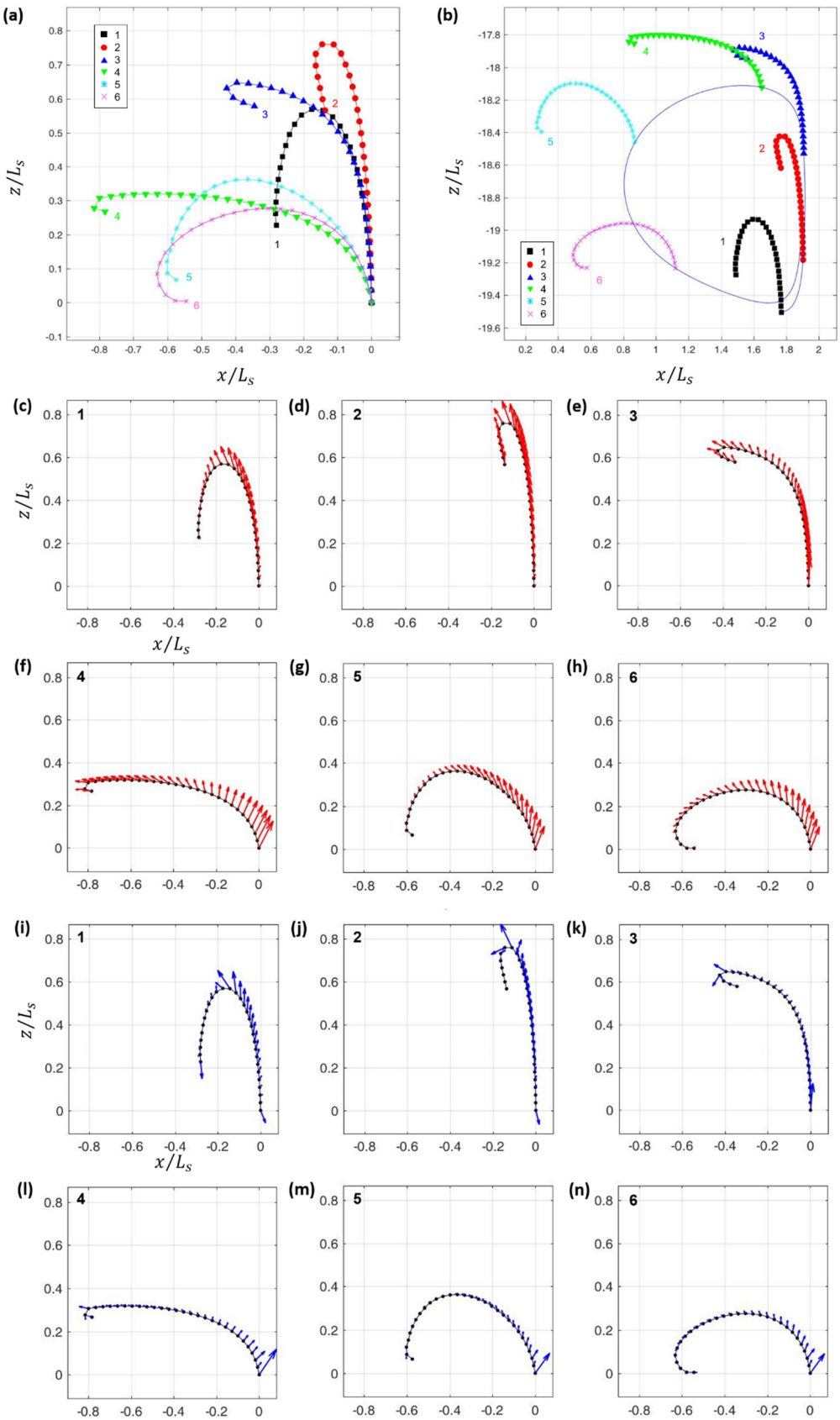

Figure A 22 Trapping $\langle V_z \rangle / V_{z,still} = 0$; (a) Shape of a filament during sedimentation in relative coordinate of the lower end. (b) Shape of a filament during sedimentation in absolute coordinate. (c)-(h): Distribution of the relative velocity vectors of the flow. (i)-(n): Distribution of the force vectors by the flow. $Bn_{vor} = 1.72$ (the number of beads: 30, length: 4.45 m, mass: 0.2 kg, viscosity: 0.5 kg/ms, vortex velocity: $U_0 = 1.5\ m/s$, size of the vortex cell: $L_c/L_s = 2$)

Dynamic Motions in Homogeneous Turbulence

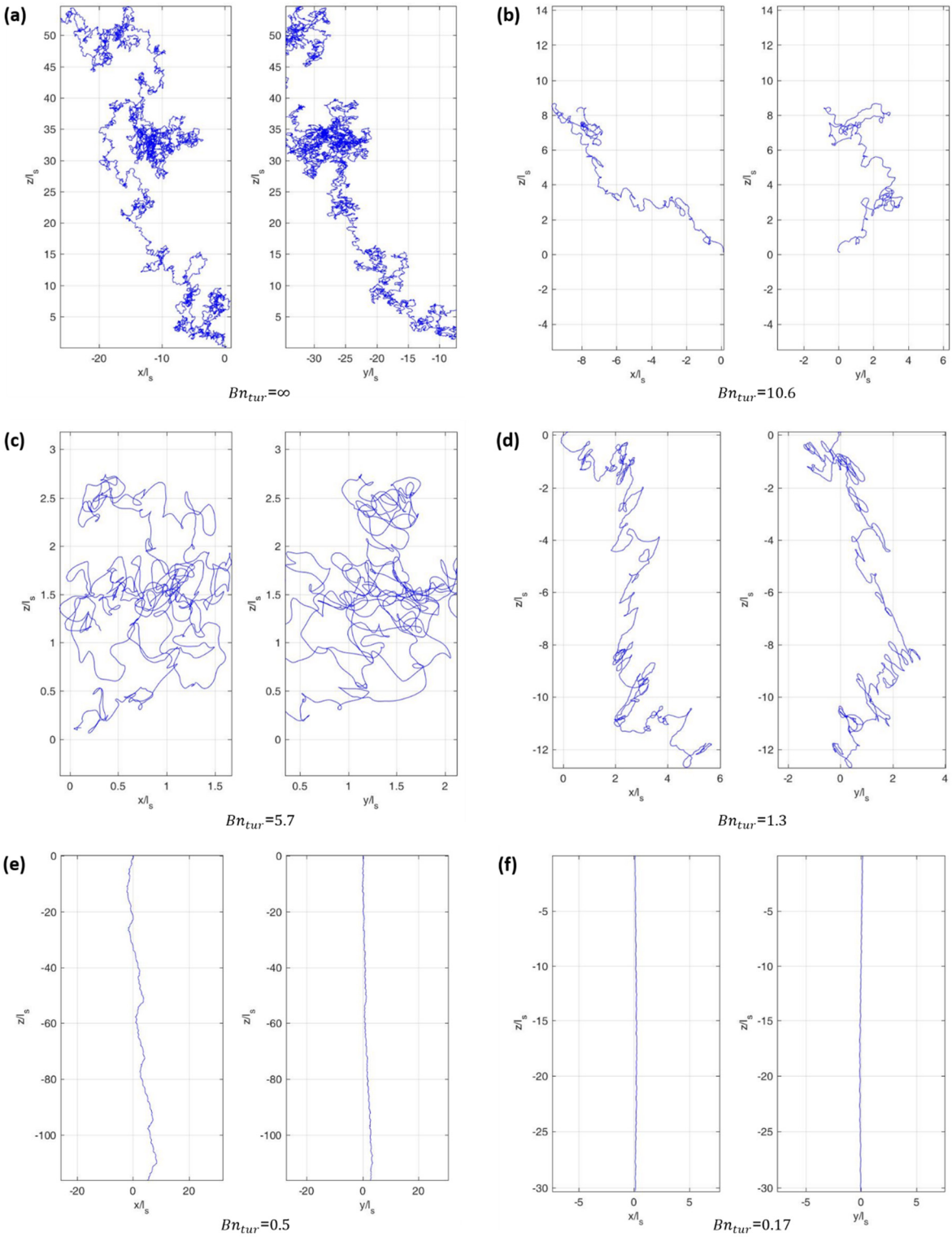

Figure A 23 Trace plots in homogeneous turbulence. (the number of beads: 30, length: 4.45 m, viscosity: 0.2 kg/ms) (a) $Bn_{tur} = \infty$ (mass: $0.61 \times 10^{-4}\ kg$, $\sigma = 0.578$, $u' = 0.381$, $v' = 0.799$, $w' = 0.471$), (b) $Bn_{tur} = 10.6$ (mass: $0.05\ kg$, $\sigma = 0.713$, $u' = 0.633$, $v' = 0.772$, $w' = 0.725$), (c) $Bn_{tur} = 5.7$ (mass: $0.02\ kg$, $\sigma = 0.714$, $u' = 0.510$, $v' = 0.860$, $w' = 0.728$), (d) $Bn_{tur} = 1.3$ (mass: $0.1\ kg$, $\sigma = 0.831$, $u' = 0.735$, $v' = 0.686$, $w' = 1.030$), (e) $Bn_{tur} = 0.5$ (mass: $0.2\ kg$, $\sigma = 0.647$, $u' = 0.712$, $v' = 0.477$, $w' = 0.722$), (f) $Bn_{tur} = 0.17$ (mass: $1\ kg$, $\sigma = 1.012$, $u' = 1.118$, $v' = 1.251$, $w' = 0.509$) ; Unit of σ, u', v', w': $[m/s]$

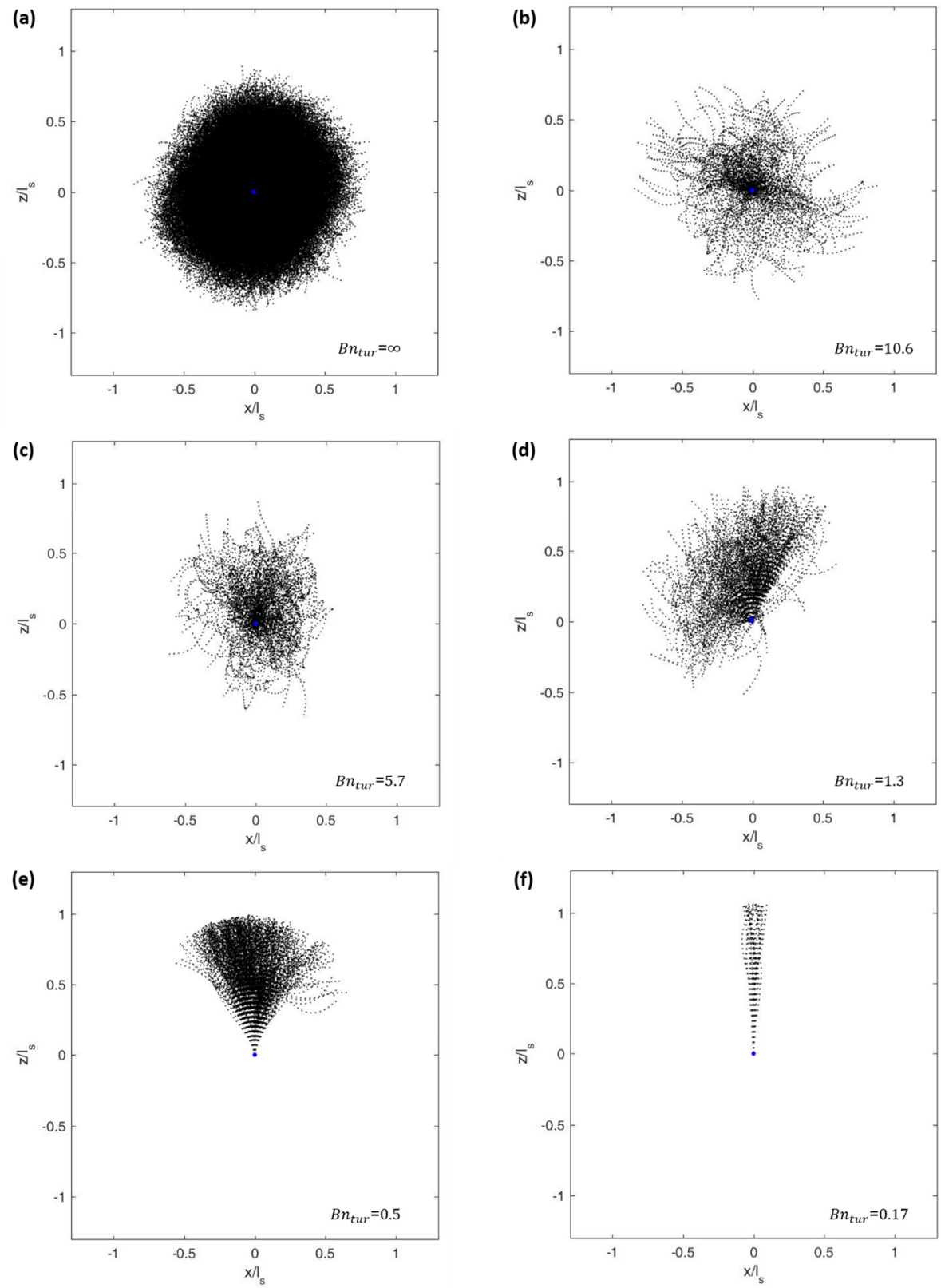

Figure A 24 Projection plots of the filament structure in homogeneous turbulence in the relative coordinate of the lower end. (the number of beads: 30, length: 4.45 m, viscosity: 0.2 kg/ms) (a) $Bn_{tur} = \infty$ (mass: $0.61 \times 10^{-4}\ kg$, $\sigma = 0.578$, $u' = 0.381$, $v' = 0.799$, $w' = 0.471$), (b) $Bn_{tur} = 10.6$ (mass: $0.05\ kg$, $\sigma = 0.713$, $u' = 0.633$, $v' = 0.772$, $w' = 0.725$), (c) $Bn_{tur} = 5.7$ (mass: $0.02\ kg$, $\sigma = 0.714$, $u' = 0.510$, $v' = 0.860$, $w' = 0.728$), (d) $Bn_{tur} = 1.3$ (mass: $0.1\ kg$, $\sigma = 0.831$, $u' = 0.735$, $v' = 0.686$, $w' = 1.030$), (e) $Bn_{tur} = 0.5$ (mass: $0.2\ kg$, $\sigma = 0.647$, $u' = 0.712$, $v' = 0.477$, $w' = 0.722$), (f) $Bn_{tur} = 0.17$ (mass: $1\ kg$, $\sigma = 1.012$, $u' = 1.118$, $v' = 1.251$, $w' = 0.509$) ; Unit of σ, u', v', w': $[m/s]$

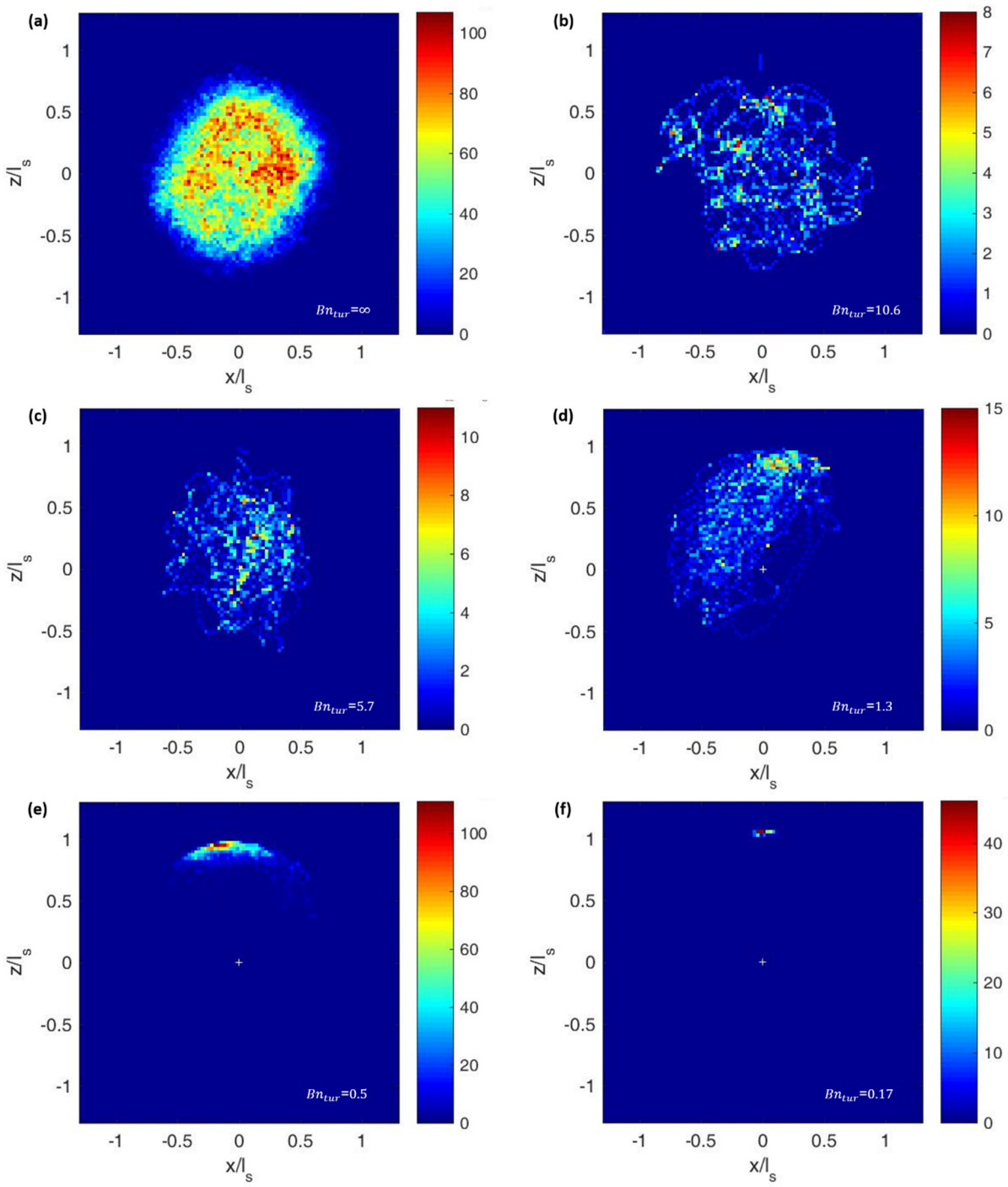

Figure A 25 Projected spatial frequency of the end point of the filament. (the number of beads: 30, length: 4.45 m, viscosity: 0.2 kg/ms) (a) $Bn_{tur} = \infty$ (mass: $0.61 \times 10^{-4}\ kg$, $\sigma = 0.578$, $u' = 0.381$, $v' = 0.799$, $w' = 0.471$), (b) $Bn_{tur} = 10.6$ (mass: $0.05\ kg$, $\sigma = 0.713$, $u' = 0.633$, $v' = 0.772$, $w' = 0.725$), (c) $Bn_{tur} = 5.7$ (mass: $0.02\ kg$, $\sigma = 0.714$, $u' = 0.510$, $v' = 0.860$, $w' = 0.728$), (d) $Bn_{tur} = 1.3$ (mass: $0.1\ kg$, $\sigma = 0.831$, $u' = 0.735$, $v' = 0.686$, $w' = 1.030$), (e) $Bn_{tur} = 0.5$ (mass: $0.2\ kg$, $\sigma = 0.647$, $u' = 0.712$, $v' = 0.477$, $w' = 0.722$), (f) $Bn_{tur} = 0.17$ (mass: $1\ kg$, $\sigma = 1.012$, $u' = 1.118$, $v' = 1.251$, $w' = 0.509$) ; Unit of σ, u', v', w': $[m/s]$

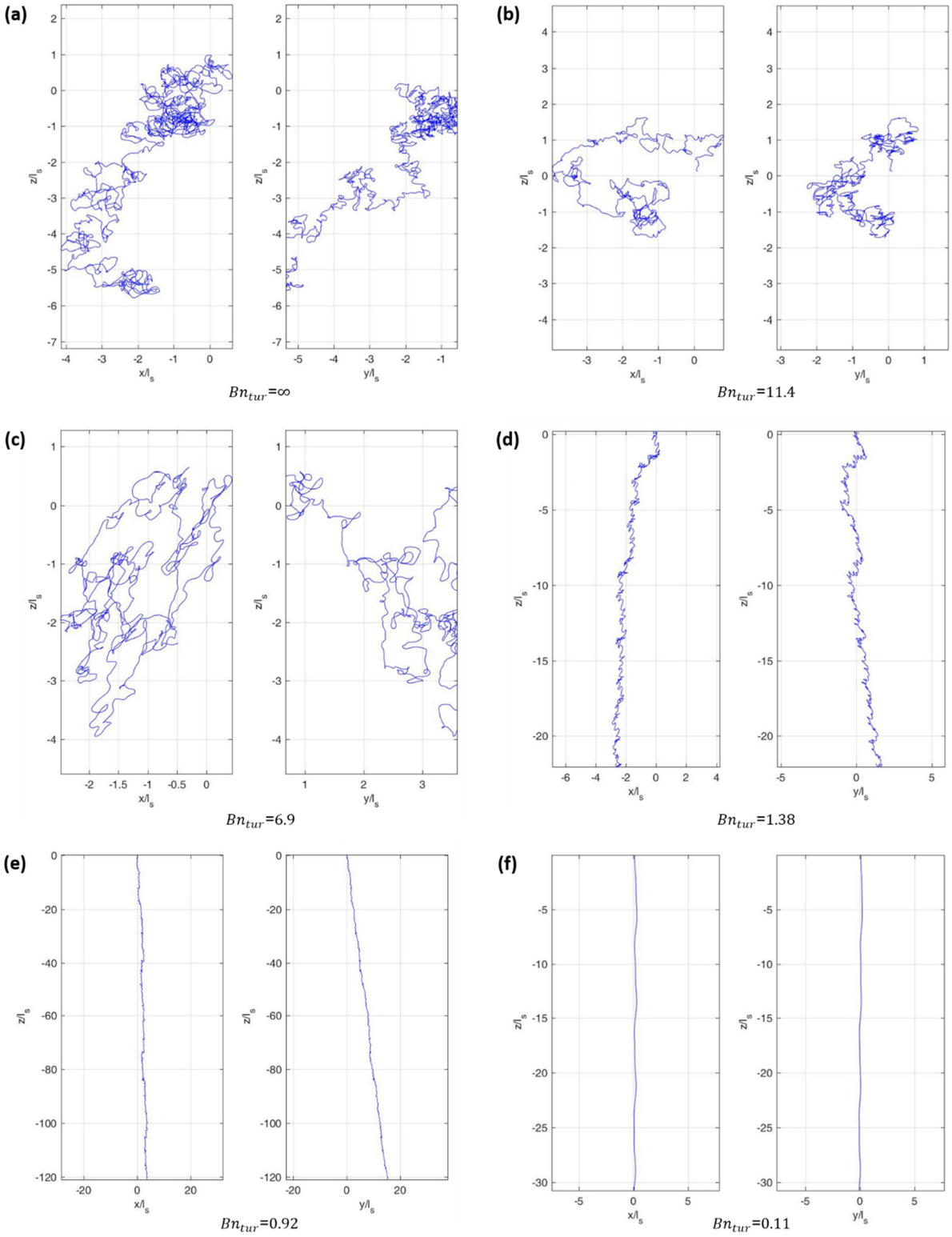

Figure A26 Trace plots in homogeneous turbulence. (the number of beads: 30, length: 4.45 m, viscosity: 0.2 kg/ms) (a) $Bn_{tur} = \infty$ (mass: $0.61 \times 10^{-4}\ kg$, $\sigma = 0.917$, $u' = 0.849$, $v' = 1.109$, $w' = 0.756$), (b) $Bn_{tur} = 11.4$ (mass: $0.01\ kg$, $\sigma = 0.696$, $u' = 0.526$, $v' = 0.961$, $w' = 0.504$), (c) $Bn_{tur} = 6.9$ (mass: $0.02\ kg$, $\sigma = 0.870$, $u' = 0.746$, $v' = 0.929$, $w' = 0.923$), (d) $Bn_{tur} = 1.38$ (mass: $0.1\ kg$, $\sigma = 0.889$, $u' = 0.889$, $v' = 0.804$, $w' = 0.968$), (e) $Bn_{tur} = 0.92$ (mass: $0.2\ kg$, $\sigma = 1.177$, $u' = 1.1302$, $v' = 0.981$, $w' = 1.383$), (f) $Bn_{tur} = 0.11$ (mass: $1\ kg$, $\sigma = 0.637$, $u' = 0.479$, $v' = 0.844$, $w' = 0.524$) ; Unit of σ, u', v', w': $[m/s]$

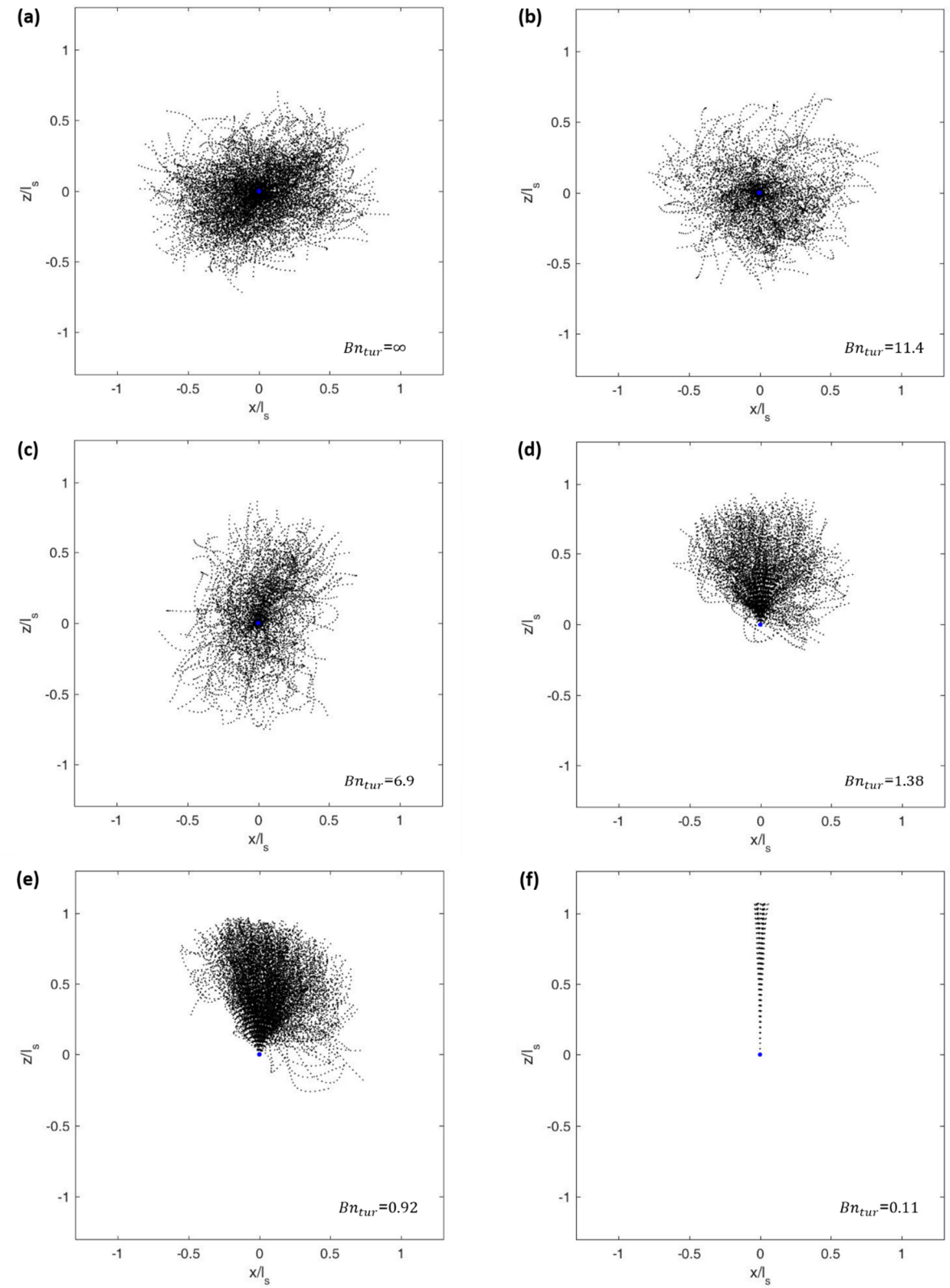

Figure A 27 Projection plots of the filament structure in homogeneous turbulence in the relative coordinate of the lower end. (the number of beads: 30, length: 4.45 m, viscosity: 0.2 kg/ms) (a) $Bn_{tur} = \infty$ (mass: $0.61 \times 10^{-4}\ kg$, $\sigma = 0.917$, $u' = 0.849$, $v' = 1.109$, $w' = 0.756$), (b) $Bn_{tur} = 11.4$ (mass: $0.01\ kg$, $\sigma = 0.696$, $u' = 0.526$, $v' = 0.961$, $w' = 0.504$), (c) $Bn_{tur} = 6.9$ (mass: $0.02\ kg$, $\sigma = 0.870$, $u' = 0.746$, $v' = 0.929$, $w' = 0.923$), (d) $Bn_{tur} = 1.38$ (mass: $0.1\ kg$, $\sigma = 0.889$, $u' = 0.889$, $v' = 0.804$, $w' = 0.968$), (e) $Bn_{tur} = 0.92$ (mass: $0.2\ kg$, $\sigma = 1.177$, $u' = 1.1302$, $v' = 0.981$, $w' = 1.383$), (f) $Bn_{tur} = 0.11$ (mass: $1\ kg$, $\sigma = 0.637$, $u' = 0.479$, $v' = 0.844$, $w' = 0.524$) ; Unit of σ, u', v', w': $[m/s]$

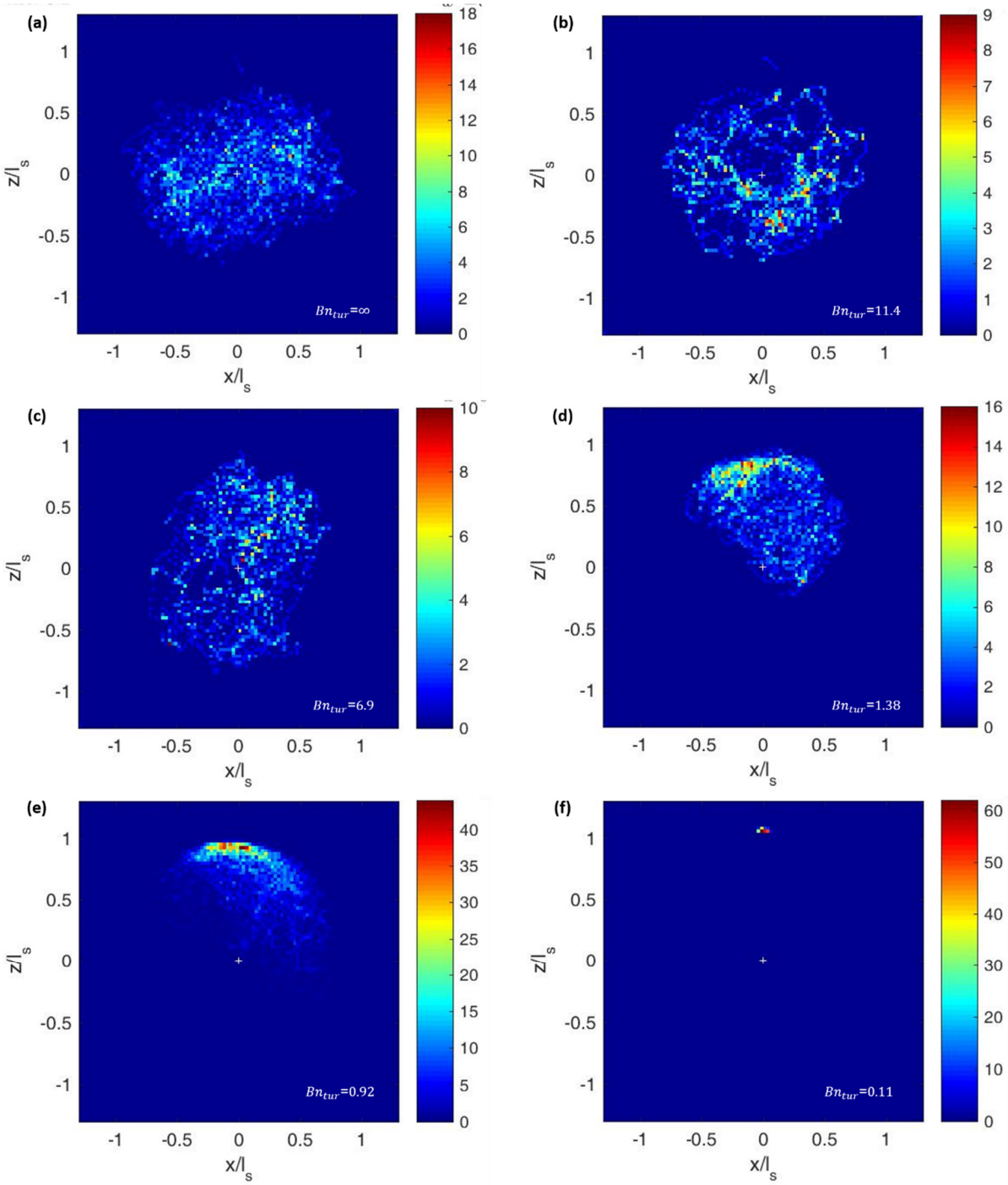

Figure A 28 Projected spatial frequency of the end point of the filament. (the number of beads: 30, length: 4.45 m, viscosity: 0.2 kg/ms) (a) $Bn_{tur} = \infty$ (mass: $0.61 \times 10^{-4}\ kg$, $\sigma = 0.917$, $u' = 0.849$, $v' = 1.109$, $w' = 0.756$), (b) $Bn_{tur} = 11.4$ (mass: $0.01\ kg$, $\sigma = 0.696$, $u' = 0.526$, $v' = 0.961$, $w' = 0.504$), (c) $Bn_{tur} = 6.9$ (mass: $0.02\ kg$, $\sigma = 0.870$, $u' = 0.746$, $v' = 0.929$, $w' = 0.923$), (d) $Bn_{tur} = 1.38$ (mass: $0.1\ kg$, $\sigma = 0.889$, $u' = 0.889$, $v' = 0.804$, $w' = 0.968$), (e) $Bn_{tur} = 0.92$ (mass: $0.2\ kg$, $\sigma = 1.177$, $u' = 1.1302$, $v' = 0.981$, $w' = 1.383$), (f) $Bn_{tur} = 0.11$ (mass: $1\ kg$, $\sigma = 0.637$, $u' = 0.479$, $v' = 0.844$, $w' = 0.524$) ; Unit of σ, u', v', w': $[m/s]$

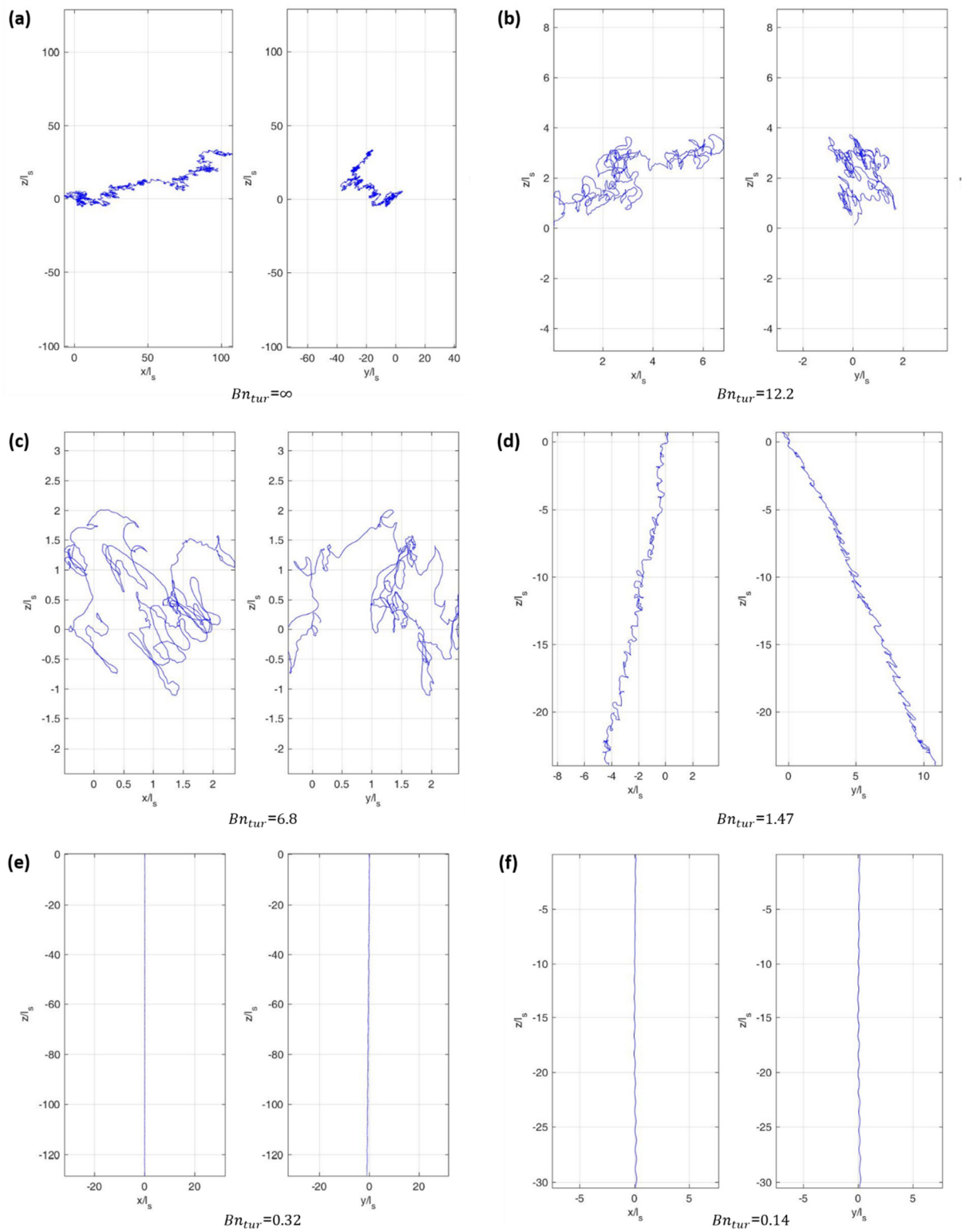

Figure A 29 Trace plots in homogeneous turbulence. (the number of beads: 30, length: 4.45 m, viscosity: 0.2 kg/ms) (a) $Bn_{tur} = \infty$ (mass: $0.61 \times 10^{-4}\ kg$, $\sigma = 0.520$, $u' = 0.687$, $v' = 0.414$, $w' = 0.411$), (b) $Bn_{tur} = 12.2$ (mass: $0.01\ kg$, $\sigma = 0.744$, $u' = 0.614$, $v' = 0.570$, $w' = 0.980$), (c) $Bn_{tur} = 6.8$ (mass: $0.02\ kg$, $\sigma = 0.853$, $u' = 0.802$, $v' = 0.506$, $w' = 1.132$), (d) $Bn_{tur} = 1.47$ (mass: $0.1\ kg$, $\sigma = 0.950$, $u' = 0.766$, $v' = 1.129$, $w' = 0.920$), (e) $Bn_{tur} = 0.32$ (mass: $0.2\ kg$, $\sigma = 0.420$, $u' = 0.405$, $v' = 0.482$, $w' = 0.366$), (f) $Bn_{tur} = 0.14$ (mass: $1\ kg$, $\sigma = 0.830$, $u' = 0.823$, $v' = 0.948$, $w' = 0.700$) ; Unit of σ, u', v', w': $[m/s]$

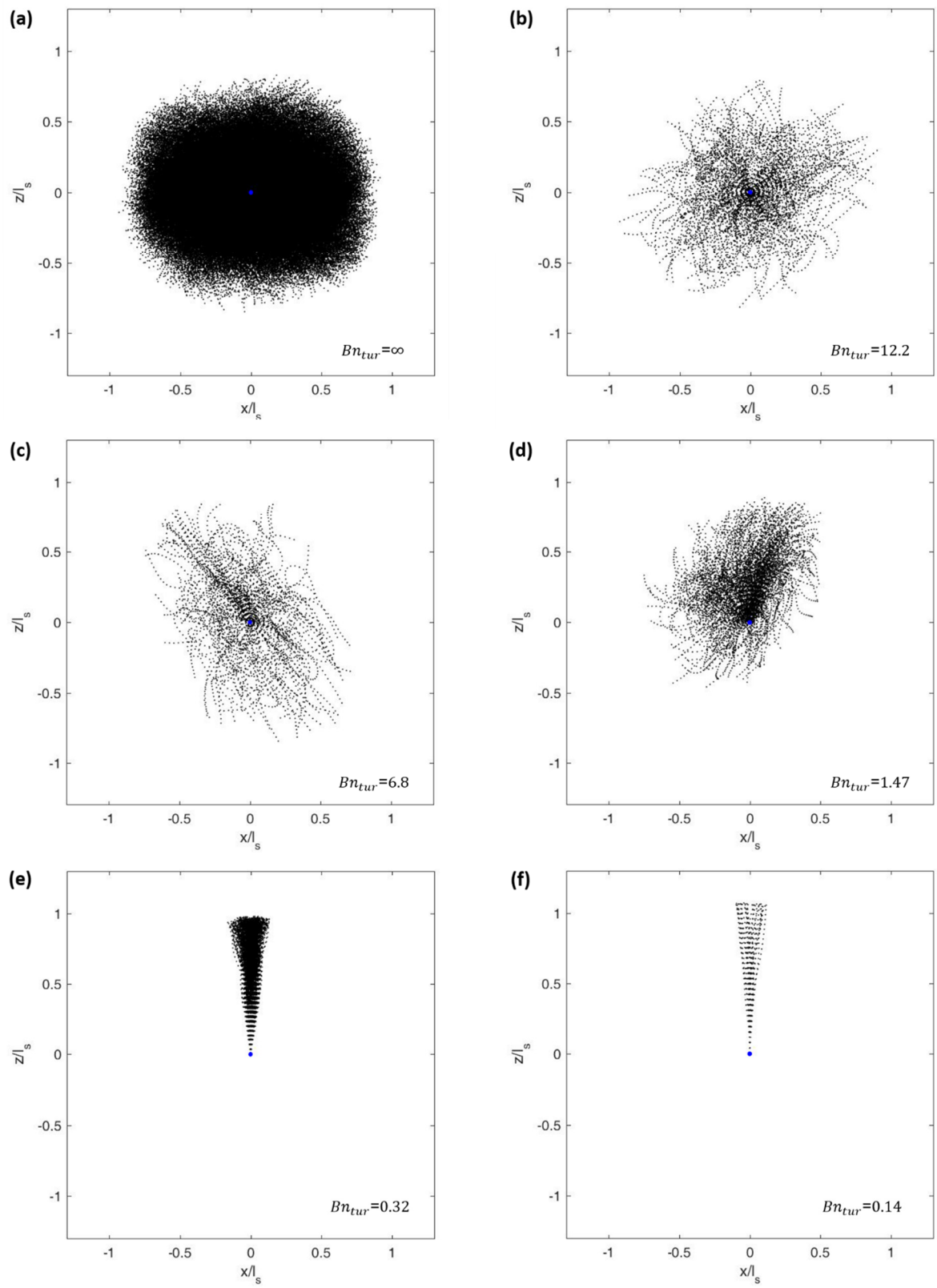

Figure A 30 Projection plots of the filament structure in homogeneous turbulence in the relative coordinate of the lower end. (the number of beads: 30, length: 4.45 m, viscosity: 0.2 kg/ms) (a) $Bn_{tur} = \infty$ (mass: $0.61 \times 10^{-4}\ kg$, $\sigma = 0.520$, $u' = 0.687$, $v' = 0.414$, $w' = 0.411$), (b) $Bn_{tur} = 12.2$ (mass: $0.01\ kg$, $\sigma = 0.744$, $u' = 0.614$, $v' = 0.570$, $w' = 0.980$), (c) $Bn_{tur} = 6.8$ (mass: $0.02\ kg$, $\sigma = 0.853$, $u' = 0.802$, $v' = 0.506$, $w' = 1.132$), (d) $Bn_{tur} = 1.47$ (mass: $0.1\ kg$, $\sigma = 0.950$, $u' = 0.766$, $v' = 1.129$, $w' = 0.920$), (e) $Bn_{tur} = 0.32$ (mass: $0.2\ kg$, $\sigma = 0.420$, $u' = 0.405$, $v' = 0.482$, $w' = 0.366$), (f) $Bn_{tur} = 0.14$ (mass: $1\ kg$, $\sigma = 0.830$, $u' = 0.823$, $v' = 0.948$, $w' = 0.700$) ; Unit of σ, u', v', w': $[m/s]$

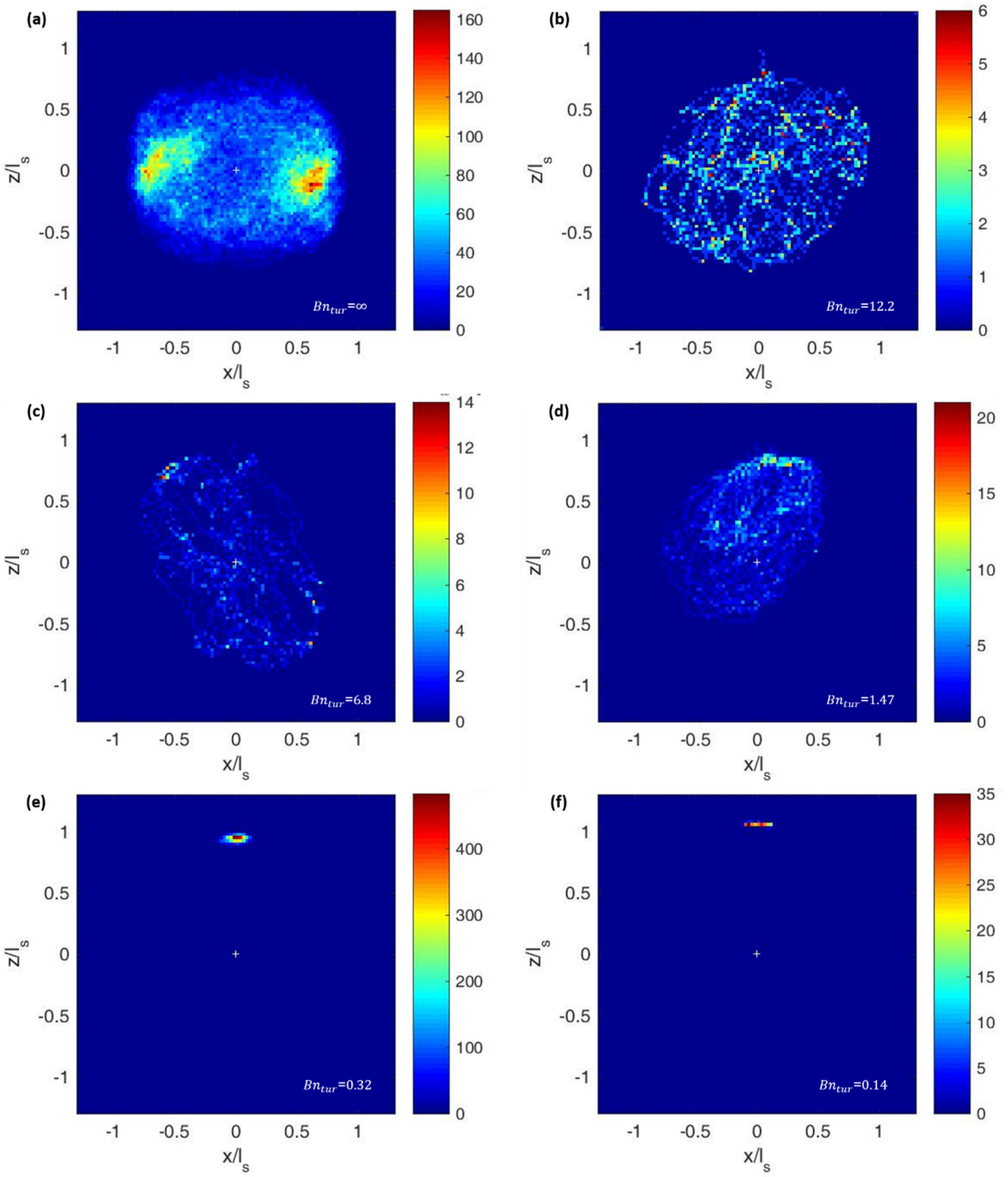

Figure A 31 Projected spatial frequency of the end point of the filament. (the number of beads: 30, length: 4.45 m, viscosity: 0.2 kg/ms) (a) $Bn_{tur} = \infty$ (mass: $0.61 \times 10^{-4}\ kg$, $\sigma = 0.520$, $u' = 0.687$, $v' = 0.414$, $w' = 0.411$), (b) $Bn_{tur} = 12.2$ (mass: $0.01\ kg$, $\sigma = 0.744$, $u' = 0.614$, $v' = 0.570$, $w' = 0.980$), (c) $Bn_{tur} = 6.8$ (mass: $0.02\ kg$, $\sigma = 0.853$, $u' = 0.802$, $v' = 0.506$, $w' = 1.132$), (d) $Bn_{tur} = 1.47$ (mass: $0.1\ kg$, $\sigma = 0.950$, $u' = 0.766$, $v' = 1.129$, $w' = 0.920$), (e) $Bn_{tur} = 0.32$ (mass: $0.2\ kg$, $\sigma = 0.420$, $u' = 0.405$, $v' = 0.482$, $w' = 0.366$), (f) $Bn_{tur} = 0.14$ (mass: $1\ kg$, $\sigma = 0.830$, $u' = 0.823$, $v' = 0.948$, $w' = 0.700$); Unit of σ, u', v', w': $[m/s]$

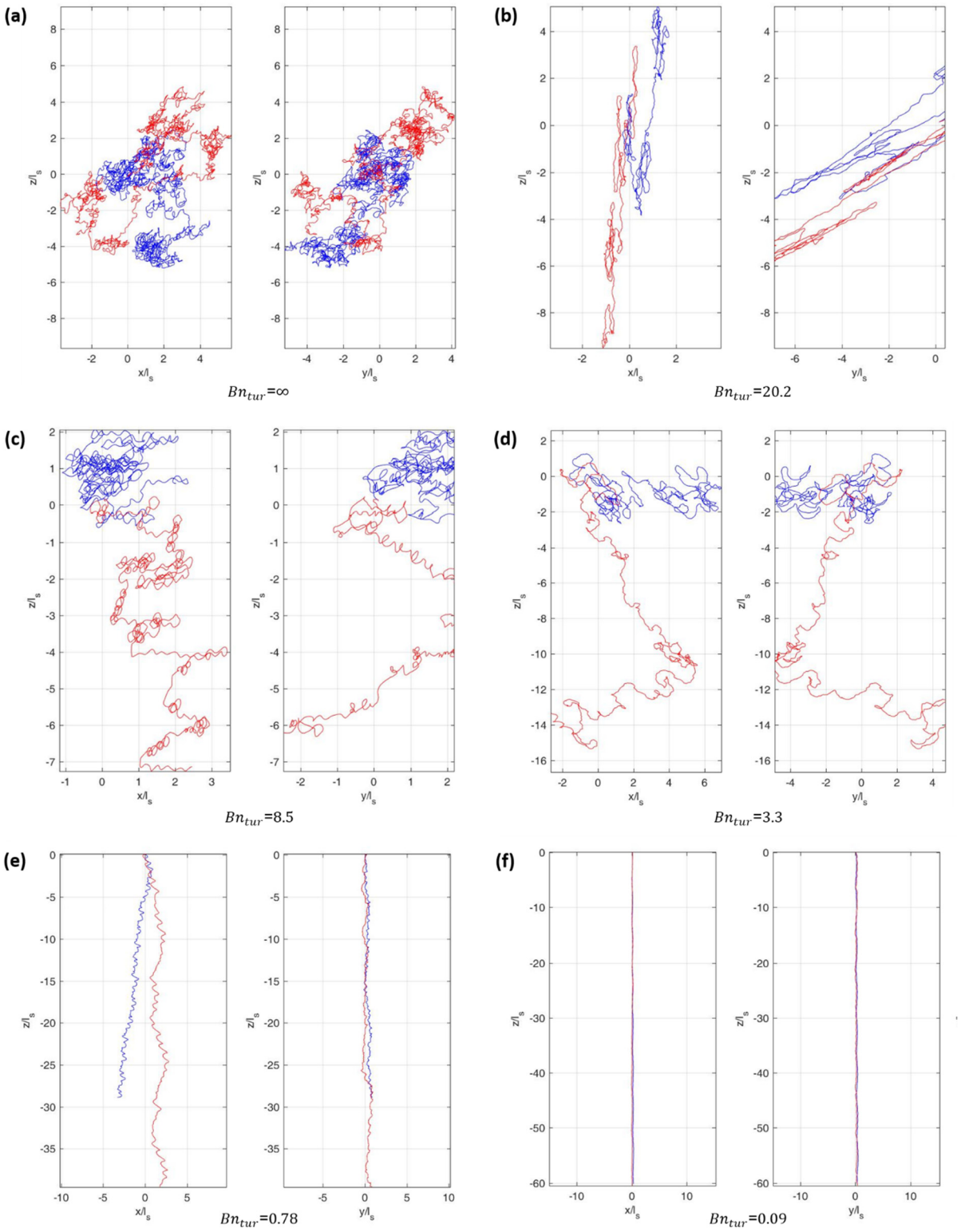

Figure A 32 Trace plots of two different ballooners in an identical homogeneous turbulence. (blue line: a filament-like ballooner, red line: a point-like ballooner; the number of beads: 30, length: 4.45 m, viscosity: 0.2 kg/ms) (a) $Bn_{tur} = \infty$ (mass: $0.61 \times 10^{-4}\ kg$, $\sigma = 0.858$, $u' = 0.803$, $v' = 0.884$, $w' = 0.883$), (b) $Bn_{tur} = 20.2$ (mass: $0.01\ kg$, $\sigma = 1.229$, $u' = 0.475$, $v' = 1.764$, $w' = 1.093$), (c) $Bn_{tur} = 8.5$ (mass: $0.02\ kg$, $\sigma = 1.072$, $u' = 0.984$, $v' = 1.085$, $w' = 1.140$), (d) $Bn_{tur} = 3.3$ (mass: $0.05\ kg$, $\sigma = 1.063$, $u' = 1.106$, $v' = 1.130$, $w' = 0.944$), (e) $Bn_{tur} = 0.78$ (mass: $0.1\ kg$, $\sigma = 0.503$, $u' = 0.593$, $v' = 0.548$, $w' = 0.330$), (f) $Bn_{tur} = 0.09$ (mass: $1\ kg$, $\sigma = 0.554$, $u' = 0.364$, $v' = 0.524$, $w' = 0.716$) ; Unit of σ, u', v', w': $[m/s]$

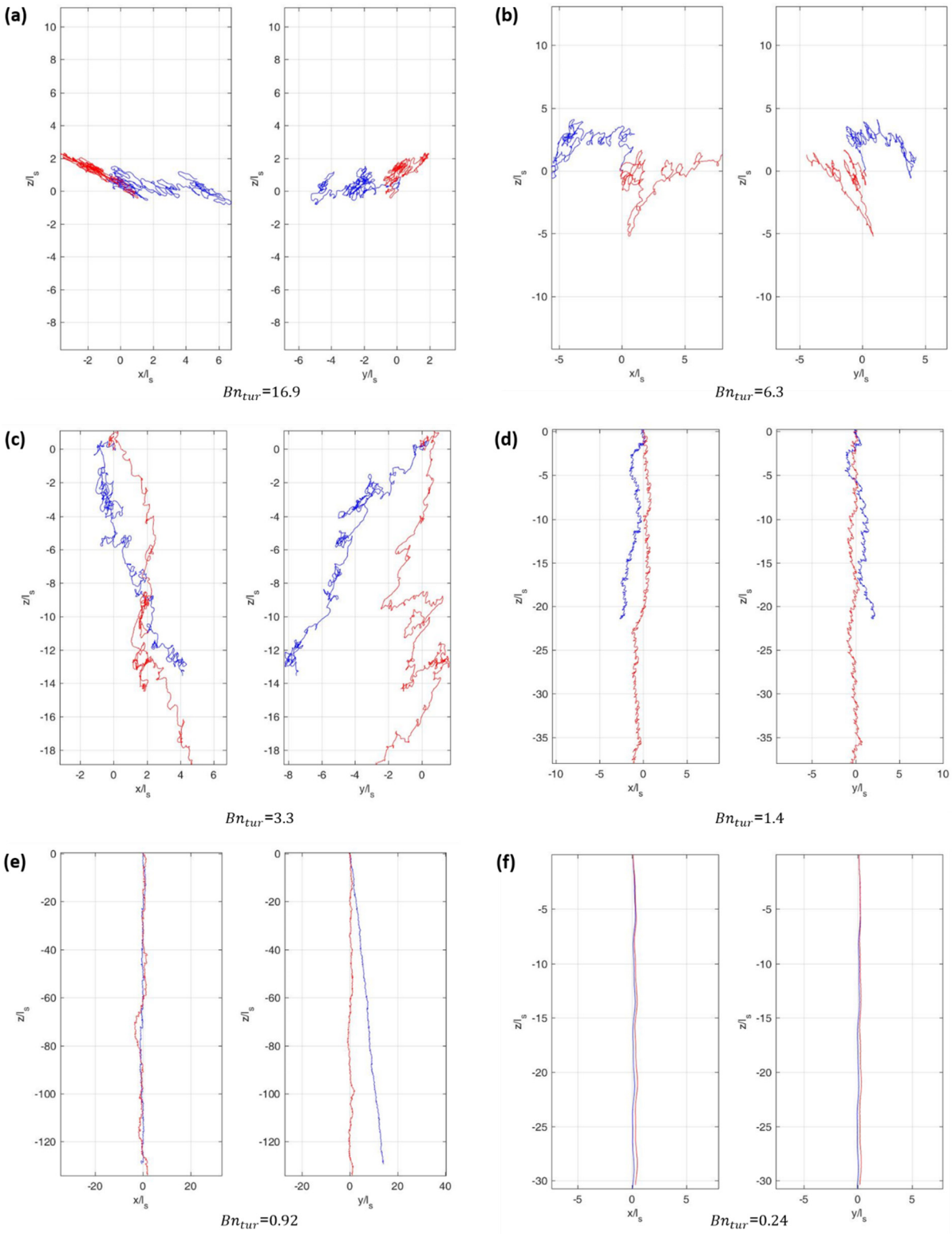

Figure A 33 Trace plots of two different ballooners in an identical homogeneous turbulence. (blue line: a filament-like ballooner, red line: a point-like ballooner; the number of beads: 30, length: 4.45 m, viscosity: 0.2 kg/ms) (a) $Bn_{tur} = 16.9$ (mass: $0.01\ kg$, $\sigma = 1.034$, $u' = 1.365$, $v' = 0.757$, $w' = 0.879$), (b) $Bn_{tur} = 6.3$ (mass: $0.02\ kg$, $\sigma = 0.793$, $u' = 0.695$, $v' = 0.605$, $w' = 1.019$), (c) $Bn_{tur} = 3.3$ (mass: $0.05\ kg$, $\sigma = 1.060$, $u' = 0.849$, $v' = 0.947$, $w' = 1.325$), (d) $Bn_{tur} = 1.4$ (mass: $0.1\ kg$, $\sigma = 0.889$, $u' = 0.889$, $v' = 0.804$, $w' = 0.967$), (e) $Bn_{tur} = 0.92$ (mass: $0.2\ kg$, $\sigma = 1.177$, $u' = 1.130$, $v' = 0.981$, $w' = 1.384$), (f) $Bn_{tur} = 0.24$ (mass: $0.5\ kg$, $\sigma = 0.761$, $u' = 0.860$, $v' = 0.615$, $w' = 0.786$) ; Unit of σ, u', v', w': $[m/s]$

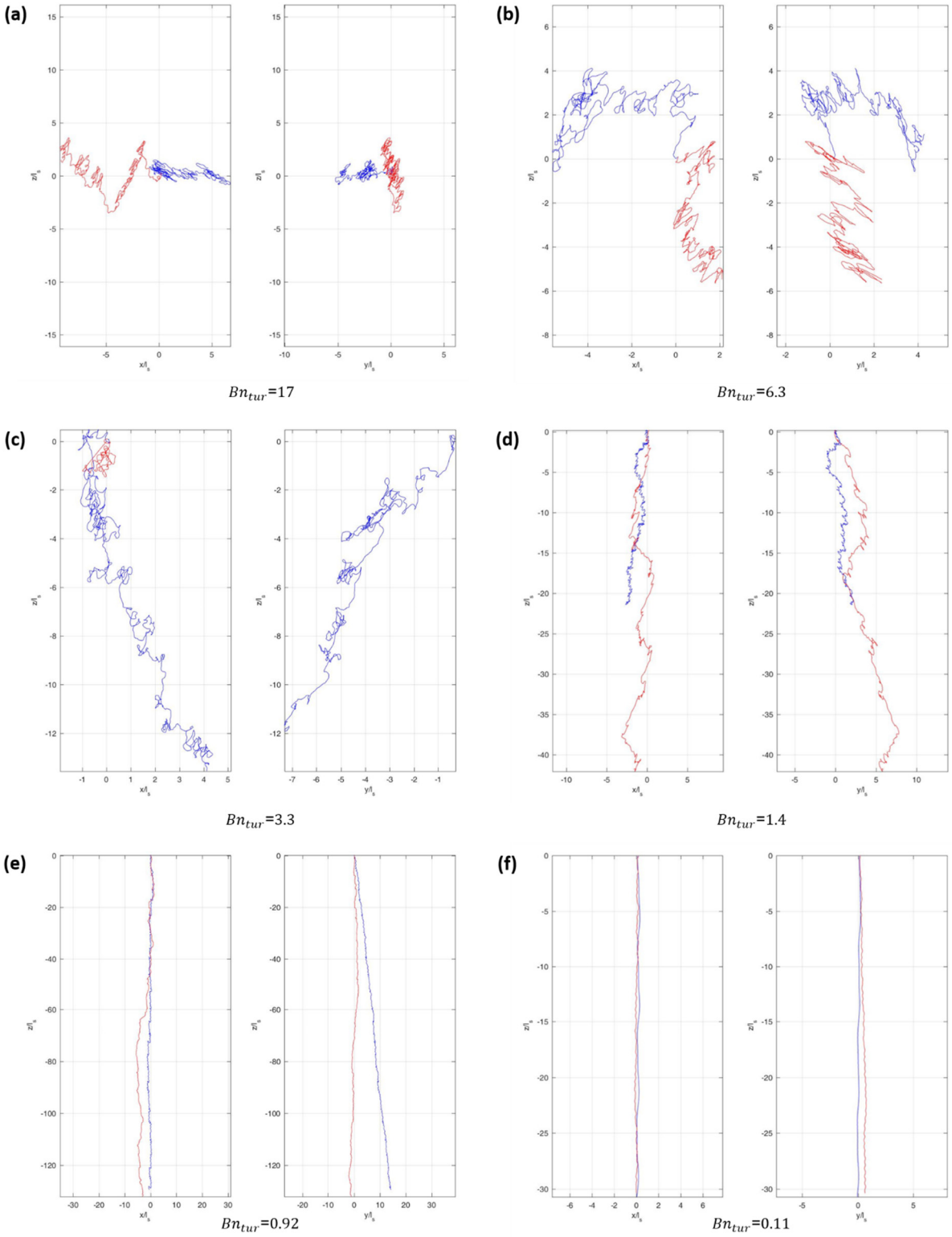

Figure A 34 Trace plots of two different ballooners in an identical homogeneous turbulence. (blue line: a filament-like ballooner, red line: a point-like ballooner; the number of beads: 30, length: 4.45 m, viscosity: 0.2 kg/ms) (a) $Bn_{tur} = 17$ (mass: $0.01\,kg$, $\sigma = 1.034$, $u' = 1.365$, $v' = 0.757$, $w' = 0.879$), (b) $Bn_{tur} = 6.29$ (mass: $0.02\,kg$, $\sigma = 0.793$, $u' = 0.695$, $v' = 0.605$, $w' = 1.019$), (c) $Bn_{tur} = 3.3$ (mass: $0.05\,kg$, $\sigma = 1.060$, $u' = 0.849$, $v' = 0.947$, $w' = 1.325$), (d) $Bn_{tur} = 1.4$ (mass: $0.1\,kg$, $\sigma = 0.889$, $u' = 0.889$, $v' = 0.804$, $w' = 0.967$), (e) $Bn_{tur} = 0.92$ (mass: $0.2\,kg$, $\sigma = 1.177$, $u' = 1.130$, $v' = 0.981$, $w' = 1.384$), (f) $Bn_{tur} = 0.11$ (mass: $1\,kg$, $\sigma = 0.637$, $u' = 0.479$, $v' = 0.844$, $w' = 0.524$) ; Unit of σ, u', v', w': $[m/s]$

Appendix B

Calculation of Anisotropic Particle Drag in the High Knudsen Number Flows

While the drag of a spherical particle is well understood in the wide range of the Knudsen number flow, the drag of an isotropic particle (non-spherical particle) is not well studied. Recently, Tian et al. showed systematic description of that (2017). The rarefaction effect of the air on the nanoscale filament is investigated based on the methodology for an elongated ellipsoid particle and a long cylinder. Here, the methodologies are introduced.

i. Continuum Regime

Drag force of a non-spherical particle in the low-Reynolds number and low Knudsen number flows is described as (B. 1). d_L is a characteristic length of the particle. K refers as a dynamic shape factor and represent the characteristics of its geometry (Tian et al. 2017).

$$F_{D,con} = 3\pi\eta U d_L K \tag{B. 1}$$

a. Elongated Ellipsoid

In the case of an elongated ellipsoid, d_L is the lateral diameter of the ellipsoidal particle. β refers the slenderness (aspect ratio) of the particle (see Eqn. (B. 2)). The dynamic shape factors for the elongated ellipsoid are Eqns. (B. 3) and (B. 4) (Jefferry 1922, Oseen 1927, Tian et al. 2017).

$$\beta = \frac{L}{d_L} \tag{B. 2}$$

$$K_{\perp} = \frac{8(\beta^2 - 1)}{3\left[\left\{(2\beta^2 - 3)\ln\left(\beta + \sqrt{\beta^2 - 1}\right)/\sqrt{\beta^2 - 1}\right\} + \beta\right]} \tag{B. 3}$$

$$K_{\parallel} = \frac{4(\beta^2 - 1)}{3\left[\left\{(2\beta^2 - 1)\ln\left(\beta + \sqrt{\beta^2 - 1}\right)/\sqrt{\beta^2 - 1}\right\} - \beta\right]} \tag{B. 4}$$

b. Long Cylinder

The dynamic shape factor for a long cylinder is as follow (Burgers 1938):

$$K_{\parallel} = \frac{2\beta}{3[ln(2\beta) - 0.72]} \tag{B. 5}$$

ii. Free Molecular Regime

Drag of non-spherical particles in the free molecular regime are expressed as follow (Dahneke 1973a, Tain et al. 2017):

$$F_{D,free} = \frac{1}{2}\pi\eta U d_L K' \tag{B. 6}$$

a. Elongated Ellipsoid

The shape factors for an elongated ellipsoid in the free molecular regime are expressed as the Eqns. (B. 7)-(B. 11) (Dahneke 1973a, Tain et al. 2017).

$$K'_{\perp} = \frac{\beta}{Kn}\left[E_p\left\{4 + \left(\frac{\pi}{2} - 1\right)\alpha\right\} + \frac{G_p}{F_p^2}\left(2 + \frac{4F_p^2 + \pi - 6}{4}\right)\alpha\right] \tag{B. 7}$$

$$K'_{\parallel} = \frac{\beta}{Kn}\left[2E_p\alpha + \frac{G_p}{F_p^2}\left\{F_p^2(4 - 2\alpha) - 4 + \left(3 - \frac{\pi}{2\beta^2}\right)\alpha\right\}\right] \tag{B. 8}$$

$$E_p = \frac{\sin^{-1} F_p}{F_p} \tag{B. 9}$$

$$F_p = \sqrt{1 - \frac{1}{\beta^2}} \tag{B. 10}$$

$$G_p = \frac{1}{\beta} - E_p \tag{B. 11}$$

b. Long Cylinder

The shape factor for a long cylinder in the free molecular regime is as follow (Dahneke 1973a, Tain et al. 2017):

$$K'_{\parallel} = \frac{1}{Kn}\left[\left(2\beta + \frac{\pi}{2} - 2\right)\alpha + 4\right] \tag{B. 12}$$

iii. Transition Regime

The formulation of the transition regime drag for a non-spherical particle is enabled by employing Cunningham correction which has been used for a sphere (Dahneke 1973b). This description well expresses the drag forces of a non-spherical particle in the continuum flow regime and the free molecular regime and also the smooth transition between both flow regimes. The anisotropic effect of a non-spherical particle in the transition regime is expressed by introducing “adjusted sphere” method and varying its diameter (Tian et al. 2017). The Eqns. (B. 13)-(B. 20) show the transition regime drag for an elongated ellipsoidal particle (Fan and Ahmadi 2000).

$$F_{D,tran} = \frac{F_{D,con}}{Cc(d_{adj})} = \frac{3\pi\eta U d_L K}{Cc(d_{adj})} \tag{B. 13}$$

$$Cc(d_{adj}) = 1 + \frac{d_L}{d_{adj}} Kn\left(1.257 + 0.4e^{\frac{-1.1 d_{adj}}{Kn\, d_L}}\right) \tag{B. 14}$$

$$d_{adj\perp} = \frac{1.657 d_L \beta}{16(\beta^2 - 1)}(A \cdot B) \tag{B. 15}$$

$$d_{adj\parallel} = \frac{1.657 d_L \beta}{8(\beta^2 - 1)}(C \cdot D) \tag{B. 16}$$

$$A = \frac{2\beta^2 - 3}{\sqrt{\beta^2 - 1}} \ln\left(\beta + \sqrt{\beta^2 - 1}\right) + \beta \tag{B. 17}$$

$$B = E_p\left[4 + \left(\frac{\pi}{2} - 1\right)\alpha\right] + \frac{G_P}{F_p^2}\left(2 + \frac{4F_p^2 + \pi - 6}{4}\right)\alpha \tag{B. 18}$$

$$C = \frac{2\beta^2 - 1}{\sqrt{\beta^2 - 1}} \ln\left(\beta + \sqrt{\beta^2 - 1}\right) - \beta \tag{B. 19}$$

$$D = 2E_p\alpha + \frac{G_P}{F_p^2}\left[F_p^2(4 - 2\alpha) - 4 + \left(3 - \frac{\pi}{2\beta^2}\right)\alpha\right] \tag{B. 20}$$

Tangential momentum accommodation coefficient (TMAC) is used as a particle momentum accommodation coefficient. The TMAC of the air on flat surface differs according to materials of the surfaces. The value ranges from 0.71 to 0.9 (Acharya et al. 2019). It is regarded that the roughness of the material is related to this variation. The value of 0.8 is used in order to investigate the rarefaction effect of the air on the ballooning fibres among different estimated and measured values (Millikan 1923a, Dahneke 1973a, Karniadakis et al. 2005, Agrawal and Prabhu 2008, Yamaguchi et al. 2011, Hemadri et al. 2018, Acharya et al. 2019).